



Discrete Element Modelling of Geocell-Reinforced Railway Ballast  
and Experimental Examination of Geocell Failure Mechanisms

**Yang Liu**

BSc. Eng. (Hons)

THESIS SUBMITTED IN FULFILMENT OF THE REQUIREMENT FOR THE  
DEGREE OF DOCTOR OF PHILOSOPHY

The University of Adelaide

Faculty of Engineering, Computer and Mathematical Sciences

School of Civil, Environmental and Mining Engineering

October 2018

**Copyright© 2018**

**Yang Liu**

**All rights reserved**

*To my parents  
Jing Liu and Airong Huo,  
my beloved wife Mengjie  
and my family*

**INTENTIONALLY BLANK**



# Table of Contents

---

<b>List of Figures</b>	<b>VII</b>
<b>List of Tables</b>	<b>XV</b>
<b>List of Publications</b>	<b>XVII</b>
<b>Abstract</b>	<b>XIX</b>
<b>Declaration</b>	<b>XXI</b>
<b>Statement of Originality</b>	<b>XXIII</b>
<b>Acknowledgements</b>	<b>XXV</b>
<b>Chapter 1. Introduction</b>	<b>1</b>
1.1 Research Background	3
1.2 Discrete Element Modeling	9
1.3 Research Aims	11
1.4 Thesis Layout	12
<b>Chapter 2. Literature Review</b>	<b>15</b>
2.1 Experimental Study	17
2.1.1 Static loading	20
2.1.2 Cyclic loading	23
2.1.3 Influencing factors	26
2.2 Numerical Simulations	28
2.3 Ballast Degradation & Breakage	30
2.4 Geocell-Reinforced Railway Ballast	37
2.5 Geocell Failure Mechanisms	42
<b>Chapter 3. Three-Dimensional Modelling of Geocell-Reinforced Straight and Curved Ballast Embankments (Paper 1)</b>	<b>46</b>
3.1 Abstract	50
3.2 Introduction	51
3.3 Model Development	54
3.3.1 Particle contact	55
3.3.2 Material calibration	55

3.4	Modeling Procedure	64
3.4.1	Straight embankment	65
3.4.2	Curved embankment	69
3.4.3	Monotonic and cyclic loading	70
3.5	Results and Discussion	73
3.5.1	Straight embankment	73
3.5.2	Curved embankment	86
3.6	Conclusions	96
	Acknowledgement	98
	Notations	99
<b>Chapter 4.</b>	<b>Failure Mechanisms of Geocell Cell-walls and Junctions (Paper 2)</b>	<b>100</b>
4.1	Abstract	104
4.2	Introduction	105
4.3	Experimental Program	108
4.3.1	Materials	109
4.3.2	Testing procedures	111
4.4	Results and Discussion	121
4.4.1	Cell-wall: Uniaxial tensile strength	122
4.4.2	Cell-wall: Trapezoidal tearing strength	125
4.4.3	Cell-wall: Creep test	129
4.4.4	Junctions: Tensile strength	134
4.4.5	Junction: Shear strength	137
4.4.6	Junction: Seam Strength	139
4.4.7	Junction: Split strength	142
4.4.8	Ductility ratio	145
4.5	Conclusions	149
<b>Chapter 5.</b>	<b>Three-Dimensional Discrete Element Modelling of Geocell-Reinforced Ballast Considering Breakage (Paper 3)</b>	<b>152</b>
5.1	Abstract	156
5.2	Introduction	157
5.3	Discrete Element Modeling	160

5.3.1	Contact model .....	160
5.3.2	Materials .....	162
5.3.3	Material calibration .....	168
5.3.4	Ballast chamber model .....	179
5.3.5	Monotonic and cyclic loading .....	183
5.4	Results and Discussion .....	185
5.4.1	Monotonic loading .....	185
5.4.2	Cyclic loading .....	199
5.5	Conclusions .....	212
<b>Chapter 6.</b>	<b>Conclusions .....</b>	<b>214</b>
6.1	Research Contributions .....	216
6.2	Limitations and Recommendations .....	218
<b>References</b>	<b>.....</b>	<b>222</b>
<b>Appendix A: Copy of Paper 1 (as published)</b>	<b>.....</b>	<b>238</b>

**INTENTIONALLY BLANK**

# List of Figures

---

Figure 1.1 Components of a conventional ballasted railway track (Selig & Waters, 1994): (a) longitudinal view; (b) cross-sectional view. ....	4
Figure 1.2 Sources of ballast fouling (Selig & Waters, 1994). ....	5
Figure 1.3 Geocell panel (Yang, 2010a): (a) folded and (b) outstretched. ....	7
Figure 1.4 Typical geocell application in slope stabilization and the force induced by soil movement at different locations (PrestoGeosystems, 2009). ....	8
Figure 1.5 General modelling procedure of Discrete Element Modelling (Itasca, 2009b). ....	10
Figure 2.1 Typical testing setup in existing experimental study (Yang, 2010b) ....	20
Figure 2.2 Schematics of the laboratory testing program (Indraratna et al., 2015) ....	25
Figure 2.3 Ballast breakage index (BBI) calculation method (Indraratna et al., 2005) ....	33
Figure 2.4 Particle sizes and shapes considered in the numerical simulation (Hossain et al., 2007) ....	34
Figure 2.5 Triaxial tests capture ballast breakage conducted by Hossain et al. (2007) ....	35
Figure 2.6 Schematic illustration of cyclic triaxial chamber (Indraratna & Nimbalkar, 2013) ....	37
Figure 2.7 Embankment model geometry (Leshchinsky & Ling, 2013a) ....	38
Figure 2.8 Geocell configurations for parametric study (Leshchinsky & Ling, 2013a) ....	39
Figure 2.9 Numerical model of geocell-reinforced railway structure (Leshchinsky & Ling, 2013b) ....	40
Figure 2.10 Calibration model used by Satyal et al. (2018): (a) unreinforced model, (b) reinforced model. ....	41
Figure 2.11 Testing procedures for geocell recommended by Cheng (1993): (a) cell-wall tensile strength test; (b) junction tensile strength test; (c) junction shear strength test; (d) junction seam strength test; (e) junction split strength test. ....	43

Figure 3.1 Information on cell size and wall depth: (a) folded and (b) outstretched (250 W × 250 L × 100 D mm for a cell). . . . .	52
Figure 3.2 Geocell tensile strength test: (a) setup and detail of representative tested specimen; (b) front view in DE simulation; (c) side view in DE simulation. . . . .	56
Figure 3.3 Tensile strength of geocell specimen. . . . .	58
Figure 3.4 Triaxial test specimen simulated by: (a) spheres; (b) clumps. . . . .	61
Figure 3.5 Triaxial compression test results: (a) deviator stress vs. axial strain; (b) volumetric strain vs. axial strain. . . . .	63
Figure 3.6 Straight embankment: (a) cross section; (b) plan view. . . . .	66
Figure 3.7 Geocell panel: (a) at embankment base; (b) 50 mm above the base; (c) 3D perspective: infilled with ballast; and (d) 3D perspective: simulated using spheres. . . . .	68
Figure 3.8 Curved embankment cross section. . . . .	70
Figure 3.9. Forces acted on curved embankment. . . . .	72
Figure 3.10 Vertical displacement for straight embankment under monotonic loading. . . . .	74
Figure 3.11 Vertical displacement for straight embankment under cyclic loading. . . . .	79
Figure 3.12 Contact forces drawn at the same scale for straight embankment after the 20 <sup>th</sup> cycle: (a) unreinforced; (b) geocell at base; and (c) geocell 50 mm above the base. . . . .	82
Figure 3.13 Total displacement vectors drawn at the same scale for straight embankment after the 20 <sup>th</sup> cycle: (a) unreinforced; (b) geocell at base; (c) geocell 50 mm above the base; (d–f) zoomed-in views of the left-hand-side unreinforced sections of three embankments. . . . .	84
Figure 3.14 Total displacement vectors drawn at the same scale for geocell panel after the 20 <sup>th</sup> cycle: (a) geocell on base; (b) geocell at 50 mm above the base. . . . .	85
Figure 3.15 Monotonic loading-induced sleepers movement in curved embankment: (a) Vertical displacement, (b) lateral displacement. . . . .	87
Figure 3.16 Cyclic loading-induced sleepers movement in curved embankment: (a) vertical displacement; (b) lateral displacement. . . . .	88

Figure 3.17 Contact forces drawn at the same scale for the curved embankment after the 20 <sup>th</sup> cycle: (a) unreinforced; (b) geocell at base; and (c) geocell 50mm above the base. ...	90
Figure 3.18 Total displacement vectors drawn at the same scale for the curved embankment after the 20 <sup>th</sup> cycle: (a) unreinforced; (b) geocell at base; and (c) geocell 50mm above the base. ....	91
Figure 3.19 Total displacement vectors drawn at the same scale for geocell panel after the 20 <sup>th</sup> cycle: (a) geocell on base; (b) geocell at 50 mm above the base. ....	92
Figure 3.20 Illustration on the calculation methodology of strain in geocell: (a) before displacement; (b) after displacement. ....	93
Figure 3.21 Locations of maximum strain. ....	95
Figure 4.1. Geocell components. ....	105
Figure 4.3. Junction seam strength test (ASTM, 1993). ....	107
Figure 4.4. Details of the geocell junction ....	110
Figure 4.5. Typical stress-displacement relationship of HDPE (Kwon & Jar, 2008). ....	111
Figure 4.6. University of Adelaide Instron machine. ....	111
Figure 4.7. Uniaxial tensile strength test on geocell wall: (a) specimen configurations, (b) specimens cut from the plain area of the cell-wall, and (c) testing overview. ....	113
Figure 4.8. Trapezoidal tearing strength test: (a) specimens, (b) clamping technique, (c) testing schemes. ....	114
Figure 4.9. Prepared sample and dimension. ....	115
Figure 4.10. Creep test: (a) schematic and (b) test setup. ....	116
Figure 4.11. Junction strength tests: (a) uniaxial tensile strength, (b) shear strength, (c) peel strength and (d) split strength. ....	119
Figure 4.12. Specimens for testing of geocell junctions (from left to right): tensile strength test, split strength test, shear strength test, and seam strength test. ....	119
Figure 4.13. Clamped specimens: (a) tensile strength, (b) shear junction strength, (c) seam strength, and (d) split strength. ....	120

Figure 4.14. Stress–elongation relationship of geocell cell-wall subjected to uniaxial tensile force. ....	122
Figure 4.15. Failure modes of cell-wall specimens subjected to uniaxial tension: (a) and (c) sudden failure, (b) and (d) ductile failure mode of HDPE. ....	124
Figure 4.16. Force–elongation relationship of geocell cell-wall subject to tearing. ....	127
Figure 4.17. Inconsistencies in perforations between two cell-wall specimens: (a) specimen A, (b) specimen B. ....	127
Figure 4.18. The progressive failure of cell-wall specimen CW-TTS-3 at different elongations: (a) 0 mm, (b) 70 mm, (c) 115 mm, (d) 160 mm, and (e) 180 mm. ....	128
Figure 4.19. Failure modes of cell-wall specimens subjected to a tearing force (left to right: specimens 1–5). ....	129
Figure 4.20. Strain-time relationship of three tested specimens. ....	131
Figure 4.21. Final form of specimens: (a) specimen 1 (51 kg loading), (b) specimen 2 (55 kg loading), (c) specimen 3 (59.5 kg loading). ....	133
Figure 4.22. Stress-elongation relationship of the geocell junction subjected to a uniaxial tensile force. ....	134
Figure 4.23. Failure modes of the geocell junction subjected to uniaxial tension: (a) initial stage (pre-peak), (b) failure mode 1 (post-peak), (c) failure mode 2 (post-peak), and (d) ruptured specimen 1. ....	136
Figure 4.24. Force-elongation relationship of geocell junction subjected to shear force. ....	137
Figure 4.25. Failure modes of geocell junctions subjected to shear force: (a) oblique view and (b) side view during testing, and (c) failed specimen. ....	139
Figure 4.26. Stress-elongation relationship of tested geocell junctions when subjected to a peeling force. ....	140
Figure 4.27. Failure modes of geocell junctions subjected to peeling force: (a) during testing, (b) strip failure, (c) weld failure. ....	141
Figure 4.28. Stress-elongation relationship of geocell junctions subjected to splitting. ..	142



Figure 4.29. Failure modes of geocell junctions subjected to a splitting force: (a) during testing; (b) junction failure; (c) cell-wall strip failure. ....	144
Figure 4.30. Cell-wall and junction test results: (a) post-peak elongation versus pre-peak elongation, (b) strength versus pre-peak elongation. ....	148
Figure 5.1 Illustration of contact models: (a) linear contact model, (b) linear parallel-bond contact model. (Adapted from Itasca (2009a)) .....	161
Figure 5.2 Particle size distribution of ballast assemblies in DEM simulation. ....	165
Figure 5.3 DEM model generation: (a) plan view of geocell pocket, (b) geocell-reinforced ballast model, (c) illustration of embedded and ballast filled geocell pocket.....	167
Figure 5.4 Unconfined compressive strength test: (a) test setup, (b) trimmed specimen. ....	169
Figure 5.5 UCS modeling: (a) DEM model, (b) stress–strain relationship of test and simulation results. ....	170
Figure 5.6 Point load test: (a) laboratory test setup, (b) simulation setup illustration. ....	172
Figure 5.7 Schematics of the cell-wall and junction specimens and test setups: (a) cell-wall specimen, (b) cell-wall UTS test setup, (c) junction specimen, and (d) junction SS test setup. ....	174
Figure 5.8 DEM simulation of the UTS test for the cell-wall and junction specimens: (a) cell-wall specimen loaded by moving top loading spheres, and (b) junction specimen loaded by moving top loading spheres.....	176
Figure 5.9 Calibration results of cell-wall and junction models: (a) cell-wall in the UTS test, and (b) junction in the SS test.....	178
Figure 5.10 Ballast chamber model in the DEM simulation: (a) cross-sectional view, and (b) plan view. ....	180
Figure 5.11 Ballast chamber models: (a) Test 1: unreinforced, (b) Test 2: reinforced model with geocell placed on the base, (c) Test 3: reinforced model with geocell placed 100 mm above the base, and (d) Test 4: reinforced model with geocell placed 200 mm above the base.....	182

Figure 5.12 Contact pressure distribution between sleeper and ballast. ....	184
Figure 5.13 Applied axial stress versus stress relationships of all model tests under monotonic loading. ....	186
Figure 5.14 Displacement vectors, drawn at the same scale, for ballast beneath the sleeper subjected to monotonic loading for different model tests: (a) Test 1: unreinforced, (b) Test 2: geocell on the base, (c) Test 3: geocell placed 100 mm above the base, and (d) Test 4: geocell placed 200 mm above the base. ....	189
Figure 5.15 Number of ballast particle breakages versus settlement of all model tests under monotonic loading. ....	190
Figure 5.16 Contact force distribution on a cross-section beneath the sleeper centre: (a) Test 1: geocell unreinforced, (b) Test 2: geocell on the base, (d) Test 3: geocell placed 100 mm above the base, and (d) Test 4: geocell placed 200 mm above the base. ....	194
Figure 5.17 Distribution of ballast breakage under monotonic loading: (a) Test 1: unreinforced, (b) Test 2: geocell on the base, (d) Test 3: geocell placed 100 mm above the base, and (d) Test 4: geocell placed 200 mm above the base. ....	195
Figure 5.18 Deformation and displacement of geocell pocket under monotonic loading: (a) Test 2: geocell on the base, (b) Test 3: geocell placed 100 mm above the base, and (c) Test 4: geocell placed 200 mm above the base. ....	198
Figure 5.19 Locations of geocell rupture: (a) Test 2: geocell on the base, and (b) Test 4: geocell placed 200 mm above the base. ....	199
Figure 5.20 Settlement versus number of cycles relationships: (a) Test 1: unreinforced, (b) Test 2: geocell on the base, (d) Test 3: geocell placed 100 mm above the base, and (d) Test 4: geocell placed 200 mm above the base. ....	201
Figure 5.21 Number of breakages versus number of cycles. ....	203
Figure 5.22 Distribution of ballast breakage under cyclic loading: (a) Test 1: unreinforced, (b) Test 2: geocell on the base, (d) Test 3: geocell placed 100 mm above the base, and (d) Test 4: geocell placed 200 mm above the base. ....	207

Figure 5.23 Geocell displacement and deformation contours under cyclic loading drawn at the same scale: (a) Test 1: unreinforced, (b) Test 2: geocell on the base, (d) Test 3: geocell placed 100 mm above the base, and (d) Test 4: geocell placed 200 mm above the base.· 211

**INTENTIONALLY BLANK**

# List of Tables

---

Table 2.1 Summary of experimental studies on geocell-reinforced structure .....	18
Table 2.2 Summary of numerical studies on geocell-reinforced structure .....	29
Table 2.3 Summary of studies on ballast breakage and degradation using DEM .....	31
Table 2.4 Summary of parametric study conducted by Satyal et al. (2018).....	41
Table 3.1 Micro-properties for geocell .....	57
Table 3.2 Clump templates developed for ballast.....	61
Table 3.3 Micro-properties for ballast clumps.....	64
Table 3.4 Geocell panel strains.....	95
Table 4.1 Specimen dimensions. ....	118
Table 4.2 Specimen designation. ....	121
Table 4.3. Shrinkage ratios of three tested specimens. ....	133
Table 4.4. Ductility ratio for geocell walls and junctions under different test conditions.	147
Table 5.1 Ballast shapes used in DEM simulation. ....	164
Table 5.2 Micro-properties of the materials in the UCS DEM model.....	171
Table 5.3 Micro-properties of parallel-bonds for cell-wall and junction. ....	177
Table 5.4 Load calculation model proposed by Sadeghi (2008). ....	184
Table 5.5 Parameters used for the calculation of maximum contact pressure.....	184
Table 5.6 Ballast breakage and failure strength results categorized by layers under monotonic loading. ....	193
Table 5.7 Ballast breakage results categorized by ballast shape and test model under monotonic loading. ....	196
Table 5.8 Ballast breakage and failure strength results categorized by layers under cyclic loading. ....	205

Table 5.9 Final particle size distributions. ....	208
Table 5.10 Ballast breakage results categorized by ballast shape and test model under cyclic loading. ....	210

# List of Publications

---

**Liu Y, Deng A, Jaksa M. (2015).** Discrete element modelling of geocell-reinforced track ballast under static and cyclic loading. *Proceeding of the 12th Australia–New Zealand Conference on Geomechanics*. Wellington, New Zealand. p. 279–86.

**Liu Y, Deng A, Jaksa M. (2018).** Three-dimensional modelling of geocell-reinforced straight and curved ballast embankments. *Computers and Geotechnics*. 102(53-65). [**as of Chapter 3**]

**Liu Y, Deng A, Jaksa M. (2018).** Failure Mechanisms of Geocell Cell-walls and Junctions (under review) [**as of Chapter 4**]

**Liu Y, Deng A, Jaksa M. (2018).** Three-Dimensional Discrete Element Modeling of Geocell-Reinforced Ballast Considering Breakage (under review) [**as of Chapter 5**]

**INTENTIONALLY BLANK**



# Abstract

---

Rail transport is one of the major means of conveyance of passengers and goods worldwide. Due to the cyclic impact of trains, breakage and rearrangement occurs to the ballast in the trackbed of a railway. As a result, the trackbed is prone to lateral creep and subsidence, which is deemed to undermine the serviceability of rail tracks, and likely cause catastrophic failure of the tracks. To gauge the serviceability of the tracks, a significant amount of expense is spent annually to maintain the serviceability of rail tracks. To minimise this expense, a variety of engineered methods have been suggested and attempted to reinforce the ballast of the trackbed, such as embedment of geosynthetics into the ballast layer. Of these geosynthetics solution, geocells are an emerging and promising option of reinforcing railway ballast. However, to date, the study of geocell-reinforced railway is much limited, possibly due to the high-cost involved in an experimental or field-testing program, and the difficulties of modeling railway ballast with the currently available simulation technics.

To gain an insight of the geocell reinforcement, numerical studies have been carried out to examine the mechanical responses of geocell-reinforced railway ballast. This research adopts a commercially available Discrete Element Method (DEM) software package, *Particle Flow Code (PFC) 3D* to simulate the interaction between the geocell and the discrete particles of ballast. Both monotonic and cyclic loading environments are assessed, and ballast breakage is considered. Displacements and stresses at both micro- and macro-scales are assessed for control and reinforced scenarios. This study demonstrates that the geocell can effectively reduce settlement and ballast breakage. The geocell stiffens its

embedded layer and reduces stress propagation into the underlying layer. The outcomes of this study seek to encourage likely reduction in trackbed thickness and width, to save construction cost and improve the sustainability of the railway trackbed.

Furthermore, the presented study experimentally examines the responses of geocell junctions and cell-walls under various loading conditions. An extensive testing program has been undertaken to assess the geocell junctions and geocell walls. A ductility ratio is developed to measure the rapidness of failure under different short-term loading scenarios for both the cell-wall and junction. The observed failure patterns are presented and an evaluation of the implications of the practical uses of geocells is drawn.

# Declaration

---

I certify that this work contains no material which has been accepted for the award of any other degree or diploma in my name in any university or other tertiary institution and, to the best of my knowledge and belief, contains no material previously published or written by another person, except where due reference has been made in the text. In addition, I certify that no part of this work will, in the future, be used in a submission in my name for any other degree or diploma in any university or other tertiary institution without the prior approval of the University of Adelaide and where applicable, any partner institution responsible for the joint award of this degree.

The author acknowledges that copyright of published works contained within this thesis resides with the copyright holder(s) of those works. I give permission for the digital version of my thesis to be made available on the web, via the University's digital research repository, the Library Search and also through web search engines, unless permission has been granted by the University to restrict access for a period of time.

**Signed:**

**Date:** 29/10/2018

**INTENTIONALLY BLANK**

# Statement of Originality

---

I, Yang Liu, hereby certify that this work contains no material which has been accepted for the award of any other degree or diploma in my name in any university or other tertiary institution and, to the best of my knowledge and belief, contains no material previously published or written by another person, except where due reference has been made in the text. In addition, I certify that no part of this work will, in the future, be used in a submission in my name for any other degree or diploma in any university or other tertiary institution without the prior approval of the University of Adelaide and where applicable, any partner institution responsible for the joint award of this degree.

I give consent to this copy of my thesis when deposited in the University Library, being made available for loan and photocopying, subject to the provisions of the Copyright Act 1968. The author acknowledges that copyright of published works contained within this thesis resides with the copyright holder(s) of those works. I also give permission for the digital version of my thesis to be made available on the web, via the University's digital research repository, the Library Search and also through web search engines, unless permission has been granted by the University to restrict access for a period of time.

**Signed:**

**Date:** 29/10/2018

**INTENTIONALLY BLANK**

# Acknowledgements

---

First and foremost, I owe an enormous debt of gratitude to my primary supervisor, Dr. An Deng, for his time, patience, guidance and continual support throughout my Ph.D. candidature. His encouragement is of great value to me and this thesis would not have been possible without his commitment and contribution. In addition, I especially, wish to appreciate his support during my leave of absence for full-time employment and working away in regional Australia. Although I was unable to fully commit to study during that period of time, his encouragement and prompt assistance made our first publication, as well as the subsequent manuscripts possible. My sincere acknowledgement is also extended to my co-supervisors, Prof. Mark Jaksa, for his insightful feedback and invaluable support during my research candidature as well as proofreading my papers.

I wish to acknowledge Mr. Dale Hudson and other technician staff from the laboratories of the School of Civil, Environmental and Mining Engineering for providing guidance and assistance for the experimental works. In addition, I wish to thank my fellow postgraduate students: Zhongyuan Fu, Can Wang and Changtai Zhou, who have become my friends and provided me with technical support in PFC programming during my candidature. Further, I wish to acknowledge the kind assistance given by the administrative staff at the University of Adelaide.

I would also like express my profound gratitude to my parents, Jing and Airong, for their unconditional and selfless love from the beginning to the end, especially during my study

in Australia in the past nine years. Their dedication, continuous encouragement and support have made my academic achievements possible and inspired me to become a better person.

I am also grateful to my beloved wife, Mengjie. It is a great pleasure and fortune for me to share my life journey with her since we met in Australia nine years ago. Her selfless sacrifices and effort to comfort me during challenging situations have always motivated me to keep moving. For her endless love, patience and support, I am nothing short of grateful.

Finally, I would like to thank the University of Adelaide for rewarding me the Adelaide Graduate Research Scholarship and Australian Government Research Training Program Scholarship, which offered me a peace of mind financially and allowed me to concentrate on my doctoral program.



## **Chapter 1. Introduction**

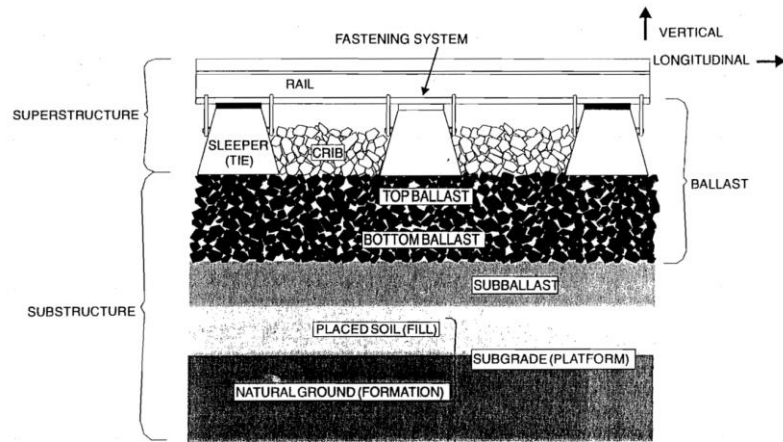
---

**INTENTIONALLY BLANK**

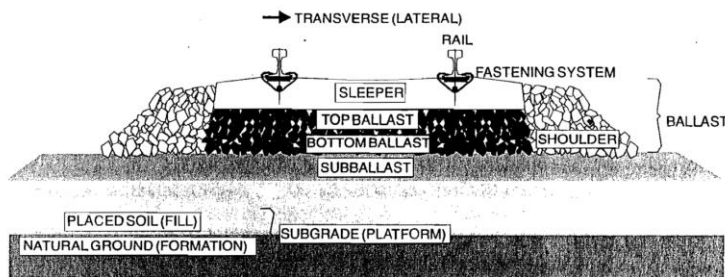
## **1.1 Research Background**

Railway networks have been adopted worldwide as one of the primary transport systems for both freight and passenger purposes. The conventional railway track is constructed on ballast, which is commonly made of gneiss, basalt, granite and quartzite (Raymond & Diyaljee, 1979). A railway structure can be categorised into two major components, superstructure and substructure (Figure 1.1). The superstructure is consisted of rails, sleepers and fastening system while the substructure is consisted of ballast, sub-ballast and subgrade. Among the sub-components of the substructure of a railway track, the ballast is of crucial importance. As per Selig and Waters (1994), the ballast performs many critical functions including but not limited to:

- Provide resistance against vertical (including uplift), lateral and longitudinal forces induced by train traffic;
- Retain structural and geometrical soundness of the superstructure of a railway track by reducing track settlement and lateral deformation;
- Provide immediate drainage to prevent water accumulation;
- Damp traffic loading from the sleeper bearing area for underlying substructure components.



(a)



(b)

Figure 1.1 Components of a conventional ballasted railway track (Selig & Waters, 1994):

(a) longitudinal view; (b) cross-sectional view.

To retain the performance of railroad, adequate and immediate drainage shall be maintained. Numerous studies have confirmed that insufficient drainage commonly leads to reduction in track bearing capacity and excessive pore water pressure, which could severely damage the track geometry and result in catastrophe (Huang et al., 2009; Indraratna et al., 2014). Ballast fouling, the intrusion of fine particles from various sources deteriorate the track drainage. As a consequent of increasing freight capacity and operating speed in recent decades, ballast fouling has inevitably become a primary source of deteriorating track drainage. According to Selig and Waters (1994), ballast fouling is

resulted from various components of a railroad structure, as shown in Figure 1.2. It can be seen that ballast breakdown contributes primarily to the deterioration of rail track condition so that it is of paramount importance to study the breakage behaviour of ballast and possible alleviative approach. Therefore, the topic on improving the performance of the ballast layer has attracted a substantial amount of research. Among these researches, geosynthetics have been adopted as means of reinforcements for railway ballast, including geocell.

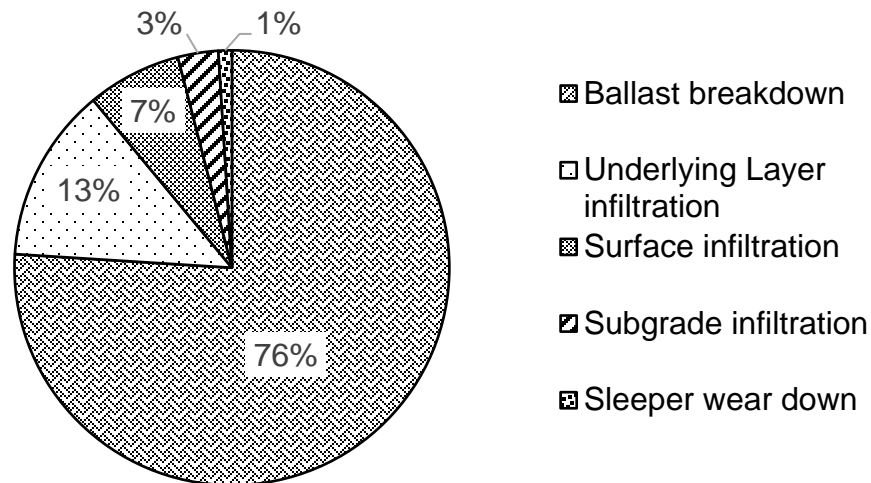


Figure 1.2 Sources of ballast fouling (Selig & Waters, 1994).

Geocell, a cellular confinement system, was originally developed by the US Army Corps of Engineering to increase the bearing capacity of poor subgrade (Webster & Alfords, 1978). Geocell is commonly made of high-density polyethylene (HDPE), polyester or other polymer material. The cell-walls are commonly perforated to allow drainage and provide interlocking with infill materials. Geocell is generally sold in folded form [Figure 1.3 (a)],

whereupon it can be outstretched into its 3-dimensional (3D) shape and is infilled with granular material, as shown in Figure 1.3 (b). Outstretching the material into 3D setting provides space to accommodate infills, erect walls to confine the infills, and in the meantime, weave individual cell infills into an integrated mattress. The integrated mattress has been acknowledged to increase strength and stiffness of the infills, which is in favour of a variety geotechnical engineering application including but not limited to load bearing, slope/channel protection and earth retention. The confinement provided by geocell not only can improve the load-bearing function the infill material, but also can significantly reduce vertical movement of the composite system. The tensile strength of the cell-wall and adjacent geocell pockets provide passive resistance against lateral spreading of infill material, which in turn reduce stress induced by vertical loading propagate into underlying foundation (Mandal & Gupta, 1994). In addition, Yuu et al. (2008) have concluded that geocell can substantially increase the strength and stiffness of a granular layer. Although geocell has presented itself as a possible solution for mitigating engineering issues in railway structure such as settlement and breakage reduction, there has been very limited studies on the geocell-reinforced railway ballast.

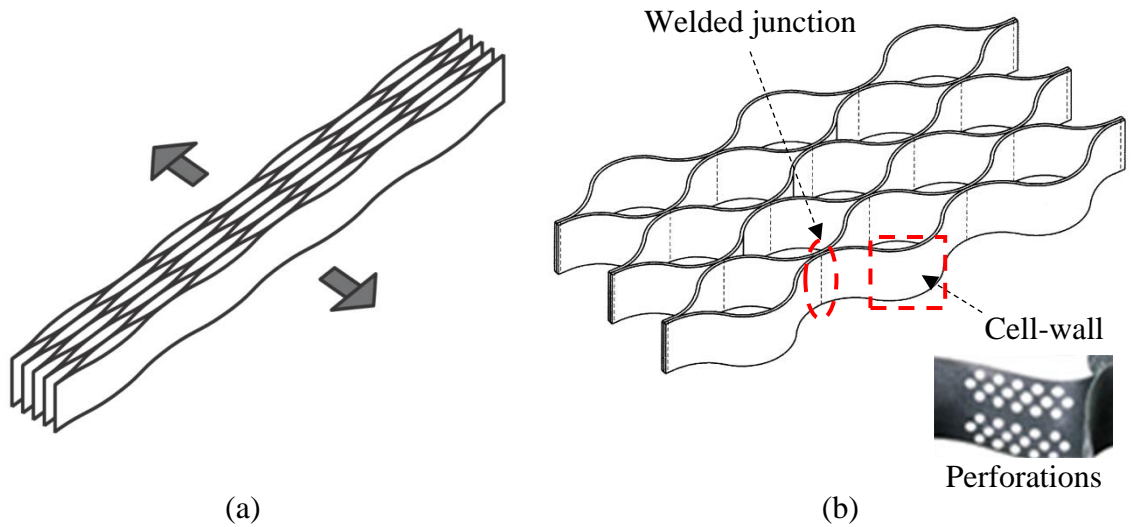


Figure 1.3 Geocell panel (Yang, 2010a): (a) folded and (b) outstretched.

In addition, despite the fact that geocell has been used as reinforcement in a range of geotechnical applications in past few decades, limited studies on its under-load behaviour and failure mechanisms have restricted it from serving infrastructures from cost-effective and safety perspectives. Geocells are typically subjected to gravity load of infill materials on steep slopes or channels. On the slope, as shown in Figure 1.4, both geocell junctions and cell-walls are subjected to soil action from all directions. In these scenarios, geocell is required to withstand high tensile and shear stresses in both the cell-wall and the welded junctions to prevent breaking of cell-walls and separation of junctions. However, there is a lack of standardized testing methods on geocells, and a lack of detailed investigations into their failure mechanisms. Consequently, design uncertainties and unforeseen failure patterns have impeded the application of geocell in some engineering fields, such as railway engineering. Cheng (1993) suggested additional failure mechanisms that could occur in cell-walls and junctions, and corresponding testing procedures. However, these

tests have not been implemented to assess the performance of contemporary geocell products.

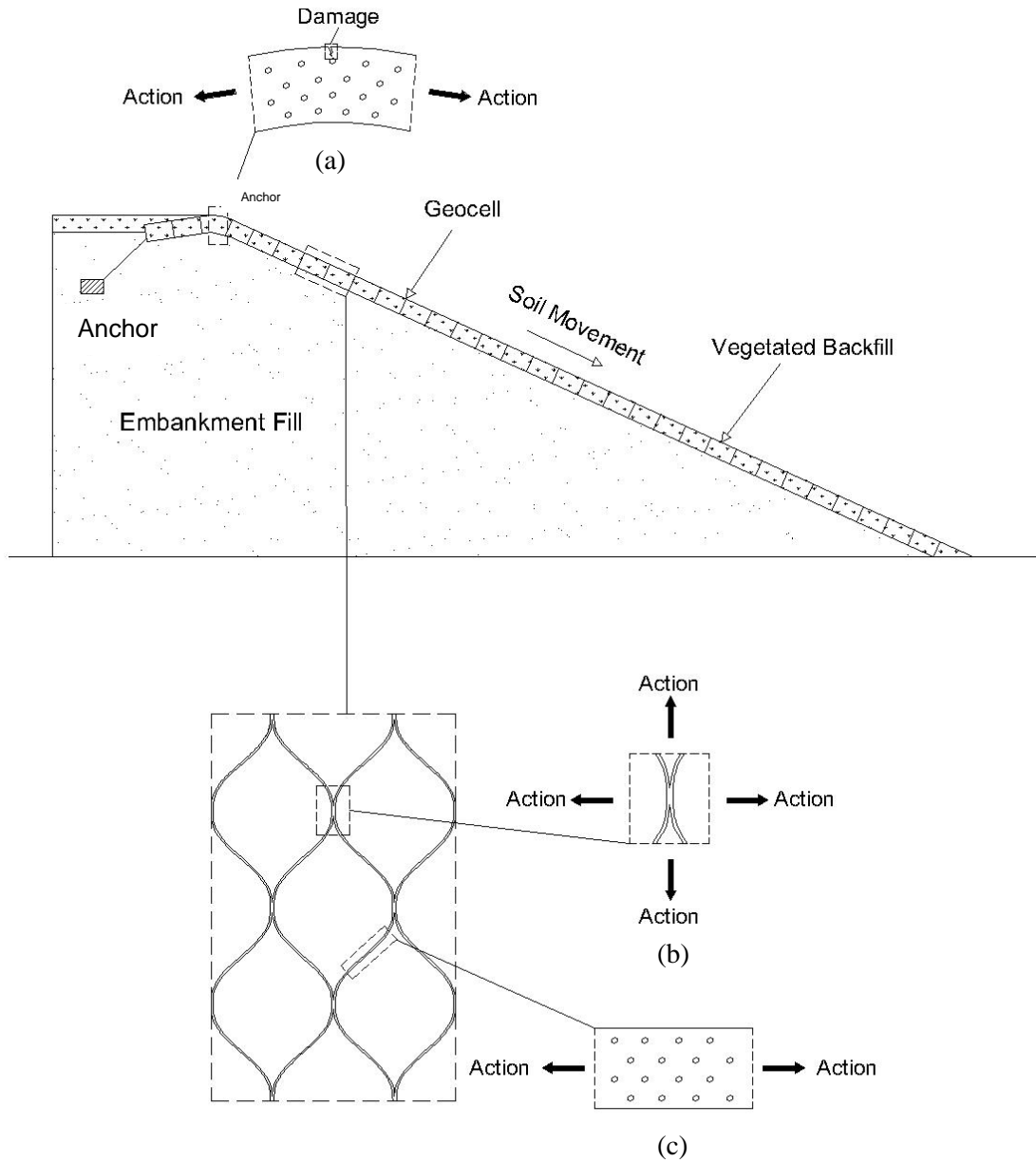


Figure 1.4 Typical geocell application in slope stabilization and the force induced by soil movement at different locations (PrestoGeosystems, 2009).



The current research aims to broaden the scope of research on geocell-reinforced railway structure through Discrete Element Modelling (also known as Distinct Element Modelling). On the other hand, the failure mechanisms of geocell are examined experimentally to facilitate safer and more efficient application in the field of geotechnical engineering and encourage standardization of additional testing scheme on the contemporary geocell products.

## **1.2 Discrete Element Modeling**

Discrete Element Modelling (DEM) was originally introduced by Cundall and Strack (1979a) for solving rock-mechanics problems. Since then, DEM is applied in a range of industry sectors including food manufacturing, natural resource and mining etc. DEM allows finite displacements and rotations of discrete bodies, including complete detachment, and recognizes new contacts automatically as the calculation progresses. This feature is in great favour of simulating soil behaviour and it has therefore become increasingly popular in geotechnical engineering in the past decades. The calculations performed in the DEM alternate between the application of Newton's second law to the particles and a force-displacement law at the contacts. Newton's second law is used to determine the motion of each particle arising from the contact and body forces acting upon it, while the force-displacement law is used to update the contact forces arising from the relative motion at each contact. The general modelling procedure can be referred to Figure 1.5.

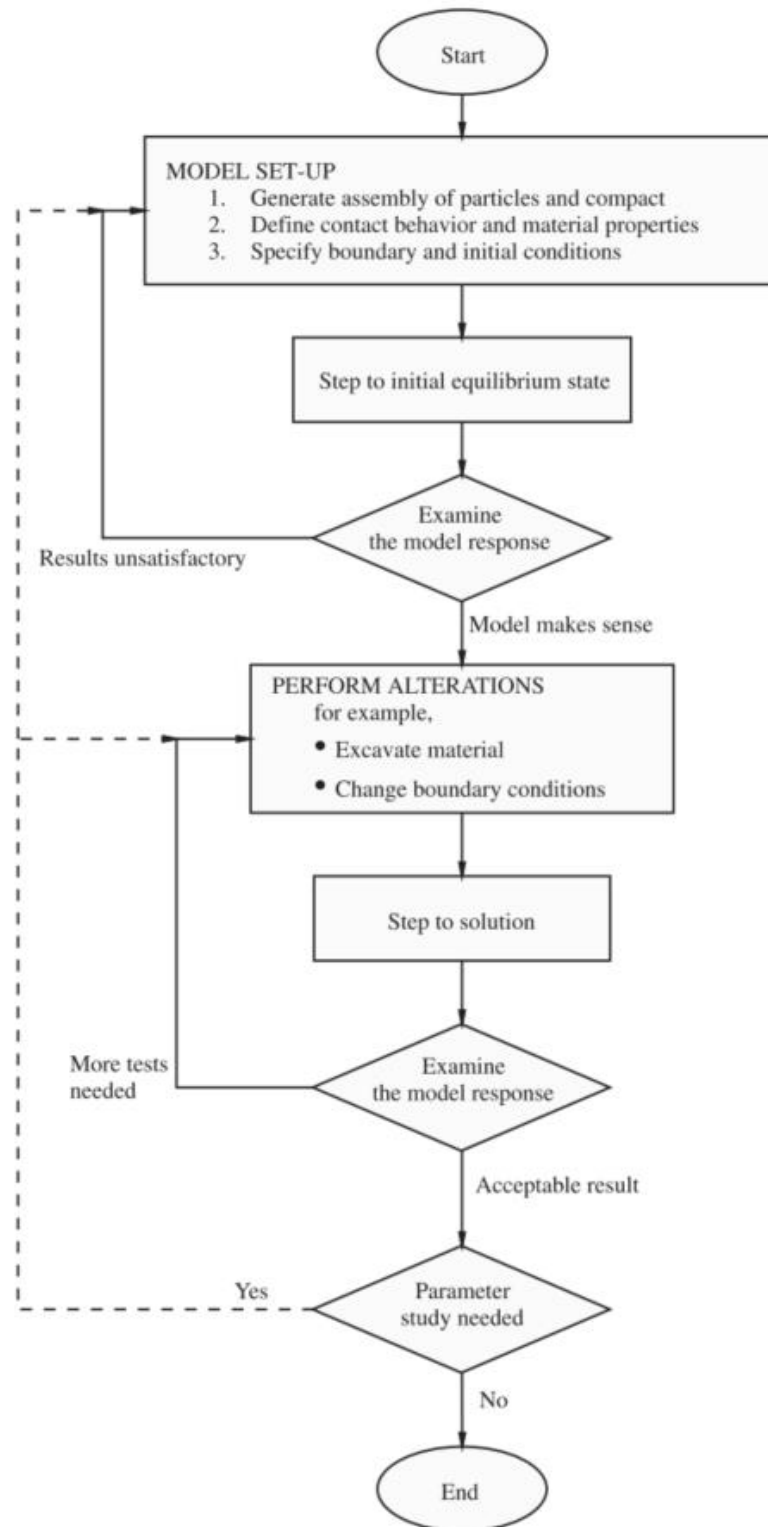


Figure 1.5 General modelling procedure of Discrete Element Modelling (Itasca, 2009b).

In the current research, Particle Flow Code (PFC3D) is adopted to simulate laboratory tests (i.e., for calibration) and pilot-scale ballasted railway structures. Listed are the primary reasons that DEM is of particular interest for the proposed of the current research:

- The modelling does not require invention of complicated constitutive model with obscure parameters and assumptions. Particle assemblies typically require fewer parameters to yield simulation results, whereas similarities with reality. The parameters could be calibrated through small and simple laboratory tests.
- DEM possesses the ability to accurately model large-grained material with high angularity such as ballast. Additonally, ballast breakage can be simulated through bonding
- The geocell can be presented as bonded partical so that micromechanical behaviour can be observed, such as rupture zone and fractures. This will improve the understanding on the vulnerability and failure mechansims of geocell.

### **1.3 Research Aims**

The research activities proposed in this study aim to gain a better understanding on behaviour of geocell and its failure mechanism to facilitate its application in civil engineering field. Specifically, the following research gaps are addressed:

1. To develop and establish a DEM framework used to simulate geocell-reinforced railway ballast;
2. To examine the mechanical responses of geocell-reinforced railway such as settlement response and lateral spreading;

3. To examine the micro-mechanical behaviour of geocell-reinforced railway ballast and conduct detailed analysis on ballast breakage;
4. To conduct parametric study on the reinforcing effects caused by different embedment depth; and
5. To explore the failure mechanism of geocell through experimentation to facilitate future application and standardisation of testing scheme.

#### **1.4 Thesis Layout**

This thesis consists of six chapters. Chapter 1 provides an overview of the background of this research while gaps in past research are identified. Chapter 2 provides a summary of existing literatures with emphasis on the application of DEM in modelling railway ballast, numerical simulation and experimental study of geocell-reinforced ballast as well as currently available testing standards for geocell products.

Chapter 3 includes the first journal paper published in *Computers and Geotechnics*. This paper presents a DEM framework of scaled geocell-reinforced straight and curved railway ballast embankment. The study adopts a simplified geocell panel and multiple shapes to represent varying angularities of ballast infill and models their responses under monotonic and cyclic loading conditions. For the reinforced embankment models, a parametric study is conducted on the geocell embedment depth to examine its influences. The results are presented on both macro- and micro-mechanical levels, including stress/number of cycles versus displacement (in both vertical and lateral directions), displacement vectors and

contact force chains. The simulation results are compared with laboratory test results extrapolated from existing studies where possible.

Chapter 4 includes the second journal paper submitted to *Geotextile & Geomembrane*. This paper presents the outcomes obtained in a test conducted to examine geocell failure mechanisms. Extensive experimentations are conducted in order to examine the strengths and different failure modes of geocell under various loading scenarios. The cell-wall and junction components are tested separately with different loading conditions; the cell-wall component is subjected to uniaxial tensile load, trapezoidal tearing load long-term (creep) gravity load; the junction component is subjected to uniaxial tensile load, shear load, peeling load and split load. A ductility ratio is developed to measure the rapidness of failure under different loading conditions for both cell-wall and junction. Finally, the observed failure patterns and an evaluation of the implications of the practical uses of geocell, are discussed.

Chapter 5 includes the third journal paper submitted to *Computers and Geotechnics*. This paper presents a 3D discrete element model developed to examine performance of geocell-reinforced ballast capturing ballast breakage. A geocell-reinforced railway ballast box is adopted to represent a below-sleeper section of the railway structure. The geocell model employs the realistic shape of a geocell and ballast particles are modelled by breakable clusters with various geometric characters. The geocell-reinforced ballast box is subjected to both monotonic and cyclic loading conditions. Parametric studies are conducted on the geocell embedment depth and ballast shape. For each test, ballast settlement and geocell

responses are recorded and comparisons are made with previous studies. The ballast breakage behaviours, including number of breakages, location distributions, failure strength, breakage diameters and shape effects, are captured and analysed. This study demonstrates that geocell can effectively reduce settlement and ballast breakage, regardless of the loading condition.

Chapter 6 presents a summary of this research program which outlines its outcomes and contributions. Finally, limitations of this research study and recommendations for future study are discussed.

## **Chapter 2. Literature Review**

---

**INTENTIONALLY BLANK**



This chapter presents a review of the existing literature that are relevant to this research. The review is categorised into four parts. Firstly, an overview is presented on the past studies of geocell-reinforced geotechnical structures. Secondly, the application of DEM in modelling railway ballast is summarised and the modelling technics are examined. Thirdly, a detailed assessment of previous studies on geocell-reinforced ballast is provided. And lastly, the current assessment criteria of geocell is reviewed.

## **2.1 Experimental Study**

Experimental studies on geocell dated back to 1970s (Webster & Alfords, 1978; Webster & Watkins, 1977). Their studies mainly focused on the feasibility of introducing confining effect of geocell to reinforce or stabilise infrastructures. To achieve this, the studies considered the improving confinements of poorly-graded beach sand by optimising the properties and geometry of the geocell. Later on, studies conducted from 1980s to 1990s broadened the scopes of research and investigated a number of influencing factors of the geocell, such as aspect ratio, material tensile stiffness of geocell material, strength and density of infill material, subgrade condition, loading type and location, and its conjunctive use with other planar geosynthetic reinforcements. Recent studies have been more focused on the performance of geocell-reinforced geotechnical structures including foundation, pavement, footing, embankment and retaining walls, such as Dash and Bora (2013); Moghaddas Tafreshi et al. (2013), while some attempted to develop analytical solutions (strain-strain behaviour) for the implementation of geocell. A full review of experimental studies can be referred to Table 2.1.

Table 2.1 Summary of experimental studies on geocell-reinforced structure

<b>Reference</b>	<b>Purpose of study</b>	<b>Application</b>	<b>Infill material</b>	<b>Load Type</b>
Webster and Watkins (1977)	Performance evaluation	Pavement	Sand	Static
Webster and Alford (1978)	Performance evaluation	Pavement	Sand	Static
Mandal and Gupta (1993)	Performance evaluation	Foundation	Clay	Static
Dash et al. (2003)	Performance evaluation	Foundation	Clay	Static
Sitharam and Sireesh (2006)	Performance evaluation	Foundation	Sand / clay	Static
Madhavi and Somwanshi (2009)	Performance evaluation	Footing	Sand	Static
Dash et al. (2007)	Performance evaluation	Foundation	Clay	Static
Pokharel et al. (2010)	Determine influencing factors	Foundation	Sand	Static
Yang (2010b)	Performance evaluation	Foundation	Sand / Clay	Static / Cyclic
Sireesh (2010)	Settlement prediction	Foundation	Clay	Static
Dash (2012)	Load-carrying mechanism	Foundation	Sand	Static
Xu and Wang (2013)	Performance under extreme weather	Foundation	unspecified	Static
Marto et al. (2013)	Reinforcing effect	Foundation	Sand	Static / Cyclic
Dash and Bora (2013)	Performance evaluation	Foundation	Clay	Static

Table 2.1 (Continued)

Tafreshi et al. (2014)	Performance evaluation	Foundation	Sand / Granulated tyres	Cyclic
Pokharel (2010)	Design method development	Foundation / Pavement	Sand / Clay	Static / Cyclic
Thakur (2007)	Performance evaluation	Pavement	Recycled asphalt	Static / Cyclic
Bortz et al. (2011)	Reinforcing effect	Pavement	Mix asphalt	Static
Yang et al. (2012)	Performance evaluation	Pavement	Sand	Cyclic
Tanyu, Lau, et al. (2013)	Performance evaluation	Pavement	Gravel	Cyclic
Thakur et al. (2013b)	Creep behaviour	Pavement	Recycled asphalt	Static
Dash et al. (2003)	General behaviour	Circular footing	Sand / clay	Static
Tafreshi and Dawson (2010)	Compare to geotextile reinforcement	Strip footing	Sand	Static
Tafreshi and Khalaj (2012)	Reinforcing effect	Square footing	Sand	Cyclic
Cowland and Wong (1993)	Performance evaluation	Embankment	Clay	Static
Leshchinsky (2012)	Performance evaluation	Embankment	Ballast	Static / Cyclic
Sitharam and Hegde (2013)	Performance evaluation	Embankment	Settled red mud	Static
Rajagopal et al. (1999)	Triaxial behaviour	-	Sand	Triaxial Compression
Wang et al. (2008)	Shear behaviour	-	Silty gravel	Shear
Manju and Latha (2013)	Interfacial friction	-	Sand	Shear

Figure 2.1 provides an overview of typical test setup used in an experimental study. As can be seen, the geocell is generally laid on subgrade soil and backfilled with granular material such as sand and gravel. The infill material is then compacted, and the subgrade model is subjected to static or cyclic loadings. Of the above factors developed to categorise past studies on geocell-based infrastructures, loading type is of major significance in that the factors largely categorise studies into two areas: static loading, and cyclic loading. The two areas of study are discussed in detail below.

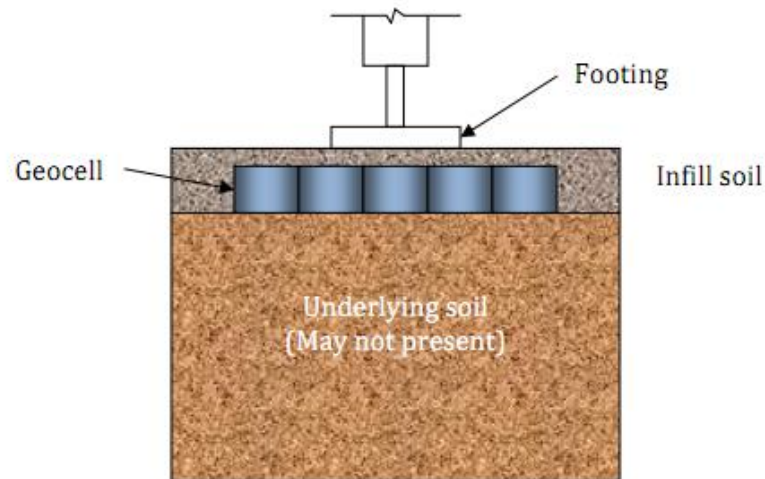


Figure 2.1 Typical testing setup in existing experimental study (Yang, 2010b)

### 2.1.1 Static loading

Static loading is one of the predominant areas with regards to geocell based earthworks. A large portion of studies are identified falling into this area and many of them concentrated on the bearing capacity of geocell-reinforced base courses under static loading. The purposes of these studies were: (1) to demonstrate the benefits of using geocell by comparing the reinforced earthworks with earthworks constructed without, and (2) to

conduct parametric studies so as to optimise the performance of the earthworks when geocells are embedded. To achieve the purposes, investigations were conducted to achieve load-displacement curves of geocell based earthworks established various loading environments. In addition to the base courses reinforced by geocells, soil layers beneath the reinforced courses were also examined with regards to displacement profile and vertical earth pressure distribution. Such studies are beneficial in that they help examine the extent of impact geocell reinforcements bring onto adjacent soil masses.

Most of the previous experimental studies demonstrated that the geocell can significantly increase the bearing capacity and the stiffness of the granular soil (sand and aggregate). For example, Mitchell et al. (1979) showed that the effective modulus of the geocell reinforced sand is about 2 to 3 times that of unreinforced sand. Dash et al. (2003) found that the bearing capacity of geocell reinforced sand could be up to seven times more than the bearing capacity of the unreinforced sand.

Sitharam and Sireesh (2006) reported the influence on the performance of footing rested on different soils if placing a base geogrid layer below geocell mattress. The study showed that regardless of soils tested, the additional layer of base geogrid below the geocell mattress enhances the performance of the footings in terms of load bearing capacity and stiffness of foundation. However, the efficacy of base geogrid reinforcement becomes negligible if the height of the geocell mattress is set high. The provision of an additional base geogrid layer below the geocell reinforcement significantly improves the load bearing capacity of the sand bed, the sand overlying soft clay bed, and the soft clay, compared with

the use of a geocell mattress alone. Furthermore, the base geogrid plus the geocell mattress prevents surface deformation (such as heave/settlement) of fill materials.

Tafreshi and Dawson (2010) compared the benefits of using woven-geotextile formed geocell with using planar woven-geotextile as reinforcement. It shows the geocell reinforcement in reinforcing a sand layer significantly increases load bearing capacity of footings examined in the study, reduces the footings settlement, and decreases the surface heave of the footing bed, relative to planar reinforcement. This comparative investigation implies that less material is needed in a geocell based course compared to a planar one, whereas achieving improvement in bearing capacity and footing settlement.

In addition to the studies on sand and clay, experimental studies, although being limited, were conducted on geocell based gravel/aggregate base courses, such as Leshchinsky (2012). He conducted research on performance enhancement of an embankment embedded with geocell reinforced gravel. His experimental study found that embedding geocell in gravel course of the embankment significantly increased effective stiffness of the course. Geocell confinement effectively reduced the vertical settlement that occurred under the loading plate placed on top of the embankment. Also, geocell can effectively reduce lateral spreading of ballast, especially the ballast beneath the geocell.

Thakur et al. (2013b) studied the vertical stress-displacement response, stiffness, creep behaviour of unreinforced and geocell-reinforced recycled asphalt pavement (RAP) bases, tensile creep behaviour of geocell, and the key factors influencing the creep behaviour of

RAP bases such as the degree of confinement, applied vertical stress, and fill cover to the RAP bases. They concluded that confinement of geocell significantly increased the strength of the sample and reduced its initial deformation. The rate of creep of the RAP and a further reduction could be achieved when the RAP was fully confined. Creep deformations decreased with an increase in the degree of confinement and a decrease in the applied vertical stress. The majority of the creep deformations in geocell-confined RAP bases were attributed to the RAP. Hence, well-graded aggregate helped mitigate creep deformations of geocell-confined RAP.

### **2.1.2 Cyclic loading**

Compared to static loading, geocell based earthworks subjected to cyclic loading has been subjected to fewer studies. This may contribute to the complexity and high cost of running the test (Pokharel, 2010). Sekine et al. (1994) constructed a 3.5 m long, 7 m wide railroad section to investigate the geocell reinforced railroad base. This particular study discovered that the geocell was effective in reducing the deformation of the road bed when the bearing capacity of the subgrade was low. Mhaiskar and Mandalt (1995) also demonstrated the benefit of using geocell in reducing the permanent deformation of pavements under a repeated load. Instead of constructing a road section, they conducted the repeated load test inside a test box. The test results showed that geocell-reinforced base performed distinctly better than the geotextile reinforced base and the unreinforced base.

Researchers including (Dash et al., 2003; Madhavi et al., 2009; Mandal & Gupta, 1993; Sitharam & Sireesh, 2006) mentioned the load spreading action of the reinforced layer and

a subsequent reduction in the vertical stress in the layer underlying the geocell layer. They showed that there is an increased performance on the footing over a buried geocell layer even with the geocell mattress width equal to the width of the footing. The geocell mattress transfers the footing load to a deeper depth through the geocell layer. An increase in the bearing capacity of the geocell mattress with an increase in the ratio of cell height to cell width was observed by Rea and Mitchell (1978) and Mandal and Gupta (1993). Dash et al. (2003) found that the load carrying capacity of the foundation bed increased with a rise in the cell height to diameter ratio, up to a ratio of 1.67, beyond which further improvements were marginal. The optimum ratio reported by Rea and Mitchell (1978) was around 2.25. Dash et al. (2001) reported an optimum ratio of about 1 for geocell supported embankments constructed over soft clays. Table 1 summarises several previous researches about the effect of geocell optimum parameters of soil reinforcement illustrated.

Leshchinsky (2012) also conducted research on the enhancement from utilising geocell in gravel embankment under cyclic loading. It has been reported that under cyclic loading, the reinforced embankments attained stabilisation and exhibited structural resilience more rapidly than without reinforcement. When geocell was absent, vertical settlement and lateral settlement continued despite lower stress amplitude than that applied in the reinforced cases. With geocell confinement, a stable and final settlement and lateral spreading was attained quite rapidly, which implies mobilization of the reinforcement.

Indraratna et al. (2015) conducted large-scale cubical triaxial tests to investigate the behaviour of reinforced and unreinforced subballast under cyclic loading. Granular



material with an average particle size ( $D_{50}$ ) of 3.3 mm and geocell with a depth of 150 mm and nominal area of 463,103 mm<sup>2</sup> were used in this study. The experimental results confirmed that the geocells influenced the subballast behaviour under cyclic loading, particularly at low confining pressure and high frequency. The additional confining pressure induced by the geocell reduced its vertical and volumetric strains. The optimum confining pressure required to reduce excessive volumetric dilation also was identified in this study. An empirical model using a mechanistic approach was proposed to determine the additional confinement induced by the geocells, as well as the practical implications of the experimental outcomes. The detailed testing scheme of this study is presented in Figure 2.2.

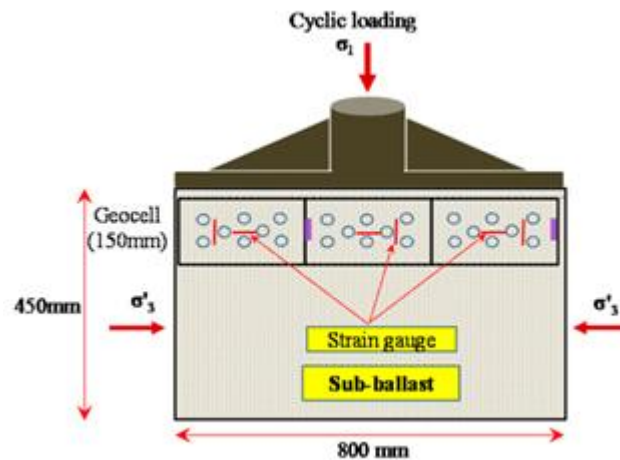


Figure 2.2 Schematics of the laboratory testing program (Indraratna et al., 2015)

The results of this study showed that the plane-strain response was governed by three main factors: (1) the number of load cycles ( $N$ ), (2) the confining pressure ( $\sigma'_3$ ), and (3) the frequency of cyclic loading ( $f$ ). The following conclusions can be drawn from this study:

- An increased confinement offered by geocells helped to reduce the vertical and volumetric strains of subballast. The geocell benefit was observed mainly at low confining pressure ( $\sigma'_3 \leq 15$  kPa) and at higher frequency ( $f \geq 20$  Hz). The geocells had relatively no impact on the behaviour of subballast at an optimum confining pressure ( $\sigma'_3 = 30$  kPa) but were enough to reduce dilation. At this confining pressure no tensile strains were mobilized in the geocell (i.e., no extra confinement).
- Increased frequency led to higher vertical strain at the same number of cycles. At higher frequencies, the zone of stable shakedown in the subballast was reached at a higher number of cycles. Whereas unreinforced samples did not reach a level of stable shakedown even after half a million cycles, the geocell-reinforced specimen reached shakedown depending on the frequency. At a higher confining pressure ( $\sigma'_3 = 30$  kPa), frequency had less influence on the behaviour of unreinforced and reinforced subballast.
- By reinforcing subballast with geocells, the allowable train speed can be increased by approximately 5–25% to that applicable for track that usually has low confinement in the field.
- Geocells were found to have a profound influence on improving resiliency (i.e., increased resilient modulus) and also decreased the corresponding settlement by approximately 12–25% compared with unreinforced subballast.

### 2.1.3 Influencing factors

The influence of the dimension of the cell (or pocket) was studied usually by changing the cell width  $w$  and the cell height  $h$ . Generally, the bearing capacity increases with the increase of cell height and decrease of the cell width. Rea and Mitchell (1978) found that

the optimum cell height to cell width ratio ( $h/w$ ) was around 2.25, beyond which the improvement was less significant. The optimum ratio of footing diameter  $D$  to cell width  $w$  suggested by Rea and Mitchell was about 1.5 to 2.0. Mitchell et al. (1979) performed some laboratory tests on geocell reinforced sand without underlying soft soil and found that the bearing capacity and the modulus of the geocell reinforced soil appeared to increase with the number of joints per unit area under the footing. Mitchell et al. (1979) also confirmed that the optimum cell height to cell width ratio ( $h/w$ ) were 2 to 3, respectively. In addition, for a given geocell height and a geocell width to height ratio, the elastic modulus of the geocell played a more important role than the seam strength in improving the performance of geocell-reinforced soil (Mhaiskar & Mandalt, 1995). Mitchell et al. (1979) found that an aggregate cover on top of the geocell-reinforced section did not contribute towards the increase of the bearing capacity; however, it provided the protection to the geocell. It has also been reported that a denser infill is advantageous. Rea and Mitchell (1978) studied the effect of subgrade stiffness on the ultimate bearing capacity of the geocell-reinforced sand. They observed that higher subgrade stiffness resulted in greater ultimate bearing capacity of reinforced sand and the improvement was valid in case of resistance to repeated loads.

Recent study conduct by Pokharel et al. (2010) concludes factors which influence the performance of geocell under static load. They are: (1) the shape of cell, (2) elastic modulus of geocell, (3) thickness of cell, (4) infill material, and (5) number of cell. The findings are summarised as following:

- Circular geocells provides higher stiffness and bearing capacity for reinforced base courses than elliptical geocells.
- Elastic modulus of geocell plays a major role in affecting the performance of geocell-reinforced base courses. The geocell of higher elastic modulus shows higher stiffness and bearing capacity of reinforced base courses.
- A thinner geocell-reinforced base rested on a firm subgrade shows a higher bearing capacity than a thicker geocell-reinforced base rested on the same subgrade.
- Multi-cell reinforcement could further improve the performance of the sand as compared with single geocell reinforcement.

## **2.2 Numerical Simulations**

The numerical studies on geocell-reinforced structures are summarised in Table 2.2. As can be seen, the number of studies is considerably less than experimental study. However, broader research scope is shown, extended from foundations, pavements and footings to retaining walls and slope stability. In addition, owing to the advent of high performance computer programs and machines, numerical simulation-based studies have been increasing in the last few years.

Table 2.2 Summary of numerical studies on geocell-reinforced structure

Reference	Application	Infill material	Software	Technique / Dimensions
Mhaiskar and Mandalt (1995)	Foundation	Clay	ANSYS	FEM / 3D
Han et al. (2008)	Foundation	Sand/ Grav.	FLAC	FEM / 3D
Latha et al. (2009)	Foundation	Sand	GEOFEM	FEM / 2D
Madhavi and Somwanshi (2009)	Foundation	Sand	FLAC	FEM / 3D
Yang (2010b)	Foundation	Sand / Clay	FLAC	FEM / 3D
Hegde and Sitharam (2015a)	Foundation	Sand	FLAC	FEM / 3D
Han and Yang (2012)	Pavement	Sand	FLAC	FEM / 3D
Leshchinsky and Ling (2013c)	Railway support	Ballast	ABAQUS	FEM / 3D
Dapeng et al. (2013)	Slope stabilization	unspecified	FLAC	FEM / 2D
Mehdipour et al. (2013a)	Slope stabilization	Sand / Clay	FLAC	FEM / 2D
Wang et al. (2013)	Slope stabilization	Sand	ABAQUS	FEM / 3D
Madhavi and Rajagopal (2007)	Embankment	Sand	GEOFEM	FEM / 2D
Leshchinsky (2012)	Embankment	Gravel	ABAQUS	FEM / 3D
Leshchinsky and Ling (2013a)	Embankment	Gravel	ABAQUS	FEM / 3D
Chen, Wu, et al. (2013b)	Retaining wall	Sand	FLAC	FEM / 2D
Knight and Bathurst (1998)	Conduit support	Sand	GEOFEM	FEM / 2D

### **2.3 Ballast Degradation & Breakage**

Railway ballast particles undergo significant breakage under repeated train load. Breakage of ballast particles, especially highly angular fresh ones, causes an increase in settlement, contributing to track degradation. The quantitative analysis of the influence of breakage on the stress-strain properties of ballast can be performed either experimentally or numerically. It is found that the breakage of particles influences the strength and deformation behaviour of rail ballast (Indraratna, Ionescu, et al., 1998; Indraratna et al., 2005; Indraratna & Salim, 2002; Lackenby et al., 2007). It is well established in granular media that when grain breakage occurs, the internal angle of friction and the associated dilation angle decrease, while facilitating further compression (Indraratna & Nimbalkar, 2013). Larger particle sizes with high grain angularity increase the extent of particle breakage during dilation (Indraratna & Salim, 2002; Lackenby et al., 2007; McDowell & Bolton, 1998). It has been reported that highly angular aggregates break easily at the corners even at small confining pressures, leading to a significant reduction of the friction angle (Indraratna et al., 2011). The presence of microfissures in blasted and quarried aggregates also exacerbate breakage during shearing (Marsal 1967; Lade et al. 1996). A number of studies have been carried out on the degradation characteristic of railway ballast in recent decades and these studies are summarized in Table 2.3.

Table 2.3 Summary of studies on ballast breakage and degradation using DEM

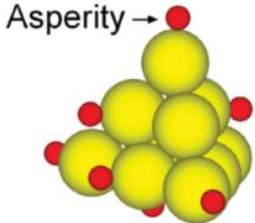
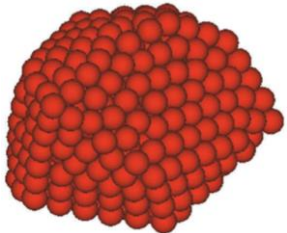
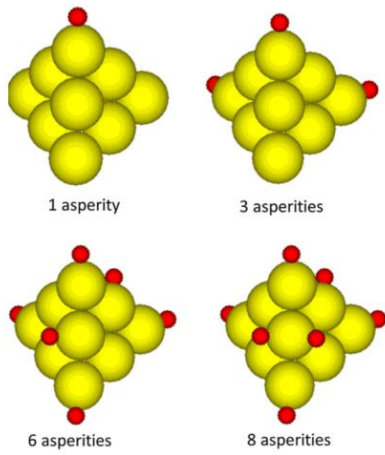
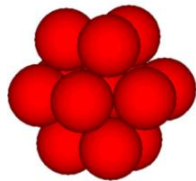
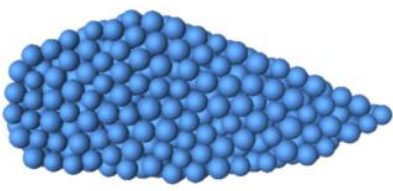
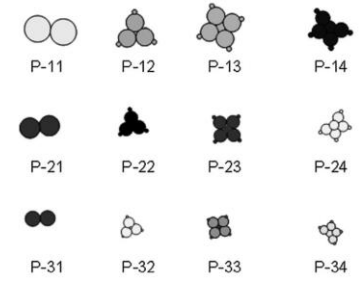

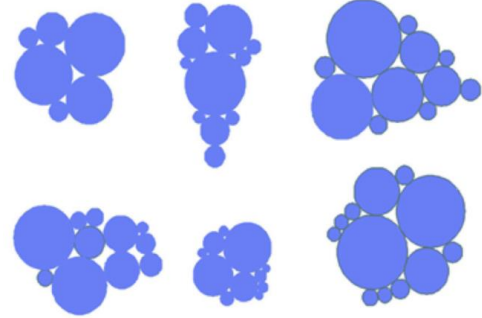
Studies	Ballast model
Lu and McDowell (2008)	 <p>Asperity →</p>
Lu and McDowell (2010)	
Yan et al. (2014)	
McDowell and Li (2016)	 <p>1 asperity      3 asperities 6 asperities      8 asperities</p>
Xu et al. (2017)	
Wang et al. (2017)	

Table 2.3 (Continued)

<p>Hossain et al. (2007)</p>	
<p>Xiao et al. (2017)</p>	
<p>Ngo et al. (2017)</p>	

Indraratna et al. (2005) introduced a new breakage index specifically for railway ballast to quantify the magnitude of degradation. The evaluation of the ballast breakage index (BBI) employs the change in the fraction passing a range of sieve sizes (Figure 2.3). By utilising a linear particle size axis, BBI can be found from Equation 2.1, where the parameters A and B are defined in Figure 2.3.

$$BBI = \frac{A}{A+B}$$

Equation 2.1



where A is shift in the particle size distribution (PSD) curve after the test, and B is potential breakage. On a PSD plot, the potential breakage B is defined by the area between the arbitrary boundary of maximum breakage and the final PSD curve. This particular approach has been widely adopted by Australian railway authorities in recent years for the assessment of trackbed performance.

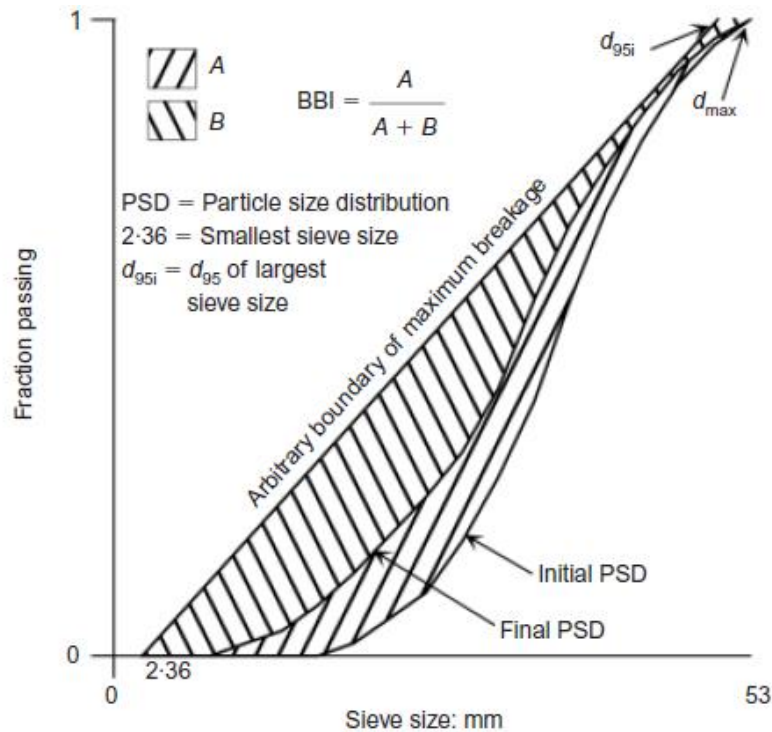


Figure 2.3 Ballast breakage index (BBI) calculation method (Indraratna et al., 2005)

Hossain et al. (2007) employs a DEM approach (PFC 2D) to study the effect of angular ballast breakage on the stress-strain behaviour of a ballast foundation under different confining pressures. The property of angularity that enables particle interlocking contributes to enhanced confining pressure, which is absent in the case of rounded (spherical) particles that offer much less internal friction. Progressive images of breakage

and the grain assembly deformations at various cycles are presented to describe the breakage mechanisms in the ballast foundation. Comparative results of the grain assembly deformation capturing breakage at different loading conditions provide an indication of the acceptable levels of breakage in rail track environments. An assembly of ballast particles of irregular shapes was considered, and the angularity of the particles was modelled by clumping two to nine circular particles together to form single particles of twelve different sizes, as shown in Figure 2.4.

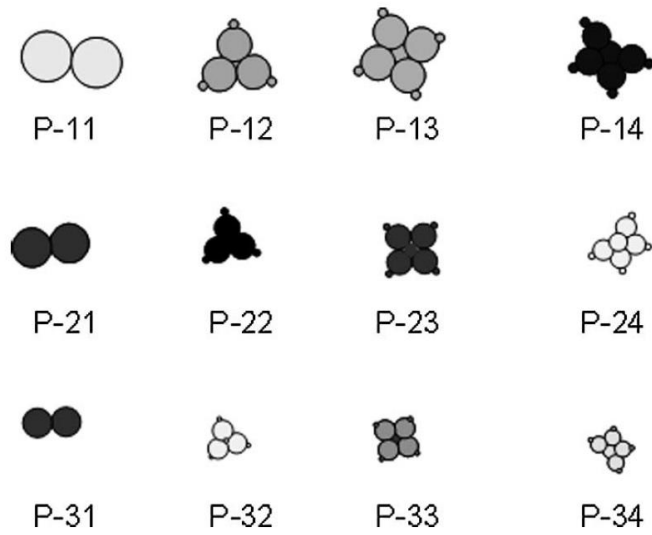


Figure 2.4 Particle sizes and shapes considered in the numerical simulation (Hossain et al., 2007)

Figure 2.5 shows the simulation model in PFC 2D. The left and right platens provided the confining pressure in the range 10–50 kPa. Given the typical 25–30 tonne axle load of trains, a maximum cyclic deviatoric stress of 500 kPa was found to be appropriate for the analysis. In this strain-controlled test, sub-stepping (i.e. accelerating the platen to achieve

the desired deviatoric stress in  $n$  steps) has been introduced to keep the applied cyclic deviatoric stress in the range between 50 kPa and 550 kPa. The test was continued for cyclic loading under a stable cyclic deviatoric stress up to 6,000 cycles.

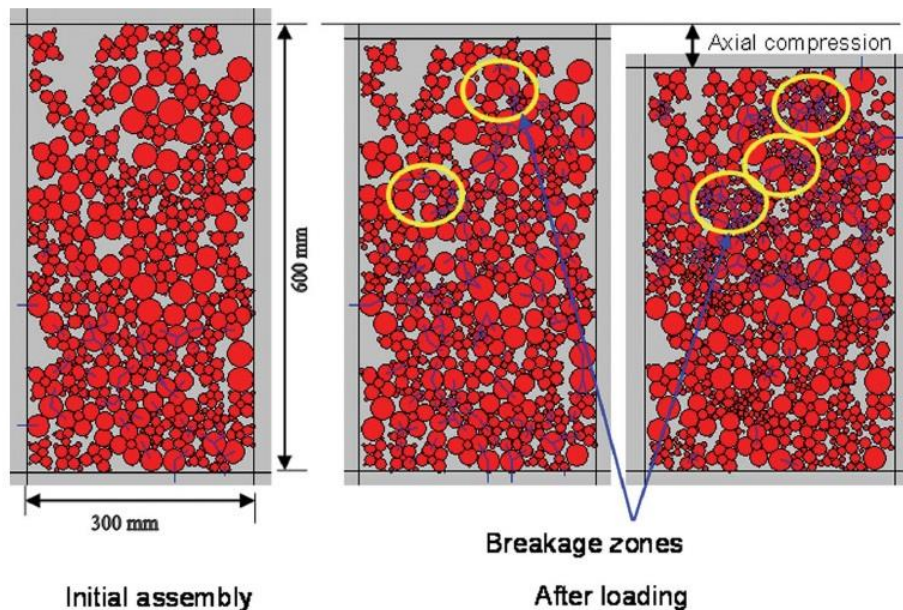


Figure 2.5 Triaxial tests capture ballast breakage conducted by Hossain et al. (2007)

From the analysis, it has been observed that the breakage of particles has significant influence on the settlement and volumetric strains. The analysis also demonstrated that breakage is a function of confining pressure, where minimum breakage for coarse particles such as ballast occurs around a confining pressure of 30 kPa. For lower confining pressure, breakage occurs under dilating conditions. At much higher confining pressures (50 kPa or more), breakage occurs under contracting conditions. Under dilating conditions, corner breakage is the most pronounced, whereas under compression splitting across particles is expected.

Indraratna and Nimbalkar (2013) investigated the stress-strain degradation response of railway ballast stabilized with geosynthetics. The primary objective of this study was to evaluate the deformation and degradation of railroad ballast under a large number of cycles and to study the influence of the type and tensile stiffness of the reinforcement on the overall performance of the railroad ballast. However, laboratory tests alone do not provide incisive and cost-effective means to gain a full insight into the complex mechanisms of breakage and associated stress deformation characteristics of railroad ballast at intermediate load cycles. Therefore, a numerical analysis (FEM) was carried out by implementing an extended elastoplastic constitutive formulation to capture particle breakage, as well as the effect of geosynthetic reinforcement on the stress-strain behaviour of railroad ballast during cyclic loading. The shear and volumetric deformation mechanisms in the granular substructure are both of a plastic nature (i.e., they are activated after a certain level of stress has been exceeded, and the magnitude of these strains remains relatively constant as soon as unloading occurs). The authors conducted a series of cyclic drained tests was conducted on fresh railroad ballast with biaxial geogrid, nonwoven geotextile, and geo-composite inclusions placed at the ballast-subballast and subballast-subgrade interfaces. The set-up of the experimental testing is shown in Figure 2.6.

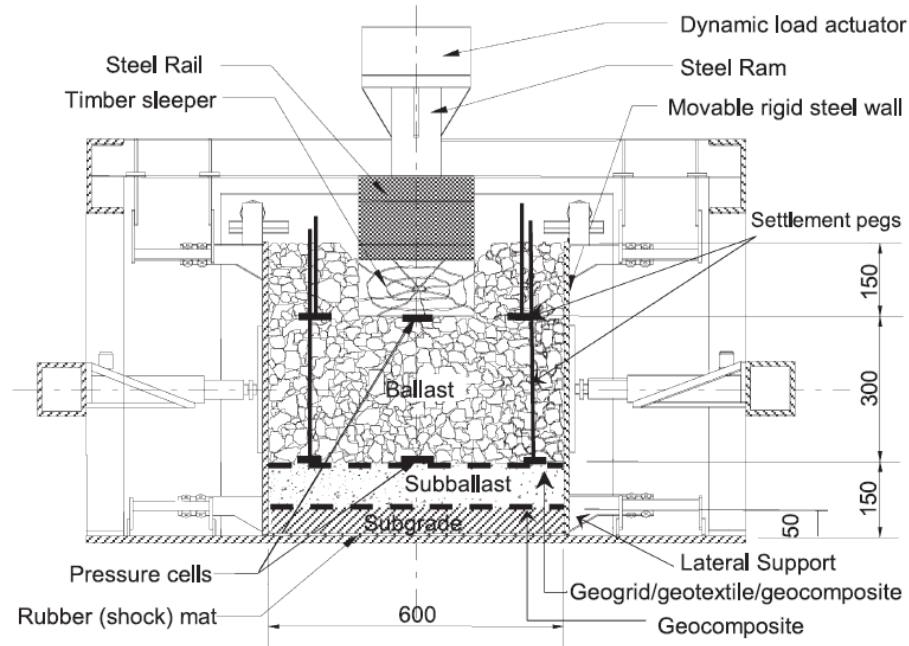


Figure 2.6 Schematic illustration of cyclic triaxial chamber (Indraratna & Nimbalkar, 2013)

The fresh ballast stabilised with geotextile reinforcement showed marginally more degradation in this range of particle sizes compared with ballast stabilized with geogrid. This also explains the lower displacement of ballast when it was reinforced with geogrid. As expected, the geo-composite was the most effective at reducing ballast breakage. It was further observed that the double reinforcement was better than the single reinforcement in terms of reducing ballast breakage. Therefore, it can be said that geosynthetic products provide great potential in mitigating trackbed deterioration and in reducing maintenance costs. However, in this particular study, the performance of geocell was not assessed.

#### 2.4 Geocell-Reinforced Railway Ballast

There are very limited number of research in past to study geocell-reinforced railway ballast, possibly due to the difficulties and high-cost in the construction of a field or

laboratory sample. On the other hand, the simulation of a full-scale geocell-reinforced railway structure is extremely computational-intensive, especially in DEM environment (Chen et al., 2012a).

Leshchinsky and Ling (2013a) carried out a monotonic and cyclic loading tests on pilot-scale geocell-reinforced ballast embankment as shown in Figure 2.7. A parametric study was carried out on the geocell placement layout as shown in Figure 2.8. This experimental study only captured the macro-mechanical responses of the reinforced ballast embankment such as settlement and lateral spreading as well as the condition of geocell prior to and after the tests.

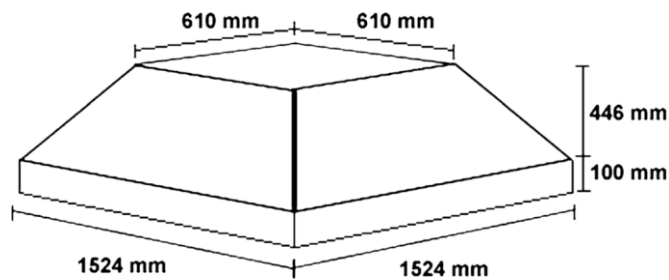


Figure 2.7 Embankment model geometry (Leshchinsky & Ling, 2013a)



Figure 2.8 Geocell configurations for parametric study (Leshchinsky & Ling, 2013a)

Leshchinsky and Ling (2013b) simulated a full-scale railway structure reinforced by geocell (Figure 2.9). The track ballast was modelled, using the finite element method (FEM), as a non-associative elastic-plastic material and behaves with Drucker-Prager yield criterion. The deformation and strength properties were obtained from triaxial compression tests. The foundation was modelled as an elastic material to simply demonstrate the effects of a compressible, soft soil without considering any time-dependent behaviour, such as consolidation. The geocell was modelled as an elastic material and the shape of the geocell was modelled with a simplified rhomboidal shape.

A series of simulations were performed on the railway geometry in order to determine the effects of geocell stiffness, ballast strength, and foundation compressibility. Performing a parametric study on realistic geometry and applications could allow insight into its



performance in actual railroads. Analyses were performed by varying ballast strength to simulate inferior track material, foundation stiffness to simulate compressible subgrades, and geocell stiffness to observe the effect of reinforcement material on overall performance.

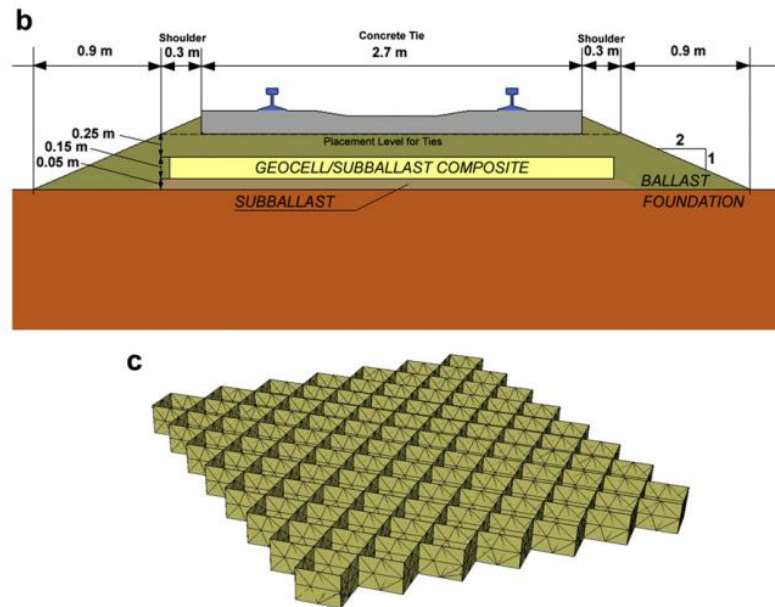


Figure 2.9 Numerical model of geocell-reinforced railway structure (Leshchinsky & Ling, 2013b)

Satyal et al. (2018) furthered the Finite Element (FE) numerical simulation conducted by Leshchinsky and Ling (2013b). This study examined the efficacy of geocell-reinforced ballast railway structure over soft subgrade materials. Different geocell configurations, subgrade CBR values and embankment geometry were altered for parametric studies. The numerical model was created by commercial software package ABAQUS and was calibrated against laboratory tests which involved unreinforced and geocell-reinforced ballast box as shown in Figure 2.10.



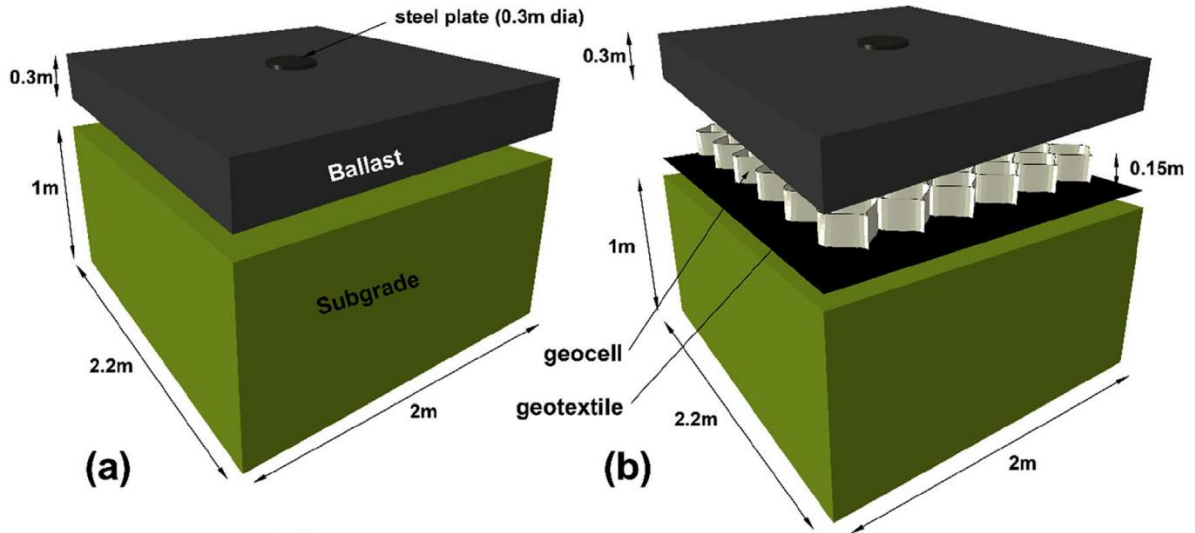
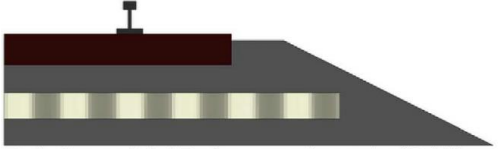
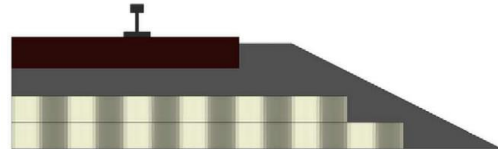
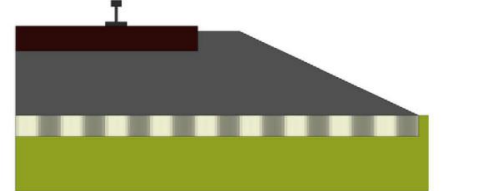


Figure 2.10 Calibration model used by Satyal et al. (2018): (a) unreinforced model, (b) reinforced model.

Table 2.4 Summary of parametric study conducted by Satyal et al. (2018)

Reinforcement conditions	Model schematic	Embankment height (mm)		
		600	450	300
Reinforced below tie	<p>Reinforced below tie (R T)</p>	✓	✓	✓
Reinforced below shoulder	<p>Reinforced below shoulder (R S)</p>	✓	✓	✓
Reinforced to full width	<p>Reinforced full width (R FW)</p>	✓	✓	✓

Table 2.4 (Continued)

Reinforced 150mm above subgrade	 <p>Reinforced 0.15 above subgrade (R HI)</p>	✓	✓	-
Reinforced with double geocell layers	 <p>Reinforced with 2 layers (R TWO)</p>	✓	✓	-
Reinforced 150mm below subgrade	 <p>Reinforced 0.15m below subgrade (R LO)</p>	✓	✓	✓

## 2.5 Geocell Failure Mechanisms

The junctions of the geocell product are critical knots that are fabricated to support and transfer high loads. As a result, the junctions are located in places that are most vulnerable to damage, and so cause unbalanced load transfer or even the failure of entire geocell panels (Cheng, 1993). Cheng (1993) suggested that the damage of geocell junctions takes three forms: shear [Figure 2.11 (c)], which means that one strip is displaced relative to the strip adjacent to first strip's direction; peel [Figure 2.11 (d)], which means that one strip is displaced relative to the panel that is perpendicular to the first strip's direction; split [Figure 2.11 (e)], which means that two of the four strips occurring in a junction are pulled relative to the other two and are perpendicular to the junction. According to manufacturers' product specifications, the current testing method performed on geocell is limited to seam strength tests, specified in Cheng (1993), which examines the weld strength by applying uniaxial tensile force.

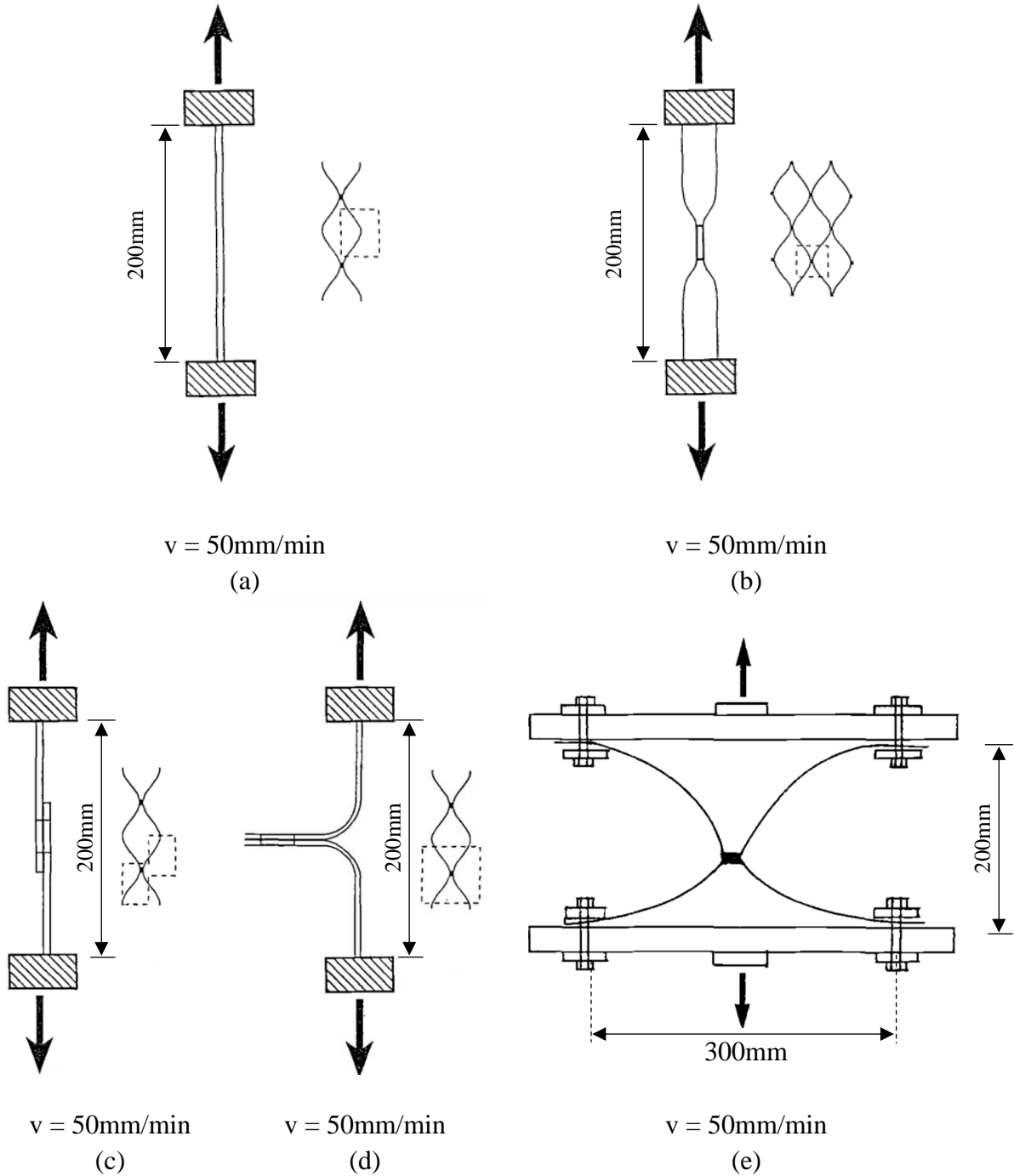


Figure 2.11 Testing procedures for geocell recommended by Cheng (1993): (a) cell-wall tensile strength test; (b) junction tensile strength test; (c) junction shear strength test; (d) junction seam strength test; (e) junction split strength test.

There is also no established testing standard for cell-wall. The testing method for plastic material can be referred to, but it is limited to short-term uniaxial tensile strength tests. The potential failure mechanism shown in has not yet been established as a required testing program for geocell products. This is important because there are potential failure mechanisms can also be identified at the transition zone of embankment crests and slopes. In these cases, the geocell wall is bent, and it is stretched at the top. If damage occurs on top of the perforation as indicated in Figure 1.4 (a), the strength of the geocell wall is significantly reduced and subsequent soil movement can potentially result in global failure. Therefore, it is essential that the failure mechanisms of cell-wall, and its corresponding strength under tensile load when the cell-wall suffers from minor damage (e.g. cut, tear), are investigated. In addition, the permanent deformation has long been a concern in the use of geosynthetics in a variety of geotechnical applications (Becker & Nunes, 2015; Sawicki, 1998; Thakur et al., 2013a). However, the long-term, creep behaviour of geocell cell-wall has not yet been assessed under tensile/gravity loading condition.

**INTENTIONALLY BLANK**

**Chapter 3. Three-Dimensional Modelling of  
Geocell-Reinforced Straight and Curved Ballast  
Embankments (Paper 1)**

---

**INTENTIONALLY BLANK**

# Statement of Authorship

Title of Paper	Three-dimensional modelling of geocell-reinforced straight and curved ballast embankments
Publication Status	<input checked="" type="checkbox"/> Published <input type="checkbox"/> Accepted for Publication <input type="checkbox"/> Submitted for Publication <input type="checkbox"/> Unpublished and Unsubmitted work written in manuscript style
Publication Details	Liu Y, Deng A, Jaksa M. Three-dimensional modeling of geocell-reinforced straight and curved ballast embankments. Computers and Geotechnics. 2018;102(53-65).

## Principal Author

Name of Principal Author (Candidate)	Yang Liu
Contribution to the Paper	Conducting literature review, numerical simulation, data interpretation and drafting manuscript.
Overall percentage (%)	70%
Certification:	This paper reports on original research I conducted during the period of my Higher Degree by Research candidature and is not subject to any obligations or contractual agreements with a third party that would constrain its inclusion in this thesis. I am the primary author of this paper.
Signature	Date 23/8/2018

## Co-Author Contributions

By signing the Statement of Authorship, each author certifies that:

- i. the candidate's stated contribution to the publication is accurate (as detailed above);
- ii. permission is granted for the candidate to include the publication in the thesis; and
- iii. the sum of all co-author contributions is equal to 100% less the candidate's stated contribution.

Name of Co-Author	An Deng
Contribution to the Paper	Supervising development of the work and revising manuscript.
Signature	Date 23 August 2018

Name of Co-Author	Mark Jaksa
Contribution to the Paper	Co-supervision of research and manuscript editing.
Signature	Date 24/8/18

Please cut and paste additional co-author panels here as required.



**INTENTIONALLY BLANK**

### **3.1 Abstract**

This paper outlines a three-dimensional modelling study conducted on straight and curved geocell-reinforced embankments. The study uses the discrete element method to represent varying angularities of ballast infill and models their mechanical response under monotonic and cyclic loading conditions. The simulation results show good agreement with test results and the case studies indicate that the geocell enhances embankment stiffness under monotonic loading and improves its resilience when subjected to cyclic loading. The geocell more evenly distributes stresses within the ballast embankments. The reinforced ballast embankments also exhibit less vertical displacement and lateral spreading than the unreinforced ballast embankments do.

**Keywords:** discrete element; railway embankment; ballast; geocell; cyclic.

### **3.2 Introduction**

As time progresses, trains travel faster, railways become longer and convey heavier goods, and more stringent safety standards mandate a higher level of below-rail alignment for longer design periods. However, the main below-rail ballast layer, which is referred to in the present study as the ballast embankment, eventually becomes misaligned due to ballast breakage and rearrangement (Hossain et al., 2007; Indraratna et al., 2014; Salim & Indraratna, 2004; Yan et al., 2014). As a result, the embankment is prone to subsidence and lateral spreading, which undermines the safety of the tracks. The damage to the embankment is more pronounced on sharp track curves where the train creates large centrifugal forces, which can result in significant settlement in the track embankment, which exacerbates rail misalignment. Poor track geometry results in significant expenditure due to ballast inspection, maintenance and sometimes reconstruction. For example, in the year ending 30 June 2016, the Australian Rail Track Corporation (ARTC) – one of Australia’s largest rail network owners – expended more than \$AUD188 million on railway infrastructures maintenance work, accounting for 22.3% of their total revenue in the same year (ARTC, 2016a). To minimize this expenditure, studies (Chen et al., 2012b; Leshchinsky & Ling, 2013a, 2013b) have successfully applied geosynthetics to reinforce embankments. Of the suite of available geosynthetics, geocells provide a promising means to reinforce railway embankments (Leshchinsky & Ling, 2013a, 2013b).

The geocell, as shown in Figure 3.1, is a cellular confinement system developed to reinforce granular infills. The system is supplied in a folded form and, when in use, outstretched into a honeycomb-like, three-dimensional (3D) panel. The stretched panel

provides a space to accommodate and confine the infill materials and facilitates the joining of individual cell panels into an integrated mattress. When fully outstretched, the panel usually measures a couple of meters in width and up to 20 meters in length, with an individual cell space of around 250 mm square, in width, and between 75 to 200 mm deep. The panel size and the cell space can be varied as part of the manufacturing process to suit individual requirements. The cell wall, which is around 5 mm thick, commonly consists of high-density polyethylene (HDPE) or other polymer material, and is perforated to allow water drainage, facilitate root growth between cells and provide interlocking with the infill.

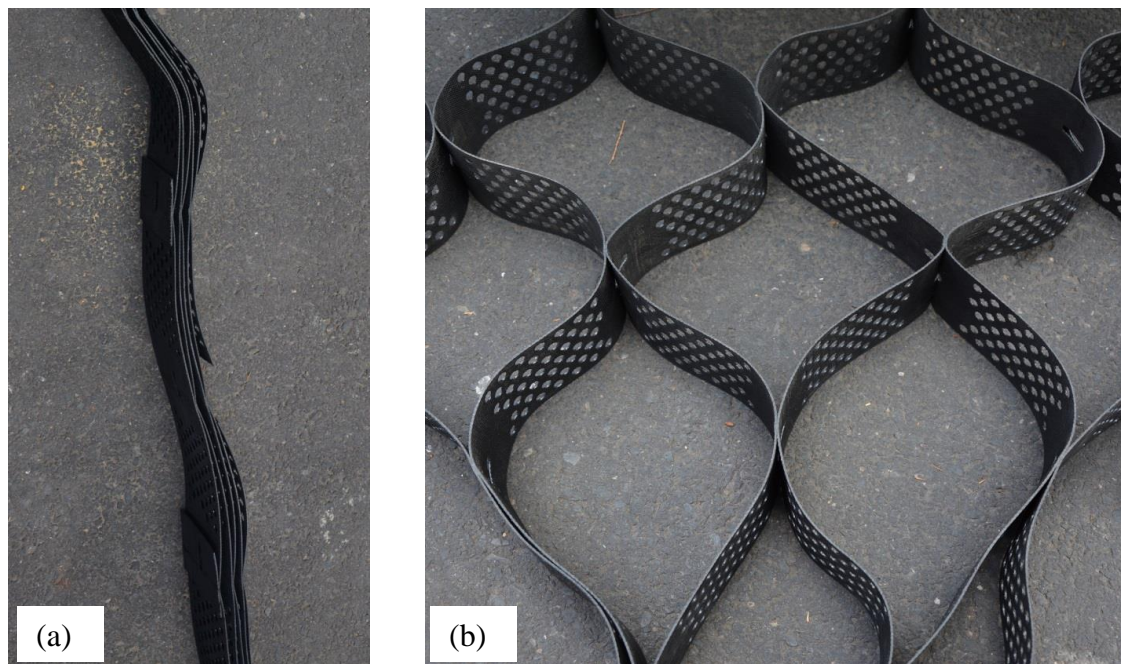


Figure 3.1 Information on cell size and wall depth: (a) folded and (b) outstretched (250 W × 250 L × 100 D mm for a cell).

Geocell panels have been widely used in a variety of infrastructures, such as foundations and subbases (Dash, 2012; Hegde & Sitharam, 2015a; Moghaddas Tafreshi et al., 2015;

Oliaei, 2017; Tanyu, Aydilek, et al., 2013; Yang et al., 2012), slopes (Mehdipour et al., 2013a), retaining structures (Chen, Wu, et al., 2013a) and embankments (Madhavi Latha & Rajagopal, 2007; Zhang et al., 2010). All of these studies have shown that using geocells improves performance of the infrastructures by reinforcing the granular infill materials. More recently, Leshchinsky and Ling (2013a, 2013b) conducted a prototype test and a finite element (FE) analysis on a geocell-reinforced railway embankment. Their studies confirmed the superiority of the geocell in reinforcing the embankment. Similar approaches were attempted in other studies (Nishiura et al., 2017; Xu et al., 2017; Zhang et al., 2012). In parallel with the FE method, Liu et al. (2015) employed the discrete element method (DEM) to examine the performance of straight, geocell-reinforced embankments. As a further step, this study extends the DEM approach to curved embankments. Additional work includes the advanced contact model used to simulate the geocell and the examination on geocell embedment depth.

The DEM possesses the capability to represent, with appropriate engineering accuracy, distinct ballast particles and to simulate particle motion (Cundall & Strack, 1979a). The method does not rely on a constitutive model for continuum media; rather, it incorporates a contact model developed between the individual particles. The method is also able to replicate variable angularities of the ballast, and similarly reflects variable material micro-properties, such as stiffness and friction (Chen et al., 2012b; Irazábal et al., 2017; Itasca, 2009b). More importantly, it enables 3D modeling. This is particularly important for the accurate simulation of the 3D geocell panel, as 2D modeling neglects, or at least simplifies, the interaction between cells and so underestimates the performance of the geocell panel.

However, an additional calibration stage is required in order to yield simulated behaviour substantially similar to that observed in reality. Further, it is not possible to simulate a full-scale structure as replacing a continuum with particle assemblies is computationally intensive. Thus, the simulation of a full-scale railway structure in DEM is beyond current computational capacity and the scope of this study.

This study adopts the commercially-available DEM program, Particle Flow Code in 3 Dimensions (PFC3D) version 4.0 (Itasca, 2009b), to simulate a geocell-reinforced embankment. The railway embankment examples included in the paper are established in accordance with the relevant codes of practice, which are discussed later. The paper aims to establish a DEM-based framework for modelling railway ballast and to evaluate the performance of incorporating geocells in ballasted embankments. Chen et al. (2012b) adopted DEM to simulate geogrid-reinforced railway ballast and successfully demonstrated the capability of using DEM in modelling geosynthetics-reinforced ballast. The methodologies used in (Chen et al., 2012b), such as material generation, have inspired the framework proposed in the current study. Improvements have also been made in the geometric complexity of ballast model as well as in the behaviours and contact models of geocell and ballast in DEM.

### **3.3 Model Development**

This section outlines the development of the ballast-geocell model in PFC3D and provides details of the particle contact and the calibration of the geocell and ballast assemblage.

### **3.3.1 Particle contact**

DEM simulation is governed by the physical contact between particles. The contacts are present as a combination, in series and/or parallel, of the following basic physical elements: a bond, slider, spring and dashpot. When applying an external force to an assemblage of particles, the contacts between them determine how individual particles will respond and where they will travel at each time step in the simulation. PFC3D incorporates the contact mechanism and allows the user to encode a material-oriented, contact, constitutive model. Once validated, the model is implemented to reproduce the mechanical response of the material used in any desirable field application. The model usually defines a set of material micro-properties, such as particle stiffness, bond strength and friction coefficient, which are determined through material calibration tests.

### **3.3.2 Material calibration**

In this section the procedures for calibrating the input parameters for the geocell and railway ballast in PFC3D are discussed.

#### *3.3.2.1 Geocell*

The geocell material was calibrated by conducting a tensile strength test. The test setup is shown in Figure 3.2. A geocell strip was cut from a full panel and cropped into a standard specimen shape for tensile strength testing, in accordance with AS 1145.3 (SAI, 2001). The specimen was tested using an Instron mechanical device [Figure 3.2 (a)] and three replicates, as the one illustrated in Figure 3.2 (a), were tested to obtain representative results. The stress–displacement relationship of the averaged results was then compared

with the DEM simulation. The DEM simulation involved discretising the specimen strip into 32 equal-sized spheres – an object in PFC3D for modelling materials (Itasca, 2009b). The 32 spheres are arranged in two columns, forming a strip [Figure 3.2 (b) and (c)]. Each sphere is assigned an equivalent diameter of 5 mm, and so the sphere-based strip (5 mm thick  $\times$  10 mm wide  $\times$  80 mm long) is equal in size to the specimen section, which is elongated during the test.

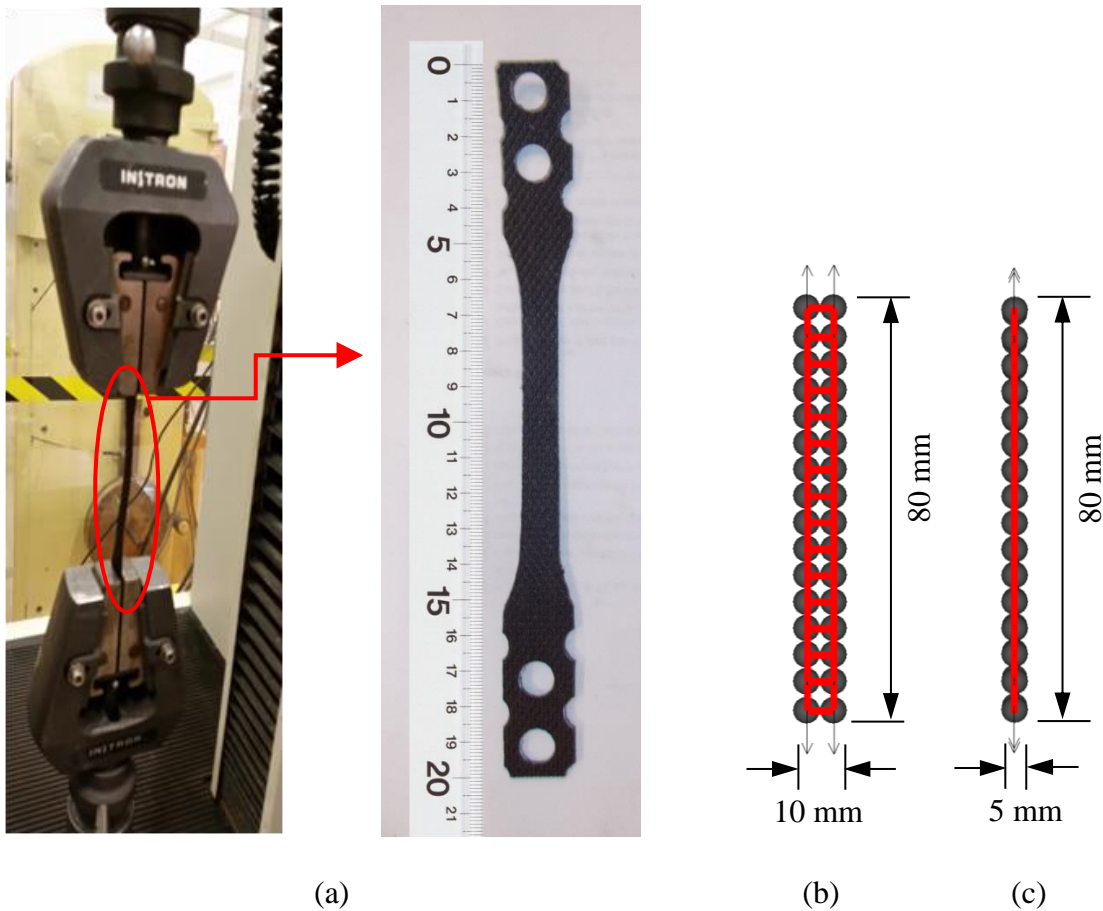


Figure 3.2 Geocell tensile strength test: (a) setup and detail of representative tested specimen; (b) front view in DE simulation; (c) side view in DE simulation.



Table 3.1 Micro-properties for geocell

Micro-property	Value
Density $\rho$ (kg/m <sup>3</sup> )	$1.0 \times 10^3$
Normal stiffness $k_n$ (N/m)	$3.2 \times 10^3$
Shear stiffness $k_s$ (N/m)	$3.2 \times 10^3$
Parallel-bond normal stiffness $\bar{k}_n$ (N/m <sup>3</sup> )	$2.8 \times 10^4$
Parallel-bond shear stiffness $\bar{k}_s$ (N/m <sup>3</sup> )	$4.5 \times 10^4$
Parallel-bond normal strength $\bar{\sigma}_c$ (N/m <sup>2</sup> )	$6.8 \times 10^4$
Parallel-bond shear strength $\bar{\tau}_c$ (N/m <sup>2</sup> )	$6.5 \times 10^4$
Parallel-bond radius $\bar{R}$ (mm)	2.5
Tensile strength $\bar{\sigma}_t$ (N/m <sup>2</sup> )	$5.598 \times 10^4$
Softening stiffness $\widetilde{k}_s$ (N/m <sup>3</sup> )	$2.75 \times 10^4$
Normal stiffness in tension $\widetilde{k}_n$ (N/m)	$3.2 \times 10^4$
Friction coefficient $\mu$	0.3

Table 3.1 shows the material micro-properties used to simulate the behaviour of the geocell. The properties were determined using the formulation proposed by Potyondy and Cundall (2004) and the stress–displacement results presented in Figure 3.3. As can be seen, close agreement is obtained between the simulation and test results. Both sets of results show a very close peak strength, a clear elongation process and similar residual strength. The agreement was achieved by encoding a ductile model (Itasca, 2009b) to provide a softening slope. A previous study (Liu et al., 2015) used conventional linear parallel-bond which can

only provide a linear-elastic stress-strain response before reaching peak tensile strength. The ductile model is a modification, rather than a replacement to the contact-bond, and it is invoked when brittle failure occurs in bonded particles, so that the geocell model does not experience sudden failure when it reaches its peak tensile strength. Instead, the bond reduces its strength to behave like HDPE; the material from which the geocells used in this study are manufactured from. As can also be observed, there is a disparity between the simulation and experimental results in the elastic regions. This phenomenon can be attributed to the nature of the parallel-bond, which is essentially designed to model linear-elastic behaviour. The model incorporates three contacts: stiffness (i.e. springs), a parallel bond and a slip. As a further note, the micro-properties shown in Table 3.1 were attained using an iterative approach – harmonizing the simulations with the test results (Itasca, 2009b). Whilst this approach is somewhat indirect, satisfactory outcomes are obtained. The geocell model obtained a yielding strain  $\epsilon_y=11.02\%$  and a failure strain  $\epsilon_f=46.7\%$ ; identified as points A and B respectively in Figure 3.3.

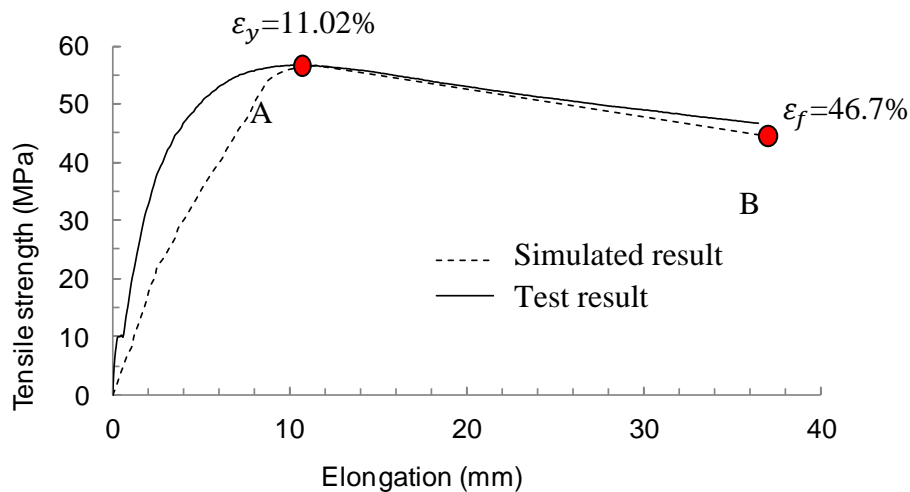


Figure 3.3 Tensile strength of geocell specimen.

### 3.3.2.2 *Ballast*

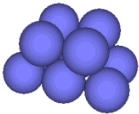

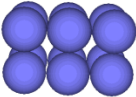
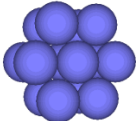
Railway ballast is usually produced by blasting and/or fragmenting a rock mass, and hence exhibits variable angularities. Past studies (Le Pen et al., 2013; Lim & McDowell, 2005; Yan et al., 2014) have demonstrated the importance of accurately modelling the particle angularities, and suggested that reflecting angularities in simulations better reproduces the actual behavior of the ballast. To achieve this, four ‘clump templates’ were developed: trapezoidal, triangular, rectangular and hexagonal (Table 3.2), which account for the major geometric shapes of ballast infills. Clumps are groups of ‘slaved’ spheres that are firmly bonded together. In the modeling undertaken in the present study, debonding within the clump is prohibited, so as to focus on the motion of the ballast and eliminate the possibility of problems associated with breakage.

The calibration of the ballast is similar in concept to that of the geocell. Lim and McDowell (2005) suggested the use of a triaxial test simulation to calibrate the ballast in PFC3D, and test results by Indraratna *et al.* [4] Indraratna, Ionescu, et al. (1998) were used for this purpose. As suggested by Lim and McDowell (2005) and (Lu & McDowell, 2010), the interlocking of the clumps was represented by applying a weak and breakable parallel bond between two contacting clumps. The bond can reconstitute at a new contact if particles rearrange. In addition, the membrane used to confine a sample is represented as a wall and assumed to be frictionless (Chen et al., 2012b). As PFC adopts the lower friction coefficient of two contacting entities, the friction between the clumps and the membrane is ignored. This approach is also adopted in subsequent ballast embankment models, which helps focus on the mechanical response of the geocell-reinforced ballast. Similarly, the

sleepers situated on the top of the embankment act merely as loading platens and the friction between the sleepers and the ballast is ignored.

The test setup, as shown in Figure 3.4, comprises a cylindrical cell of 300 mm in diameter x 600 mm high. The cell is initially filled with a number of spheres of varying diameters, 20 mm to 50 mm [Figure 3.4 (a)], in accordance with the ballast grading characteristics specified by Indraratna, Ionescu, et al. (1998). The spheres are then replaced [Figure 3.4 (b)], in equal volume, with the clump templates shown in Table 3.2. The replacement is conducted in equal allocations among the four templates, and at random orientations within the cell. It is important to note that particle overlap occurs when assigning the clump templates to the spheres due to the created clump angularities. To negate this effect, as well as a prestressing problem, the top cap of the cell is allowed to move upward at an extremely slow rate of 0.1 mm/s until an equilibrium of inter-clump contact forces is achieved (Lim & McDowell, 2005). The equilibrium is determined by the ratio of the average mechanical solve ratio, defined as unbalanced force over the average value of the sum of contact forces, body forces and applied forces over all particles. The ratio is set as  $1 \times 10^{-3}$ , which is small enough to signal the equilibrium. The specimen porosity at equilibrium is 0.39, which is the average measured by two spheres. The spheres, 300 mm diameter each, are inscribed in the triaxial chamber. The spheres sit edge-to-edge, enabling the most occupation of the chamber space. The inscribing avoids possible boundary effect of the chamber. A total of 632 clumps (i.e. 7,584 spheres) are incorporated in the specimen.

Table 3.2 Clump templates developed for ballast

Clump template	Geometry	Number of spheres
Trapezoidal		10
Triangular		10
Rectangular		12
Hexagonal		14

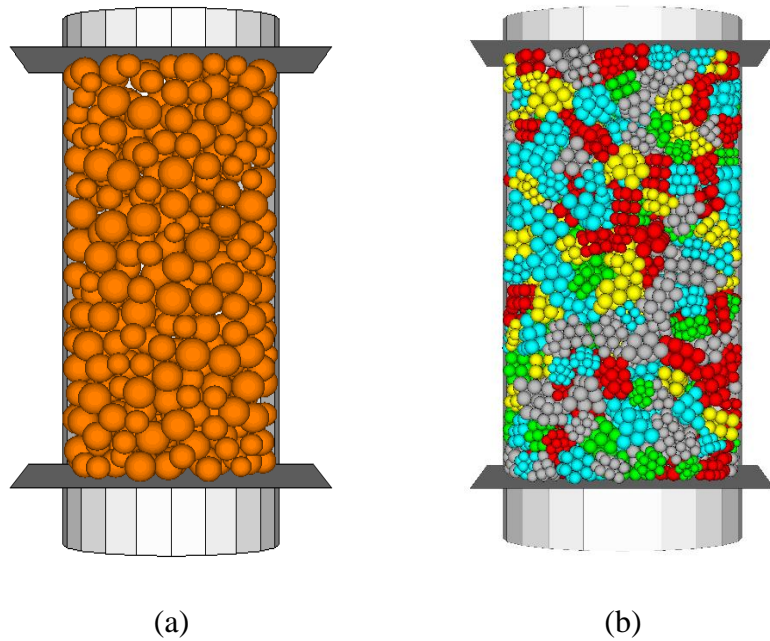
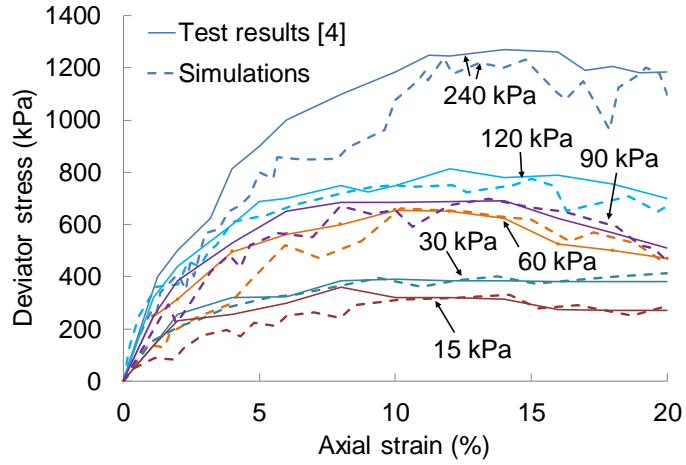
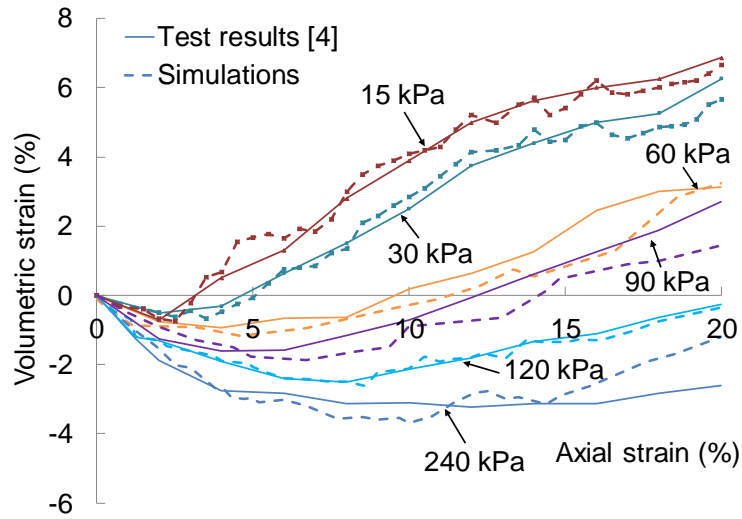


Figure 3.4 Triaxial test specimen simulated by: (a) spheres; (b) clumps.

The specimens are then subjected to triaxial compression tests at 6 different confining pressures: 15, 30, 60, 90, 120 and 240 kPa. The loading is achieved by moving top wall downward at a rate of 0.045 mm/s and the tests continue until an axial strain of 20% is attained. It should be noted that all loading rates used in this study have been selected by trial and error to achieve desirable numerical stability while reasonable computational effort is spent. A numerical, servo-control algorithm [26] is incorporated in the simulation to maintain a constant confining pressure throughout the respective loading phases. The top loading wall is assigned with following micro-properties: a normal stiffness of  $1 \times 10^{10}$  N/m; shear stiffness of  $1 \times 10^{10}$  N/m and a friction coefficient of 0.5 (i.e.  $\tan 27^\circ$ ). The wall stiffnesses are higher than the ballast stiffness in order to prevent ballast penetration. Figure 3.5 shows the simulation and test results of the triaxial tests. The simulation was achieved by encoding a linear contact model (Itasca, 2009b) and using the micro-properties provided in Table 3.3, which were obtained through trial and error. The micro-properties show that the model, similar to that for the geocell, also incorporates the three contacts: stiffness, a parallel bond and a slip. Similarly, close agreement is found across the entire series of confining pressures. The accuracy of the simulations is further validated by the dilation observed under lower confining pressures and contraction under higher ones. These results demonstrate that the material properties and encoded models are capable of appropriately modelling the mechanical behaviour of the ballast.



(a)



(b)

Figure 3.5 Triaxial compression test results: (a) deviator stress vs. axial strain; (b) volumetric strain vs. axial strain.

Table 3.3 Micro-properties for ballast clumps

Micro-property	Value
Density $\rho$ (kg/m <sup>3</sup> )	$2.5 \times 10^3$
Normal stiffness $k_n$ (N/m)	$5 \times 10^9$
Shear stiffness $k_s$ (N/m)	$5 \times 10^9$
Parallel-bond normal stiffness $\bar{k}_n$ (N/m <sup>3</sup> )	$1.8 \times 10^5$
Parallel-bond shear stiffness $\bar{k}_s$ (N/m <sup>3</sup> )	$1.8 \times 10^5$
Parallel-bond normal strength $\bar{\sigma}_c$ (N/m <sup>2</sup> )	$6 \times 10^{10}$
Parallel-bond shear strength $\bar{\tau}_c$ (N/m <sup>2</sup> )	$6 \times 10^{10}$
Parallel-bond radius $\bar{R}$ (mm)	1.0
Frictional coefficient $\mu$	1.0

---

### 3.4 Modeling Procedure

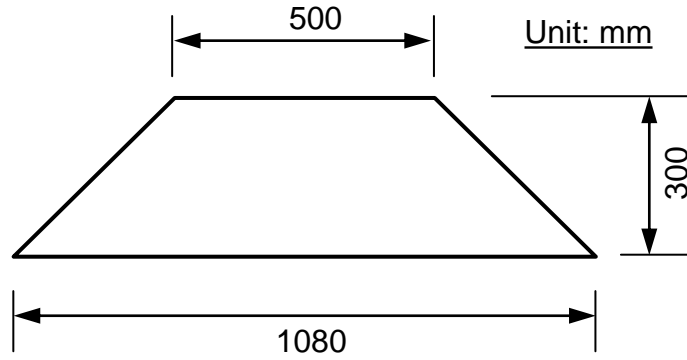
A full-scale embankment simulation is computationally, extremely time-consuming, owing to the large number of spheres needed to simulate the geocell and ballast infills, and is beyond current and available computer capability. This concern has been confirmed in a similar simulation study (Chen et al., 2012b). Therefore, the embankment is scaled down by a factor of five in terms of its crest and base width with regards to the actual dimensions specified by ARTC (2016b, 2017). In this context, there are still approximately 78,000 spheres incorporated in the reinforced embankment. The scaling does not significantly influence performance comparison made between the reinforced and unreinforced embankments, as both embankments are subject to the same level of scaling. Moreover, the scaled embankment is comparable in size with the one adopted in a prototype test



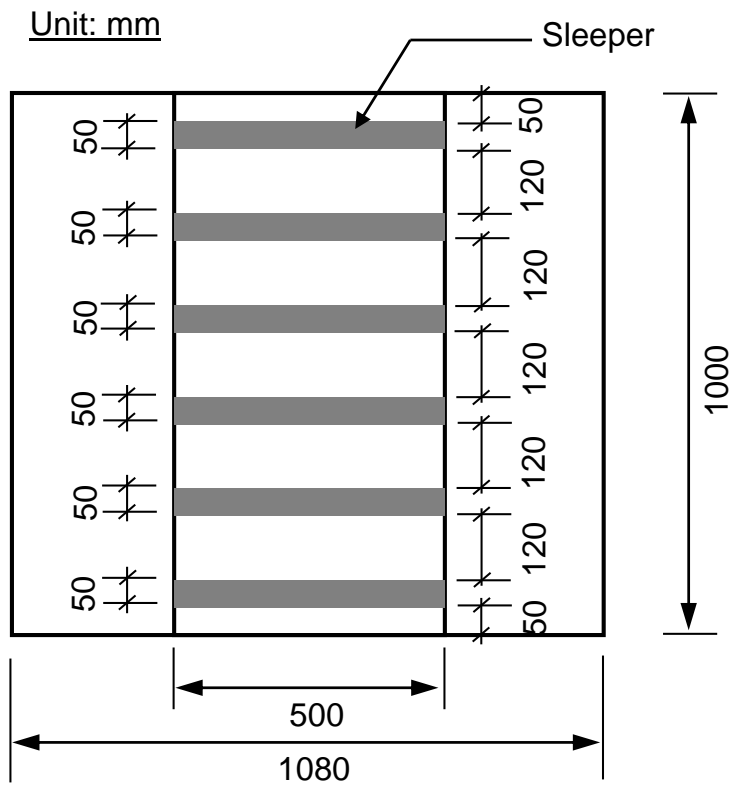
(Leshchinsky & Ling, 2013a) and so provides an opportunity to validate the simulation results against those from the test. In order to focus on the contribution of the geocell to embankment stability, a simplified track assemblage is adopted, where only sleepers are included in the DEM model and rails, fastenings and anchors are excluded.

### **3.4.1 Straight embankment**

The straight rail embankment is summarized in Figure 3.6. A crest width of 500 mm, base width of 1,080 mm, height of 300 mm and a length of 1,000 mm are adopted. The gradient of its shoulder slope is approximately 1:1. Six sleepers, each 50 mm wide and 500 mm long, are founded on the crest at an edge-to-edge spacing of 120 mm. The sleepers were simulated using stiff walls – an object in PFC3D for materials with line segments (Itasca, 2009b), which exhibit dimensions of actual, heavy-duty, prestressed concrete sleepers. As the contact forces between two contacting objects are governed by their stiffnesses, the sleepers are assigned with the micro-properties used for the loading wall in the triaxial simulation, enabling a consistent stress–strain behaviour of the ballast assembly. Considering the 2D nature of the embankment (i.e. no longitudinal movement of the infill), the front and rear cross-sections were simulated using non-movable walls, with normal and shear stiffnesses of  $1 \times 10^{10}$  N/m, and a higher friction coefficient of 1.0 (i.e.  $\tan 45^\circ$ ) to reflect the ballast-to-ballast friction along the section boundaries. In order to reflect embankment subsidence caused by the underlying subgrade, the subgrade was also represented by a wall, with lower normal and shear stiffnesses of  $1 \times 10^8$  N/m, and a friction coefficient of 0.5.



(a)



(b)

Figure 3.6 Straight embankment: (a) cross section; (b) plan view.

The role of the geocell in the stability of rail embankments is examined by placing the geocell at two different levels within the ballast layer: at the base of the embankment

[Figure 3.7 (a)] and 50 mm above the base [Figure 3.7 (b)]. At each level, as shown in Figure 3.7 (c), the geocell panel is centred within the ballast-filled embankment. The panel [Figure 3.7 (d)] includes 8 cells and measures 748 mm  $\times$  480 mm edge-to-edge. Each cell is 75 mm deep and 175 mm  $\times$  175 mm wide. The long and short sides of the panel are aligned with the embankment's longitudinal and transverse directions, respectively. The short side is less than the width of embankment crest, so that a 10 mm margin is present along the embankment crest edges. In the longitudinal direction, the panel length is 252 mm shorter than the extension of the embankment, which negates boundary effects associated with the panel. The geocell panel is longitudinally divided into two halves: A and B. Representative cell junctions are marked as a to g for subsequent displacement analysis. As is required by PFC3D, the geocell material is also simulated by a layer of spheres. The spheres are aligned and bonded together contiguously using the micro-properties shown previously in Table 3.1. A total of 12,762 spheres are used to generate the entire geocell panel.

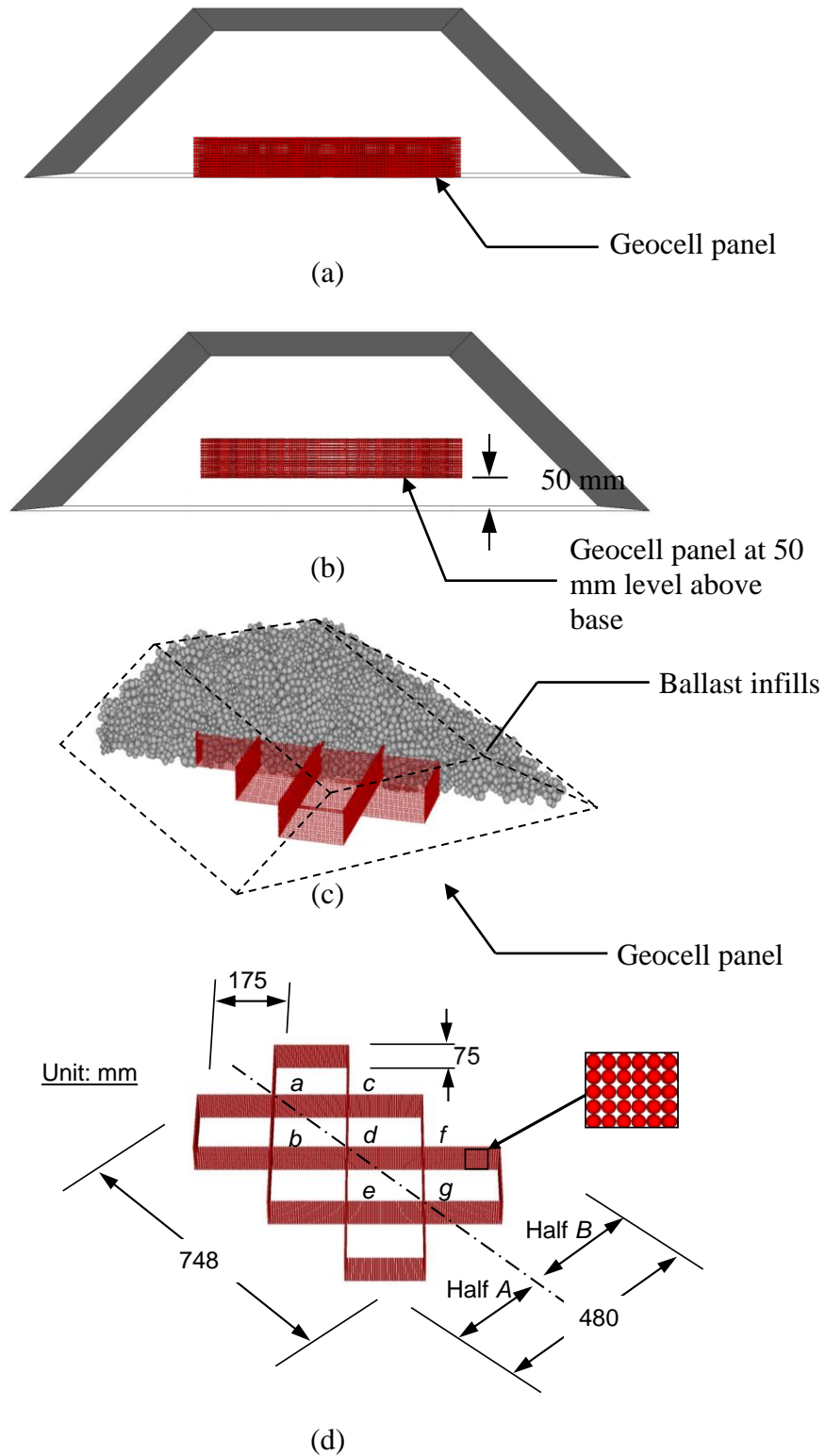


Figure 3.7 Geocell panel: (a) at embankment base; (b) 50 mm above the base; (c) 3D perspective: infilled with ballast; and (d) 3D perspective: simulated using spheres.

The ballast infill is generated using the procedures similar to those used in the ballast triaxial calibration. Temporary walls are generated first on the embankment slopes and crest as boundaries. The geocell and associated bonds are then generated within the pre-defined boundaries, followed by generation of ballast and corresponding parallel-bond. The geocell can deform freely and it is breakable during this process. It should be noted that the ballast is generated in three layers (i.e. 100 mm thick each). As contact forces between clumps are created due to overlapping during clumps generation, additional time steps are permitted between the generations of each layer, so that previous layers can reach equilibrium (i.e. release contact forces). The temporary walls prevent the escape of clumps due to the contact forces and they are permitted to move slowly outward until the inter-clump contact forces dissipate, upon which they are removed. During the ballast generation process, no constraint is applied to the interaction between the geocell and ballast. This is to reflect the actual placement of ballast in the field. A total of 4,002 clumps (i.e. 56,083 spheres) are used for the infill in the situations where a geocell panel is used. For the unreinforced embankment, similar numbers of clumps (4,106) and spheres (57,479) are generated for the infill.

### **3.4.2 Curved embankment**

A horizontally-curved embankment has its outer rail elevated to provide a banked curvature. This super-elevation, also known as a cant, serves the purpose of providing a centripetal force to balance the centrifugal force exerted by the train's motion, which in turn allows the train to negotiate bends at higher speed. Figure 3.8 shows a diagram of the curved embankment used in this study. The diagram is similar to that for the straight embankment

except for the 5% gradient adopted at the crest. This gradient is set in accordance with ARTC (2016b) and the value corresponds to the typical limit of super-elevation for an intrastate line in Australia. Compared with the straight embankment, the curved embankment uses the same geocell arrangements and material micro-properties, and a similar number of spheres for the geocell and ballast.

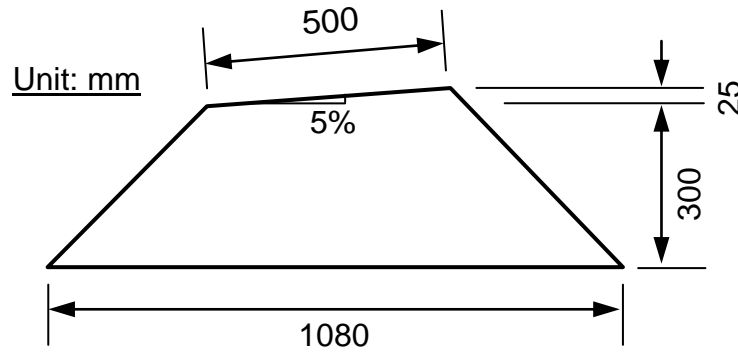


Figure 3.8 Curved embankment cross section.

### **3.4.3 Monotonic and cyclic loading**

This sub-section describes the monotonic and cyclic loading adopted in the study. The aim of the monotonic loading is to determine the embankment subsidence in response to a slowly increasing vertical load and is similar in nature to a plate load test. For the straight embankment, the numerical model constrains the sleepers to move in a downward direction along a trajectory normal to the crest. The sleepers advance at a rate of 0.1 mm/s to cause the embankment to settle at the desired strain of 20% (60 mm). The modest value of the loading rate improves the simulation accuracy by allowing sufficient time to calculate the inter-particle contact forces. The strain-limiting value is consistent with that used in the triaxial calibration and helps predict the load extremes that the embankments can sustain.

The monotonic loading applied to the curved embankment acted at an angle of inclination  $\theta$  (i.e.,  $54.5^\circ = \arctan(P_L/P_V)$ ) (Figure 3.9), where  $P_V$  is the vertical applied load and is calculated to equal 125 kPa for a 30-tonne axle load of a heavy haul train wagon (ARTC, 2017);  $P_L$  is the lateral load acting on the sleepers and equal to the centrifugal force as:

$$P_L = \frac{mv^2}{R} \quad (1)$$

where  $m$  is the axle load,  $v$  is the speed of the train, and  $R$  is the horizontal curve radius. ARTC [34] specifies  $R = 200$  m as the minimum allowable horizontal curve radius for a heavy haul line. Thus,  $P_L$  is approximately 175 kPa when the haul train wagon passes through the curve at the ARTC's design speed of 60 km/h (ARTC, 2014). The values for the vertical load, radius and design speed are adopted to reflect adverse situations in practice and so amplify the loading conditions and expedite the simulation process. To achieve a displacement direction at the angle  $\theta$ , the sleepers advance at a lateral rate of 0.14 mm/s and vertical rate of 0.1 mm/s; that is, at a velocity ratio of 1.4, which is equivalent to the  $P_L/P_V$  ratio.

Cyclic loading, on the other hand, is of higher significance in regard to the assessment of the long-term serviceability of railway embankments. For the straight embankment, a vertical load of  $P_V = 125$  kPa, which reflects a full-scale 25-tonne heavy freight train passing through, was applied normal to the sleepers in the form of loading-complete unloading-reloading cycles. Although the geometry of the railway structure and geocell is downscaled, the strength and mechanical behavior are calibrated against laboratory and

full-scale experimentation, therefore no scale factor is applied to the loading values. The load applied has been shown to be frequency-independent, as reported by Shenton (1978). Due to the long computational time when performing the simulation, a total of 20 loading cycles were performed for each simulation. Even with this somewhat modest number, the simulations utilized the full capability of the PC hardware (Intel core i7-4500U, 8GB DDR3L 1333 RAM with integrated Intel HD Graphics 4400) and the entire modelling process took approximately two months to complete. Albeit with the constraint of computational time, the simulations provide indicative observations of embankment subsidence and the performance of geocells in the early stages of the cyclic loading. Similar simulations were applied to the curved embankment, except for the load applied. The resultant force ( $P_R$ ) of the vertical ( $P_V$ ) and lateral ( $P_L$ ) loads was calculated as 215 kPa and acted at an angle of  $\theta$  with respect to the vertical direction (Figure 3.9). It is worth mentioning that for both straight and curved embankment subject to cyclic loading cases, all sleepers advance simultaneously at the same rates. No lag is applied to the sleepers to reflect train passage as the freight can pass the sleepers gap in an extremely short period of time over a 1-meter embankment.

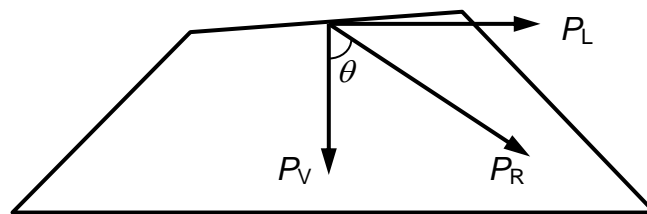


Figure 3.9. Forces acted on curved embankment.



Local damping was activated for ballast clumps only to absorb the vibration energy generated in the cyclic loading process. The clumps tend to rebound and occasionally escape from the embankment boundaries during the unloading phases, as a result of accumulated internal forces. The introduction of a damping coefficient,  $\zeta$ , facilitates the dissipation of these forces in the agitated clumps and allows the ballast assembly to cease oscillating more rapidly (Itasca, 2009b). In this study, the local damping ratio was set to 1.0.

### **3.5 Results and Discussion**

#### **3.5.1 Straight embankment**

Figure 3.10 shows the vertical displacement of the sleepers plotted against the applied vertical load for the straight embankments under monotonic loading, where the results of the numerical simulations from this study are compared with the test results presented by Leshchinsky and Ling (2013a). The simulated vertical displacement is the average of the 6 sleepers and the load is the average resistance measured at the base of the sleepers [Figure 3.6 (b)]. The boundary effects caused by the walls in longitudinal direction are neglected in this study as the individual data set for each sleeper shows insignificant differences in axial stress value. Unlike traditional FE analysis, the results of the DEM modelling show a somewhat irregular curve with slight fluctuations. These are associated with the rearrangement of clumps as the applied load increases. Overall, the vertical displacement rises with increased load for the three design cases, without defined yielding for the range of loads applied. It is clear that using a geocell panel has a noticeable influence on the vertical displacement of the embankment. With the same applied load, the geocell-reinforced embankment exhibits less vertical displacement than that of the unreinforced

embankment. Specifically, given a load of 125 kPa, the vertical embankment displacements are 18.9 mm, when the geocell is located 50 mm above the base, 27.9 mm when the geocell is founded at the base, and 29.5 mm when the embankment is unreinforced. As shown in Figure 3.10, the performance of the geocell reinforcement is in agreement with the test results presented by Leshchinsky and Ling (2013a), who conducted a similar monotonic loading test on a geocell-reinforced ballast embankment. This implies that incorporating a geocell panel in a railway embankment will reduce vertical displacement, and placing it 50 mm above the base, yields superior performance to that when the geocell is placed at the base. The superiority can be attributed to the position of geocell. The suspended geocell limits the loading propagating into the bottom 50 mm layer, which minimizes the settlement and lateral spreading of the bottom layer.

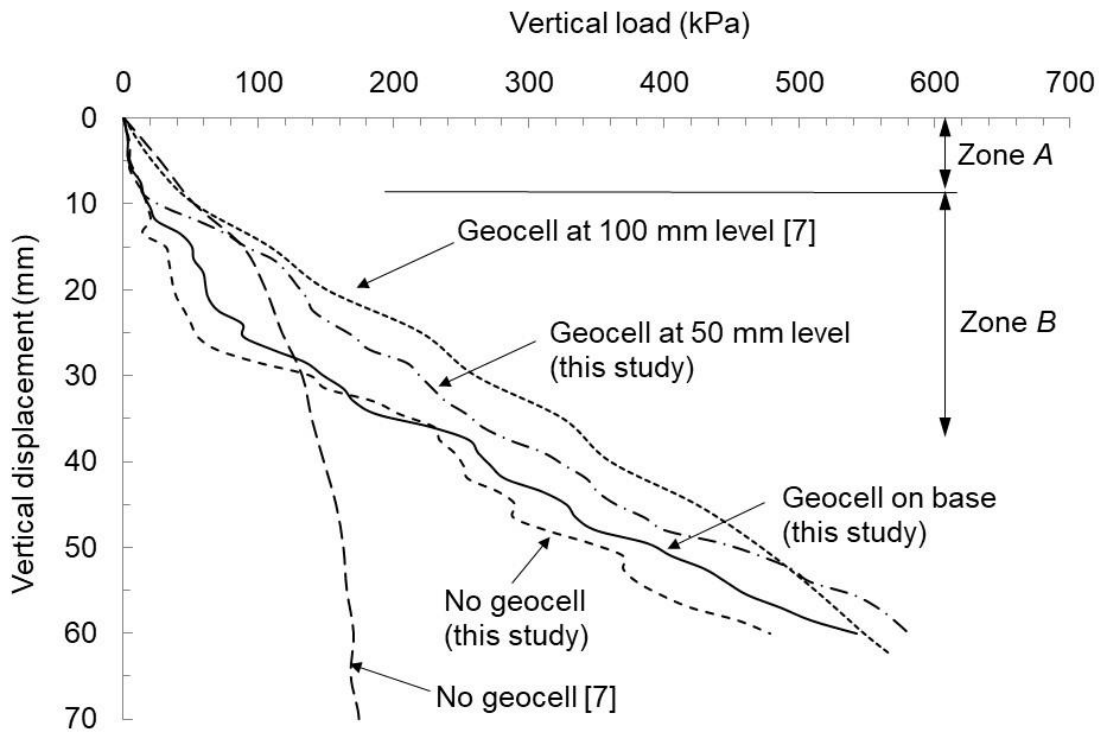


Figure 3.10 Vertical displacement for straight embankment under monotonic loading.

The monotonic loading curves, given in Figure 3.10, can be subdivided into two zones: *A* and *B*, which correspond, respectively, to vertical displacements of less than 10 mm and those beyond 10 mm. In *Zone A*, the early stages of vertical embankment displacement, the sleepers displace in a similar fashion across the three cases examined and exhibit largely equal stiffness. This implies that the ballast skeleton supports the majority of the load when the load remains at a relatively low level, and the geocell is ‘at rest’ and contributes little to the embankment stiffness. In *Zone B*, where the vertical displacement exceeds 10 mm, the geocell demonstrates a strain-hardening effect. It aids in reinforcing the ballast skeleton and increases the stiffness of the embankment. As a result, for an equal vertical displacement, the geocell-reinforced embankment is able to support a higher load than the unreinforced embankment. Due to the curves fluctuation, however, there is a section disagreeing the comparison. Where the vertical load falls into 165 to 220 kPa, the reinforced embankment with geocell at base experiences slightly higher vertical displacement than the unreinforced does, with a maximum difference of 2.3 mm. The curves fluctuation is caused by the DE simulation attaining convergence at some time steps. In addition, placing a geocell 50 mm above the base provides an improved stiffness response than placing it at the base.

Figure 3.10 also presents a comparison of the stiffness development between the simulation results and the prototype test results presented by Leshchinsky and Ling (2013a) who placed geocell at 100 mm above base. The inclusion of this set of experimental data is not for making quantitative comparison against the results obtained from this study (place

geocell at 50 mm above base). The intention is to claim that by suspending geocell within ballast embankment, further improvements can be made, and it has been validated by previous experimentation. As can be seen, both sets of results show a short segment of low stiffness, in the early stages of monotonic loading, followed by a more prolonged development of improved stiffness. Once the results enter Zone *B*, placing geocell at 100 mm above the base becomes more advantageous in reducing sleeper's displacement than placing geocell at 50 mm does. The displacement difference is up to 5.2 mm when the vertical load reaches 285 kPa. From this point onward, the reinforcing effect decreases and the two curves cross over where the vertical load increases to 498 kPa. Afterward, placing geocell at 50 mm offers better performance until the end of simulation. Overall, both studies indicate that suspending geocell within the ballast embankment can yield better load-bearing performance. This agreement, however, is not observed with the unreinforced embankments. Strain-softening was observed in the test embankment, whereas the simulated embankment exhibits strain-hardening throughout. Therefore, the unreinforced test embankment yields a lower secant stiffness than in the simulation: 2,916 kPa/m for the test and 7,975 kPa/m for the simulation, at a vertical displacement of 60 mm.

This disagreement arises mainly from the unconfined nature (in both longitudinal and transverse directions of the embankment) of the prototypical test conducted by Leshchinsky and Ling (2013a). The ballast can move freely in both directions, whereas the longitudinal movement is prohibited in the current models by installing two boundary walls. In addition, the difference between the test and simulated ballast infill, as well as other factors such as embankment geometry, loading plate size, geocell strength and boundary

conditions, may also contribute to the significant difference in vertical displacement. The gravel that was used in the test is smaller on average than the ballast used in the simulation ( $D_{50} = 15.5$  mm and 35 mm, respectively) and so yields a lower shear strength. This is confirmed by the respective triaxial test results; for example, a shear strength of approximately 400 kPa for the gravel in the test (Leshchinsky & Ling, 2013a) and 700 kPa for the coarser aggregate in the simulation, when subjected to the same confining pressure of 90 kPa. The lower shear strength for the gravel leads to its strain-softening behaviour and lower stiffness. It is interesting to note that the discrepancy occurred with the unreinforced embankment, whose behaviour is dissimilar to that of the reinforced embankment. This implies that the use of a geocell panel is able to mitigate potentially ‘weak’ properties of the ballast infill and increase stiffness through its reinforcement effects.

Figure 3.11 shows sleeper’s vertical displacement plotted against the number of load cycles for the straight embankment under cyclic loading. It is evident that the geocell is effective in reducing vertical displacement associated with cyclic loading. During the initial 5 loading cycles (Zone A), all three cases exhibit a high displacement rate. Similar behaviour is observed in a previous study (Chen et al., 2012b) where geogrid is used. The early-stage quick displacement also agrees with the results obtained by (Selig & Waters, 1994) who found that the relatively rapid displacement in the early stage is associated with the poorly consolidated nature of infills. In Zone A, the vertical displacement is reduced due to the use of geocell. However, no noticeable difference is observed between placing geocell at base and 50 mm above the base. The role of geocell becomes more pronounced as the cycle

number increases which is suggested by the noticeably slower displacement rates in Zone B (5<sup>th</sup> to 20<sup>th</sup> loading cycle). This phenomenon can be attributed to the passive-confinement mechanism of geocell. Where cyclic loading continues, the infills is further compacted, stiffening the geocell mattress, which in turn provides better reinforcement to the ballast embankment. In Zone B, placing geocell at 50 mm above base outperforms placing geocell at base. The reinforcing effect improves slightly along with the increase of load cycle number, resulting in a final vertical displacement of 45.5 mm versus 52.3 mm if placing geocell at base. Interestingly, Chen et al. (2012b) who installed geogrid in ballast embankment as reinforcement at 50, 100 and 150 mm concluded otherwise. Their study reported that placing geogrid at lower levels (i.e. 50 mm above subgrade) better prevents the displacement. There is no clear reason to this disagreement, but the two geosynthetic materials work in different modes: cell confinement by the geocell and grid-particle friction by the geogrid. It is suggested that the confinement matter works better if placed next to the load on ground; the geogrid is placed at a lower level where the load becomes spread and reduced.

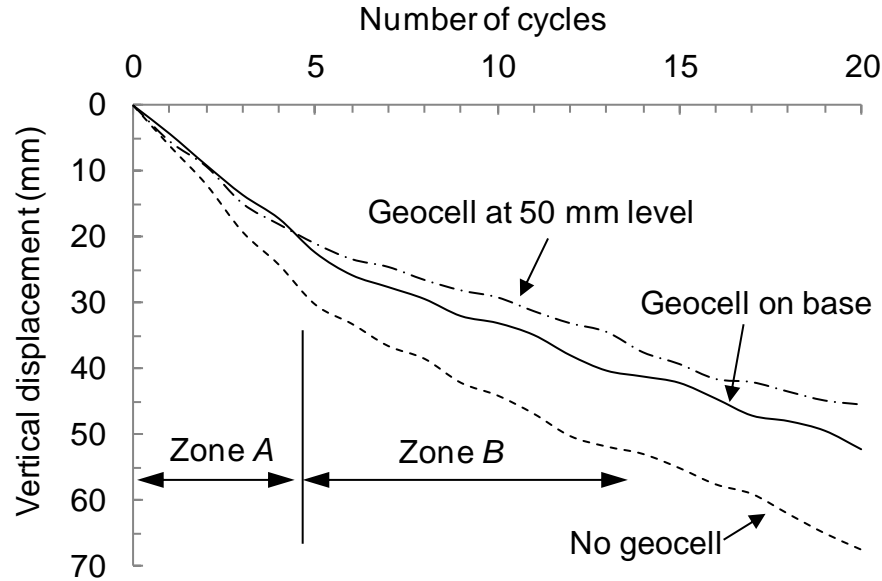


Figure 3.11 Vertical displacement for straight embankment under cyclic loading.

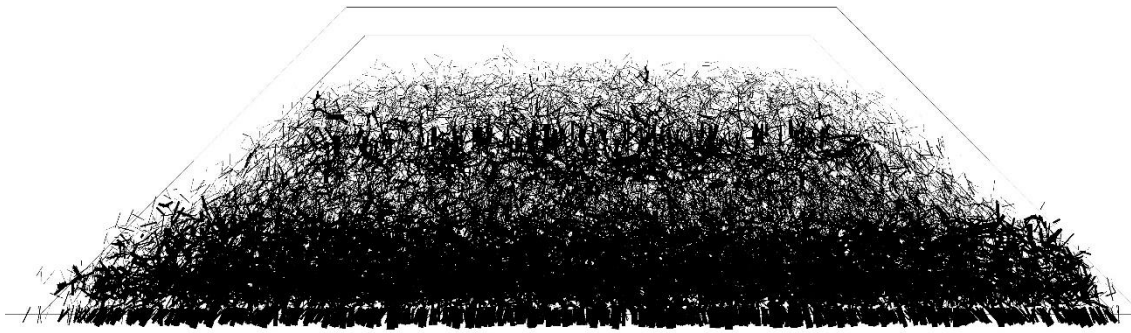
Comparison to the past study (Leshchinsky & Ling, 2013a) has been made in the final vertical displacement only as the original displacement versus loading cycle relationship is unavailable. After the 20<sup>th</sup> cycle, the simulations show higher vertical displacement than that indicated by tests. The vertical displacement is 67.5 mm for the simulation and approximately 48 mm for the unreinforced embankment test; and 52.3 mm when placing geocell at 50 mm above base for the simulation and approximately 31 mm for the test of the embankment incorporating the geocell at the 100 mm above base. In addition to the compaction effort, other factors that may contribute to the final settlement difference are the size effect at the plate-infill interface and the geocell types used. The simulations use a sleeper of 50 mm × 500 mm and infill of  $D_{50} = 35$  mm, and the test used a square plate, 356 mm × 356 mm in size, and infill of  $D_{50} = 15.5$  mm. The smaller sleeper-infill size ratio for the simulations results in the sleepers ‘punching’ to a greater extent into the infill than the test does. This punching effect likely reduces with depth as the lateral resistance (arching)

of the infill between neighbouring sleepers increases, and the displacement stabilizes. On the other hand, Leshchinsky and Ling (2013a) adopted Novel Polymeric Alloy (NPA) geocell which exhibits higher stiffness and tensile strength (27 MPa) than typical HDPE geocell (Le Pen et al., 2013; Yang et al., 2012). The material strength difference can also prevent embankment settlement.

In order to gain a greater insight into the force distribution and transmission mechanism of unreinforced and reinforced ballast embankments, as shown in Figure 3.12, contact forces are drawn at the same scale for the straight embankments after the 20<sup>th</sup> cycle. The contact forces are observed through the front cross section of the respective embankments. It can be seen that the contact forces develop in different patterns between the unreinforced and reinforced embankments. The unreinforced embankment shows an uneven distribution of contact forces. The forces adjacent to the base of the embankment are more concentrated than elsewhere in the embankment. In contrast, the contact forces for the geocell-reinforced embankments are distributed more evenly. This even distribution of contact forces helps eliminate overstressing of the infill and reduces the likelihood of localized displacement and/or failure, thus improving the resilience of the embankment. In addition, an increase in the maximum and average contact forces within the ballast are recorded among the three cases simulated. The unreinforced case exhibits the lowest contact force value comparing to the two reinforced cases. This difference can be attributed to the higher internal contact forces induced by a reduced settlement. The internal stress caused by loading cannot dissipate through particle movement as it is restricted by the geocell panel. The highest contact force is observed where the geocell panel is placed 50 mm above the base, which

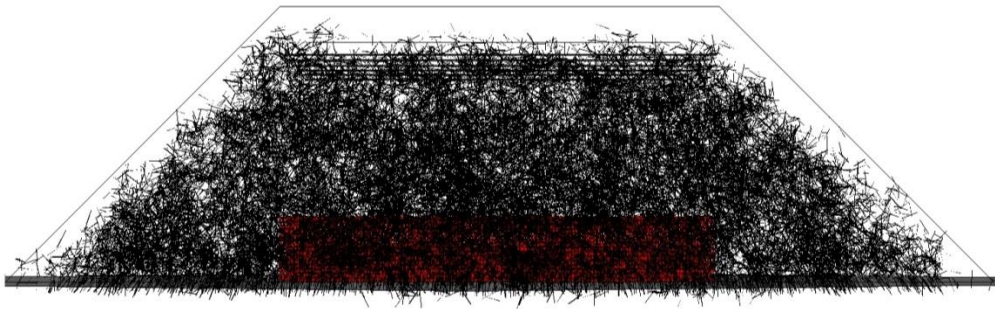


implies less ballast movement should be expected. This observation agrees with results shown in Figure 3.10 (monotonic loading case). That is, at the same settlement, the reinforced cases sustain loads greater than the unreinforced case does.



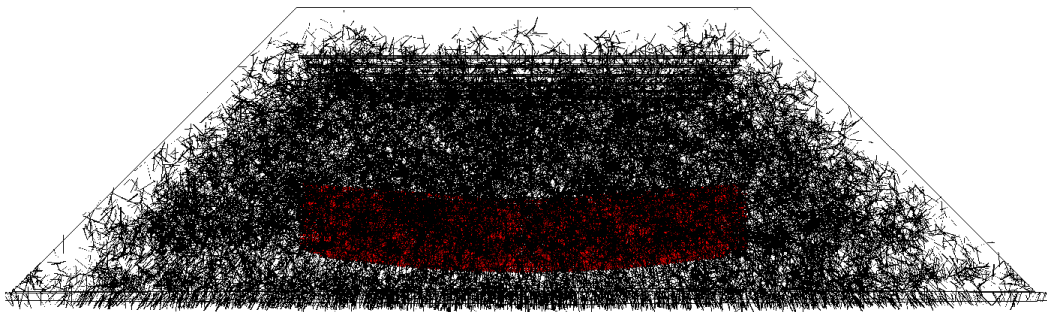
Max. Contact Force:  $7.55 \times 10^6$  N    Average Contact Force:  $4.77 \times 10^5$  N

(a)



Max. Contact Force:  $8.74 \times 10^6$  N    Average Contact Force:  $5.34 \times 10^5$  N

(b)

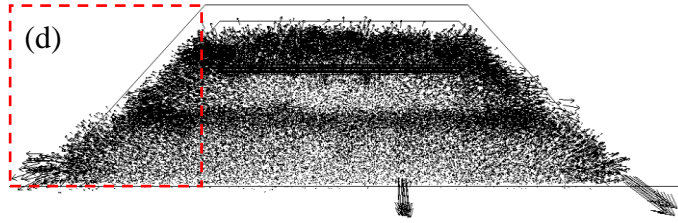


Max. Contact Force:  $9.95 \times 10^6$  N    Average Contact Force:  $6.28 \times 10^5$  N

(c)

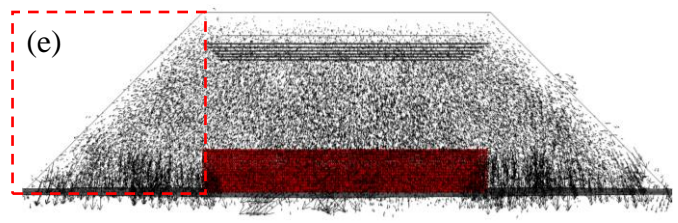
Figure 3.12 Contact forces drawn at the same scale for straight embankment after the 20<sup>th</sup> cycle: (a) unreinforced; (b) geocell at base; and (c) geocell 50 mm above the base.

Figure 3.13 shows the total particle displacement vectors (i.e. the combination of vertical and lateral displacement) of the ballast after the 20<sup>th</sup> cycle, again drawn at the same scale as that shown previously to allow visualization of the microstructure strain evolution of the embankments. Figure 3.13 (c) is tilted by 5 degrees for better visualization of the displacement vectors, which causes the vectors appear slightly denser and longer. Apart from the reduced particle displacement, the major difference between the unreinforced and the reinforced embankments lies in the direction of the ballast displacement. The infill in the reinforced embankments [Figure 3.13 (b and c)] displace mainly toward the base, whereas the infill in the unreinforced embankment [Figure 3.13 (a)] tends to move laterally. This can be better visualized in Figure 3.13 (d-f) which provide zoomed-in views of the left-hand-side unreinforced sections of three embankments. These observations confirm the ability of the geocell panel to prevent the ballast infill from spreading. That is, the geocell panel helps restrain the confined infill equivalent to that of a relatively rigid pad. In this way, the pad effectively absorbs overlying loads and transfers them downward, avoiding or reducing lateral spreading. This is consistent with the distribution of contact forces shown previously in Figure 3.12 (b and c), where the contact force concentration is less significant at the base of the embankments and thus reduces embankment displacement. The central part of the elevated geocell panel [Figure 3.13 (c)] undergoes modest subsidence (approximately 10 mm), which suggests slight lateral movement of the infill underlying the panel.



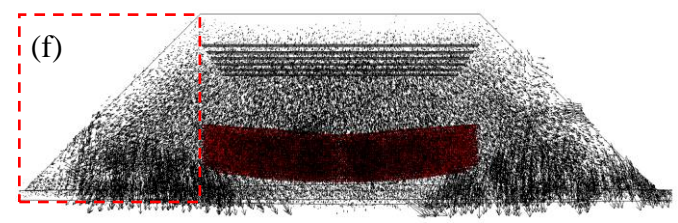
Max. Displacement: 33.1 mm Average Displacement: 18.1 mm

(a)



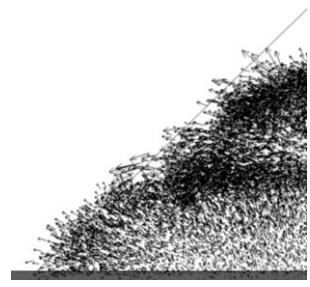
Max. Displacement: 16.5 mm Average Displacement: 9.4 mm

(b)

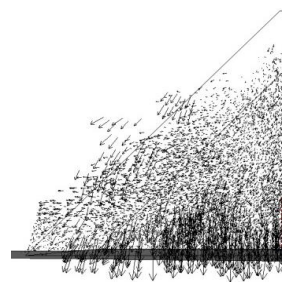


Max. Displacement: 13.4 mm Average Displacement: 7.2 mm

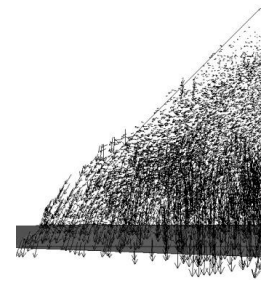
(c)



(d)



(e)



(f)

Figure 3.13 Total displacement vectors drawn at the same scale for straight embankment after the 20<sup>th</sup> cycle: (a) unreinforced; (b) geocell at base; (c) geocell 50 mm above the base; (d–f) zoomed-in views of the left-hand-side unreinforced sections of three embankments.

Figure 3.14 shows the total displacement vectors for the geocell panels after the 20<sup>th</sup> loading cycle, as well as the maximum displacements and their approximate locations. These displacement vectors are scaled up by a factor of 50 in order to achieve better visualization. As can be seen, the panels undergo a limited amount of displacement and they hence remain effectively in their original configuration after repetitive loading, demonstrating their strength. In the case where the geocell is placed at the base [Figure 3.14 (a)], the maximum displacement occurs at the bottom-left of the panel. This location shifts upward when the panel is located 50 mm above the base. The relocation implies that the geocell panel settles noticeably (10 mm approximately) together with the ballast assembly. In addition, the displacement is not position-dependent. All cell walls, at the centre and along the edges, undergo a similar level of deformation. This behaviour aids in evening out the stresses acting on the panel, eliminating local failures, maintaining its long-term reinforcement capability and, more importantly, accommodating the displacement of the infill and harmonizing the particle contact forces.

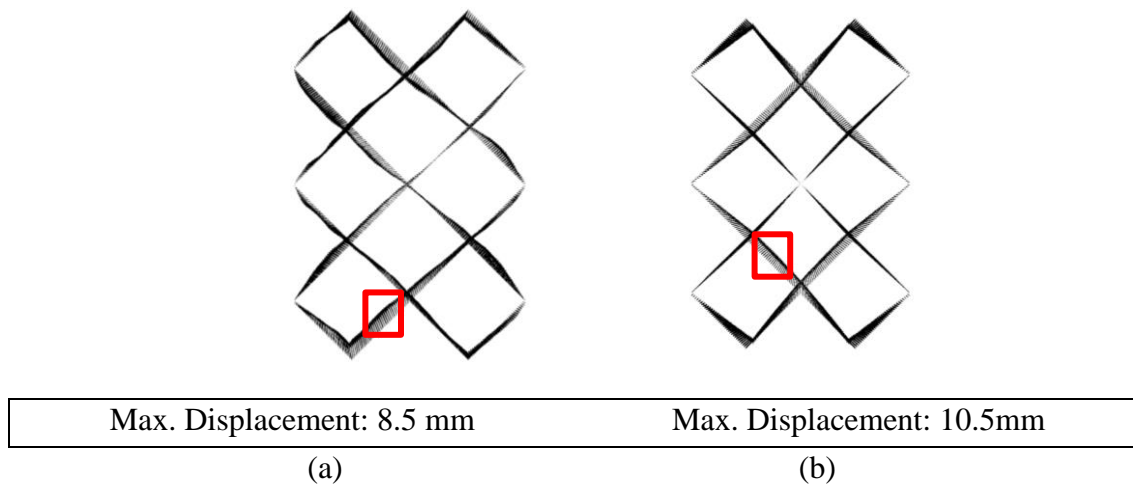


Figure 3.14 Total displacement vectors drawn at the same scale for geocell panel after the 20th cycle: (a) geocell on base; (b) geocell at 50 mm above the base.

### **3.5.2 Curved embankment**

The vertical and horizontal displacements plotted against the corresponding loads of the curved embankment that was subjected to the resultant load,  $P_R$ , (Figure 3.9) are shown in Figure 3.15. The load-vertical displacement curves [Figure 3.15 (a)] develop in a form similar to those observed with the straight embankment (Figure 3.10). Non-yielding is clearly evident upon the load of 600 kPa. The three curves exhibit largely equal stiffness when the displacement is low (i.e. less than 10 mm), where the vertical displacement mainly arises from rearrangement of the uncrushable infill (in the DEM model, in any case) and the geocell provides a marginal contribution to stiffness. The geocell's reinforcement effect becomes clear when the displacement exceeds 10 mm. It can be seen that the geocell-reinforced embankments obtain stiffness higher than that of the unreinforced embankment, and so support a greater load, given the same vertical displacement. Placing the geocell 50 mm above the base yields a higher stiffness. Similar improvement occurs in the lateral direction [Figure 3.15 (b)], where the sleepers of the reinforced embankments displace less than the sleepers of the unreinforced embankment, with an equal resultant load. This is attributed to the geocell enhancing the interlocking of the infill and so restraining the rearrangement and rotation of the ballast particles. In the later stages of loading (i.e. > 40 mm lateral displacement), lateral yielding occurs in all simulations, showing a marked displacement in response to the cyclic loading. This is a result of the sleepers having partially moved out of the region influenced by the geocell, and thus having to rely on the shoulder ballast to provide lateral resistance. This observation is valid for all simulations performed for curved embankments. Although this phenomenon is unlikely to occur in actual railways, as catastrophic accidents can be caused due to de-

railing, the results are presented for the purpose of demonstrating the improvements derived from placing geocell in railway ballast embankments.

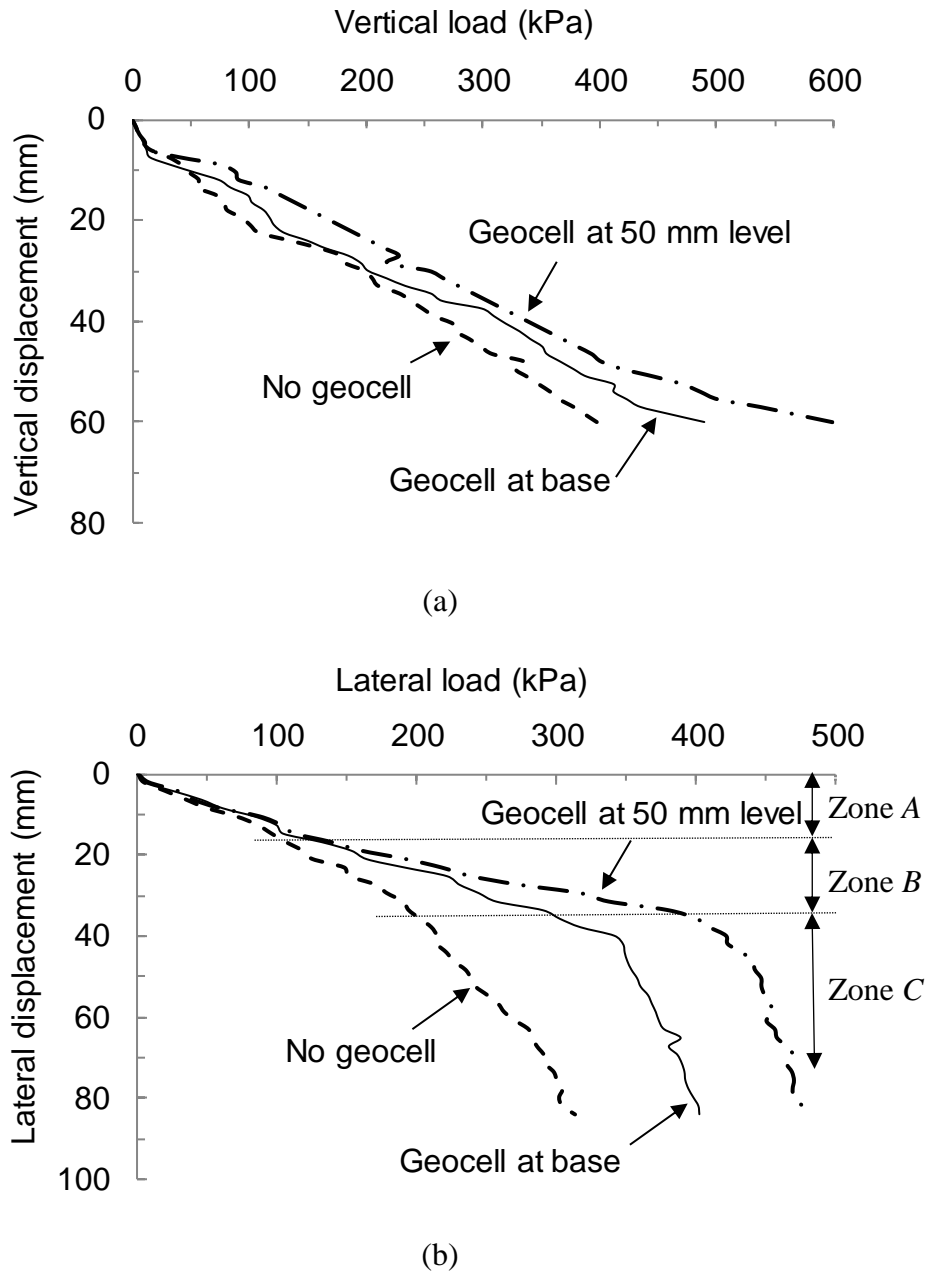


Figure 3.15 Monotonic loading-induced sleepers movement in curved embankment: (a)

Vertical displacement, (b) lateral displacement.

Figure 3.16 shows the vertical and lateral displacement of the sleepers due to cyclic loading. As was evident with monotonic loading, the geocell-reinforced embankments outperform the unreinforced embankment. The reinforced embankments exhibit less vertical and lateral displacements than those observed in the unreinforced embankment. Placing a geocell 50 mm above the base, again, better controls displacement in both the vertical and horizontal directions. The vertical displacement [Figure 3.16 (a)] is more pronounced over the first 5 cycles, and then shows a decreased rate over the remaining cycles. The lateral displacement of the sleepers is relatively high, given the low number of cycles [Figure 3.16 (b)]. This is likely caused by the unrestrained nature of the sleepers, where the restraining influence of the track structure, such as the rails, rail anchors and fastenings, were not taken into account in the simulations, as mentioned earlier. As a result, the sleepers are able to displace more freely than would occur in the field.

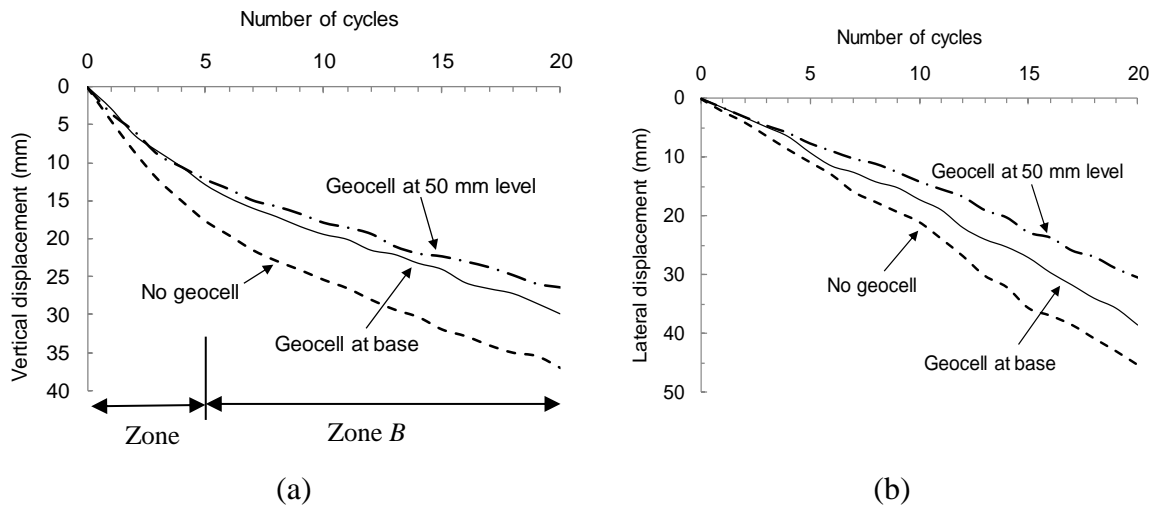


Figure 3.16 Cyclic loading-induced sleepers movement in curved embankment: (a) vertical displacement; (b) lateral displacement.

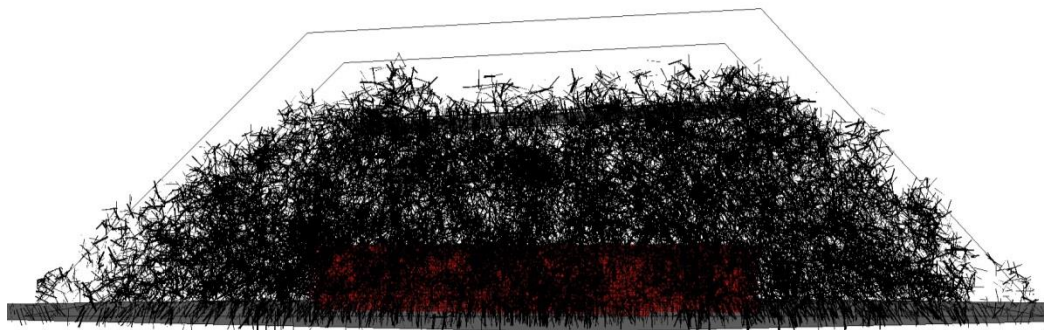


Figure 3.17 shows the inter-particle contact forces drawn at the same scale after the 20<sup>th</sup> load cycle. As for the straight embankments, the geocell panels also appear to promote an even stress distribution for the curved embankments. This is in agreement with the particle displacement vectors shown in Figure 3.18, where reduced spreading is observed for the reinforced embankments, when compared with the unreinforced embankment. Moreover, comparing the displacement vectors with those for the straight embankments (Figure 3.12) implies that the geocell panels in the curved embankments are similarly effective in forming a relatively rigid platform and to mitigate ballast spreading.



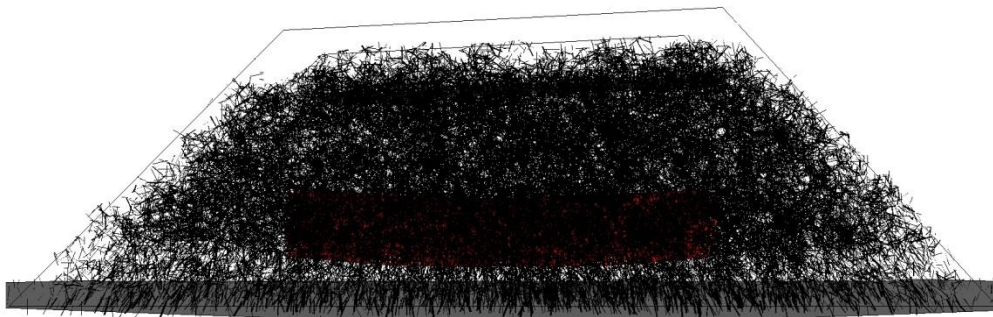
Max. Contact Force:  $8.73 \times 10^6$  N    Average Contact Force:  $4.74 \times 10^5$  N

(a)



Max. Contact Force:  $9.38 \times 10^6$  N    Average Contact Force:  $6.28 \times 10^5$  N

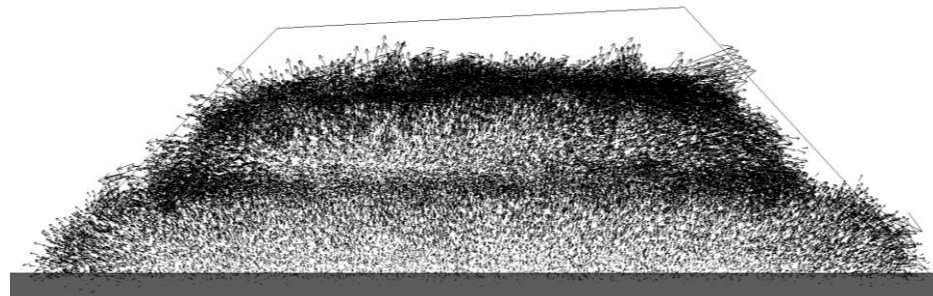
(b)



Max. Contact Force:  $1.23 \times 10^7$  N    Average Contact Force:  $8.51 \times 10^6$  N

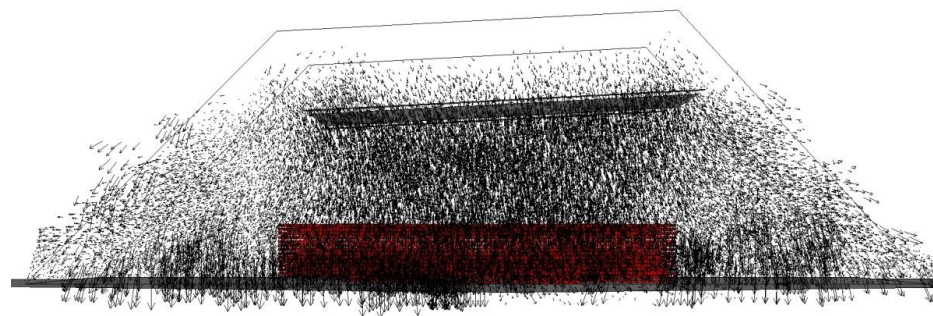
(c)

Figure 3.17 Contact forces drawn at the same scale for the curved embankment after the 20<sup>th</sup> cycle: (a) unreinforced; (b) geocell at base; and (c) geocell 50mm above the base.



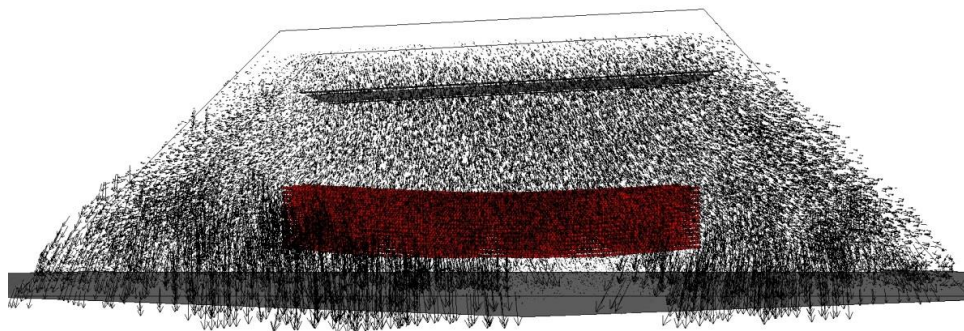
Max. Displacement: 33.1 mm    Average Displacement: 22.2 mm

(a)



Max. Displacement: 16.1 mm    Average Displacement: 10.7 mm

(b)



Max. Displacement: 14.3 mm    Average Displacement: 9.6 mm

(c)

Figure 3.18 Total displacement vectors drawn at the same scale for the curved embankment after the 20<sup>th</sup> cycle: (a) unreinforced; (b) geocell at base; and (c) geocell 50mm above the base.

Figure 3.19 shows the total displacement vectors for the geocell panels after the 20<sup>th</sup> cycle. The panels maintain their respective initial shape and demonstrate the geocell's capability to sustain the lateral load for the curved embankments. The geocell walls, in particular the walls adjacent to the longitudinal centrelines, deflect to the right – in line with the direction of the resultant forces. The concurrent deflection of the walls helps counteract the lateral load, confine the lateral load within the area of the panel, and reduce spreading of the infill along the edges. The panel situated 50 mm above the base appears to deflect slightly more than does the panel at the base. This is consistent with the geometric deformation which occurs in a 'suspended' panel [Figure 3.18 (c)], and suggests it is likely to degrade sooner than the panel located at the base. This can be examined through additional case studies, such as increasing load cycles and placing panels at higher levels in the embankment. This is, however, beyond the scope of the present paper.

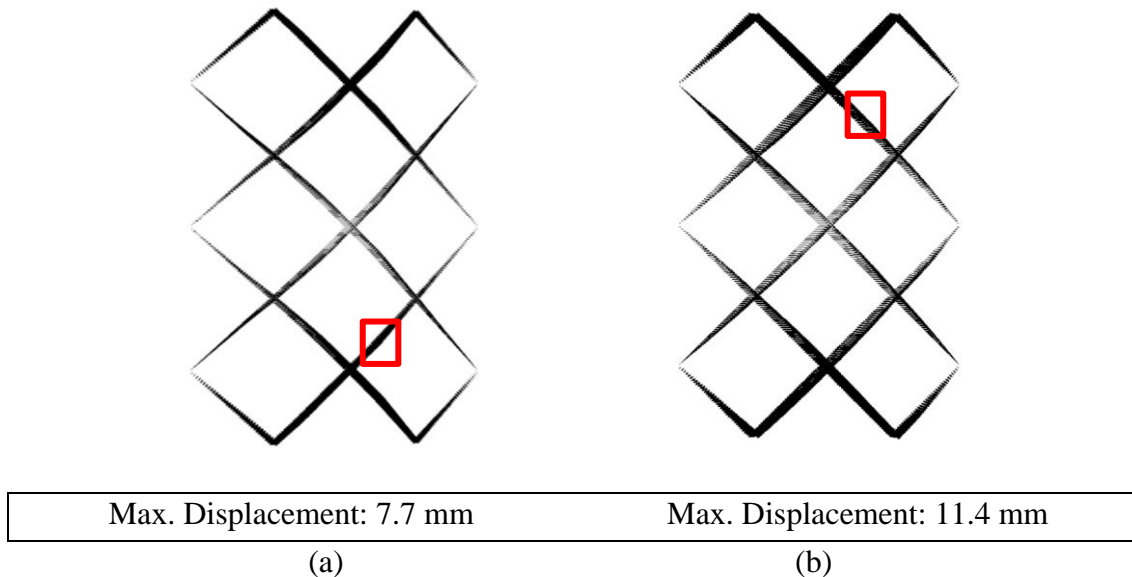


Figure 3.19 Total displacement vectors drawn at the same scale for geocell panel after the 20<sup>th</sup> cycle: (a) geocell on base; (b) geocell at 50 mm above the base.

To gain a further insight into the deflection of the geocell panel, geocell strains are captured. As illustrated in Figure 3.20, for a pair of neighbouring spheres of interest, the strain,  $\varepsilon$ , is defined as the edge-to-edge distance after displacement,  $D_1 - D_0$ , to the initial centre-to-centre distance,  $D_0$ . The strain values at locations of interest are summarized in Table 3.4. These include junctions *a* to *g*, panel halves *A* and *B*, as shown in Figure 3.7 (d), and locations of maximum strain for the geocell panels at the base and 50 mm above the base, subjected to the monotonic and cyclic loading scenarios. Panel halves *A* and *B* rest on the lower and the higher side of the embankment, respectively.

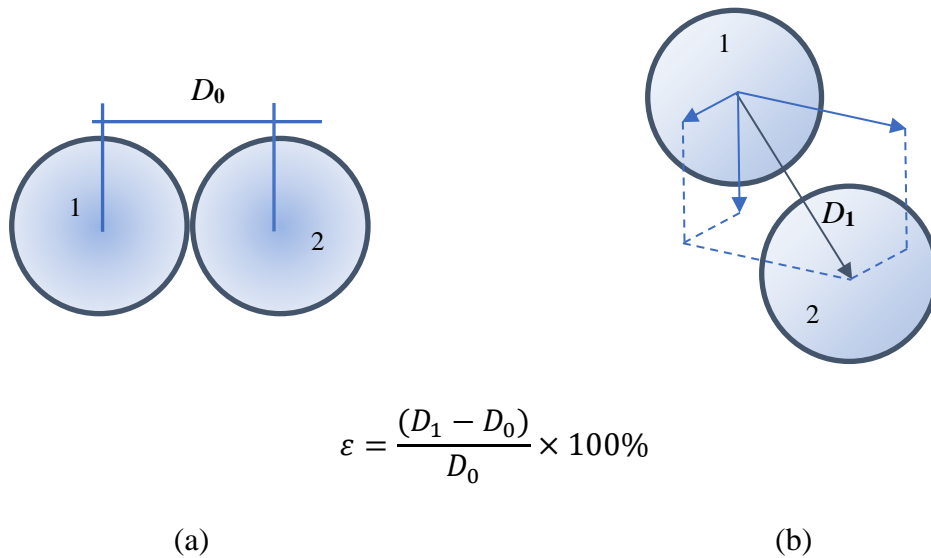


Figure 3.20 Illustration on the calculation methodology of strain in geocell: (a) before displacement; (b) after displacement.

The initial centre-to-centre distance is 5 mm, as shown in Figure 3.2 (b). The strain at a junction is calculated as the average strain of all spheres within 20 mm (i.e. 11.4% of the cell side) to the junction. The selected percentage is intended to reflect the strain in the proximity of the junction. The strain for either half panel is the average strain of all the

spheres belonging to that half panel. The strain values in Table 3.4 show that the geocell deforms at every junction with varying magnitude, for instance, ranging from 24.1% to 41.6% for the geocell at the base when subjected to monotonic loading. Where the sleepers advance less under the cyclic loading, noticeably lower strains of 14.1% on average occur to the junctions. There is a clear difference in strain between the panel halves *A* and *B*, where all other design details remain the same. For instance, the average strain is 18.5% for panel half *A* and 24.9% for panel half *B* under monotonic loading. This implies that greater deflection occurs at the part of the geocell that provides direct reaction to the inclined train load  $P_R$ . Lower strains occur to both halves where the geocell is placed 50 mm above the base than the geocell placed at the base, which agrees with the embankment displacement results shown in Figure 3.11 and 3.16. Under the monotonic loading, the entire panel is subject to a maximum strain of 39.7%, if placed at the base, and 45.6%, when placed 50 mm above. If subjected to the cyclic loading, the panel shows a maximum strain of 28.4%, when at the base, and 23.4%, when 50 mm above. The magnitude of these strains indicates that the geocell panel remains at the pre-failure state for the load levels simulated. The approximate locations, L1 to L4, where maximum strains were recorded, are highlighted in Figure 3.21; i.e. L1 for 39.7% and L2 for 45.6% under the monotonic loading scenario, and L3 for 28.4% and L4 for 23.4% under the cyclic loading scenario. There is no clear pattern to the locations of maximum strain, however, as can be seen, they are all consistent with the center of a cell-wall. This indicates that cell-walls undergo greater deflection than the junctions do, as one might expect.



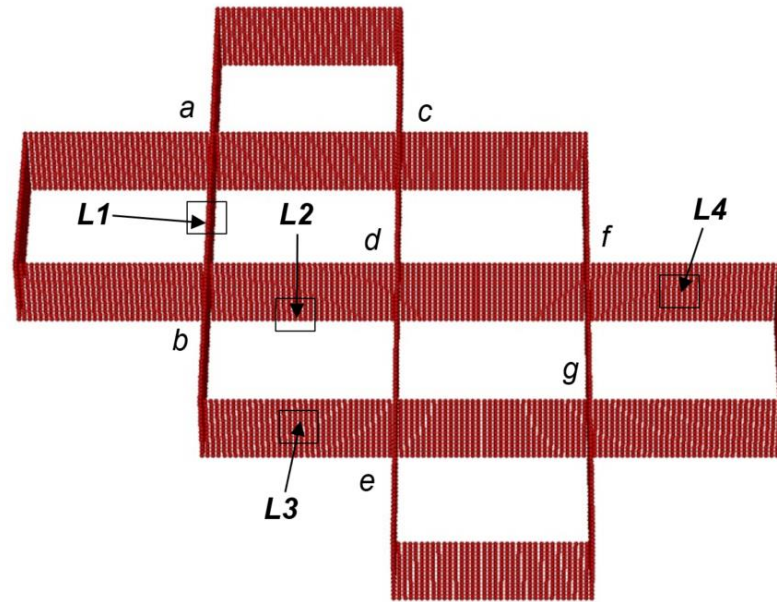


Figure 3.21 Locations of maximum strain.

Table 3.4 Geocell panel strains

Position	Strain (%)			
	Monotonic loading		Cyclic loading	
	Geocell at base	Geocell 50 mm above base	Geocell at base	Geocell 50 mm above base
Junction <i>a</i>	29.1	34.1	10.9	11.3
Junction <i>b</i>	39.2	39.8	15.6	14.8
Junction <i>c</i>	39.2	21.1	18.7	18.3
Junction <i>d</i>	24.1	29.7	13.3	13.4
Junction <i>e</i>	30.2	38.9	12.0	10.2
Junction <i>f</i>	41.6	41.2	18.0	15.3
Junction <i>g</i>	26.9	33.0	16.2	10.0
Panel half <i>A</i>	18.9	35.3	19.8	16.1
Panel half <i>B</i>	24.4	39.1	27.0	22.7
Maximum strain	39.7	45.5	28.4	23.4

### **3.6 Conclusions**

This study assesses the use of geocells in reinforcing railway ballast embankments. Discrete element modelling has been conducted, using clumped particles to simulate angular ballast, to evaluate bearing capacity, vertical displacement and lateral spreading of the embankment, as well as providing insights into the micro-behaviour of the ballast infill and the geocell, including contact forces and displacements. Straight and curved embankments have been subjected to monotonic and cyclic loading conditions and the modelling results have been compared with previous, published test results. The conclusions of this study are as follows:

1. The simulation results for the straight, reinforced embankment are in reasonably good agreement with the test results. This suggests that the discrete element modelling is valid and is an appropriate method to assess the mechanical response of railway embankments.
2. For the unreinforced, straight embankment, however, simulation results show modest agreement with the past test results. The suboptimal agreement may be attributed to the differences in the particle size distribution, embankment geometry and loading magnitude. These factors influence the embankment performance where reinforcement is not used.
3. The presence of a geocell within the ballast stiffens both straight and curved embankments. Geocell-reinforced embankments exhibit less vertical displacement and lateral spreading compared with unreinforced embankments and so aid in maintaining a safer track alignment in the longer term. The embankments with a geocell suspended 50 mm above the base are stiffer than the embankments with a geocell located at the



interface between the ballast and the subgrade. The former, however, deflects more than the latter and so risks having a reduced operational life. The geocell embedment depth results disagree with results in Chen et al. (2012b) which used geogrid to reinforce straight embankment. Their study suggests that placing geogrid at a higher level causes less vertical displacement than placing it close to the subgrade.

4. The geocell constrains the displacement of the encased ballast infill to form a relatively solid mattress. The mattress helps absorb overlying loads, increase the stiffness of the embankment, reduce spreading of the infill and balance forces in the embankment.

Whilst the study proposes a valid approach to demonstrate and examine the effects of reinforcing railway ballast with geocell, a number of limitations and assumptions were adopted to undertake successfully the DEM simulation:

1. The geocell model was calibrated solely against a series of tensile strength tests. Other properties such as puncture resistivity, flexural stiffness and torsion stiffness were not considered in the current study. Attempts will be made to incorporate these material properties in future studies to improve the reliability of the modelling framework.
2. Whilst the use of clumps provides a more accurate representation of ballast angularity, when compared with the adoption of entirely spherical particles, their shape does not fully reflect actual ballast angularities and, hence, have limited capability to simulate accurately ballast interlock and inter-particle friction. Defining the clumps as non-breakable in the simulation, may also result in overestimating the long-term performance of the embankment. It is plausible to conduct a 3D simulation of the

embankment, but the scaled-down embankment may compromise the simulation accuracy.

3. In simulation, the ballast is calibrated against the monotonic test results. The calibration can possibly improve where cyclic loading test results are available and used. However, as stated in previous study (Lu & McDowell, 2010), the calibration against cyclic test results can be extremely time consuming. Due to this reason, this calibration step was neglected, enabling a focus on the simulation of ballast embankments.
4. Due to the limited number of load cycles applied to the embankment, the results presented may not accurately reflect the long-term performance of the ballast embankment. Along with advancement in PFC3D and computational capacity, this issue can be resolved in future studies. In addition, the number and location of inter-clump parallel-bond breakage, which can provide in-sight on the ballast re-arrangement, was not recorded. It will be taken into consideration in our future studies when ballast breakage is incorporated into the modelling framework.

### **Acknowledgement**

The authors wish to thank Mr. Rod Fyfe from Geofabrics Australasia for his assistance in this research.

**Notations**

$D_0$	center-to-center distance of neighboring spheres,
$D_1$	center-to-center distance of neighboring spheres,
$D_{50}$	diameter of particles 50% finer by weight
$k_n$	normal stiffness
$k_s$	shear stiffness
$\bar{k}_n$	parallel-bond normal stiffness
$\bar{k}_s$	parallel-bond shear stiffness
$\widetilde{k}_s$	Softening stiffness
$\widetilde{k}_n$	Normal stiffness in tension
$P_L$	lateral load
$P_R$	resultant load
$P_V$	vertical load
$R$	track horizontal curve radius
$\bar{R}$	bond radius
$v$	train velocity
$\mu$	friction coefficient
$\theta$	angle of inclination
$\rho$	density
$\bar{\sigma}_c$	parallel-bond normal strength
$\bar{\sigma}_t$	tensile strength
$\bar{\tau}_c$	parallel-bond shear strength
$\zeta$	local damping coefficient
$\varepsilon$	geocell strain
$\varepsilon_y$	geocell yielding strain
$\varepsilon_f$	geocell failure strain

## **Chapter 4. Failure Mechanisms of Geocell Cell- walls and Junctions (Paper 2)**

---

**INTENTIONALLY BLANK**

# Statement of Authorship

Title of Paper	Failure mechanisms of geocell cell-walls and junctions
Publication Status	<input type="checkbox"/> Published <input type="checkbox"/> Accepted for Publication <input checked="" type="checkbox"/> Submitted for Publication <input type="checkbox"/> Unpublished and Unsubmitted work written in manuscript style
Publication Details	Submitted to Geotextile & Geomembrane.

## Principal Author

Name of Principal Author (Candidate)	Yang Liu
Contribution to the Paper	Conducting literature review, laboratory experimentation, data interpretation and drafting manuscript.
Overall percentage (%)	70%
Certification:	This paper reports on original research I conducted during the period of my Higher Degree by Research candidature and is not subject to any obligations or contractual agreements with a third party that would constrain its inclusion in this thesis. I am the primary author of this paper.
Signature	Date 23/8/2018

## Co-Author Contributions

By signing the Statement of Authorship, each author certifies that:

- i. the candidate's stated contribution to the publication is accurate (as detailed above);
- ii. permission is granted for the candidate to include the publication in the thesis; and
- iii. the sum of all co-author contributions is equal to 100% less the candidate's stated contribution.

Name of Co-Author	An Deng
Contribution to the Paper	Supervising development of the work and revising manuscript.
Signature	Date 23 August 2018

Name of Co-Author	Mark Jaksa
Contribution to the Paper	Co-supervision of research and manuscript editing.
Signature	Date 24/8/18

Please cut and paste additional co-author panels here as required.

**INTENTIONALLY BLANK**

#### **4.1 Abstract**

Geocell panels are honeycomb-like systems used to provide earth reinforcement. Strips of perforated high-density polyethylene sheets, also known as cell-walls, are welded together at locations known as junctions. The cell-wall and junctions are designed to support and transfer tensile and shear loads and the integrity of these is essential for the appropriate performance of geocells in practice. Nevertheless, there is no standardized test procedure to assess the strength of the cell-wall or junction, and limited research has been undertaken regarding the failure mechanisms of geocell panels when subjected to various loading scenarios. This paper aims to examine the responses of geocell junctions and cell-walls under various loading conditions. An extensive testing program was undertaken to assess the geocell junctions, which included uniaxial tensile, shear, peeling and splitting strength tests. The uniaxial tensile strength, trapezoidal tearing strength and creep tests were carried out on the geocell walls. A ductility ratio was developed to measure the rapidness of failure under different short-term loading scenarios for both the cell-wall and junction. This paper presents the observed failure patterns and an evaluation of the implications of the practical uses of geocells.

**Keywords:** geosynthetics, geocell, cell-wall, junction, failure mechanism.



## 4.2 Introduction

Geocells have long proved effective in a wide range of geotechnical applications, such as earth retention, erosion control and roadways (Ngo et al., 2015; Song et al., 2017; Tanyu, Lau, et al., 2013; Zhang et al., 2010). Most of today's commercial geocell products are comprised of three components: cell walls, junctions and perforations (Figure 4.1) The cell walls are integrated by welding to form a honeycomb-like panel, to provide confinement for infill materials, such as sands and gravels. Geocells are supplied in a collapsed form and are outstretched on-site and anchored in place. The panel size and the cell space can be varied as part of the manufacturing process to suit individual requirements. The cell walls are commonly perforated to enhance drainage, to facilitate root growth between cells and to provide interlocking with coarse infills.

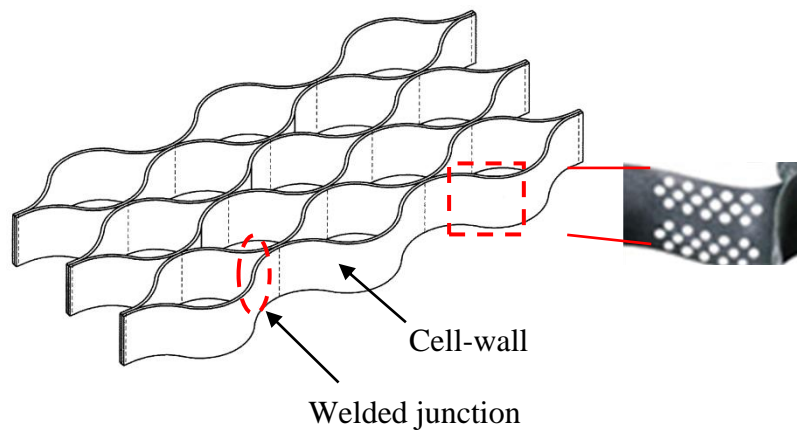


Figure 4.1. Geocell components.

Geocells are typically subjected to gravity loads from the infill materials on steep slopes or channels. On a slope, as shown in Figure 1.4(a–c), both geocell junctions and cell-walls are subjected to soil action from all directions. In such scenarios, geocells can withstand high

tearing, tensile and shear stresses in both the cell-wall and the welded junctions to prevent cell-wall rupture and separation of the junctions.

The geocell junctions are critical features that support and transfer high loads. As a result, the junctions are situated in locations that are most vulnerable to damage, and may result in unbalanced load transfer or even the failure of entire geocell panels (ASTM, 1993). Failure of the geocell junctions takes three forms: shear, where one strip is displaced longitudinally relative to the adjacent strip; peel, where one strip is displaced laterally; and tension, where two of the four strips at a junction are pulled relative to the other two and are perpendicular to the junction. However, there is a lack of standardized testing methods for geocells, and a lack of detailed investigations into their failure mechanisms. According to the manufacturers' product specifications, the current testing method performed on geocells is limited to seam strength tests, as specified by ASTM (1993), which examines the weld strength by applying a uniaxial tensile force, as shown in Figure 4.2. A 200 mm long specimen, cut from a geocell panel, is secured in the jaws of a tensile testing apparatus and a tensile strain of 50 mm/min is applied continuously until the specimen fails. Consequently, design uncertainties and unforeseen failure patterns have impeded the application of geocell in some engineering fields, such as railway engineering. ASTM (1993) suggested that additional failure mechanisms could occur in cell-walls and junctions, and corresponding testing procedures are desired. However, these tests have not been implemented to date to assess the performance of contemporary geocell products.

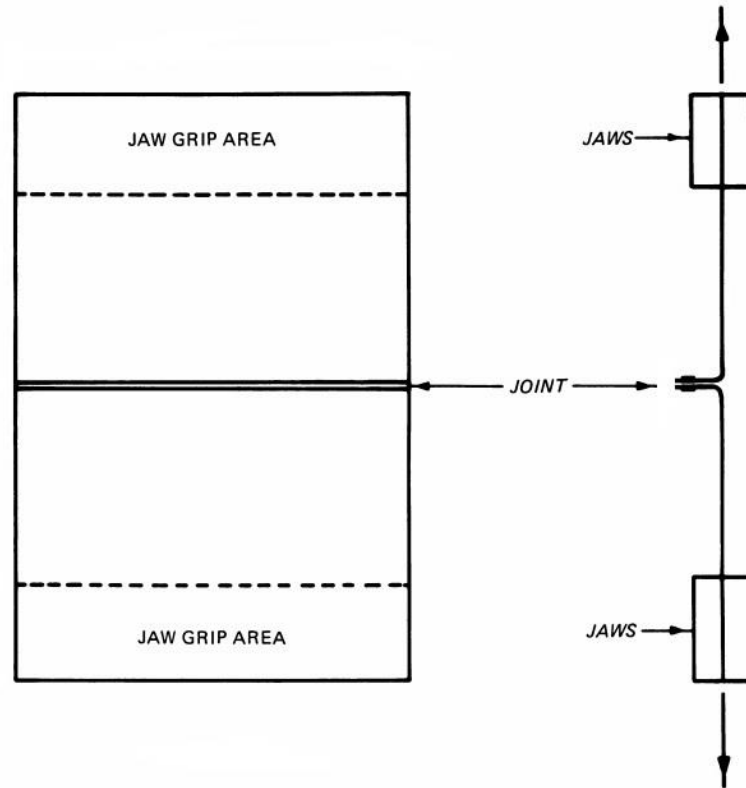


Figure 4.2. Junction seam strength test (ASTM, 1993).

There is also no established testing standard for assessing the integrity of cell-walls. Traditional testing methods for plastic materials may be adopted, but these are limited to short-term, uniaxial tensile strength tests. The potential failure mechanism that is likely to occur at the top or bottom edge of the geocell, as shown in Figure 1.4(a), has yet to be established. This type of failure occurs at the transition zone of embankment crests and slopes, where the geocell wall is subjected to a combination of flexure and tension. Where such damage occurs, the strength of the geocell wall is significantly compromised and subsequent soil movement can potentially result in global failure of the earth-reinforced embankment. Therefore, it is essential that the failure mechanisms of cell-walls, and their corresponding strength under tensile and flexural stresses, are investigated. In addition,

permanent deformation has long been a concern in the use of geosynthetics in a variety of geotechnical applications (Becker & Nunes, 2015; Sawicki, 1998; Thakur et al., 2013a). However, the long-term, creep behavior of geocell wall has yet to be assessed under tensile loading conditions.

This study incorporates a laboratory testing program to examine the failure mechanisms of geocell walls and junctions. In accordance with the likely failure modes discussed above, uniaxial tensile strength, trapezoidal tearing strength and creep tests were designed and conducted on cell-walls. Four tests, which reflect the loading conditions in practical use, were conducted on welded geocell junctions. The testing program included uniaxial tensile, shear, seam and peeling strength tests. To study the responses of geocells under various loading conditions, the stress-strain behaviors were measured along with the stiffness and peak and residual strengths. Different failure characteristics were observed from each test and were subsequently analyzed to derive the factors that affect geocell performance. Finally, this paper establishes and standardizes new testing procedures that will enable geocell manufacturers to measure and enhance the quality of existing geocell products, thereby increasing the reliability of geocell-reinforced systems.

### **4.3 Experimental Program**

This section summarizes the tests involved in the program. Detailed specimen dimensions, testing procedures and laboratory procedures are discussed.

### **4.3.1 Materials**

The experimental program was conducted on a perforated and textured commercial geocell product with a cell wall height of 100 mm. Each cell has a nominal opening area of 287 x 320 mm. The material specifications are obtained from the product brochure of a geocell manufacturer; the geocell section was fabricated using strips of high-density polyethylene (HDPE) sheet, with a density of 0.95 g/cm<sup>3</sup>, determined in accordance with ASTM D1505 (ASTM, 2010). The geocell material incorporates carbon black for ultraviolet stabilization. The content by weight of carbon black is between 1.5% to 2%, which is homogeneously distributed throughout the material. The strips are textured (rhomboidal indentations), with a thickness of 1.52 mm ( $\pm 0.15$ ), in order to increase the friction at the interface with the infill material. The indentations are distributed at a surface density of 22–31 units per cm<sup>2</sup>. The cell walls are perforated to enhance drainage and interlocking with the infill material. The cell-wall perforation proportion is 16.8% ( $\pm 1\%$ ). Individual cells are connected using full-depth, ultrasonic spot-welds and aligned perpendicular to the longitudinal axis of the strip. Figure 4.3 presents the details of the geocell junction. The length of the weld melt-point is approximately 10 mm, with a spacing of 5 mm and an average width of 3 mm.

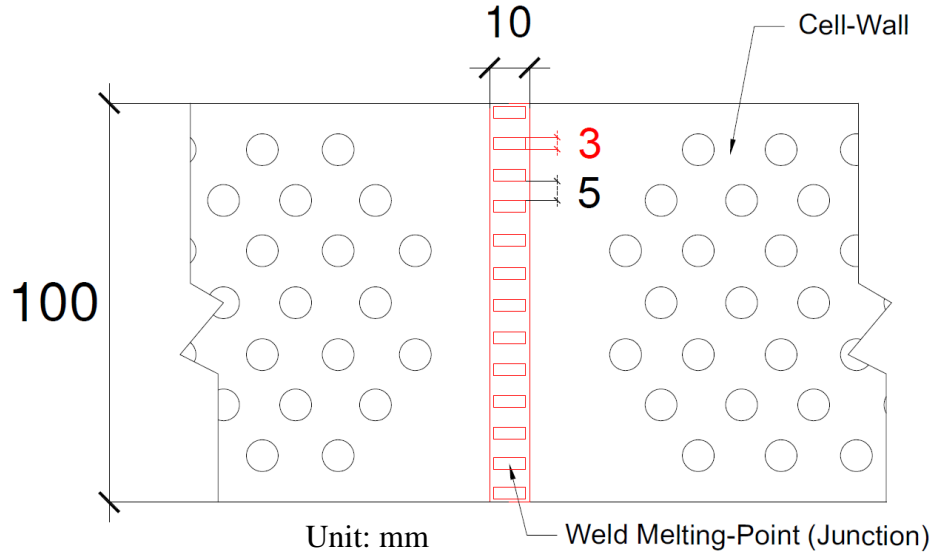


Figure 4.3. Details of the geocell junction

The typical stress-displacement relationship of HDPE, when loaded in uniaxial tension, is shown in Figure 4.4. It should be noted that this study adopts the conventional engineering stress calculation, which assumes that the stress and strain are distributed uniformly throughout the cross-section. There are two primary reasons for using this traditional approach. Firstly, most manufacturers use engineering stress to evaluate the strength and performance of their products. Secondly, it facilitates the comparison of the test measurements with the manufacturers' product specifications. As can be seen in Figure 4.4, the stress-displacement relationship typically exhibits three stages: A, B and C. Stage A is the elastic region, which is followed by a post-peak softening stage (Zone B), where the specimen decreases in strength with only slight elongation. Subsequently, the load plateaus with continuous elongation, reflected by the specimen slightly gaining strength (Zone C).

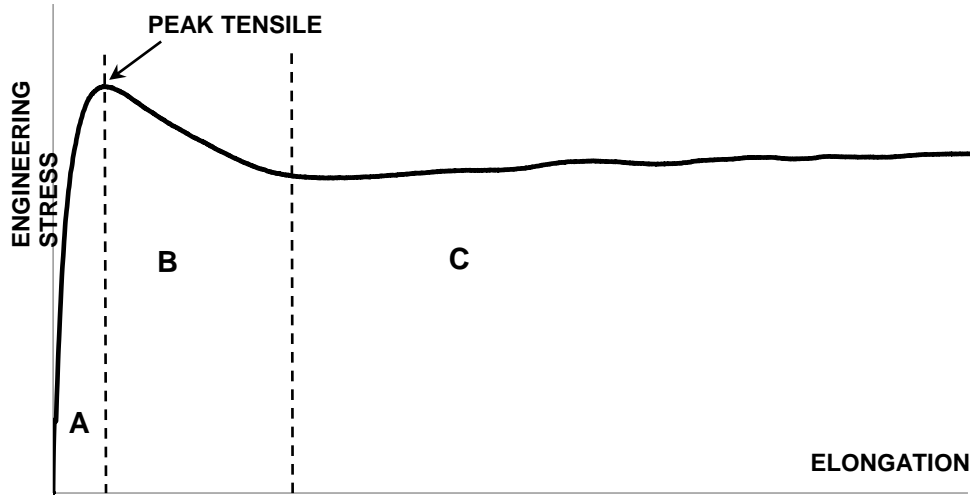


Figure 4.4. Typical stress-displacement relationship of HDPE (Kwon & Jar, 2008).

### 4.3.2 Testing procedures

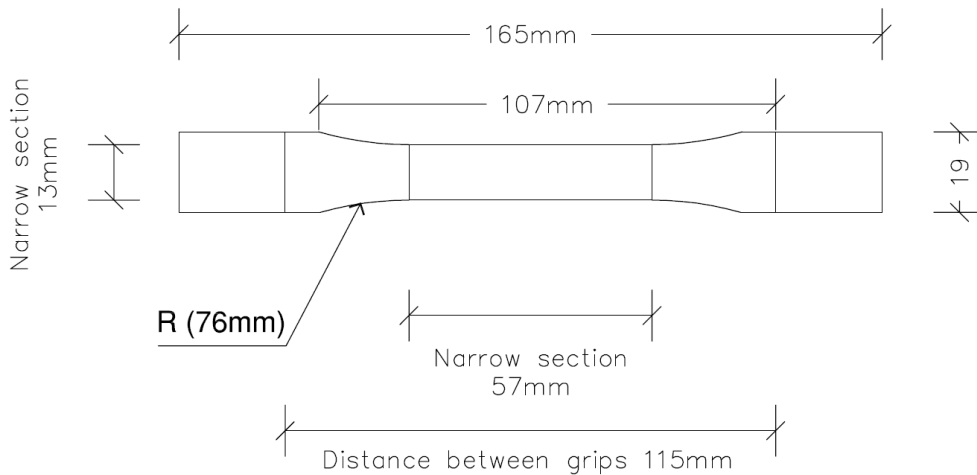
Detailed testing procedures and configurations of each test are described in this section. It should be noted that all tests were performed using an Instron tensile machine (Figure 4.5) at a temperature of  $25^{\circ} \pm 5\%$  and relative humidity of  $50\% \pm 5\%$ , to ensure that environmental effects were excluded.



Figure 4.5. University of Adelaide Instron machine.

4.3.2.1 Cell-wall: Tensile strength test

Uniaxial tensile strength tests were conducted on the plain area of the cell-wall in accordance with ASTM D638 (ASTM, 2004). The prepared specimens and testing details are shown in Figure 4.6. The gauge length of the specimens was 107 mm with a total of 58 mm gripping areas at both ends. The narrow section, where elongation occurs, was 13 mm in width. The purpose of conducting tensile strength tests on the cell-wall was to establish a reference against which the performance of the geocell junctions could be evaluated. The loading ranges of the Instron machine were set to 1,000 N in order to achieve optimal testing resolution. Once the specimen was clamped in place, the tensile force was applied by the displacement-controlled mechanism, at a rate of 50 mm/min. The elongation process continued until the specimen failed.



(a)



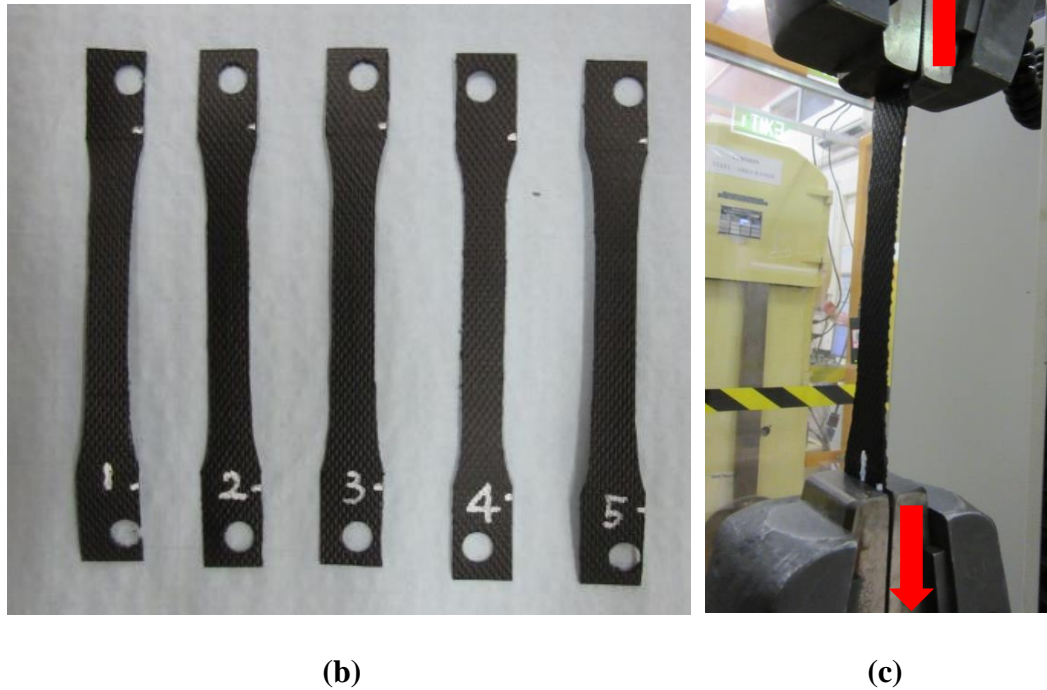


Figure 4.6. Uniaxial tensile strength test on geocell wall: (a) specimen configurations, (b) specimens cut from the plain area of the cell-wall, and (c) testing overview.

#### 4.3.2.2 Cell-wall: Trapezoidal tearing strength test

Trapezoidal tearing strength tests were conducted on the cell-walls to evaluate the strength and failure mechanisms when edge damage occurs. The test was configured against ASTM D4533 (ASTM, 1996). Five, identical specimens were prepared for this test; 75 mm high, 200 mm wide and 2 mm thick, as shown in Figure 4.7(a). The white lines marked on the specimen indicated the locations of the edges of the custom-made clamps used to fix securely the specimen [Figure 4.7(b)]. The vertical spacing between the two lines was 50 mm on the left-hand side and 100 mm on the right-hand side. The cut was made at the center of the left-hand side of the specimen to mimic the damage induced by an in-operation tearing. The clamps were positioned diagonally so that the specimen could be

torn apart from the left-hand side (i.e. the cut) as shown in Figure 4.7(c). The spacing between the two custom-made clamps was 300 mm prior to the start of the testing. As specified by ASTM (1996), in order to apply the tensile load, the Instron machine was set to displace at a fixed rate of 50 mm/min.

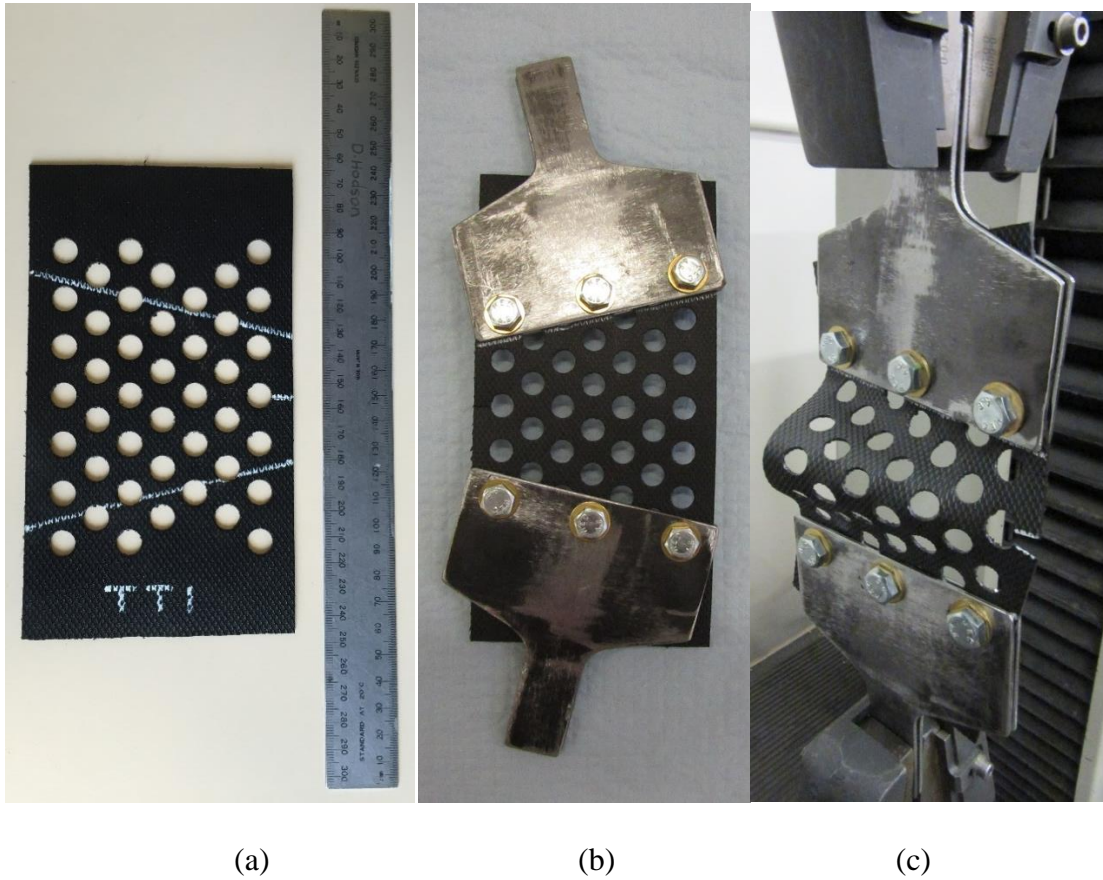


Figure 4.7. Trapezoidal tearing strength test: (a) specimens, (b) clamping technique, (c) testing schemes.

#### 4.3.2.3 Cell-wall: Creep test

The design of the specimen was guided by ASTM (2016). The specimen sizes were slightly altered to suit the available geocell product and the bespoke loading apparatus. As shown

in Figure 4.8, the specimen was 100 mm high and 200 mm wide, with a grip distance of 35 mm to ensure slipping did not occur during long-term loading. There were of a total 42, 10 mm diameter perforations in the specimen, accounting for 16.8% of the entire surface area of an individual cell-wall. These perforations reduce the strength of a cell-wall. Therefore, this particular location was chosen to be tested as it is the most vulnerable to external actions.

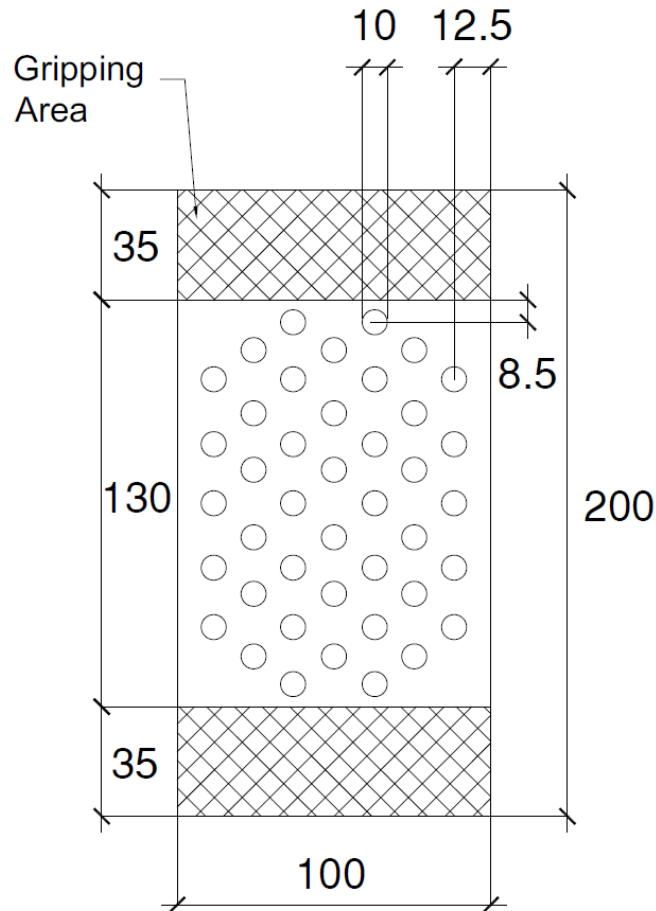


Figure 4.8. Prepared sample and dimension.

Figure 4.9 shows the rig used to perform the creep test. In order to maximize grip, the specimen was secured by a pair of clamps with screws penetrating the short edges. A linear variable differential transformer (LVDT) was installed on the face of the specimen to measure the strain rate of a fixed point, in the centerline of the specimen, and to obtain the specimen's elongation. The measurement is achieved by attaching a string to the lower clamp to transfer the differential movement between the upper and lower clamps to the LVDT and its associated recording device.

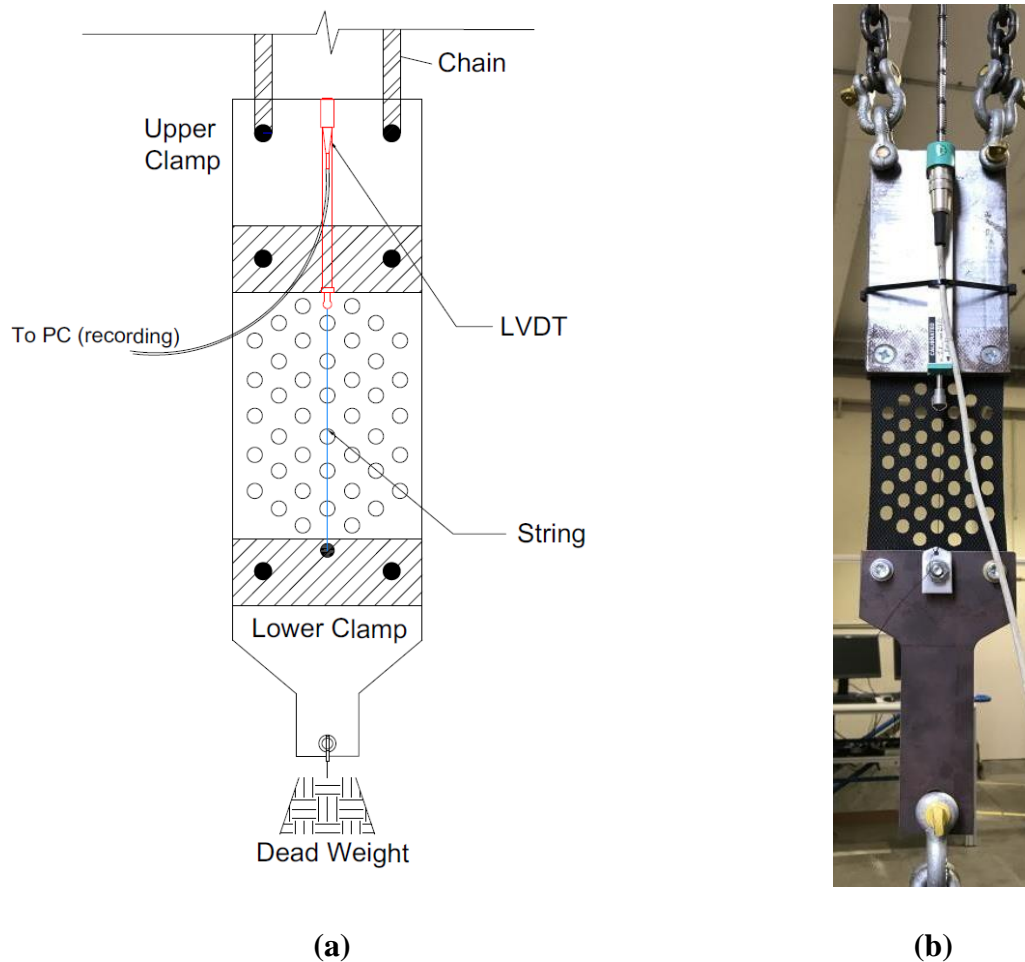


Figure 4.9. Creep test: (a) schematic and (b) test setup.

A total of five geocell specimens were tested for creep test, with different applied loads. The loads adopted were 60%, 65%, 70%, 80% and 90% of the ultimate tensile strength previously tested, which were calculated to be 51, 55, 59.5, 68 and 76.5 kg, respectively. The specimens loaded at 68 kg (80%) and 76.5 kg (90%) loads ruptured at 30 mins and 50 mins, respectively, and therefore, these results are not presented in the study due to the short load application periods. The remaining specimens were loaded for up to 2 weeks (around 300 hours), as a consequence of other demands on the laboratory. After the 2-week loading phase, contraction in the longitudinal direction was also measured by the LVDTs, due to the high elasticity of the geocell material (HDPE). Although unloading is less likely to occur once a geocell is buried beneath the ground, the extent of contraction provides an insight into the post-loading behavior of geocells when cyclic loading is considered.

For each specimen, after approximately the 2-week loading period, the applied load was released from the specimen in a single operation. The LVDTs continued recording the displacements of three geocell specimens during and after unloading, to assess the shrinkage ratio. The shrinkage ratio is defined as the reduction in geocell height (mm) divided by the maximum elongation (mm) of each specimen (perpendicular to the height), at the cessation of the creep load application. Data acquisition was terminated once zero displacement was recorded by the LVDTs.

#### *4.3.2.4 Junction: Tensile, shear, seam and split strength tests*

Four types of test were conducted at the geocell junctions: direct tensile, shear, seam and split strength tests. The experimental configurations were designed in reference to ASTM

(1993), with modifications to the specimen dimensions and setup. Since there is no standardized method available for these tests on geocell products, several specimens had to be prepared for each test for trial purposes. This enabled calibration of the dimensions of the specimens and the clamping system, to ensure that the forces were applied directly to the junction, while providing sufficient interlock between the clamp and the geocell strips to prevent slippage and premature failure. At end of the trials, 40 mm was found to be the most secure length for gripping the specimens. The distances between the clamp tips were determined to be 10.5 mm for the tensile and shear strength tests, and 30 mm for the seam and split strength tests. These distances ensure that no pre-load was applied to the specimen prior to the commencement of actual testing. The specimens used in all tests were initially cut to the correct dimensions for the tensile and split strength tests. Then, the specimens for the shear strength and seam strength tests were trimmed to their final dimensions, as shown in Table 4.1. The schematic drawings in Figure 4.10 show the loading scenario and the detailed configuration, including the clamping distance and clamp spacing. The corresponding laboratory setups are shown in Figure 4.11 and *Figure 4.12*. These loading schemes mimic the three failure forms (shear, peel and split) of the junctions, and examine their uniaxial tensile strength. The junction thicknesses of all specimens are summarized in Table 4.1.

Table 4.1 Specimen dimensions.

Test	Junction thickness (mm)	Junction length (mm)	Overall length (mm)	Clamping distance (mm)
Tensile & Shear strength	3.5	10.5	120.5	10.5
Seam & Split strength	3.5	10.5	110	30

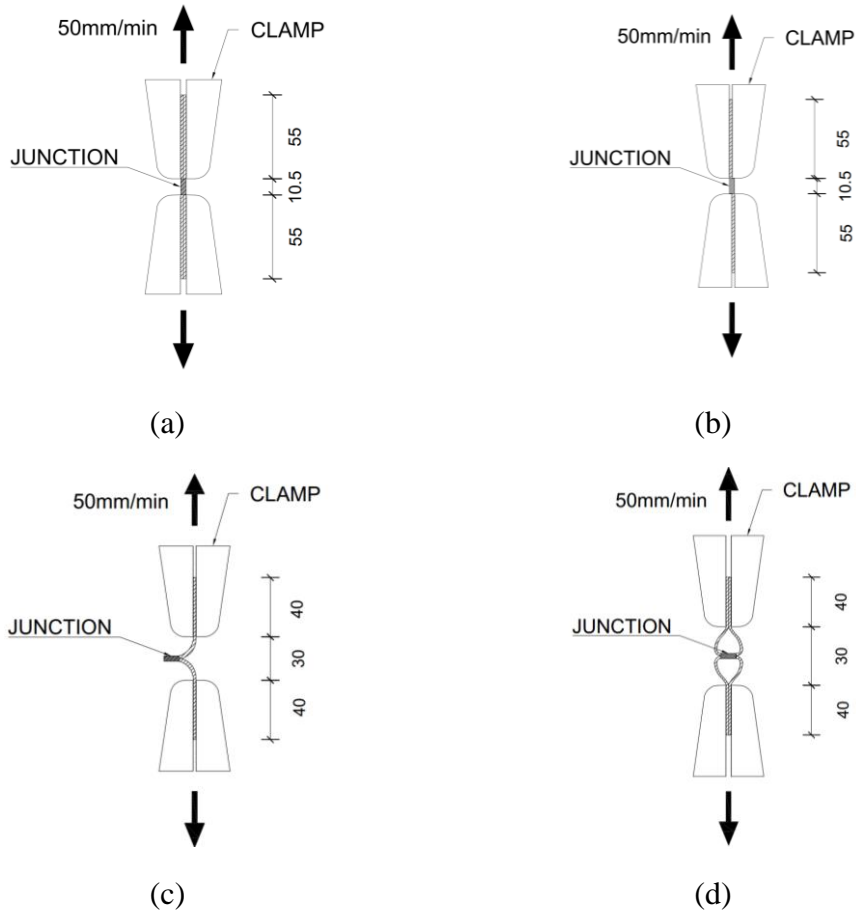
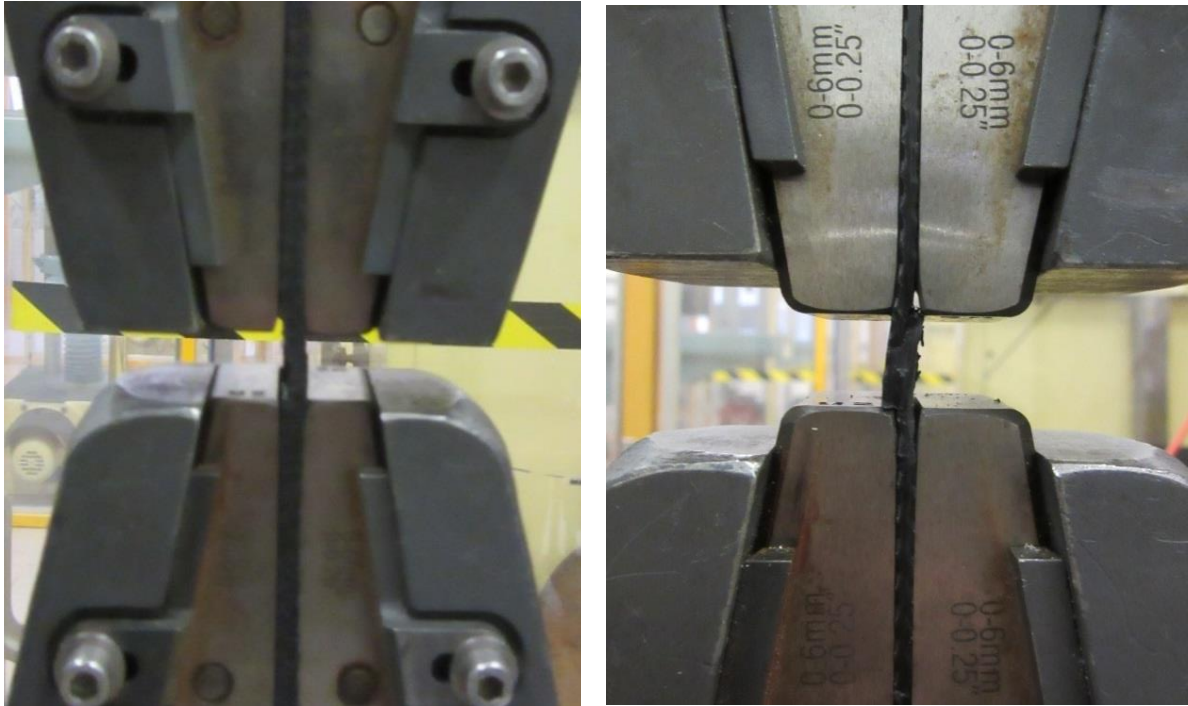


Figure 4.10. Junction strength tests: (a) uniaxial tensile strength, (b) shear strength, (c) peel strength and (d) split strength.



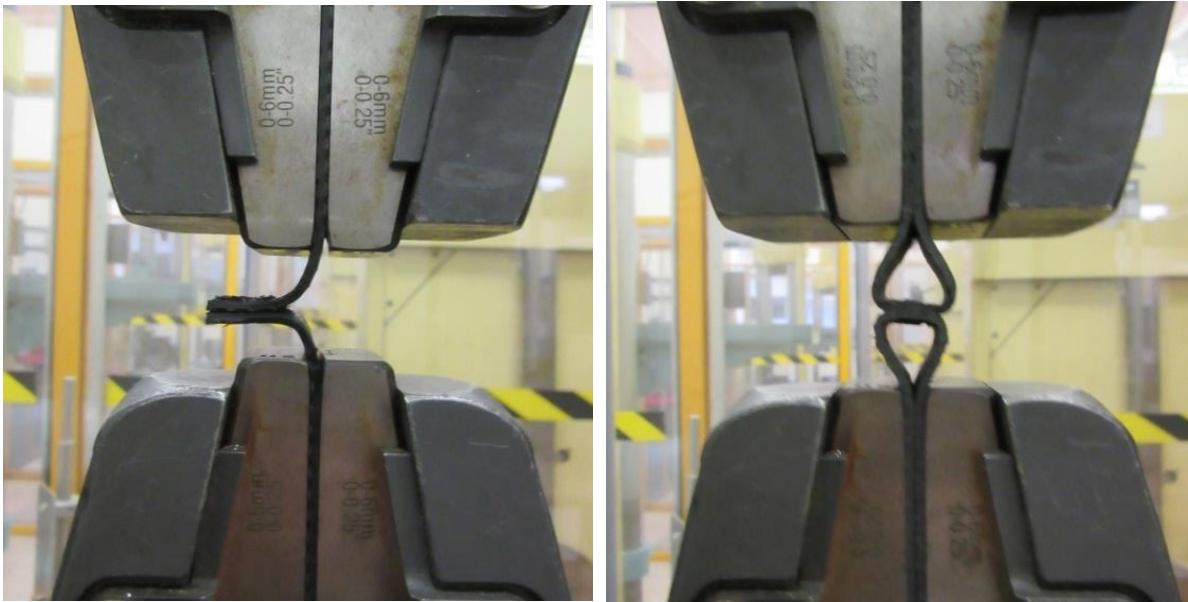
Figure 4.11. Specimens for testing of geocell junctions (from left to right): tensile strength test, split strength test, shear strength test, and seam strength test.





(a)

(b)



(c)

(d)

Figure 4.12. Clamped specimens: (a) tensile strength, (b) shear junction strength, (c) seam strength, and (d) split strength.



Table 4.2 Specimen designation.

Specimen type	Test	Designation
Geocell wall	Uniaxial tensile strength	CW-UTS
	Trapezoidal tearing strength	CW-TTS
	Creep	CW-CT
Geocell junction	Uniaxial tensile strength	J-UTS
	Shear strength	J-SS
	Seam strength	J-SMS
	Split strength	J-SPS

Each measurement was obtained at three locations along the specimen: top, bottom and middle, and average values were measured. Five replicates were initially prepared for each test. In case the results indicated clear discrepancies, additional specimens were tested, to facilitate a high level of consistency. The specimen designations for the junction and cell-wall tests are summarized in Table 4.2.

#### 4.4 Results and Discussion

This section summarizes the results of the testing program conducted on geocell walls and junctions. The results are presented in terms of engineering stress/axial force versus elongation, rather than stress-strain due to complexity resulting from different loading forms. Specifically, the stress-elongation relationship cannot be obtained for the cell-wall trapezoidal tearing strength test and the stress-strain relationship cannot be obtained for the junction split test. Implications of the results are discussed in relation to the practical implementations of geocells in geotechnical applications.

#### 4.4.1 Cell-wall: Uniaxial tensile strength

The plot of axial stress versus elongation of the cell-walls subjected to uniaxial tension is shown in Figure 4.13. The axial stress is calculated as the tensile load divided by the initial cross-sectional area of the specimen ( $19.5 \text{ mm}^2$ ). As can be seen in Figure 4.13, the initial ascending portion of all curves exhibited similar tendencies before reaching their corresponding peak tensile stresses at approximately 10 mm elongation. The tensile strengths of all specimens were very consistent; ranging from a minimum of 13.34 MPa to a maximum of 14.2 MPa. However, there were significant differences in the post-peak behavior among the five specimens tested, as a result of different failure modes. It can be seen that specimens 1, 2 and 4 did not exhibit the typical behavior of HDPE (Figure 4.4). These specimens failed relatively suddenly, when compared to specimens 3 and 5.

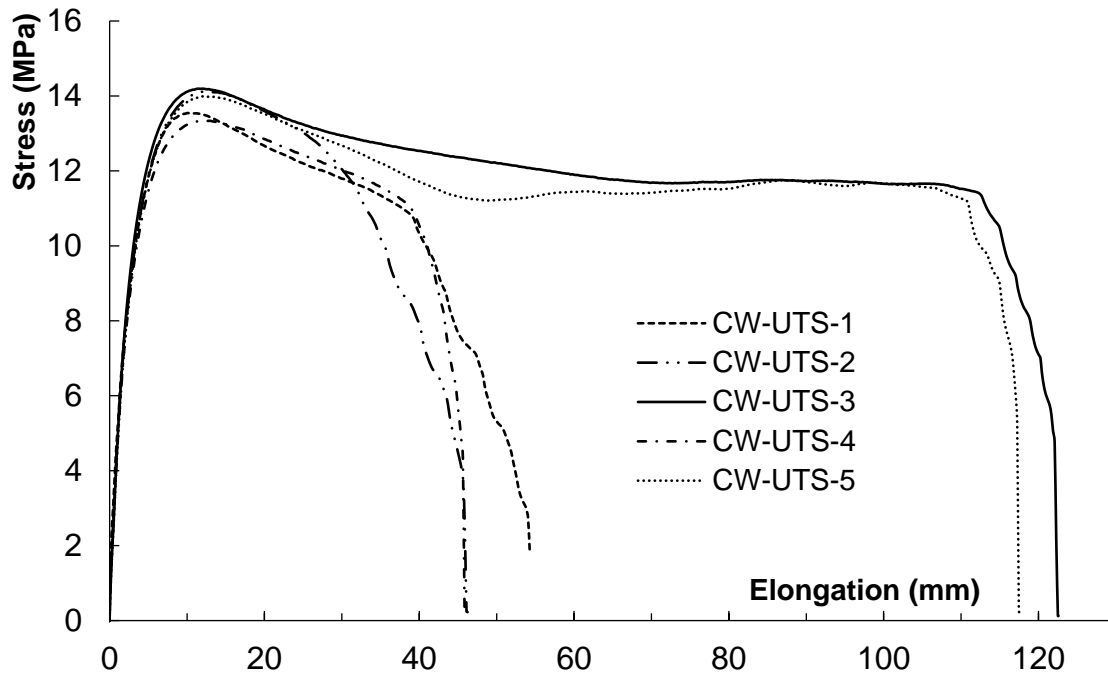


Figure 4.13. Stress–elongation relationship of geocell cell-wall subjected to uniaxial tensile force.

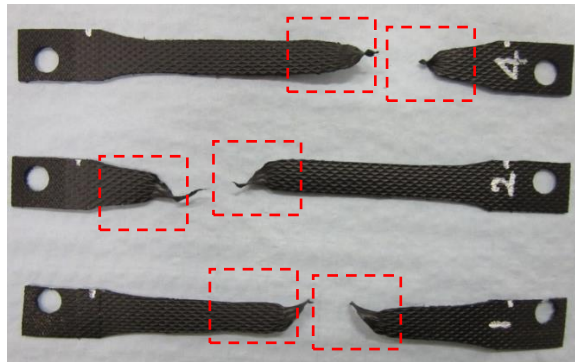
Photographs taken during the tests were able to capture the different elongation modes, as shown in Figure 4.14. Although the loading rates of the specimens were identical (50 mm/min), specimens 1, 2 and 4 fractured at elongations approximately half of those exhibited by specimens 3 and 5. It can also be seen that the two subsets of specimens experienced different failure mechanisms. The failure of the specimen 3 in Figure 4.14(a) initiated from the right-hand-side edge, then propagated towards the center (as indicated by the red arrows) and the rupture point was at the left-hand-side edge. Whereas, specimen 5, in Figure 4.14(b), elongated vertically and exhibited significant elongation. In addition, the photographs of the failed specimens are shown in Figure 4.14(c) and (d). The post-failure forms of the 5 specimens exhibit good agreement with the corresponding stress-elongation relationship. For specimens 1, 2 and 4, the rupture surfaces (highlighted by red-dashed lines) are much sharper with little elongation, whereas specimens 3 and 5 failed more gradually.



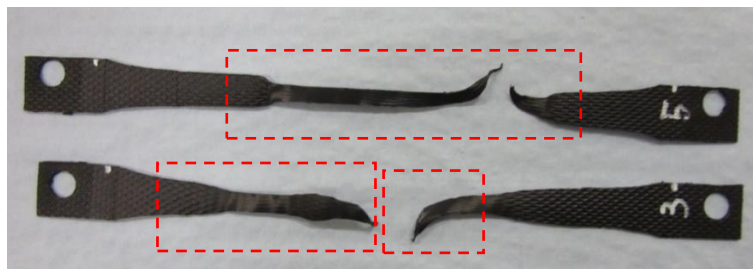
(a)



(b)



(c)



(d)

Figure 4.14. Failure modes of cell-wall specimens subjected to uniaxial tension: (a) and (c) sudden failure, (b) and (d) ductile failure mode of HDPE.

It is worth mentioning that all specimens were treated with great care such that no damage was induced during the preparation stage. All specimens were extracted from the same location from different cell-walls, and cut to the same sizes with the aid of a digital caliper (i.e. the thickness and width of each specimen were measured at three locations along the narrow section, and the variation in size was maintained within a tight tolerance of  $\pm 1\%$ ). Therefore, the different failure patterns can be attributed to the material itself, and most likely to the indented surface. Inconsistent distribution of ingredients throughout the material can result in variations in brittleness (e.g. less elongation indicates higher brittleness). As specified by the manufacturers, the tolerance of the depth of indentation is  $\pm 0.15$  mm, which is  $\pm 9.8\%$  of the designated thickness (1.52 mm). According to Meuller (2007), the surface structure of HDPE composite influence its post-yielding behavior; more rapid failure can occur at locations of stress concentration due to surface structural features, such as notches. For geocells, the deeper indentations acted as the equivalent of notches, which facilitated a brittle failure mode. This phenomenon is in agreement with previous studies (Choi et al., 2009; Meuller, 2007; Pan et al., 2017).

#### **4.4.2 Cell-wall: Trapezoidal tearing strength**

According to ASTM (1996), the trapezoidal tearing strength is defined as the axial force versus the elongation of the cell-wall under tearing force. The test results are provided in Figure 4.15. In the pre-peak region, all specimens exhibited linear behavior. The recorded peak tearing strengths ranged from 5.02 MPa to 6.22 MPa. The post-peak behavior for all specimens exhibited similar and step-like functions. Post-peak, the axial force decreased due to fracturing of the geocell section between two perforations. Subsequently, the applied

tensile force was sustained by the adjacent geocell sections where the hardening was observed on the plot. This process repeated until the specimen fully ruptured. While no significant difference was observed in the tearing strength of the five specimens, there was a noticeable difference in the elongations, ranging from 157.2 mm to 222.9 mm. These differences can be partially attributed to the inconsistencies in the specimen, such as the spacing between perforations and the edge-to-perforation distances, as shown in Figure 4.16(a) and (b), respectively. It should be noted that cell-wall specimens A and B were randomly selected from a geocell panel, which were prepared to identical dimensions. In the photographs, the perforations shown are from the same cell-wall locations in specimens A and B and the distances/spacing were measured using a digital caliper and it is evident that slight, but nevertheless meaningful, variations exist between the two specimens. As the specimens fail in a progressive manner, the perforation spacing, and edge-to-perforation distance have important effect on the elongation (e.g. larger spacing resulted in higher elongations).

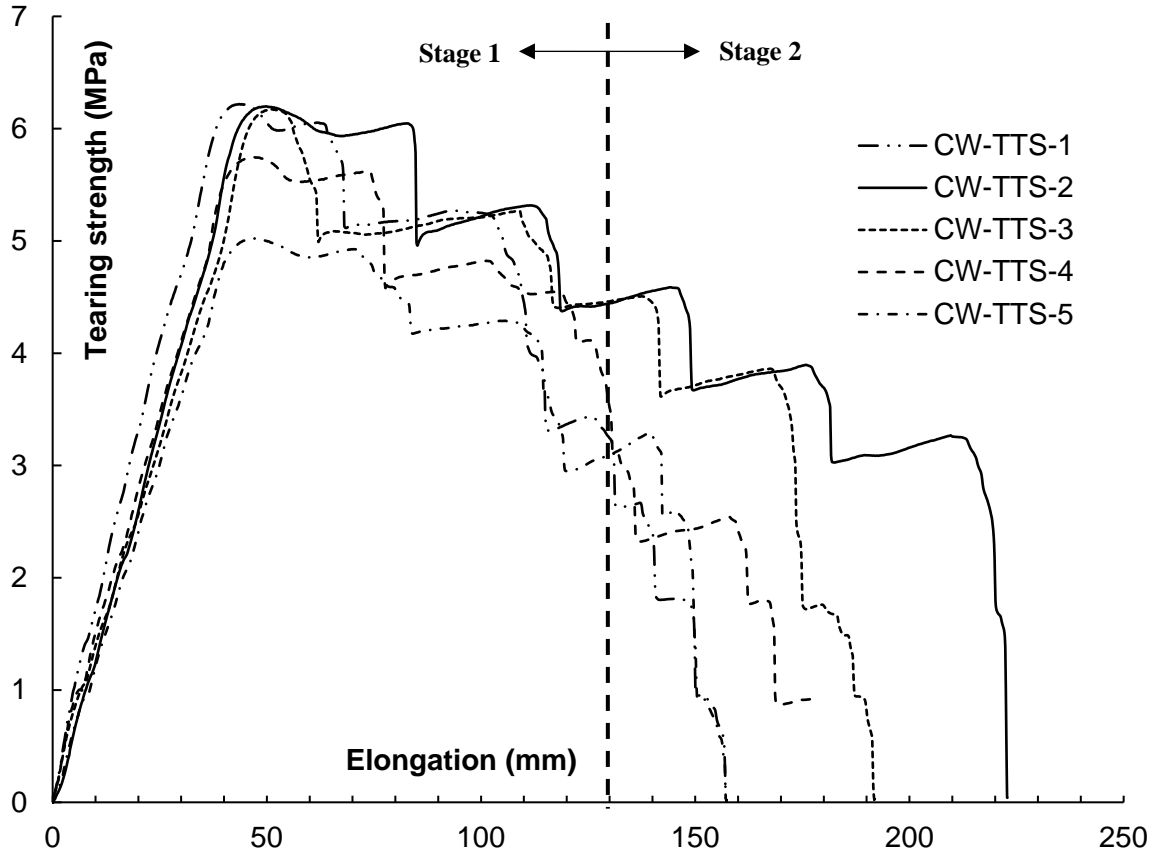


Figure 4.15. Force-elongation relationship of geocell cell-wall subject to tearing.

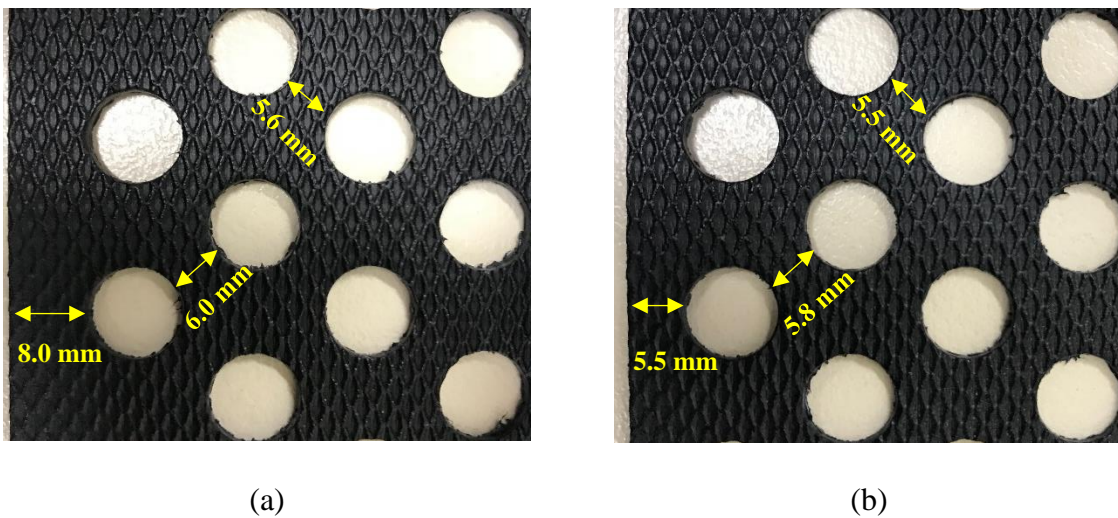


Figure 4.16. Inconsistencies in perforations between two cell-wall specimens: (a) specimen A, (b) specimen B.

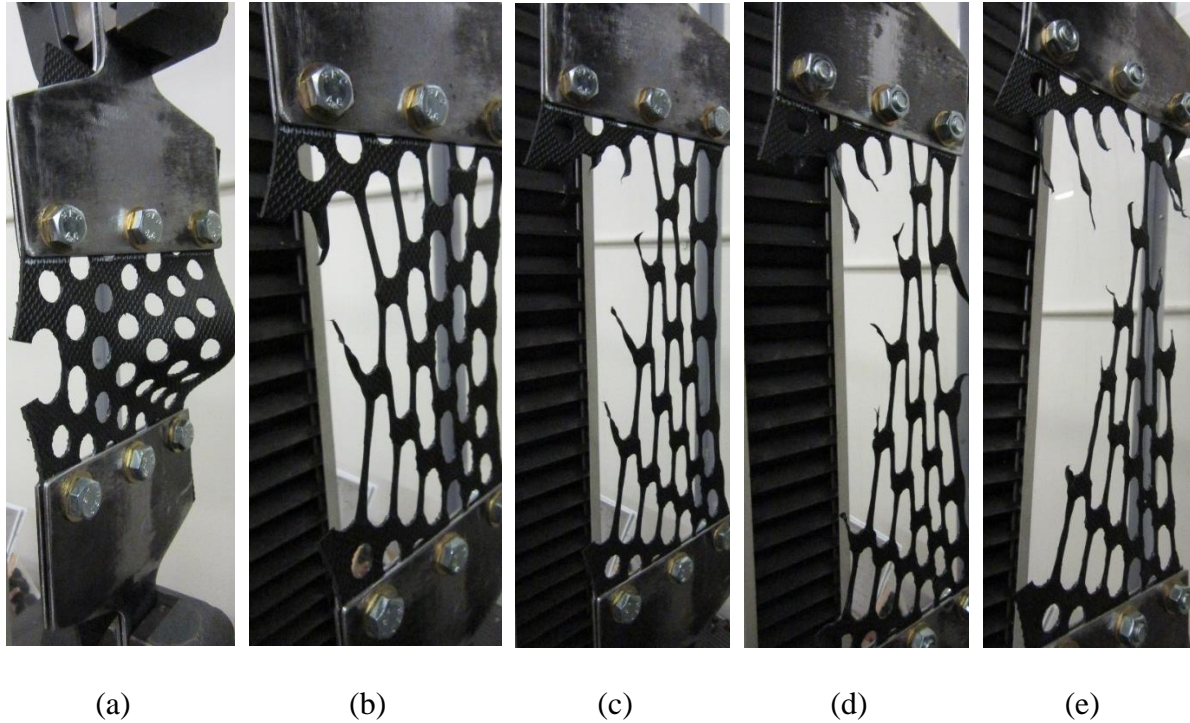


Figure 4.17. The progressive failure of cell-wall specimen CW-TTS-3 at different elongations: (a) 0 mm, (b) 70 mm, (c) 115 mm, (d) 160 mm, and (e) 180 mm.

The cell-wall specimens failed in a progressive manner, where the material between two adjacent perforations ruptured sequentially, as shown in Figure 4.17. This failure pattern explains the stepped post-peak region of the force-elongation curves. Figure 4.18 shows the five specimens after complete rupture, having been subjected to a tearing force, which facilitates the study of the failure mechanism. It can be seen that the failure patterns are identical for the five specimens. The solid arrow marks stage 1 of the failure, corresponding to stages of Figure 4.17(a) to (c) and the dashed arrow marks stage 2, corresponding to Figure 4.17(d) and (e). Both stages exhibited an inclined tearing pattern. Stage 1 initiated from the left-hand side (i.e. the cut) of the specimen, then the fracture path progressed in the upper-right direction. Once the elongation exceeded 120 mm, all



specimens started fracturing from the right-hand side, initiating stage 2 fracturing. Overall, all specimens elongated more in stage 1 than in stage 2 of the failure process, resulting in the complete rupture at the upper-right-hand side. This can be attributed to the fact that the specimen had been elongated to an extent at which the tearing force had transitioned solely to tension.

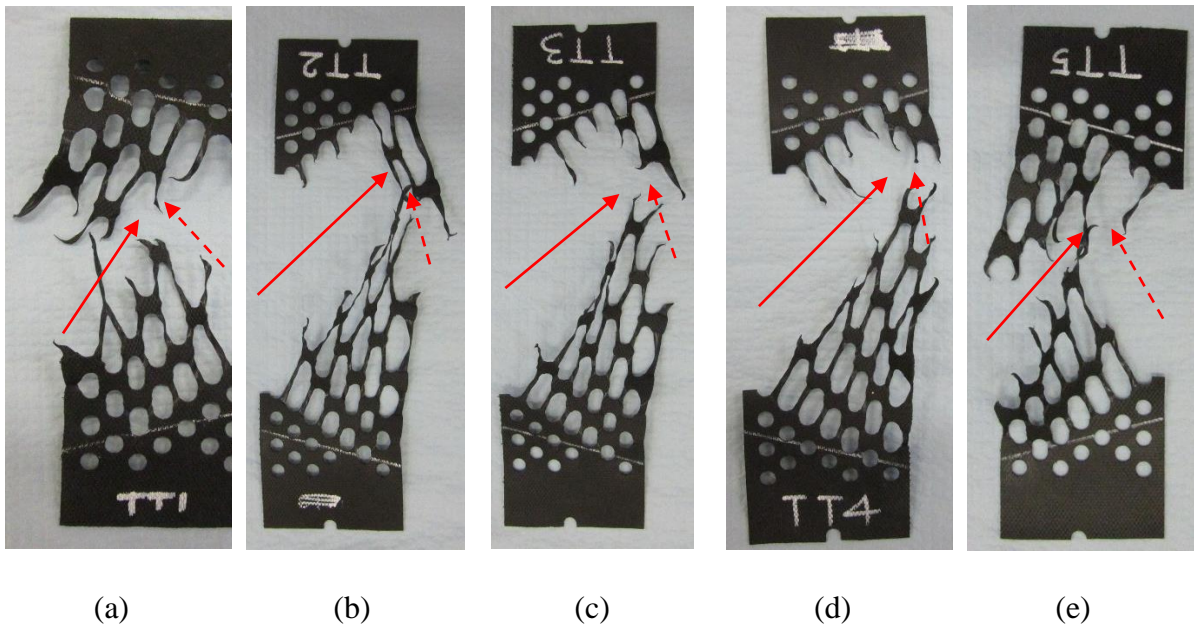
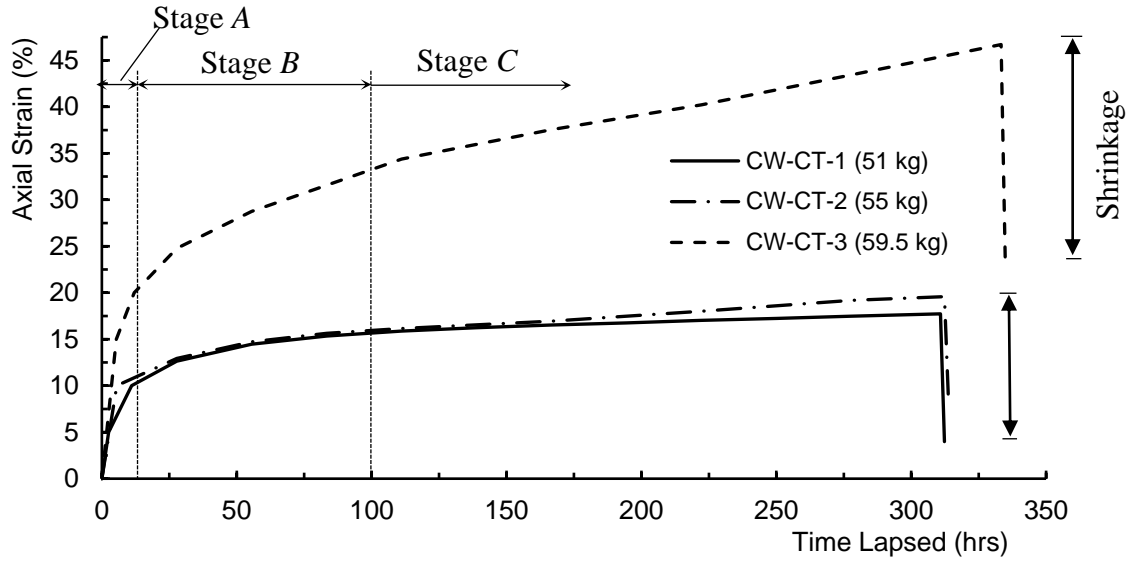


Figure 4.18. Failure modes of cell-wall specimens subjected to a tearing force (left to right: specimens 1–5).

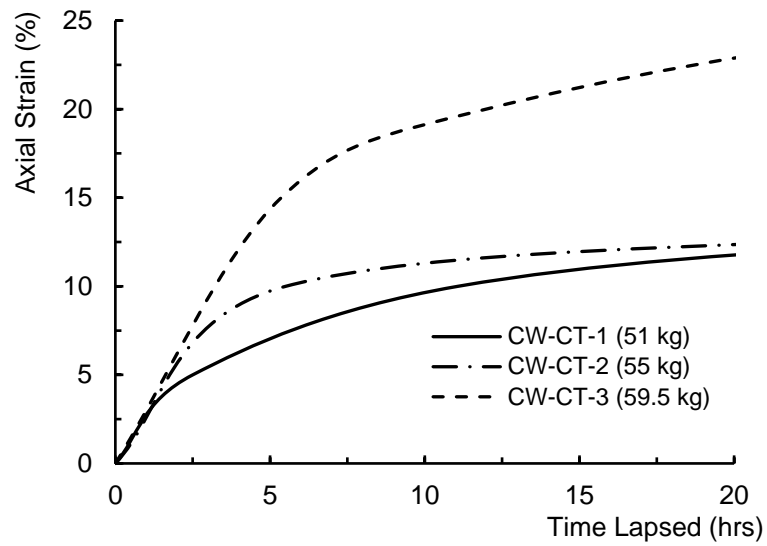
#### 4.4.3 Cell-wall: Creep test

The elongations and strains of three tested specimens are plotted against the elapsed time in Figure 4.19. The creep behavior of the three geocell specimens under different loads exhibits similar tendencies. This behavior can be divided into three stages: A, B and C, in sequence. Stage A is defined here as primary creep, where the geocell specimens experienced a higher rate of elongation while a linear, axial strain versus time relationship

was observed. For specimen 1 (51 kg loading) and specimen 2 (55 kg loading), the axial strain reached 7.5% and 6%, respectively, at the end of stage A, over a period of approximately 3 hours. Specimen 3 (59.5 kg loading) experienced a considerably higher axial strain (12.5%) during the initial 3 hours. Stage B is defined as secondary creep, where the rate of elongation decreased gradually for all three specimens; hence, the strain-time relationships formed smooth curves. The durations of stage B, for specimens 1 and 2, were similar. Both specimens entered their final stages after approximately 55 hours, while their axial strains reached 15%. Specimen 3 experienced significantly higher elongation during stage B, reaching approximately 28% axial strain. Stage C is defined as the period when all specimens returned to an approximately linear trend with minimal fluctuations. It can be seen that specimen 3 exhibited a higher elongation rate than specimens 1 and 2. The axial strains of all three specimens peaked at 17.7% (24.8 mm), 19.5% (27.4 mm) and 63.2% (65.2 mm), respectively, at approximately 300 hours prior to unloading. With all things considered, in comparison to specimen 1, the additional 4 kg applied to specimen 2, was unable to cause a significant increase in elongation, which was merely 2.5 mm longer. However, specimen 3 exhibited a dramatically higher elongation when compared to both specimens 1 and 2, which were 40.3 mm and 37.9 mm longer, respectively.



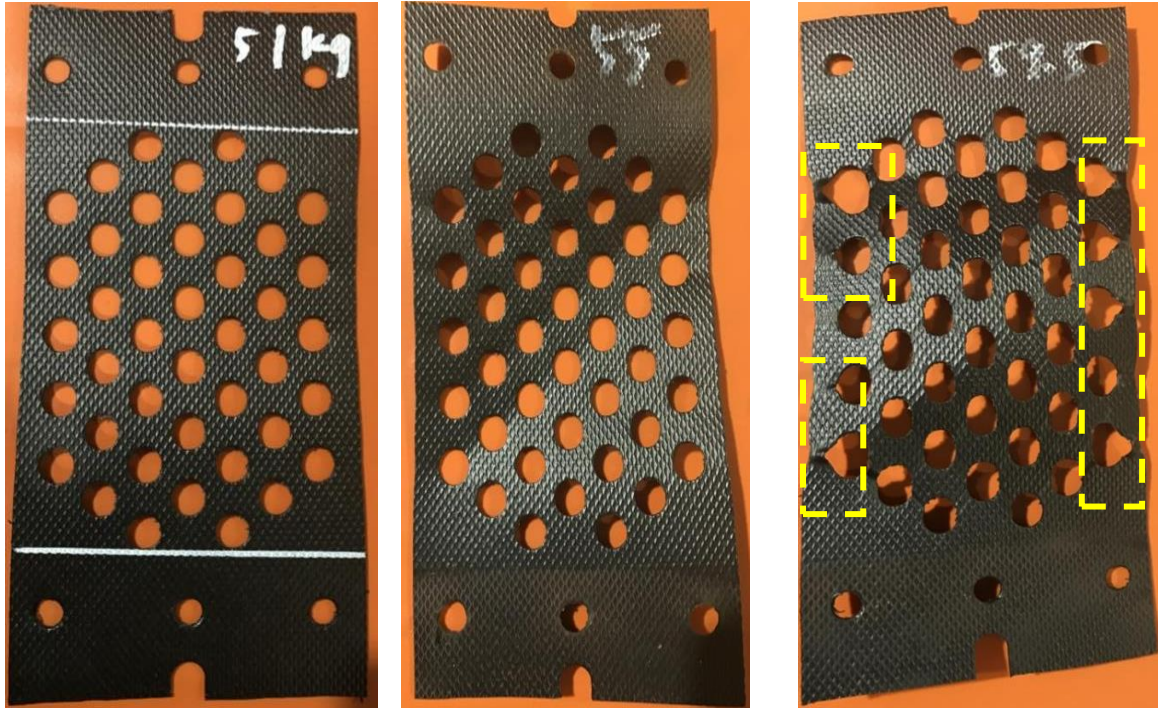
(a)



(b)

Figure 4.19. Strain-time relationship of three tested specimens.

All specimens became stable within approximately 1.5 hours of unloading and were then removed from the test apparatus. The specimen shrinkage was recorded by the LVDT and this is reflected in Figure 4.19 (a). The final forms of the three specimens are shown in Figure 4.20. Based on visual observations, specimen 1 [Figure 4.20(a)] returned almost entirely to its pre-loading form. A slight elongation can be seen in the perforations, but no deformation was evident from the creep loading. Specimen 2 [Figure 4.20(b)] deformed and deflected slightly along its edge, particularly in the area adjacent to the perforations. However, its structure and geometry remained sound, as no damage was observed. Specimen 3 exhibited minor ruptures adjacent to the edge-perforations, as outlined in yellow in Figure 4.20(c). The specimen was significantly twisted and stretched, and failure was expected to occur if the loading period or weight was increased. Table 4.3 summarizes the shrinkage ratios of the three tested specimens. The shrinkage ratio is inversely proportional to the loading value. Specimen 3 exhibited the lowest shrinkage ratio, 53.0%, while specimens 1 and 2 contracted by 79.3% and 61.5% respectively.



(a)

(b)

(c)

Figure 4.20. Final form of specimens: (a) specimen 1 (51 kg loading), (b) specimen 2 (55 kg loading), (c) specimen 3 (59.5 kg loading).

Table 4.3. Shrinkage ratios of three tested specimens.

	Specimen 1 (51 kg loading)	Specimen 2 (55 kg loading)	Specimen 3 (59.5 kg loading)
Maximum elongation (mm)	24.81	27.35	65.24
Shrinkage (mm)	19.67	16.83	34.6
Shrinkage ratio (%)	79.28	61.54	53.04

#### 4.4.4 Junctions: Tensile strength

The plot of axial stress versus elongation of both the geocell wall and junctions, subjected to uniaxial tension, is shown in Figure 4.21. Firstly, there is a noticeable difference in behavior between the junction specimens and the cell-wall strips, which is reflected by a more rapid increase in the elastic region and a sharper strength reduction in the plastic region. Among the five junction specimens, specimens 2 to 4 exhibited a similar tendency in the post-peak region, with insignificant difference in the rate of strength reduction and elongation at failure, while only specimen 1 experienced much less ductile behavior, resulting in only 23.5 mm elongation prior to failure.

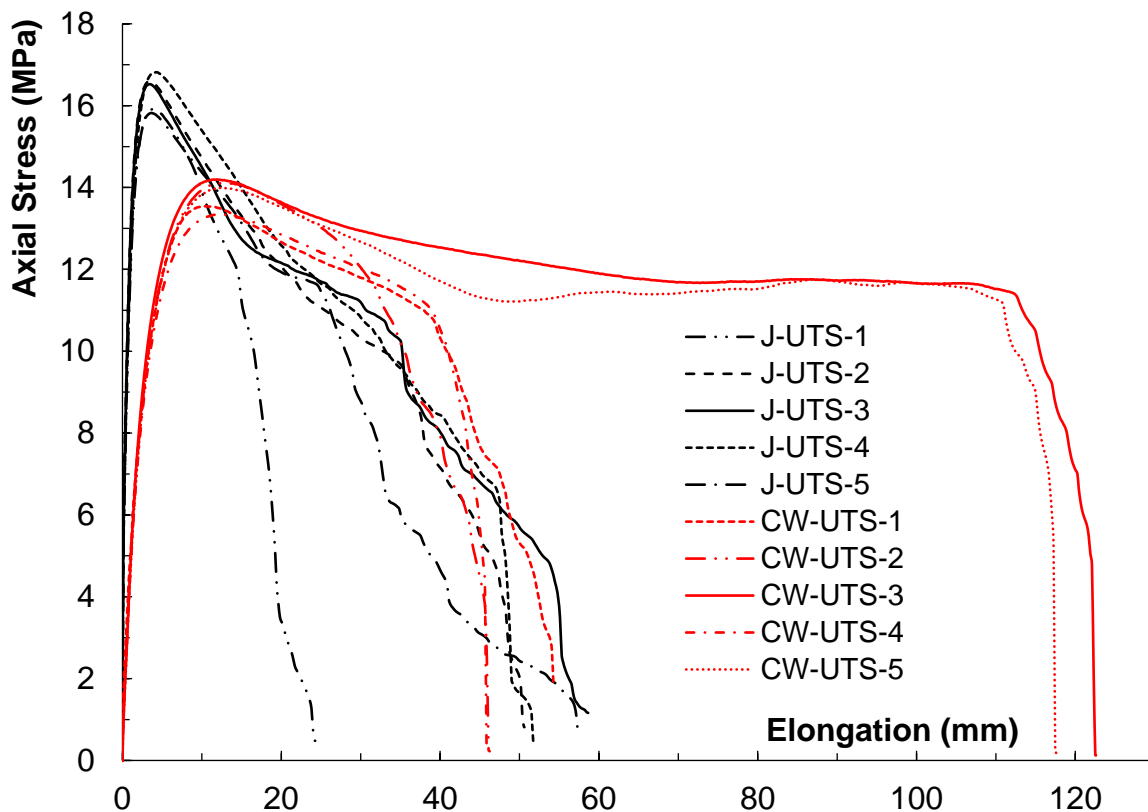


Figure 4.21. Stress-elongation relationship of the geocell junction subjected to a uniaxial tensile force.

Additionally, a higher tensile strength was expected for geocell junctions, considering the fact that the geocell junction is the welded formation of two cell-wall strips. Nevertheless, there was no significant increase in the tensile strength observed at the geocell junctions. The tensile strengths of the junction specimens ranged from 15.9 MPa to 16.5 MPa, while the cell-wall strips varied between 13.34 MPa and 14.2 MPa, which equates to a modest increase of less than 20%. This can be attributed to the welded joint generally having a lower tensile strength when compared to the HDPE material itself (Tariq et al., 2011); hence it cannot provide significant improvement in the tensile strength of a geocell junction.

Two failure modes were identified for geocell junctions under tensile loading, which can be observed in Figure 4.22(b) and (c). All specimens experienced identical behavior in their initial stage of failure, with the elongation initiating from approximately the middle of the welds, as shown in Figure 4.22(a). The initial stage was then followed by two different failure modes. Specimens 2-4 continued elongating in a vertical manner until rupture occurred. Whereas, for specimen 1, fracture was initiated from the left-hand-side after reaching its peak tensile strength and followed by rupture which propagated towards the right-hand edge. Similar failure modes were observed on the cell-wall which was attributed to the stress concentration caused by inconsistent indentation depths (cf §Cell-wall: Uniaxial tensile strength). These observations agree with the discrepancy in Figure 4.21 and provide an explanation for the brittle failure mode of specimen 1.



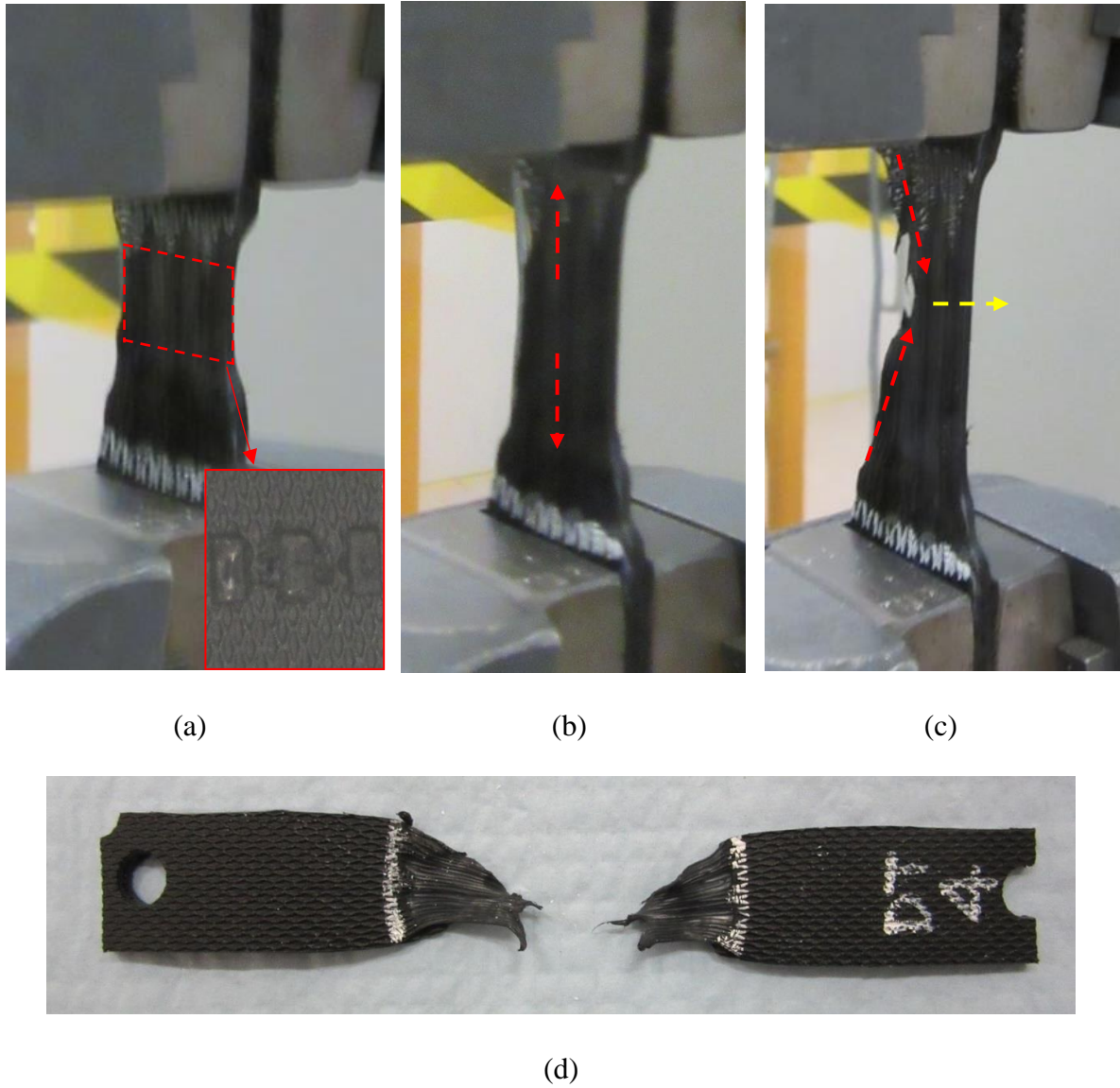


Figure 4.22. Failure modes of the geocell junction subjected to uniaxial tension: (a) initial stage (pre-peak), (b) failure mode 1 (post-peak), (c) failure mode 2 (post-peak), and (d) ruptured specimen 1.



#### 4.4.5 Junction: Shear strength

The plot of shear stress versus elongation of the geocell junctions subjected to a shear force is shown in Figure 4.23 (black lines). It can be seen, of the five specimens tested, most exhibited similar behavior. The shear stress increases almost linearly before peaking, and this is followed by a relatively sudden failure, reflected by less elongation when compared with the other tests conducted on the junction. There are only small differences between the measured peak shear strengths; ranging from 2.58 MPa to 2.98 MPa. However, some discrepancy is found in the post-peak region, reflected by different rates of strength reduction. The elongations at rupture ranged from 18.3 mm to 31.4 mm.

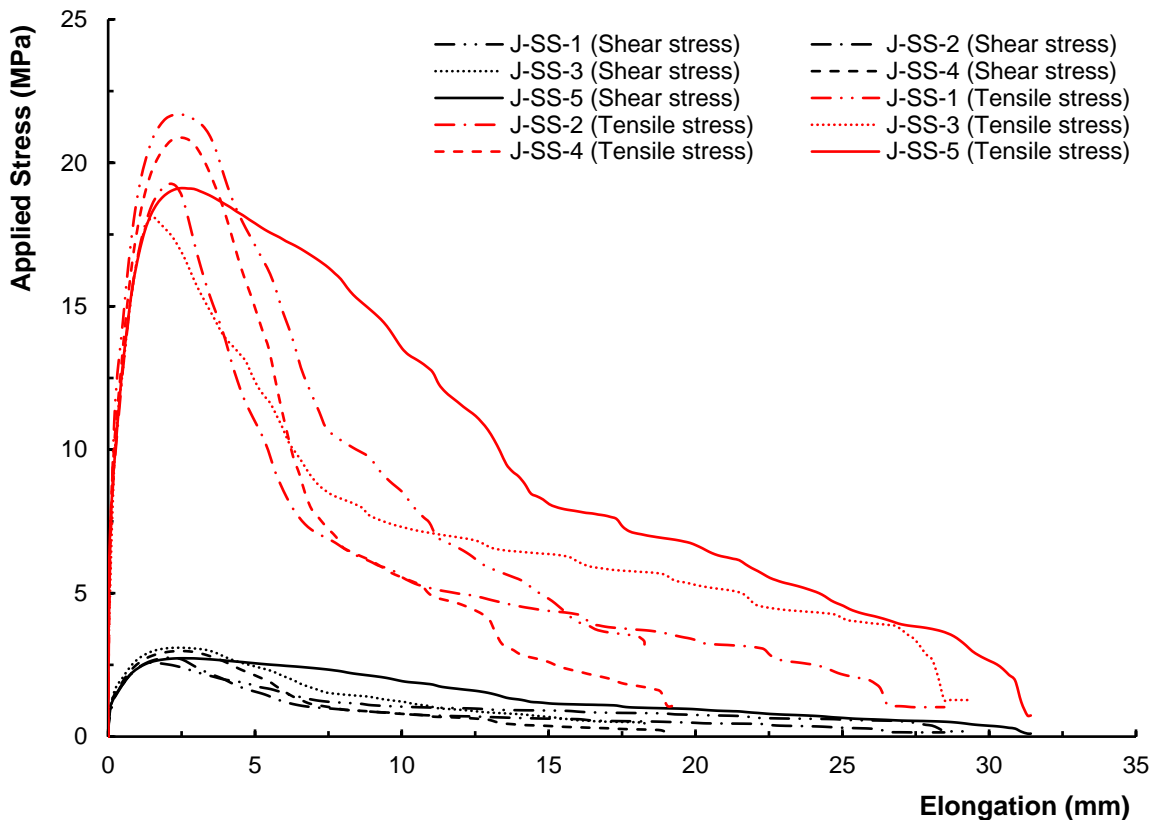


Figure 4.23. Force-elongation relationship of geocell junction subjected to shear force.

All specimens experienced similar failure modes, where rupture occurred adjacent to the junction, as shown in Figure 4.24. This indicates that the junction is unlikely to fail during shearing and the shear strength of the junction is significantly higher than the peak shear stresses obtained from the present experimental program, yet it is more vulnerable to tensile stress. This observation is confirmed by the elongation mode in Figure 4.24(b), where the specimen deformed only in the cell-wall strip, while the junction remained intact. Therefore, it is worthwhile to investigate the tensile strength of the cell-wall strips induced by the shearing action, and the tensile stress versus elongation relationships are plotted in red in Figure 4.23. Interestingly, under the action of shear, the tensile strength of the cell-wall was considerably higher than the tensile strength of a simple cell-wall specimen (cf §Cell-wall: Uniaxial tensile strength). The former had a tensile strength ranging from 18.1 MPa to 21.7 MPa, while the latter had a tensile strength ranging from 13.3 MPa to 14.2 MPa, equating to an average increase of 42%. The welded junction provides additional resistance to the cell-wall against tension, which assists the cell-wall area near the junction to support, for example, gravity loads caused by soil movement [Figure 1.4(a)].

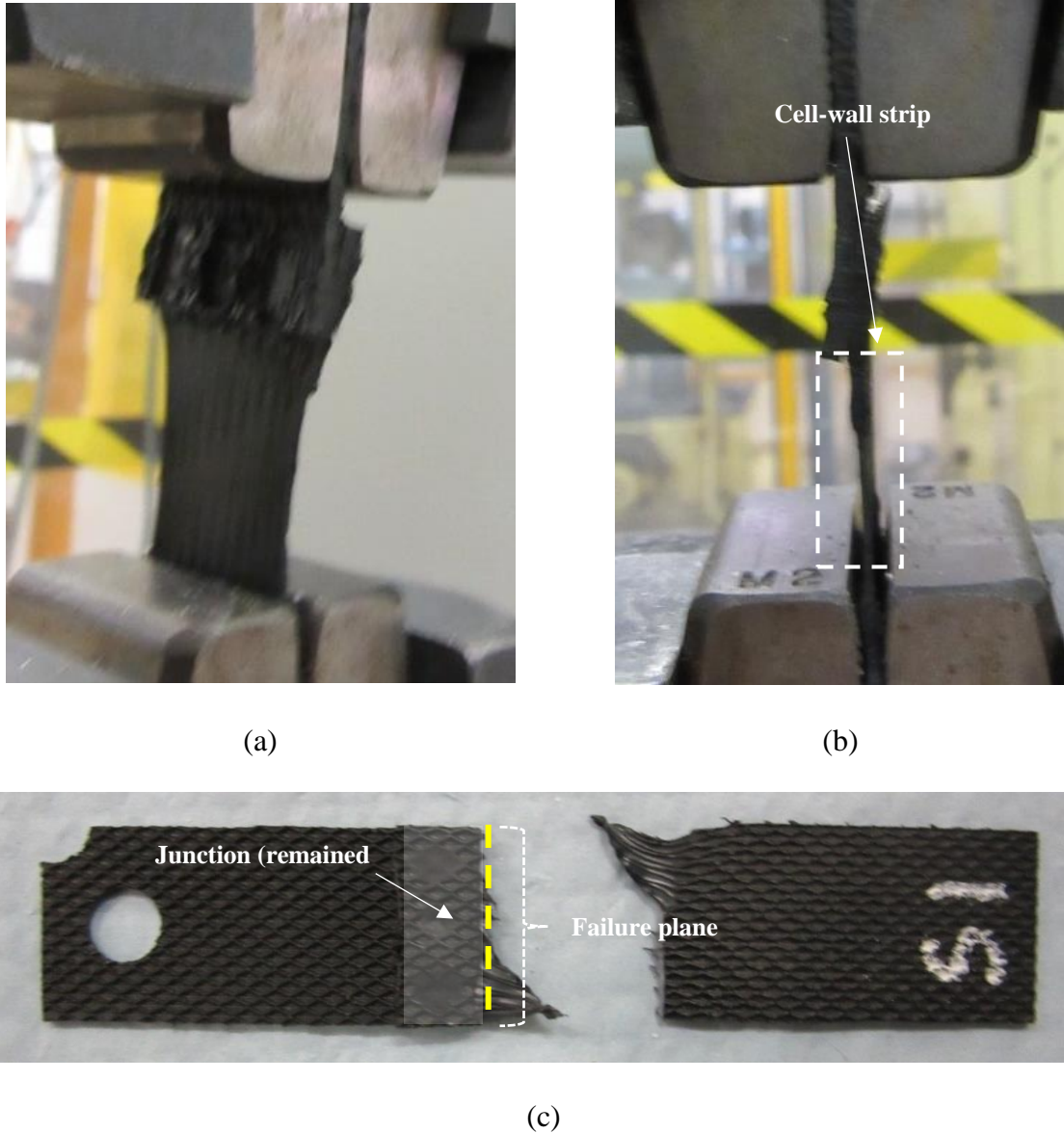


Figure 4.24. Failure modes of geocell junctions subjected to shear force: (a) oblique view and (b) side view during testing, and (c) failed specimen.

#### 4.4.6 Junction: Seam Strength

The plot of stress versus displacement of the geocell junctions when subjected to a peeling force is shown in Figure 4.25. All five tested specimens exhibit a similar trend, with a reduced rate of increase in the elastic region, followed by a dramatic strength reduction.

The maximum recorded seam strength is 8.21 MPa while the minimum seam strength 7.5 MPa across five specimens, resulting in a less 10% variation. Under the action of peeling, two failure modes were observed, as are shown in Figure 4.26. Only one (specimen 1) of the five tested specimens experienced weld fracture [Figure 4.26(c)], while the other specimens failed in the cell-wall adjacent to the weld junction. This specimen 1 (J-SMS-1) also experienced the most fluctuations throughout the loading process, as can be seen in Figure 4.25. Due to the low possibility of occurrence of this failure mode, it is considered that this is likely the result of faulty/unsatisfactory welding during manufacturing.

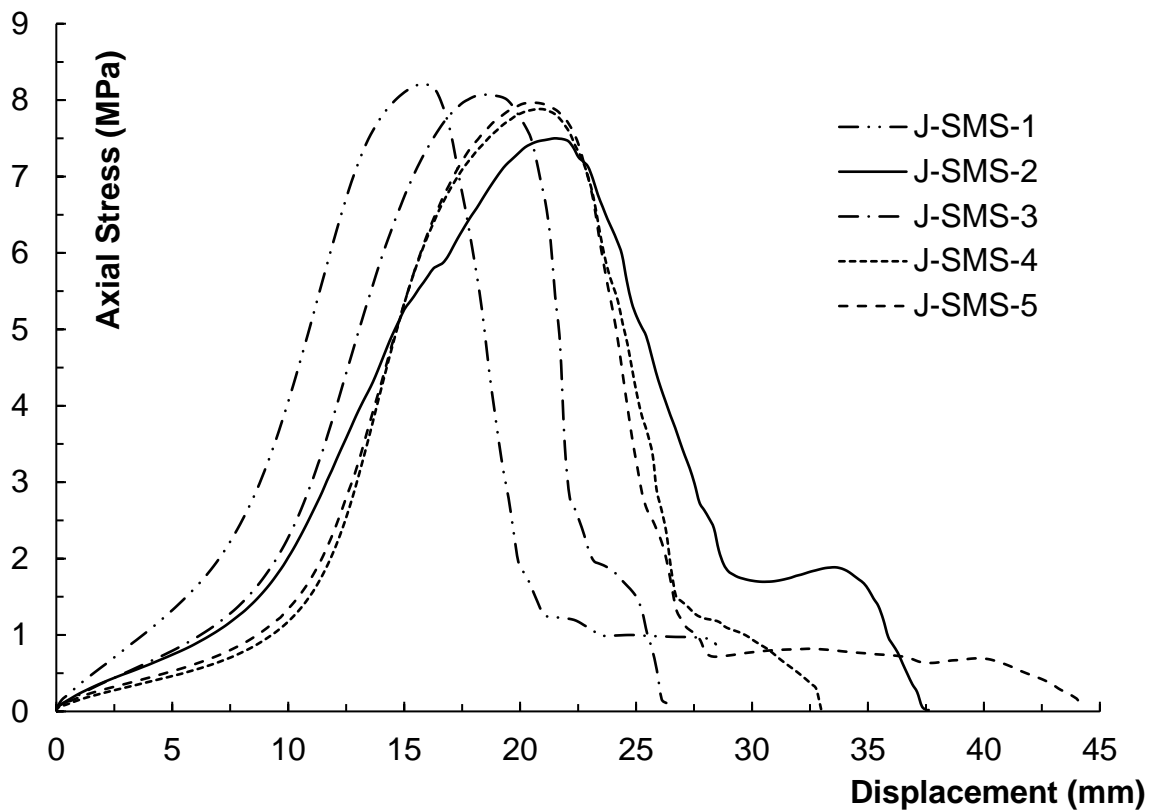
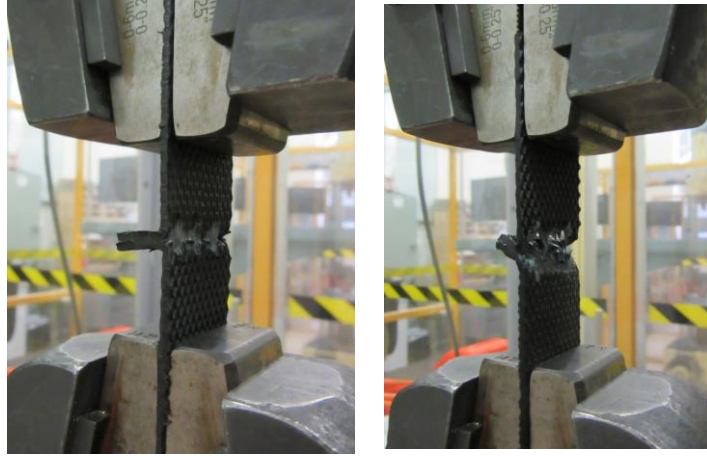
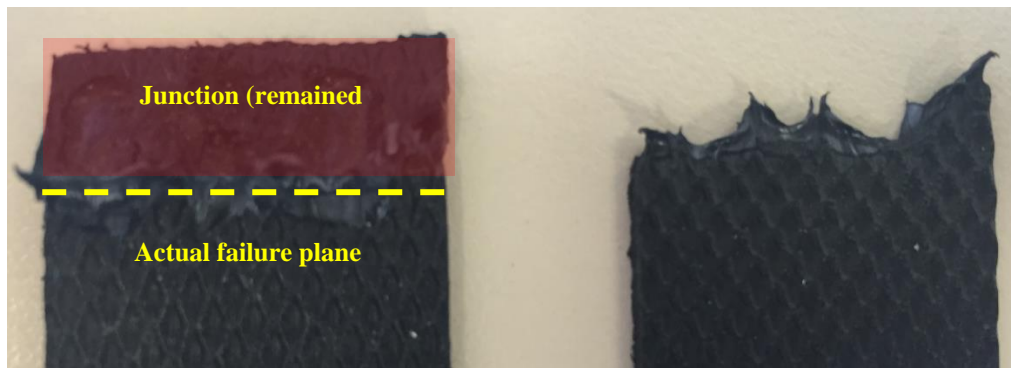


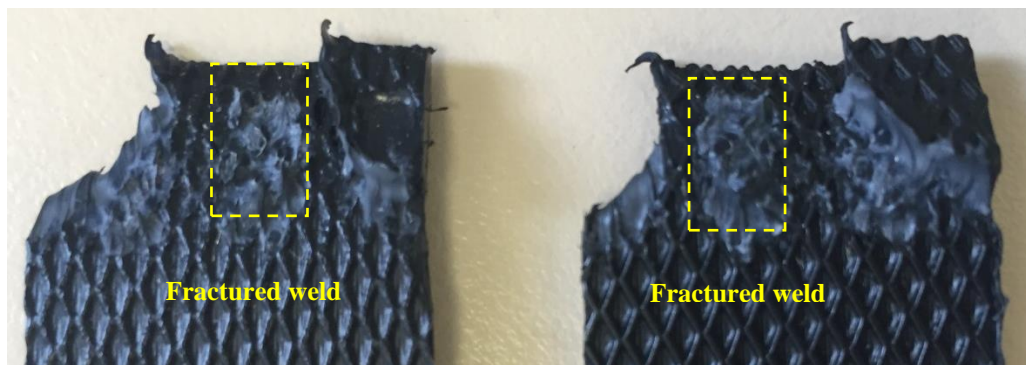
Figure 4.25. Stress-elongation relationship of tested geocell junctions when subjected to a peeling force.



(a)



(b)



(c)

Figure 4.26. Failure modes of geocell junctions subjected to peeling force:

(a) during testing, (b) strip failure, (c) weld failure.

#### 4.4.7 Junction: Split strength

The split strength test is of particular interest to this study. Unlike other loads, which occur less frequently when the geocell is placed in the field, such as in the case of pavement or slopes, the junctions are constantly subjected to a splitting force. The axial stress versus elongation results are shown in Figure 4.27. The tensile stress is calculated as the tensile force divided by the initial longitudinal cross-sectional area (262.5 mm<sup>2</sup>) of the geocell junctions. All of the results exhibit a similar nature, with variations in peak stresses and post-peak behavior. Interestingly, although the loading mechanism of the splitting force is similar to that of the peeling force, the geocell behaved differently, with significant differences in peak strengths. The minimum splitting strength (3.69 MPa) varied slightly from the maximum value (4.03 MPa). Almost all specimens experienced a rapid stress reduction post-peak, while specimen 4 increased in stress for a short period, followed by a rapid failure.

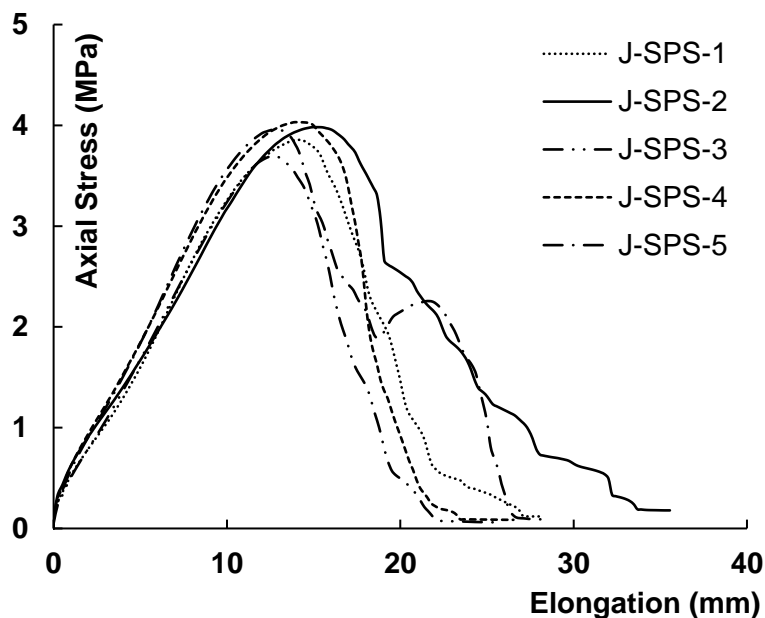
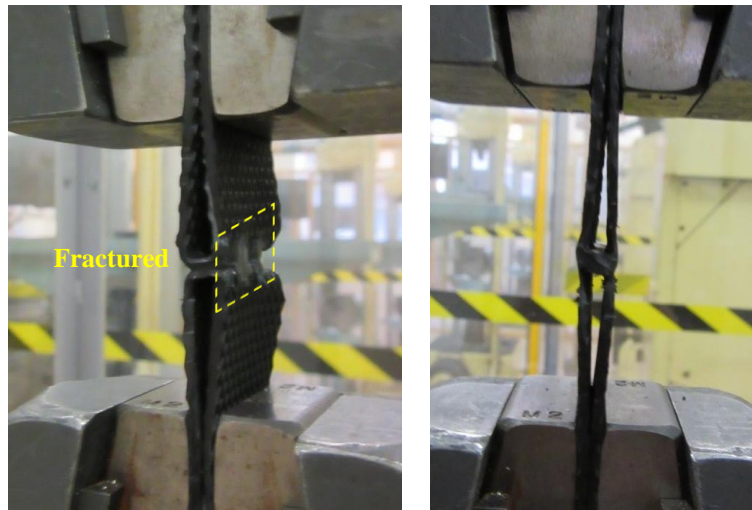
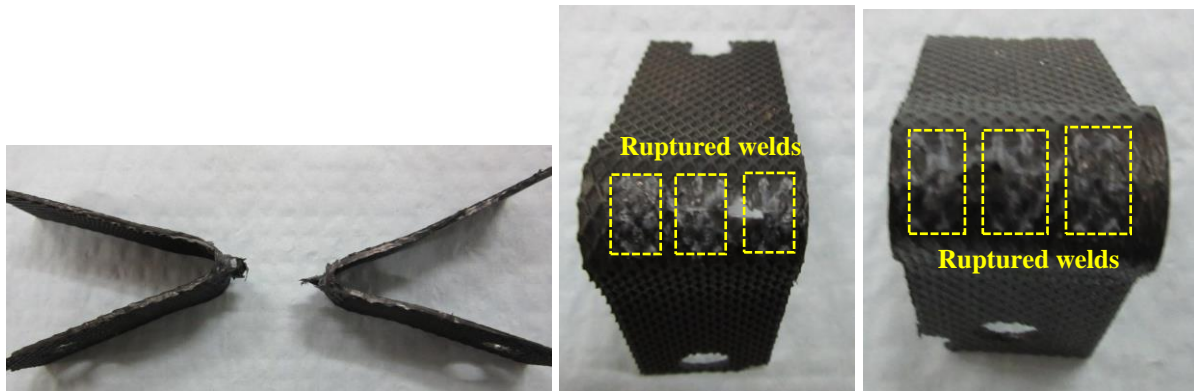


Figure 4.27. Stress-elongation relationship of geocell junctions subjected to splitting.

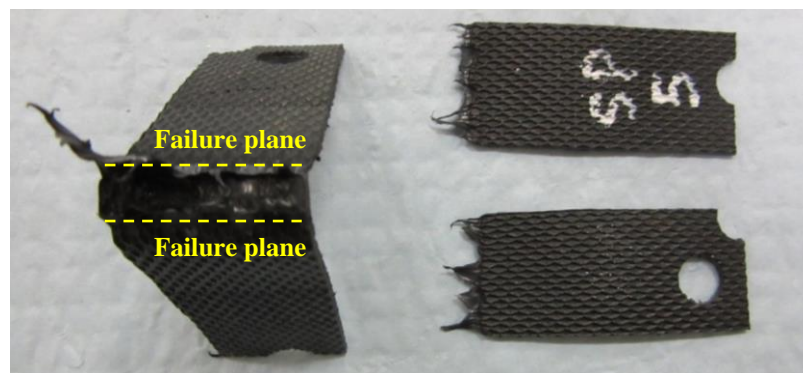
Two types of failure mechanisms were observed, as shown in Figure 4.28. The failure mode shown in Figure 4.28(b) can be described as occurring when the two welded, cell-wall strips completely separated from each other due to rupture of the weld. The failure mode shown in Figure 4.28(c) is defined as cell-wall failure, as the junction did not fail under the influence of the splitting force. The latter mode is similar to the failure condition under shearing and peeling. It should be noted that geocell junctions exhibit a higher splitting strength when the junctions experience the failure mode of complete separation. This mode was exhibited by specimens 1 and 5, which recorded the highest splitting strengths of 3.98 MPa and 4.03 MPa, respectively.



(a)



(b)



(c)

Figure 4.28. Failure modes of geocell junctions subjected to a splitting force: (a) during testing; (b) junction failure; (c) cell-wall strip failure.



As the stress-displacement relationship was obtained from the seam strength tests, the geocell junctions reached their peak strength under the splitting load, significantly slower than in other loading scenarios. This phenomenon suggests that, when geocells are used in the field (such as in slope protection), it is possible that the soil structure will experience a gradual down-slope movement prior to failure if the gravitational load exceeds that specified by the manufacturer. The post-peak behavior suggests that, once the junction reaches its splitting strength, failure occurs faster when compared with other loading conditions.

#### **4.4.8 Ductility ratio**

To assess the rate of failure in both cell-walls and junctions under short-term loading scenarios, a ductility ratio is proposed. This relationship entirely focuses on elongation and is not relevant to strength. First, the ductilities of the elastic and plastic regions are obtained from the elongations in two respective regions over the original gauge length. The ductility ratio is then calculated as the ductility of the plastic region divided by the ductility of the elastic region. Higher values indicate that the specimen reaches its peak strength quicker and experiences a less dramatic strength reduction. Figure 4.29(b) summarizes the strength versus pre-peak elongation relationship for all tests conducted on the cell-walls and junctions. The plot is helpful in evaluating the elastic response of geocells under different loading scenarios. As can be seen, the junctions provided similar strength against shear, peeling and splitting whilst also summarizes the ductility ratios of all test schemes examined in the present study. An average ratio is adopted for each test scheme.

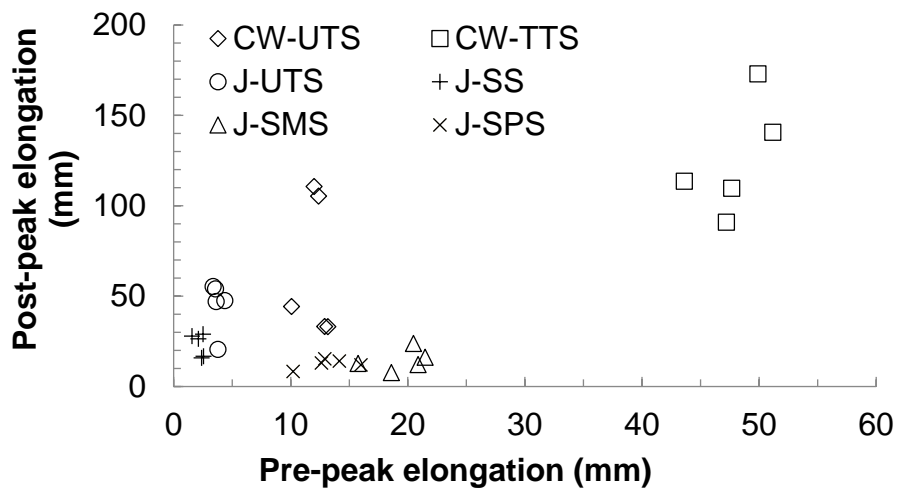
As can be seen in Table 4.4, the splitting and seam strength tests are both associated with extremely low values, which signify that the geocell junctions are more prone to failure when subjected to peeling and splitting forces (as demonstrated in this study; cf §3.6 and §3.7). These two loading scenarios may be the most typical in practical applications of geocells. The trapezoidal tearing strength tests yielded a better ratio of 2.61, which also suggests that the geocell wall is vulnerable to tearing forces even when the cell-wall is slightly damaged. The geocell junctions showed superior performance under tension and shearing, returning ductility ratios of 12.17 and 12.18, respectively. Plotting the pre-peak elongation against the post-peak elongation [(Figure 4.29(a)] provides a more direct interpretation of the ductility ratio, reflected by the locations of these data points. Being closer to the origin suggests lower resilience relative to its corresponding loading type due to small overall elongation. In addition, while most tests yielded consistent ductility ratios, the ductility ratios of uniaxial tensile strengths tests for cell-wall and junction and shear strength test for junction showed considerable scattering, reflected by the high standard deviations in Table 4.4. This is attributed to the different failure patterns as well as the inconsistencies in samples as discussed previously.

Table 4.4. Ductility ratio for geocell walls and junctions under different test conditions.

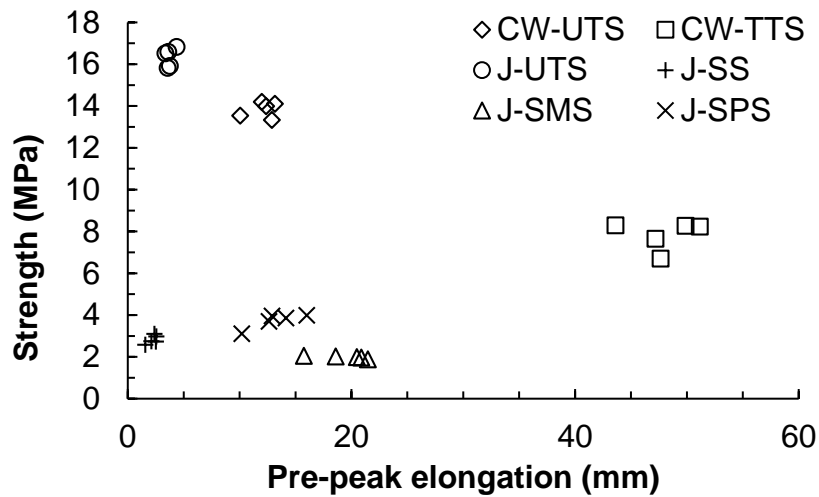
Test	Specimen	Elongation (mm)		Ductility ratio	Average ratio	Standard Deviation
		Pre-peak	Post-peak			
Uniaxial tensile strength (cell-)	1	10.05	44.22	4.40	5.45	3.23
	2	13.16	33.09	2.52		
	3	11.98	110.61	9.23		
	4	12.89	33.16	2.57		
	5	12.37	105.29	8.52		
Trapezoidal tearing strength	1	43.61	113.60	2.60	2.63	0.57
	2	49.89	172.98	3.47		
	3	51.16	140.65	2.75		
	4	47.20	90.87	1.93		
	5	47.65	109.68	2.30		
Uniaxial tensile strength	1	3.77	20.52	5.44	12.17	4.31
	2	3.63	46.99	12.94		
	3	3.37	55.28	16.42		
	4	4.36	47.54	10.89		
	5	3.57	53.98	15.14		
Shear strength (Junction)	1	1.56	27.83	17.84	11.02	4.69
	2	2.11	26.36	12.49		
	3	2.39	15.88	6.65		
	4	2.55	16.70	6.56		
	5	2.51	28.91	11.53		
Split strength (Junction)	1	14.15	14.06	0.99	0.95	0.18
	2	12.62	12.98	1.03		
	3	12.90	15.34	1.19		
	4	15.99	11.95	0.75		
	5	10.19	8.29	0.81		
Seam strength (Junction)	1	15.75	12.70	0.81	0.74	0.28
	2	21.47	16.15	0.75		
	3	18.59	7.71	0.41		
	4	20.87	12.10	0.58		
	5	20.47	23.78	1.16		

Figure 4.29(b) summarizes the strength versus pre-peak elongation relationship for all tests conducted on the cell-walls and junctions. The plot is helpful in evaluating the elastic

response of geocells under different loading scenarios. As can be seen, the junctions provided similar strength against shear, peeling and splitting whilst also exhibiting the highest ductility with respect to shear and the highest strength associated with uniaxial tension. This implies that geocell is most vulnerable against shear. In addition, the cell-wall performed well when subjected both to uniaxial tension and tearing, reflected by reasonably long elongation prior to achieving its peak strength.



(a)



(b)

Figure 4.29. Cell-wall and junction test results: (a) post-peak elongation versus pre-peak elongation, (b) strength versus pre-peak elongation.

#### **4.5 Conclusions**

This study assesses the failure mechanisms of geocells when subjected to tensile and shear loads. An experimental program, which involved six test schemes, were conducted on the cell-walls and welded junctions of the geocell. The experiments involved the application of uniaxial tension to cell-wall strips to assess their tensile capacity and creep behavior, while the junctions were subjected to four loading types: uniaxial tension; shear; peeling; and splitting. The stresses and elongation of the samples were recorded to evaluate the peak strength, and the behaviors of both the cell-wall and junctions in the elastic and plastic regions. The failure modes for all loading scenarios were observed, and implications for the operational deployment of geocells were discussed.

This study draws the following conclusions:

1. Cell-walls behave inconsistently under uniaxial tension, mainly in the post-peak region. This is reflected by some specimens exhibiting a considerably rapid strength reduction in the post-peak region, while the others exhibited behavior typical of the HDPE material. This is a result of stress concentrations caused by inconsistent indentation depth in the cell-wall.
2. Although the junctions of geocells are formed by welding two cell-wall strips, there was no significant, observed increase in tensile strength. All specimens failed relatively quickly after reaching their tensile strength.
3. The trapezoidal tearing strength was assessed using pre-cut, cell-wall specimens. All specimens failed in a progressive and diagonal manner, following the pattern of the perforations. The pre-cut specimens performed better than expected, reaching their

peak tearing strength at approximately 50 mm of elongation before the first rupture occurred. The thin strips between perforations continued to sustain the tensile force and exhibited good ductility. These strips can elongate from 6 mm up to 33 mm, which may be considered beneficial in cases where the cell-wall sustains minor damage along its edge when buried beneath the ground.

4. The creep behavior of geocells was investigated on the cell-wall under 60%, 65% and 70% of its ultimate tensile strength. As expected, all three specimens elongated considerably under a static load over the 300-hour applied loading period, while one of the specimens (#3; 59.5 kg) showed a pronounced and more rapid deformation. Although the load applied to specimen 2 was 4 kg heavier than that of specimen 1, no distinctly higher axial strain was observed. Both specimens maintained sound integrity, while slight deflections were found adjacent to the edge-perforations of specimen 2. However, specimen 3, loaded with a 4.5 kg higher load compared to specimen 2, ruptured at the edge-perforations and was close to failure.
5. A shrinkage ratio was developed to express the reduction in the height of the geocell wall with the application of the tensile, creep load. The shrinkage ratio is defined as the reduction in geocell height (mm) divided by the maximum elongation (mm) of each specimen (perpendicular to the height), at the cessation of the creep load application. It can be concluded that the shrinkage ratio is inversely proportional to the applied load. In other words, a greater load results in higher shrinkage, which indicates that geocell cell-wall is highly elastic under long-term loading. This may be considered to be a desirable feature in the practical application of geocells.

6. The geocell junctions did not exhibit significant improvement in the uniaxial tensile strength tests, when compared to the geocell wall. Although a geocell junction is the welded formation of two cell-wall strips, an modest average increase in tensile strength of 20% was recorded.
7. The results of the peeling and splitting strength tests show significant differences in peak strengths, but very similar trends in the both the elastic and plastic regions. The ascending rate of the stress-elongation curves is slower when compared with those derived from the uniaxial tensile and shear loading cases.
8. When the junction is subjected to peeling and splitting, two types of failure modes were observed: cell-wall failures adjacent to the junctions; and weld failures where the cell-wall strips completely separated from one another. It should be noted that, when weld failure occurs, the specimen typically exhibits a lower peak strength.
9. When geocell junctions were subjected to shear, the specimens did not experience shear failure at the junctions, rather all failures occurred in the cell-wall. Therefore, it is suggested that the test results be considered as a lower bound of the shear strength of the geocell junctions.
10. A ductility ratio was proposed to quantify the rate of failure for each loading case, in both the cell-walls and junctions, under short-term loading. A higher ratio indicates that the failure occurs relatively rapidly, whereas a lower ratio indicates a more gradual failure. The geocell junction fails more suddenly under uniaxial tensile and shear loading than as a result of peeling or splitting.

**Chapter 5. Three-Dimensional Discrete Element  
Modelling of Geocell-Reinforced Ballast  
Considering Breakage (Paper 3)**

---



**INTENTIONALLY BLANK**

# Statement of Authorship

Title of Paper	Three-Dimensional Discrete Element Modeling of Geocell-Reinforced Ballast Considering Breakage
Publication Status	<input type="checkbox"/> Published <input type="checkbox"/> Accepted for Publication <input checked="" type="checkbox"/> Submitted for Publication <input type="checkbox"/> Unpublished and Unsubmitted work written in manuscript style
Publication Details	Submitted to Computers & Geotechnics.

## Principal Author

Name of Principal Author (Candidate)	Yang Liu
Contribution to the Paper	Conducting literature review, numerical simulation, data interpretation and drafting manuscript.
Overall percentage (%)	70%
Certification:	This paper reports on original research I conducted during the period of my Higher Degree by Research candidature and is not subject to any obligations or contractual agreements with a third party that would constrain its inclusion in this thesis. I am the primary author of this paper.
Signature	Date 23/8/2018

## Co-Author Contributions

By signing the Statement of Authorship, each author certifies that:

- i. the candidate's stated contribution to the publication is accurate (as detailed above);
- ii. permission is granted for the candidate to include the publication in the thesis; and
- iii. the sum of all co-author contributions is equal to 100% less the candidate's stated contribution.

Name of Co-Author	An Deng
Contribution to the Paper	Supervising development of the work and revising manuscript.
Signature	Date 23 August 2018

Name of Co-Author	Mark Jaksa
Contribution to the Paper	Co-supervision of research and manuscript editing.
Signature	Date 24/8/18

Please cut and paste additional co-author panels here as required.

**INTENTIONALLY BLANK**

## **5.1 Abstract**

This paper presents a 3-dimensional discrete element modeling (DEM) study examining the settlement and breakage behavior of geocell-reinforced ballast. The reinforced ballast chamber reproduces the geocell in configuration and the ballast particles in shape and breakage characteristics. The reinforced ballast chamber is subjected to monotonic and cyclic loads. Parametric studies are conducted on the geocell embedment depth and ballast shape. For each case, ballast settlement, geocell responses and ballast breakage behavior are evaluated. This study demonstrates that the geocell can effectively reduce settlement and ballast breakage. The geocell stiffens its embedded layer and reduces stress propagation into the underlying layer.

**Keywords:** discrete element; railway ballast; geocell; breakage; cyclic loading.

## **5.2 Introduction**

Railways are an essential element of modern transport infrastructure. In traditional railroads, ballast, a coarse and angular material, is placed beneath the sleepers to provide rapid drainage and effectively distribute track loads to the underlying subgrade. However, the track drainage condition, bearing capacity and settlement characteristics are often diminished by ballast fouling (Huang et al., 2009; Indraratna et al., 2014). Overtime, the track bed becomes deformed and inadequate, particularly for freight transportation. Ballast fouling results from a range of sources, as shown in Figure 1.2, where it is clear that ballast breakdown is by far the greatest contributor to the deterioration of the rail track condition. Therefore, it is of paramount importance to study the breakage behavior of ballast and develop solutions to minimize ballast degradation.

Several studies have been conducted to investigate ballast breakage and its influence on the mechanical response of ballast. Discrete element modeling (DEM) was often used in many of the studies (e.g. (Hossain et al., 2007; Indraratna et al., 2009; Lu & McDowell, 2010; Wang et al., 2017; Yan et al., 2014)). Yan et al. (2014) and Wang et al. (2017) employed 3-dimensional (3D) DEM to study the breakage mechanism of a single ballast stone under uniaxial compressive loading. Lu and McDowell (2010) also adopted 3D DEM to simulate breakable ballast by attaching small particles to unbreakable clumps and subjected the ballast assembly to monotonic and cyclic loads under triaxial condition. Particles created in these studies account for the angularity and size of the ballast particles and successfully simulated ballast breakage. To verify the simulation results, laboratory tests on ballast breakage were conducted (Huang et al., 2009; Indraratna, Thakur, et al., 2010; Sun &

Zheng, 2017). Sun and Zheng (2017) used triaxial tests to study the effect of particle size distribution (PSD) on ballast breakage behavior. Indraratna, Thakur, et al. (2010) used both experimentation and 2D DEM, with simplified ballast shapes formed using 6 to 20 particles, to study the breakage mechanism under biaxial conditions.

To stabilize railway ballast, studies have been conducted to reinforce ballast using geosynthetics (Chen et al., 2012a; Chen, McDowell, et al., 2013; Leshchinsky & Ling, 2013c; Ngo et al., 2014; Qian et al., 2015; Wang et al., 2016). Chen et al. (2012a) used DEM to simulate the response of geogrid-reinforced ballast under confined and unconfined conditions. Similarly, Qian et al. (2015) used DEM to examine geogrid-reinforced ballast subjected to triaxial tests, whereas Liu et al. (2018) modeled a scaled-down geocell-reinforced railway track structure using DEM. However, these studies made no account of ballast breakage, which is an appropriate assumption when considering the change in performance of geosynthetic-reinforced ballast under short-term, low-stress loading conditions. Where more complex loading conditions are considered, ballast breakage should be accounted for.

DEM, a powerful modeling method developed by Cundall and Strack (1979a), possesses the capability to represent, with appropriate engineering accuracy, distinct ballast particles and to simulate particle motion (Cundall & Strack, 1979b). The method is able to replicate variable angularities of the ballast, and similarly reflects variable material micro-properties, such as stiffness and friction (Chen et al., 2012a; Irazábal et al., 2017; Itasca, 2009b). More importantly, it enables 3D modeling. This is particularly important for the accurate

simulation of a 3D geocell panel, as 2D modeling neglects, or at least simplifies, the interaction between cells and so underestimates the performance of the geocell panel. However, an additional calibration stage is required in order to yield simulated behavior substantially similar to that observed in reality.

A geocell is a cellular confinement system, of honey-comb shape, that is commonly fabricated using high-density polyethylene sheets. It is manufactured into various sizes and depths to accommodate different applications. Geocells have been widely used in a variety of infrastructure applications, such as foundations and subbases (Dash, 2012; Dash & Bora, 2013; Hegde & Sitharam, 2015b; Moghaddas Tafreshi, 2015; Oliaei, 2017; Tanyu, Aydilek, et al., 2013; Yang et al., 2012), slopes (Mehdipour et al., 2013b), retaining structures (Chen, Wu, et al., 2013a) and embankments (Madhavi Latha & Rajagopal, 2007; Zhang et al., 2010). All of these studies have shown that using geocells improves the performance of the infrastructure by reinforcing the granular infill materials. Leshchinsky and Ling (2013c) used simplified, regular quadrilaterals to model the shape of the geocell in finite element analysis to simulate geocell-reinforced ballast. Liu et al. (2018) employed a similar geocell geometry in DEM to simulate straight and curved ballast railway tracks. The simplified geocell model reduced computational effort, without compromising the accuracy of modeling the geocell behavior and its interaction with the infill material. Hegde and Sitharam (2015c) and Yang et al. (2010) used realistic geocell profiles in the FLAC3D finite element method (FEM) software to demonstrate the benefit of geocell-reinforced sand beds. However, given the continuum nature of the FEM approach, it is likely not to be as applicable to ballast as it is to sands.

The present study utilizes the 3D DEM software PFC3D 5.0 to examine the performance of geocell-reinforced railway ballast, where ballast breakage is considered. A model is developed which involves a single geocell pocket of realistic shape, embedded within a chamber filled with ballast. The size of the model is selected to reproduce a unit of the reinforced railway ballast track bed. Relevant loading scenarios are developed and examined, with a focus on the occurrence of ballast breakage and its effect on ballast performance. Comparisons are made between unreinforced and reinforced cases and the geocell layer depth is examined to optimize track bed design.

### **5.3 Discrete Element Modeling**

#### **5.3.1 Contact model**

Discrete element modeling incorporates a contact model to govern the interactions of objects in contact. There are four types of objects available in PFC 3D including a: ball, wall, clump and cluster. The ball and wall objects are the fundamental building blocks. A group of balls can be aggregated either into a clump, if the inter-ball contact in the clump is unbreakable, or a cluster, if the contact is breakable. The cluster allows for the simulation of particle breakage and is used in this study for ballast modeling.

The current study employs two contact models: linear contact and linear parallel-bond contact. The linear contact model is used for cluster-to-wall contacts and inter-cluster contacts, whereas the parallel-bond contact model is used for contacts within the geocell and those within a cluster. Schematic diagrams of the two contact models are provided in Figure 2. The linear contact model, a combination of linear and dashpot components,



allows relative rotation and slip and can only transmit compressive forces over an extremely small contact point. The linear components provide the linear elastic behavior, while the dashpot provides viscous behavior. The linear forces are produced by the constant normal ( $k_n$ ) and shear ( $k_s$ ) stiffnesses of the two contacting objects, while the dashpot forces are defined and developed by the normal ( $\beta_n$ ) and shear ( $\beta_s$ ) damping ratios. Slip between the two contacting objects is controlled by the friction coefficient ( $\mu$ ) and the activity and loss of linear contact is governed by a surface gap ( $g_s$ ). As one might expect, contact is active when the surface gap is less than or equal to zero.

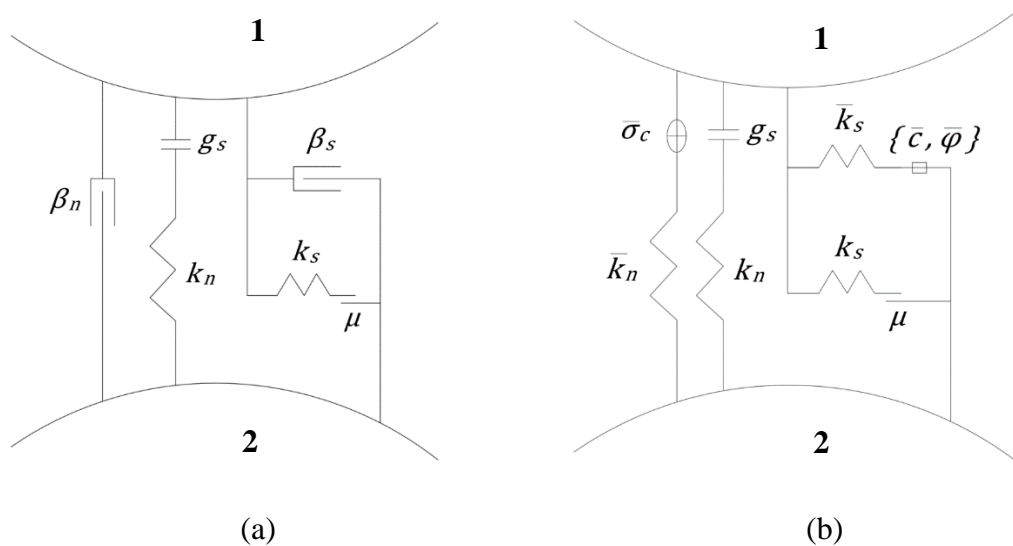


Figure 5.1 Illustration of contact models: (a) linear contact model, (b) linear parallel-bond contact model. (Adapted from Itasca (2009a))

The linear parallel-bond contact model was developed by Potyondy and Cundall (2004). It has been widely used to model a range of geomaterials, for example, sand, aggregates and geosynthetic materials (Chen, McDowell, et al., 2013; Liu et al., 2015; Liu et al., 2018; Wang & Leung, 2008; Xu et al., 2017). As shown in Figure 5.1(b), a parallel bond is the

combination of two interfaces, a linear interface, which is equivalent to the linear contact model, and a parallel-bond interface that acts in parallel to the linear interface. The parallel-bond interface is distributed over a circular cross-section lying on the contact plane and centered at the contact point. It can transmit both forces and moments, which means it can resist relative rotation until the imposed load exceeds its limiting strength. The bond strength is defined by multiple input parameters, including the normal ( $\bar{k}_n$ ) and shear ( $\bar{k}_s$ ) stiffnesses, tensile strength ( $\bar{\sigma}_c$ ), cohesion ( $\bar{c}$ ) and friction angle ( $\bar{\varphi}$ ). As with the linear contact model, the linear parallel-bond contact model is active when the surface gap ( $g_s$ ) is less than or equal to zero.

## 5.3.2 Materials

### 5.3.2.1 Ballast

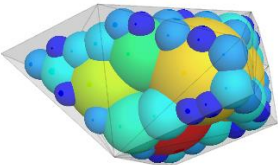
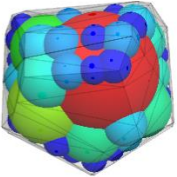
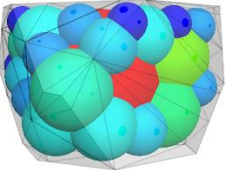
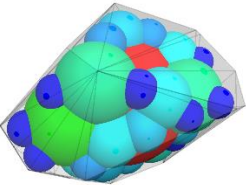
Railway ballast is usually produced by blasting and/or fragmenting a rock mass, and hence exhibits variable angularities. Past studies (Lim & McDowell, 2005; Liu et al., 2018; Lu & McDowell, 2006; Lu & McDowell, 2008; Yan et al., 2014) have demonstrated the importance of accurately modeling the particle angularities and suggested that modeling angularities in simulations better reproduces the actual behavior of the ballast. In order to do so, ballast is often simulated using clumps. However, a clump is a ‘slaved’ group of spheres which behaves as a rigid body. This implies that the contacts within a clump are fixed and the clump does not rupture under loading. Clusters are more suitable for modeling particle breakage as they incorporate parallel-bonds for the spheres within the cluster. As shown in Figure 2(b), the bond is breakable when the imposed load exceeds the bond strength. Similar to clumps, clusters aggregate spherical particles into an overall form

that resembles angular shapes or blocks. These clusters can interact with each other and approximate the behavior of an angular, blocky system (Group, 2008).

The ballast clusters are generated in a similar manner to that adopted for ballast clumps (Liu et al., 2018). Initially, cluster templates are defined corresponding to the shapes of actual ballast. Four shapes were selected from a stockpile of ballast in South Australia to represent typical ballast geometries, as shown in Table 5.1. These selected shapes were modeled using 3D using CAD software and then imported into the PFC. Based on these imported 3D models, PFC generates corresponding cluster templates in accordance with the method introduced by Taghavi (2011). The parameters control the fidelity/smoothness of the cluster by means of the ‘distance’ and ‘ratio’ user-defined parameters. The ‘distance’ corresponds to an angular measure of smoothness and expressed in degrees, as described by Taghavi (2011). The greater the ‘distance’, the smoother the clump and the greater the number of particles that are incorporated in a template. The ‘ratio’ controls the size difference between the largest and smallest particles. In the present study, a ratio of 1:5 is selected in order to reflect realistic ballast shapes in PFC, while optimizing computational effort. It should be noted that varying the clump size has no effect on the number of particles within a clump template; the spheres automatically adjust their diameters to suit the pre-defined ratio and clump sizes. Once the cluster templates were created, a bespoke code was executed to replace the group of particles in a cluster template with parallel-bonded spheres. These clusters were then calibrated.

The ballast gradation follows the Grade 60 PSD requirement specified by Australian Standard (Australia, 2015) and ARTC (2007). The gradation curves and the standard specification are shown in Figure 5.2. This study adopts a PSD that is closer to the lower boundary of the specification in order to optimize the number of ballast particles generated in the DEM model.

Table 5.1 Ballast shapes used in DEM simulation.

Template No.	Cluster Template	Shape and Angularity	Number of Particles
1		Thin, high angularity	44
2		Round, low angularity	41
3		Flat, low angularity	41
4		Plump, moderate angularity	41

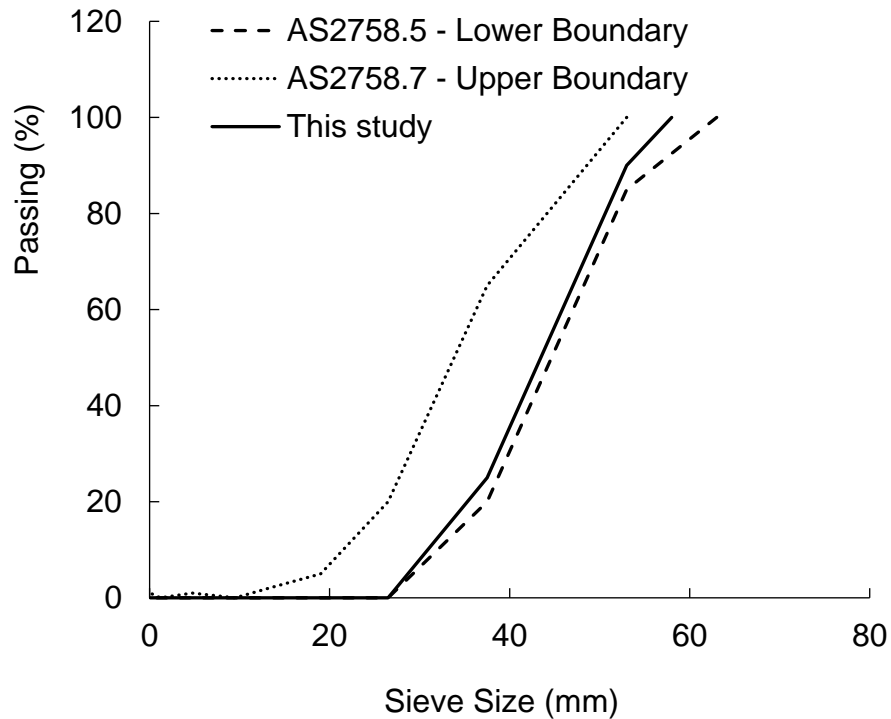


Figure 5.2 Particle size distribution of ballast assemblies in DEM simulation.

### 5.3.2.2 Geocell

A realistic form of a single geocell pocket was again created using 3D CAD software and then imported into PFC3D as a surface description. The surface description has identical geometric properties as a commercially available geocell pocket, as shown in Figure 5.3(a). The curved surface of the geocell is an improvement on the flat surface adopted by Liu et al. (2018) and thus increases the accuracy of geocell modeling. The geocell pocket measures 255 (W)  $\times$  375 (L)  $\times$  100 (D) mm, with a cell-wall thickness of 2.1 mm, and 4 mm at the junctions. It should be noted that the surface description provides an additional cell-wall thickness of 0.1 mm to assist with reducing the contact forces between the particles and the geocell walls. The implementation of a single geocell pocket optimizes computational effort, whilst also facilitating a more complex numerical model at the micro

level, which enhances the accuracy of the simulation. For example, the ballast elements are composed of a greater number of spheres to present more realistic ballast particles and, similarly, the geocell model no longer requires simplification to reduce computational effort, as has been undertaken in previous studies (Leshchinsky & Ling, 2013b; Liu et al., 2018; Ngo et al., 2015). This leads to more accurate simulation of the mechanical behaviors and ballast breakage in particular. Chen, Huang, et al. (2013) suggested that the use of a single geocell pocket may result in reduced soil strength when compared against soil reinforced with geocells incorporating multiple pockets despite the fact that more comprehensive research to confirm this conclusion. To mitigate this effect, the geocell model adopts the minimum dimensions of a commercially available geocell product, which improves the infill strength (Chen, Huang, et al., 2013). Additionally, the single geocell pocket is sufficient for the purposes of the present study, which primarily seeks to examine whether geocell can effectively alleviate ballast breakage. Figure 5.3(c) illustrates the geocell pocket embedded in the ballast chamber.

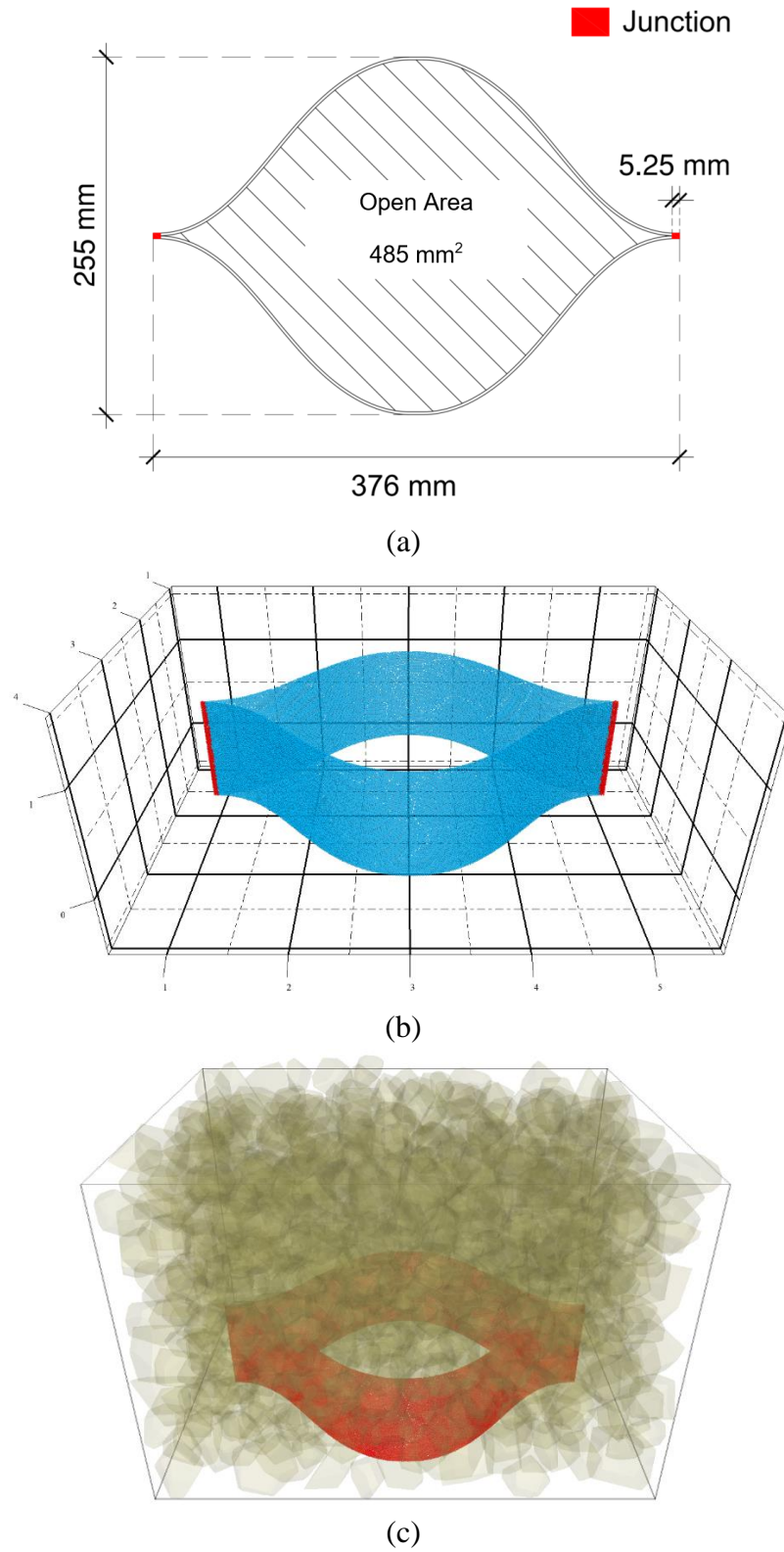


Figure 5.3 DEM model generation: (a) plan view of geocell pocket, (b) geocell-reinforced ballast model, (c) illustration of embedded and ballast filled geocell pocket.

Once the surface description is imported to PFC, 2 mm diameter spheres, with an initial porosity of 0.28, are distributed in 2 equal layers (50 mm each) within the cell-wall region. The second layer is not generated until the first layer is cycled to equilibrium state. It should be noted that the particle generation process creates overlap among the spheres. The overlaps are eliminated by cycling the system to an initial equilibrium, which is assessed by the average mechanical solve ratio, which is defined as the unbalanced force divided by the average value of the sum of the contact, body and applied forces over all of the particles. When the ratio is sufficiently small (e.g.  $1 \times 10^{-3}$ ), equilibrium is attained. The spheres that are located outside of the boundary of interest are then deleted and the porosity is recalculated to ensure no large gaps exist between the spheres. A total of 31,551 spheres are used to develop the geocell pocket, with a final porosity of 0.001. The geocell pocket generated in PFC is shown in Figure 5.3(c). Finally, the surface description and boundary wall are deleted, and all sphere-to-sphere contacts are assigned with linear parallel-bonds and the calibrated micro-properties.

### **5.3.3 Material calibration**

#### **5.3.3.1 Ballast**

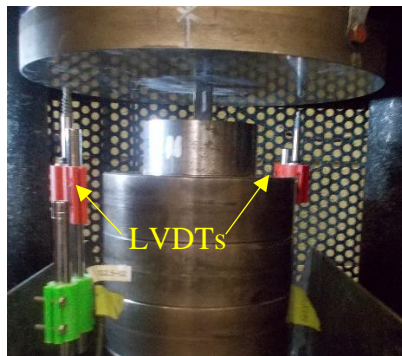
The behavior of ballast is calibrated against two tests: unconfined compressive strength (UCS) test and point load strength (PLS) test.

#### ***UCS test***

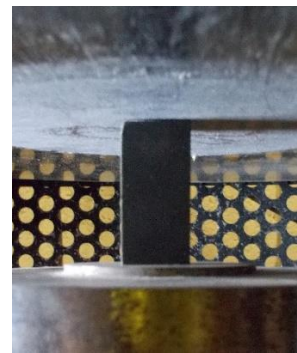
The UCS tests were conducted on three specimens collected from the ballast stockpile area in South Australia. As shown in Figure 5.4(a), the specimens were trimmed into cuboids of



15 (W) × 15 (L) × 30 (H) mm to achieve a 2:1 height-to-width ratio. It should be noted that the largest ballast samples are selected for the UCS test in order to produce effectively identical and intact specimens, and to minimize size effects. As reported by Zhang et al. (2011), the reduced sample size results in a significant increase in the UCS. The specimens were placed at the center of the compressive loading device and two sets of linear-variable differential transformers (LVDTs) were installed on the right- and left-hand sides of the specimen, as illustrated in Figure 5.4(a). The compression machine applies a loading rate of 50 N/s until failure occurs.



(a)



(b)

Figure 5.4 Unconfined compressive strength test: (a) test setup, (b) trimmed specimen.

The UCS test was simulated by compressing the same-sized specimen using two walls, as shown in Figure 5.5. The specimen was generated by using the same procedures and parameters as for the ballast clusters (Section 2.2.1). As a result, 1,655 spheres were used to generate the specimen. The spheres and clusters are equipped with either a linear contact or linear parallel-bond model, depending on the locations of concern. As with similar studies relating to ballast calibration (Li & McDowell, 2018; Lim & McDowell, 2005; Liu

et al., 2018), the iterative approach was used to determine the model micro-properties. The initial values were determined from those of similar materials examined in past studies (Liu et al., 2018; Lu & McDowell, 2010; Ngo et al., 2017). Using the micro-properties given in Table 5.2, excellent agreement in regards to the stress-strain relationship is obtained between the test and simulation results, as shown in Figure 5.5(b). As can be seen, the test and simulation results exhibit linear stress-strain behavior where the average elasticity, peak strength and corresponding strain largely agree. The test results exhibit a slight strain-hardening process which may be caused by micro-cracks within the ballast specimen closing up under loading.

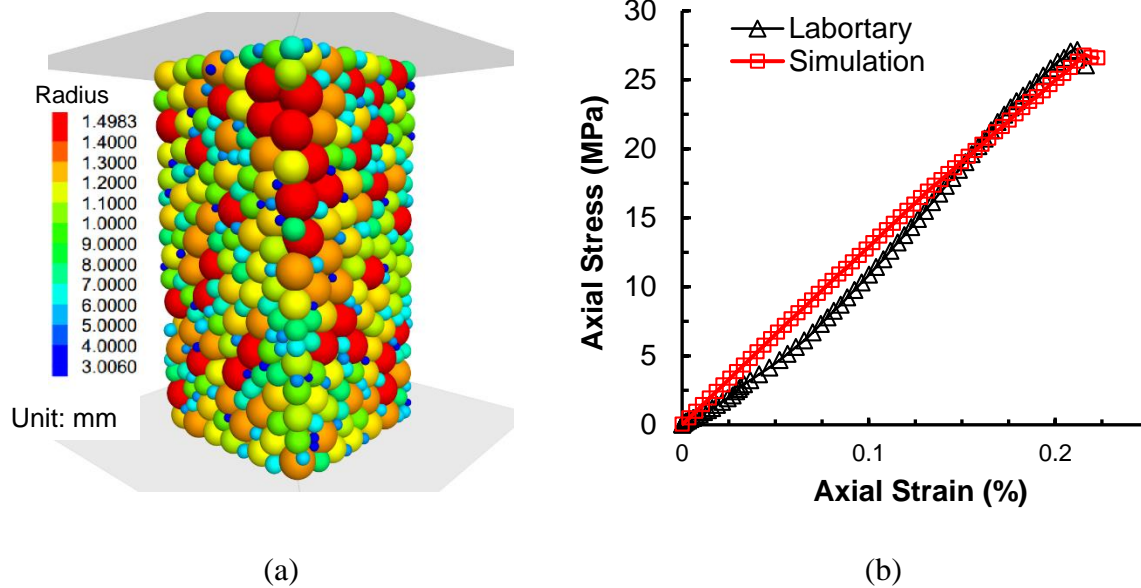


Figure 5.5 UCS modeling: (a) DEM model, (b) stress–strain relationship of test and simulation results.

**PLS test**

In addition to the UCS test, the PLS test was carried out in order to validate the micro-properties obtained for the clusters. The test was conducted on three ballast specimens that match the surface characteristics of ballast templates 1, 2 and 3 in Table 5.1. The ballast specimens were randomly selected from the same stockpile as those used in the UCS test. Figure 5.6(a) shows the hydraulic point load tester used to conduct the PLS tests. The loading was applied manually, with the load measured by the tester and displayed on its gauge. The machine stops measuring once it detects material failure. The average PLS of

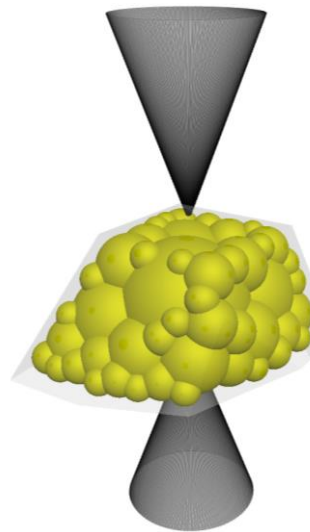
Table 5.2 Micro-properties of the materials in the UCS DEM model.

Type	Micro-properties	Value
Material	Density (kg/m <sup>3</sup> )	2,500
Linear contact (ballast – wall)	Deformability (N/m)	1.2 x 10 <sup>9</sup>
	Stiffness ratio	1
	Damping ratio	0.5
	Friction coefficient	0.28
Linear contact (inter-ballast & ballast – geocell)	Deformability (N/m)	1.2 x 10 <sup>9</sup>
	Stiffness ratio	1
	Friction coefficient	0.18
	Damping ratio	0.5
Parallel-bond (within ballast only)	Bond gap (mm)	2 x 10 <sup>-5</sup>
	Bond deformability (N/m)	1.2 x 10 <sup>8</sup>
	Bond tensile strength (N/m <sup>2</sup> )	1.7 x 10 <sup>7</sup>
	Bond cohesion (N/m <sup>2</sup> )	1.65 x 10 <sup>7</sup>
	Bond friction angle (°)	55

the three specimens is 1,256 kPa. For the simulation, the ballast clusters (Templates 1, 2 and 3) are created using a similar process to that for cluster templates. The cluster diameters are equivalent to their laboratory counterparts, i.e. 51 mm (Template 1), 48 mm (Template 2) and 47 mm (Template 3). The simulation loading setup uses a cone for the upper loading platen and a disc for the base. The disc provides stability to the ballast during the initialization phase. Once the upper cone is in contact with the cluster, the disc base is removed and replaced with a cone that is identical to the upper platen, as shown in Figure 5.4(b). Loading is achieved by displacing the upper cone at a strain rate of 0.1% per second and the ballast cluster is assigned the micro-parameters previously given in Table 5.2. The stresses imposed on the parallel-bonds are recorded when the bonds break. The three cluster templates yield an average PLS value of 1,228 kPa. This value agrees well with the test result, which validates the micro-properties obtained from the UCS test.



(a)



(b)

Figure 5.6 Point load test: (a) laboratory test setup, (b) simulation setup illustration.

### 5.3.3.2 Geocell

The calibrations of geocell cell-wall and junction were carried out using the uniaxial tensile strength (UTS) and seam strength (SS) tests, respectively. The cell-wall specimen was trimmed from a plain-area of the cell-wall and prepared in accordance with ASTM (2004). Its thickness was 2 mm and gauge length 107 mm. The narrow section, where elongation occurs, was 13 mm in width. The junction specimen was 4 mm thick, with an overall length of 75.5 mm and a width of 25 mm. The gauge length was 30 mm, which is the minimum distance that can be achieved due to the rigidity of the HDPE.

For the laboratory tests, an Instron tensile machine is used and the test setup is similar for both the cell-wall and the junction. Schematic drawings of the prepared specimens and testing schemes are shown in Figure 5.7. The cell-wall and junction specimens are clamped at both ends, with a 30 mm and 40 mm gripping area at each end, respectively. The loading ranges of the Instron machine were set to 1,000 N in order to achieve the optimal resolution. Once the specimen is clamped in place, the tensile force is applied by the displacement-controlled mechanism, at a rate of 50 mm/min (ASTM, 2004). The elongation process continued until failure of the specimen occurred.

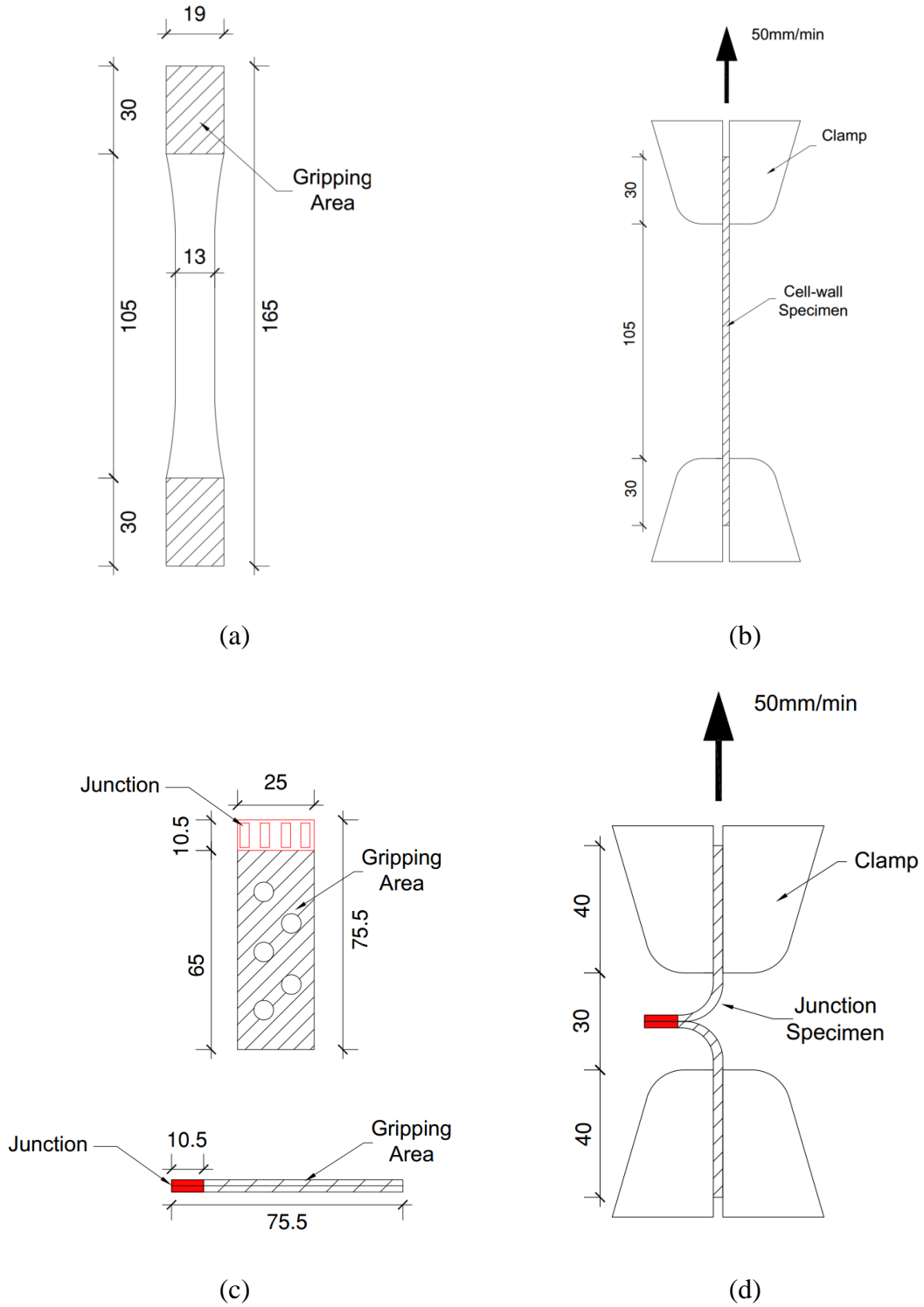


Figure 5.7 Schematics of the cell-wall and junction specimens and test setups:

(a) cell-wall specimen, (b) cell-wall UTS test setup, (c) junction specimen, and (d) junction

SS test setup.

The DEM simulation of the cell-wall UTS test involves generating the cell-wall and junction specimen from pre-defined surface descriptions, assigning parallel-bonds to the specimens, and applying the tensile load by translating the upper gripping spheres. This process is summarized in Figure 5.8. As with the ballast and geocell models described in Section 5.3.2, the material outlines were drawn in CAD software and then imported into PFC to scale [Figure 5.8(a)]. The surface descriptions have identical dimensions to the specimens used in the laboratory tests [Figure 5.7(a)]. This step is followed by distributing 2 mm diameter spheres within the pre-defined surface descriptions. It should be noted that only the gauge sections of the cell-wall and junction specimens are generated in the DEM. An additional layer of spheres with the same diameter is generated at the top and bottom to act as gripping (red) and loading (green) spheres, as shown in Figure 5.8(b) and (c), resulting in an overall height of 108 mm. For the junction SS test, the cell-wall region of the specimen is neglected in the simulation to eliminate possible elongation of the cell-wall. The specimen is generated within a box that is 25 mm in length and 10.5 mm in width, which shares identical dimensions to that of the geocell junction. The box has height of 8 mm, which is equivalent to the thickness of a geocell junction (4 mm) plus two x 2 mm thick layers of gripping and loading spheres. All parameters used in the sphere generation process are identical to those used in the geocell model generation (Section 5.3.2) to replicate trimmed cell-wall and junction strips. Subsequent to the sphere generation process, the cell-wall and junction models are cycled to their initial equilibrium. Once equilibrium is reached within the cell-wall and junction models, parallel-bonds are assigned to the cell-wall and junction models at sphere-to-sphere contacts, with separate sets of micro-properties as specified in Table 5.3. Lastly, the gripping spheres located at the

bottom are prohibited from both rotation and displacement. The remaining spheres, including the loading spheres and those forming the specimens are prohibited only from rotation. Loading, in both the UTS and SS tests, is achieved by displacing the loading spheres at a rate of 50 mm/s, which matches the loading rate used in the laboratory experimentation.

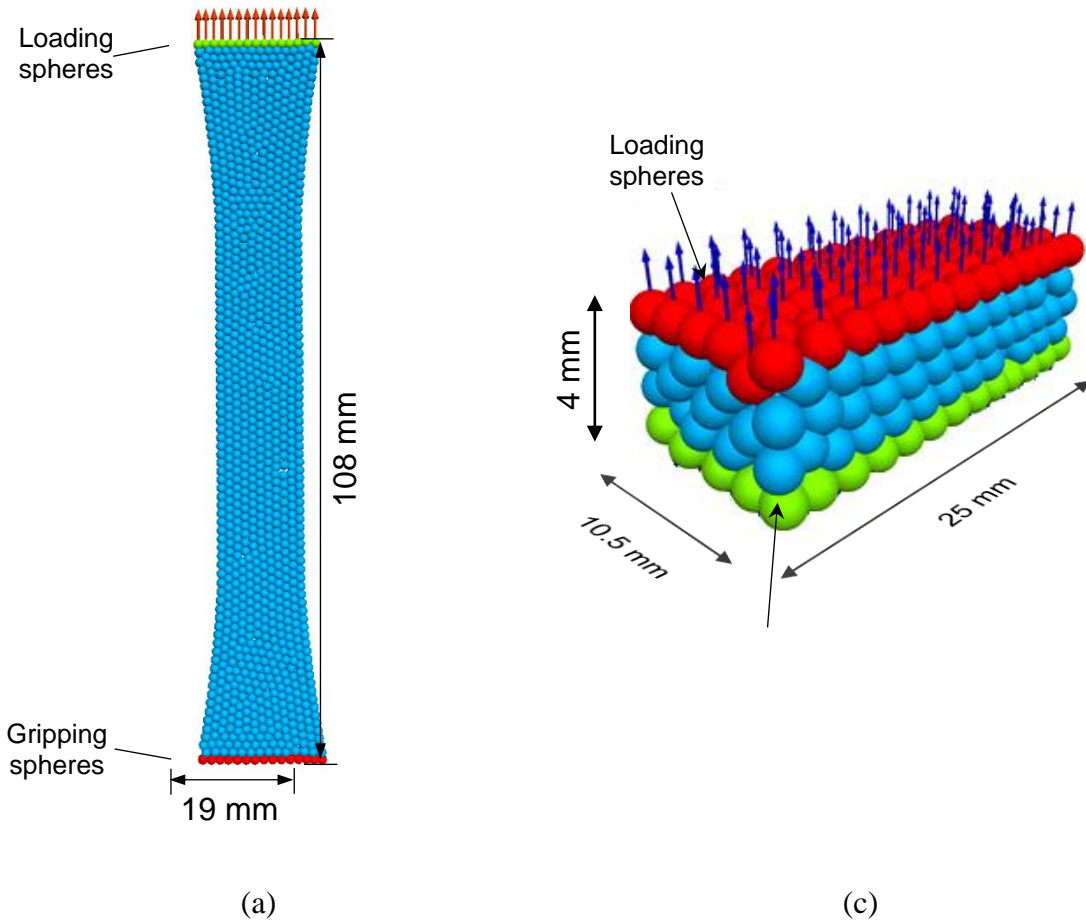


Figure 5.8 DEM simulation of the UTS test for the cell-wall and junction specimens: (a) cell-wall specimen loaded by moving top loading spheres, and (b) junction specimen loaded by moving top loading spheres.

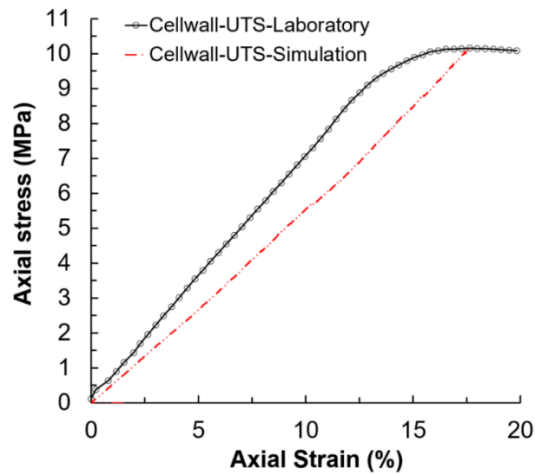


Table 5.3 Micro-properties of parallel-bonds for cell-wall and junction.

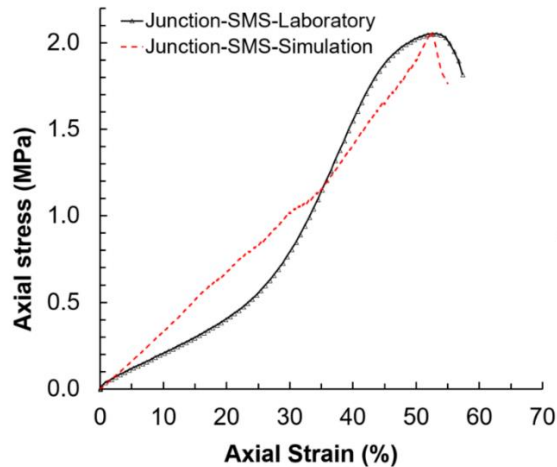
Type	Micro-properties	Cell-wall	Junction
Material	Density (kg/m <sup>3</sup> )	950	950
Linear contact (geocell - ballast)	Deformability (N/m)	1.5 x 10 <sup>6</sup>	1.5 x 10 <sup>6</sup>
	Friction coefficient	0.18	0.18
	Stiffness ratio	1.0	1.0
	Damping ratio	0.5	0.5
Parallel-bond (within geocell only)	Bond gap (mm)	0.0	0.0
	Bond deformability (N/m)	1.23 x 10 <sup>6</sup>	2.98 x 10 <sup>8</sup>
	Bond stiffness ratio	1.0	1.0
	Bond tensile strength (N/m <sup>2</sup> )	8.7 x 10 <sup>6</sup>	8.0 x 10 <sup>6</sup>
	Bond cohesion (N/m <sup>2</sup> )	1.8 x 10 <sup>6</sup>	3.98 x 10 <sup>7</sup>
	Bond friction angle (°)	0.0	0.0

The stress-strain relationships of the calibrated cell-wall and junction models, as well as their laboratory counterparts, are shown in Figure 5.9. Very close agreement is obtained between the simulation and test results with respect to the peak strengths. For the cell-wall model, the simulation yielded a peak tensile strength of 10.14 MPa at an axial strain of 17.60%, while the laboratory test yielded 10.16 MPa at 17.64% axial strain. For the junction model, a peak seam strength of 2.06 MPa was achieved at 52.38% axial strain in the simulation, while the laboratory test yielded 2.05 MPa at the same axial strain value. There are, nevertheless, discrepancies between the elastic regions in both simulations; the simulations exhibited linear behavior while the laboratory counterparts experienced

different levels of strain-hardening or softening. This is due to the linear nature of the parallel-bonds implemented in the simulation. Previous work (Liu et al., 2018) obtained a similar outcome in the elastic region, when conducting UTS test in PFC on the cell-wall. This is considered a limitation in the currently available built-in contact models. This limitation can reduce or enhance the tensile strength of the geocell model when compared to actual geocells, resulting in variations in the confinement level.



(a)



(b)

Figure 5.9 Calibration results of cell-wall and junction models: (a) cell-wall in the UTS test, and (b) junction in the SS test.

#### 5.3.4 Ballast chamber model

A full-scale railway structure simulation is computationally intensive and extremely time-consuming, owing to the large number of spheres needed to simulate the geocell and ballast infills (Liu et al., 2018). Unfortunately, full-scale modeling is beyond current and available computer capability, including supercomputers. Liu et al. (2018) downscaled the model to suit the computer capability. This downscaling solution, however, may likely underestimate performance of geocell-reinforced embankments due to the use of a smaller volume of ballast used in the simulation. To minimize the influence of downscaling and account for the available computer capability, an alternative solution is to adopt a ballast-filled chamber which is representative of the below-sleeper section. A similar approach has been adopted in previous studies (Chen et al., 2012a; Li & McDowell, 2018), which have proven to be successful in examining the performance of ballast embankments and optimizing computational effort. The geometry of the ballast chamber is given in Figure 5.10. The chamber is 450 mm in the longitudinal direction of a railway and 350 mm in cross-sectional width that can accommodate a single geocell pocket. It has a nominal ballast depth (below-sleeper) of 300 mm, which is the same as actual railways, as per ARTC (2012). The boundary effect is mitigated through assigning identical linear contact parameters to both the cluster-to-cluster and cluster-to-wall contacts.

For the geocell-reinforced model, a parametric study is conducted on the effect of geocell embedment depth,  $D$ , on the breakage behavior of the ballast. As shown in Figure 5.10(a), three embedment depths are examined:  $D_1 = 100$  mm,  $D_2 = 200$  mm and  $D_3 = 300$  mm, using the upper surface of the chamber as the reference point. As shown in Figure 11(b),

the geocell pocket is placed in line with the rail track and 37 mm longitudinally and 47.5 mm transversely from the chamber walls and, to mitigate boundary effects, the chamber walls are assigned the same linear stiffness and frictional coefficient as those for the ballast. For the sleeper, the parameters used for the loading wall in the ballast calibration process are adopted to create a consistent stress-strain behavior. The sleeper is 250 mm wide, which is consistent with the base width of heavy-duty prestressed concrete sleepers, as per specified by ARTC (2017).

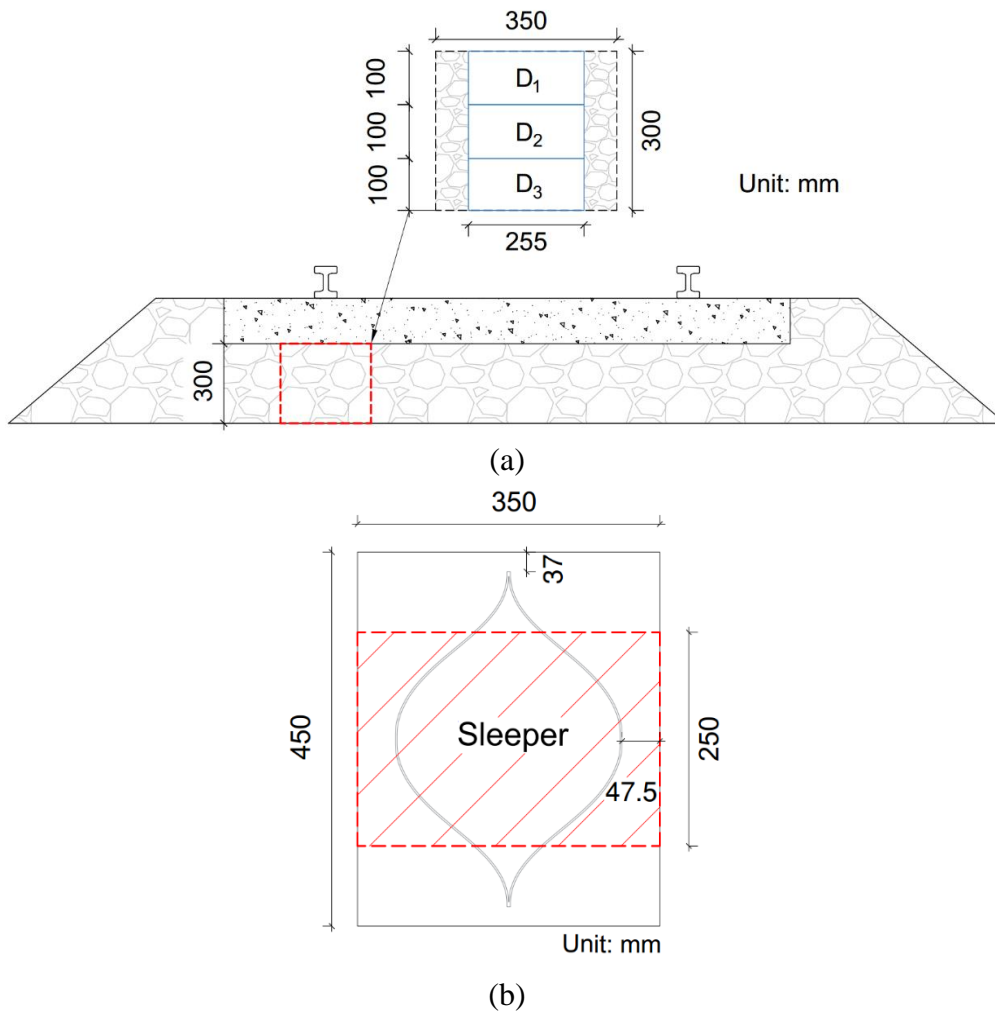
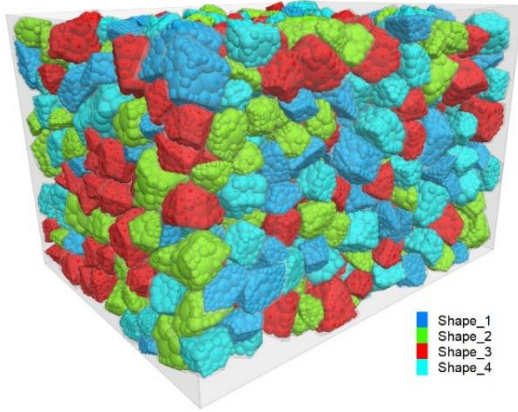


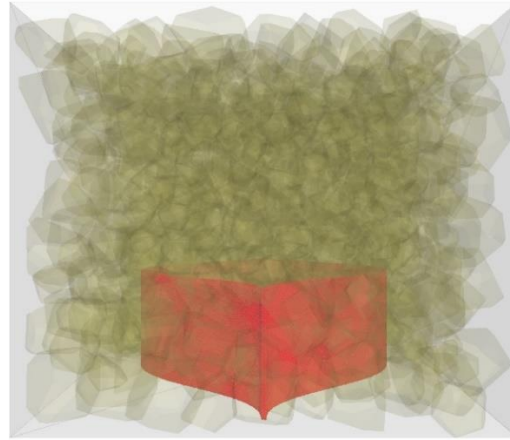
Figure 5.10 Ballast chamber model in the DEM simulation: (a) cross-sectional view, and (b) plan view.

The ballast chamber models are shown in Figure 5.11. Four ballast chamber models are developed: one unreinforced and three reinforced, depending on the depth of embedment of the geocell. The four models are numbered Test 1 to 4, respectively. For the unreinforced model, the ballast infills were generated within the chamber with an initial porosity of 0.4. The ballast assembly was cycled to equilibrium (i.e. with respect to particle overlap) under gravity of  $9.81 \text{ m/s}^2$ . The assembly rearranges to avoid overlaps at the contacts; and the porosity increases to 0.46, which was measured using six evenly distributed measurement spheres (300 mm in diameter), consistent with Wang et al. (2018). For the reinforced model, the ballast infills were generated alternating with the geocell pocket. For example, when the geocell pocket is suspended at  $D_2 = 100 \text{ mm}$ , the bottom 100 mm of ballast is generated first and cycled to equilibrium. The geocell pocket is then placed on the bottom ballast layer, using the procedures described previously in Section 2.2.2. The remaining 200 mm thick ballast layer is generated above the geocell pocket and allowed to fall into the pocket under gravity. This approach mimics the placement of ballast in actual geocells and accelerates the dissipation of the internal contact forces. Due to the inclusion of the geocell, the reinforced ballast chamber arrived at post-equilibrium porosities that are slightly greater than those of the unreinforced model. Once the ballast chamber model was established, the sleeper is generated, and subsequent loading conditions are applied.



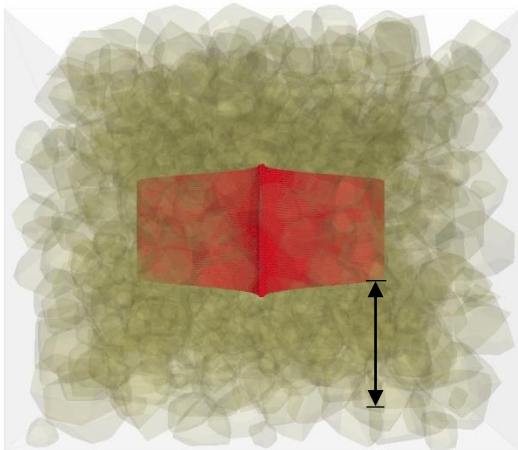
No. of ballast particles: 960  
 Initial porosity: 0.46  
 No. of parallel-bonds for the ballast:  
 110,469

(a)



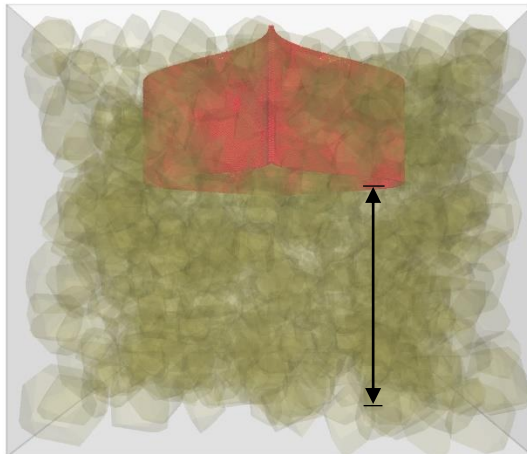
No. of ballast particles: 960  
 Initial porosity: 0.463  
 No. of parallel-bonds for: ballast: 110,474; and  
 geocell: 90,747

(b)



No. of ballast particles: 960  
 Initial porosity: 0.462  
 No. of parallel-bonds for: ballast: 110,466;  
 and geocell: 90,747

(c)



No. of ballast particles: 960  
 Initial porosity: 0.461  
 No. of parallel-bonds for: ballast: 110,469 and  
 geocell: 90,747

(d)

Figure 5.11 Ballast chamber models: (a) Test 1: unreinforced, (b) Test 2: reinforced model with geocell placed on the base, (c) Test 3: reinforced model with geocell placed 100 mm above the base, and (d) Test 4: reinforced model with geocell placed 200 mm above the base.

### 5.3.5 Monotonic and cyclic loading

Monotonic loading is applied to determine the subsidence of the ballast layer in response to a slowly increasing vertical load and is similar in nature to a plate load test. The sleepers advance at a rate of 0.02 mm/s to cause the ballast layer to settle to the desired strain of 15% (45 mm). This loading scenario provides insight on the responses of the geocell and ballast under an extreme loading condition. The slow loading rate is consistent with that adopted for the compressive strength test in the material calibration stage, which improves the simulation accuracy by allowing sufficient time to calculate the inter-particle contact forces.

Cyclic loading, on the other hand, is of higher significance in regard to the assessment of the long-term serviceability of the ballast. The current study adopts the load distribution method proposed by Sadeghi (2008), who suggested to apply the stress distribution acting on the ballast, as shown in Figure 5.12. The contact pressure is at maximum,  $W_2$ , under the rail seat position and decreases in stages as  $W_1$ ,  $W_3$  and  $W_4$  depending on the region of concern. The load calculation model is specified in Table 5.4. The load relies on several parameters, such as a dynamic coefficient ( $\emptyset$ ), wheel diameter ( $D$ ), train velocity ( $V$ ), sleeper spacing ( $S$ ) and sleeper length ( $L_s$ ) that are listed in Table 5.5. By accounting for the sleeper dimensions used in this study, the contact pressure is calculated as 150 kPa. The cyclic loading is applied with a frequency of 8.25 Hz, which corresponds to a wagon traveling at 60 km/h with an axle load of 25 t (Indraratna, Nimbalkar, et al., 2010).

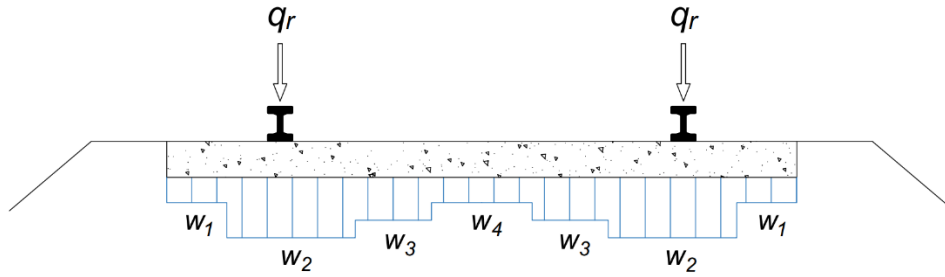


Figure 5.12 Contact pressure distribution between sleeper and ballast.

Table 5.4 Load calculation model proposed by Sadeghi (2008).

Factor	Proposed model	
Design wheel load	$P = \phi P_s$	Eq. 1
Dynamic coefficient	$\phi = 1 + 4.73 V/D$	Eq. 2
Rail seat load	$q_r = 0.474 (1.27 S + 0.238) P$	Eq. 3
Maximum contact load (After tamping)	$w_2 = 2.954 q_r / L_s$	Eq. 4

Where:  $P_s$  = monotonic wheel load (t);  $V$  = train velocity (km/h);  $D$  = wheel diameter (mm);  $S$  = sleeper spacing (m); and  $L_s$  = sleeper length (m).

Table 5.5 Parameters used for the calculation of maximum contact pressure.

Parameters	Value	Condition applied
Wheel diameter $D$ (mm)	920	Coal traffic wagon (ARTC, 2018)
Train velocity $V$ (km/h)	60	Hunter Valley coal traffic wagon (ARTC, 2014)
Sleeper spacing $S$ (m)	0.6	Typical prestressed concrete sleeper spacing on a straight line (ARTC, 2017)
Sleeper length $L_s$ (m)	2.5	Heavy duty prestressed concrete sleeper (ARTC, 2017)
Static wheel load $P_s$ (t)	12.5	Hunter Valley coal traffic wagon (ARTC, 2017)



A total of 20,000 loading cycles were performed for each of the four models. The cycle number is double the number suggested by Ngo et al. (2017), who suggested, based on laboratory observation, that the majority of the ballast deformation and degradation occurs within the initial 10,000 cycles. Therefore, the cycle number adopted in the present study is sufficient to capture the deformation and breakage behavior of ballast. Additionally, the doubled cycle number may shed light on the long-term serviceability and response of the geocell.

## **5.4 Results and Discussion**

### **5.4.1 Monotonic loading**

#### **5.4.1.1 Settlement**

The axial stress versus settlement relationships of all four models are given in Figure 5.13. All models exhibited a relatively linear behavior when subjected to monotonic loading. The stress-settlement relationships are divided into two zones: A and B. Zone A covers the initial 10 mm of settlement; Zone B ranges from 10 mm to 45 mm. In Zone A, all models underwent an initial compaction stage reflected by the more rapid settlement rate. Test 1 reached approximately 10 mm under minimal load (i.e. < 50 kPa). Tests 2–4 experienced a similar tendency, whereas the initial compaction stage was completed earlier. The ballast assemblies reached a denser state at 4 mm for Tests 2 and 3, and at 2 mm for Test 4. The differences mainly arise from the different embedment depths of the geocell. The geocell pocket provides more efficient confinement of the ballast when it is placed at a higher, rather than a lower level. This outcome is in agreement with that obtained by Liu et al. (2018). The reinforcing layer acts as a stiffened mattress, which provides passive resistance

against lateral spreading of the ballast infill, which in turn reduces the load on the sleeper propagating into the underlying foundation material. An approximately 5% reduction in porosity is recorded in all models at the end of their respective compaction stage. From that point onward, the ballast in all test models further stiffens, with an associated decrease in settlement.

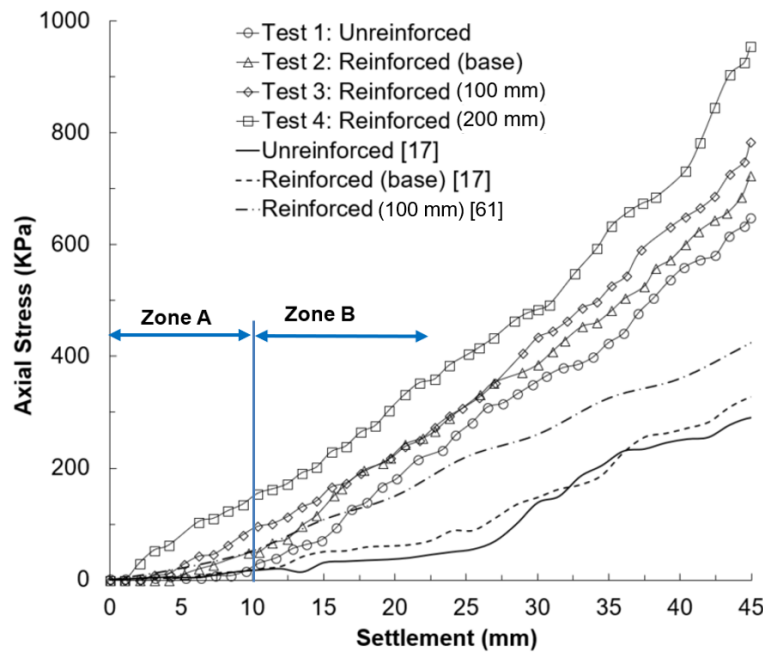


Figure 5.13 Applied axial stress versus stress relationships of all model tests under monotonic loading.

In Zone B, Tests 1 and 2 noticeably stiffen once the settlement reaches approximately 15 mm. Both of the two models then become stable, while Tests 3 and 4 maintain a slow gain in stiffness as the ballast settles. The normal stiffness, which is defined as the ratio of the applied stress divided by the settlement, is used to assess the performance of each model test. Generally, Test 1 exhibits the poorest load bearing performance, reflected by the

lowest average normal stiffness of 19.7 kPa/mm. Slight improvement in the normal stiffness is observed in Tests 2 and 3, with an average of 21.6 and 22.5 kPa/mm, respectively. The stiffness increases by 10% and 14%, respectively. Test 4 yields the best bearing performance, with a normal stiffness of 24.6 kPa/mm or 25% stiffness gain compared to the unreinforced model. The overall behavior of Tests 1 and 2 agrees with those in Liu et al. (2018), whose results are also presented in Figure 5.13 for comparison. It is shown that the bearing capacity of all of the models in the current study almost doubles the corresponding value reported by Liu et al. (2018), where the strain reaches 15%. The chamber confinement may contribute to the gain, but, as aforementioned, Liu et al. (2018) scaled down the ballast embankment model and used a lower volume of ballast assemblage, which generally underestimates the ballast bearing capacity. In addition, differences in the ballast gradation and the loading method also play important roles in the observed difference in bearing capacity. However, the current study agrees with the past studies (Leshchinsky & Ling, 2013a; Liu et al., 2018), in that suspending a geocell at a higher level yields improved bearing performance.

Investigating the displacement vectors of the ballast particles provides insights on the improved bearing capacity of the geocell-reinforced models. Figure 5.14 presents the displacement vectors of the ballast in all of the model tests. For illustration purposes, a clipped region of width 125 mm (i.e. half of the width of the sleeper) is used to extrapolate the displacement vectors of the ballast directly beneath the sleeper. There is no apparent pattern of the ballast movement in Test 1 except all ballast particles move downward and spread laterally when approaching the base. Compared to Test 1, the reinforced model tests

show a noticeable improvement in settlement reduction, irrespective of the embedment depth of the geocell pocket, which is reflected by the darker blue displacement vectors. Placing the geocell at the base showed interesting results in terms of ballast movements. Figure 5.14(c) shows a zoomed-in view of the left-hand side of the bottom 100 mm layer and the ballast movements are characterized by the red and pink arrows. Unlike the unreinforced model, the geocell pocket restricts the lateral movement of the ballast as the particles embedded in the geocell pocket force the ballast to displace downward, as indicated by the red arrows. At the center of the geocell pocket, the ballast particles restrict their own lateral movement, forming the pattern highlighted by the pink arrows. Initially, the ballast particles tend to move laterally to the opposite side as they approach the geocell pocket center from both directions. Consequently, the movement is then deflected by both sides, which results in downward movement. In addition, the geocell pocket also reduces the movement of the surrounding ballast. This enhancement is visualized in Test 3 [Figure 5.14(f)]. When compared with the unreinforced model at an identical depth, the vertical displacements of the ballast particles are significantly reduced. Furthermore, Tests 3 and 4 further validate the load-settlement responses presented in Figure 5.13 and the reinforcing mechanism of the geocell at a micro-mechanical level. In the geocell-embedded layers and the underlying ballast, settlement reductions are evident when the geocell pocket is placed 100 and 200 mm above the base.

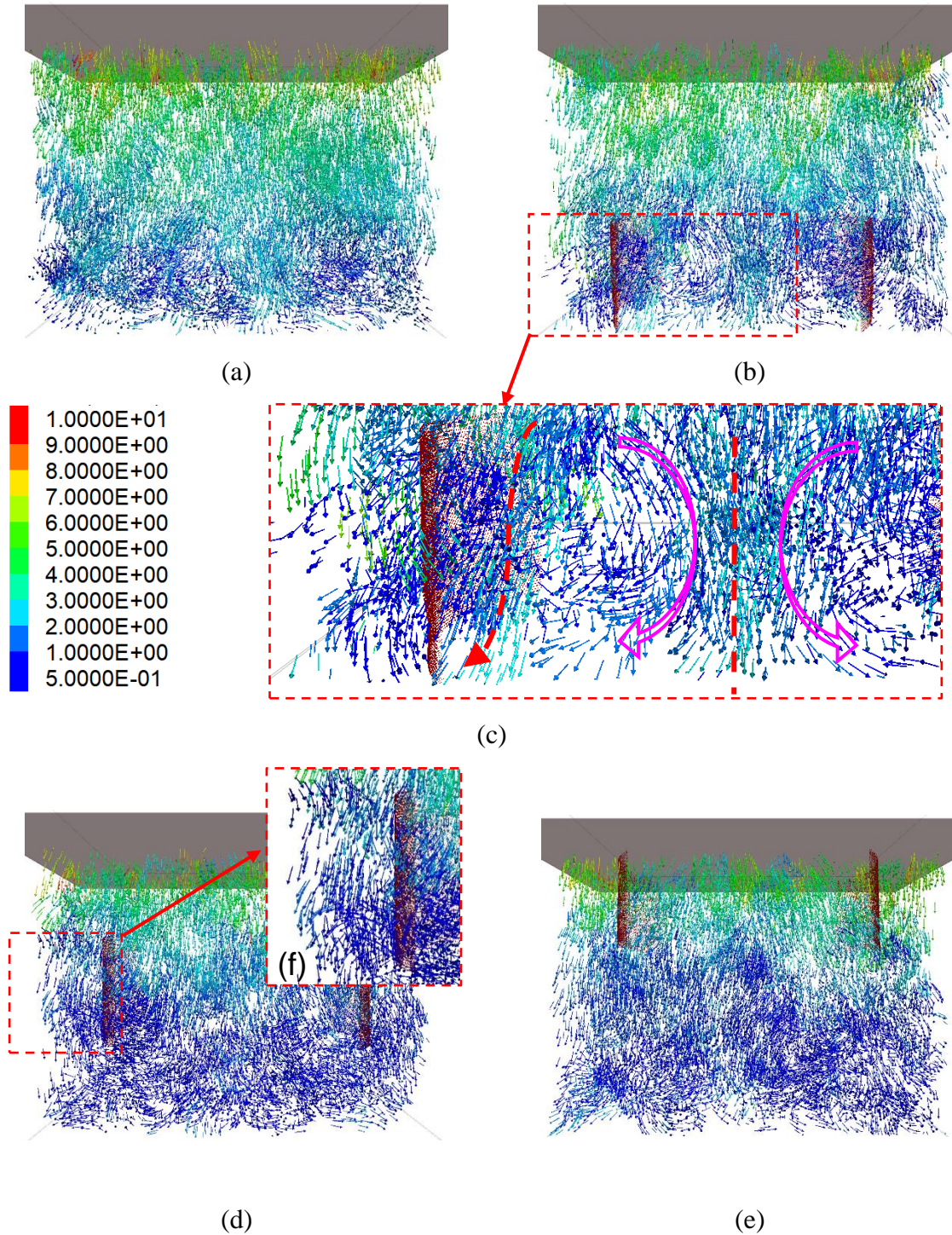


Figure 5.14 Displacement vectors, drawn at the same scale, for ballast beneath the sleeper subjected to monotonic loading for different model tests: (a) Test 1: unreinforced, (b) Test 2: geocell on the base, (c) Test 3: geocell placed 100 mm above the base, and (d) Test 4: geocell placed 200 mm above the base.

## 5.4.1.2 Ballast breakage characteristics

Figure 5.15 shows the number of ballast particle breakages versus settlement relationships of all model tests. As expected, Test 1 experienced the greatest number of breakages, whereas the lowest number is recorded in Test 2, where the geocell is placed at the base. Although Tests 3 and 4 exhibit superior bearing performance than Test 2 in the monotonic loading condition, Test 2 outperforms Tests 3 and 4 in reducing ballast breakage. To better understand the breakage behavior in unreinforced and reinforced test models, detailed analyses are conducted in relation to ballast shape, location distribution and failure strength.

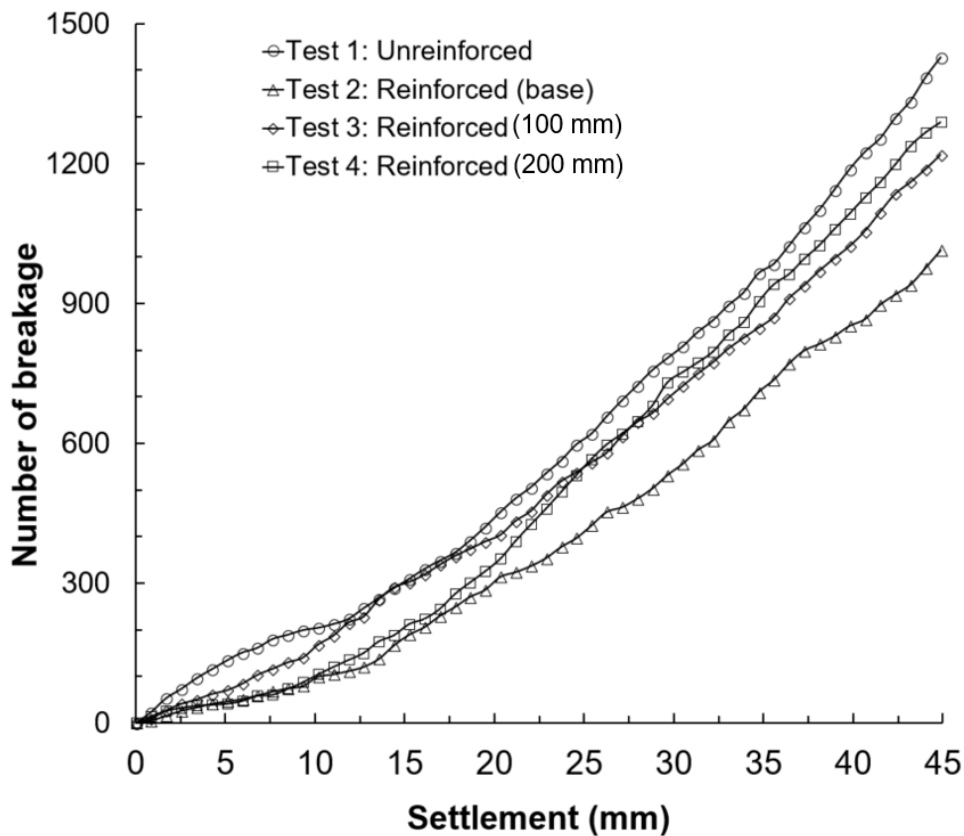


Figure 5.15 Number of ballast particle breakages versus settlement of all model tests under monotonic loading.

Table 5.6 presents the breakage and failure strength results with respect to the ballast layers where the chamber is subjected to monotonic loading. The failure strength is the stress (in kPa) imposed on a parallel-bond when breakage occurs. In each of the four test models, the uppermost layer (i.e. 200–300 mm) includes the greatest number of breakages, while the central layer (i.e. 100–200 mm) contains the least number of breakages. In Test 2, the bottom reinforced layer has the least breakages compared to the other three model tests, although the confined ballast experiences slightly higher contact forces when compared to Test 1, as shown Figure 5.17(b). Among the reinforced models, the top layer in Test 2, has the least number of breakages owing to a significantly lower applied monotonic stress. In Test 3, the central layer experienced the greatest number of breakages among the three reinforced model tests. The confined and stiffened ballast layer absorbs a proportion of the stress induced by the monotonic loading, leading to stress concentrations inside the geocell pocket. This observation is verified in Figure 5.16(c), which, as a contact force distribution map for Test 2, shows that the ballast particles confined in the central layer experience greater contact forces when compared to the corresponding layer of the unreinforced model [Figure 5.16(a)]. Owing to the central layer absorbing the load, the bottom layer in Test 2 reduces breakage by 37.7%. In Test 4, the suspended geocell pocket results in an additional 13.6% breakage within the top layer, when compared to Test 1. The uppermost layer exhibits the greatest amount of breakage due to the combined monotonic load and stress concentration [Figure 5.16(d)]. The breakage in the underlying layers reduces by 50.2% and 38%, in the central and bottom layers respectively, when compared to the corresponding layers in Test 1. The high stress in the geocell pocket is reflected by the high average failure strength of 1,536 kPa. Overall, placing the geocell at the base level leads to

a reduction in breakage of 29.7%. Strength increases due to the use of the geocell, with placement of the geocell at the base exhibiting the greatest strength gain.



Table 5.6 Ballast breakage and failure strength results categorized by layers under monotonic loading.

Test	Layer (mm)	By layer				Ballast box model			
		Number of Breakages	Breakage reduction	Average failure strength (kPa)	Strength increase	Number of Breakages	Breakage reduction	Average failure strength (kPa)	Strength increase
1	200–300	828		1390		1,436	NA	1,165	NA
	100–200	237	NA	1063	NA				
	0–100	371		1044					
2	200–300	688	16.9%	1481	6.58%	1,010	29.7%	1,288	10.5%
	100–200	121	48.9%	1214	14.20%				
	0–100 (reinforced)	201	45.8%	1171	12.10%				
3	200–300	823	0.6%	1479	6.45%	1,218	15.2%	1,284	10.2%
	100–200 (reinforced)	164	30.8%	1279	20.39%				
	0–100	231	37.7%	1095	4.86%				
4	200–300 (reinforced)	941	–13.6%	1536	10.53%	1,289	10.2%	1,261	8.2%
	100–200	118	50.2%	1151	8.29%				
	0–100	230	38.0%	1097	5.08%				

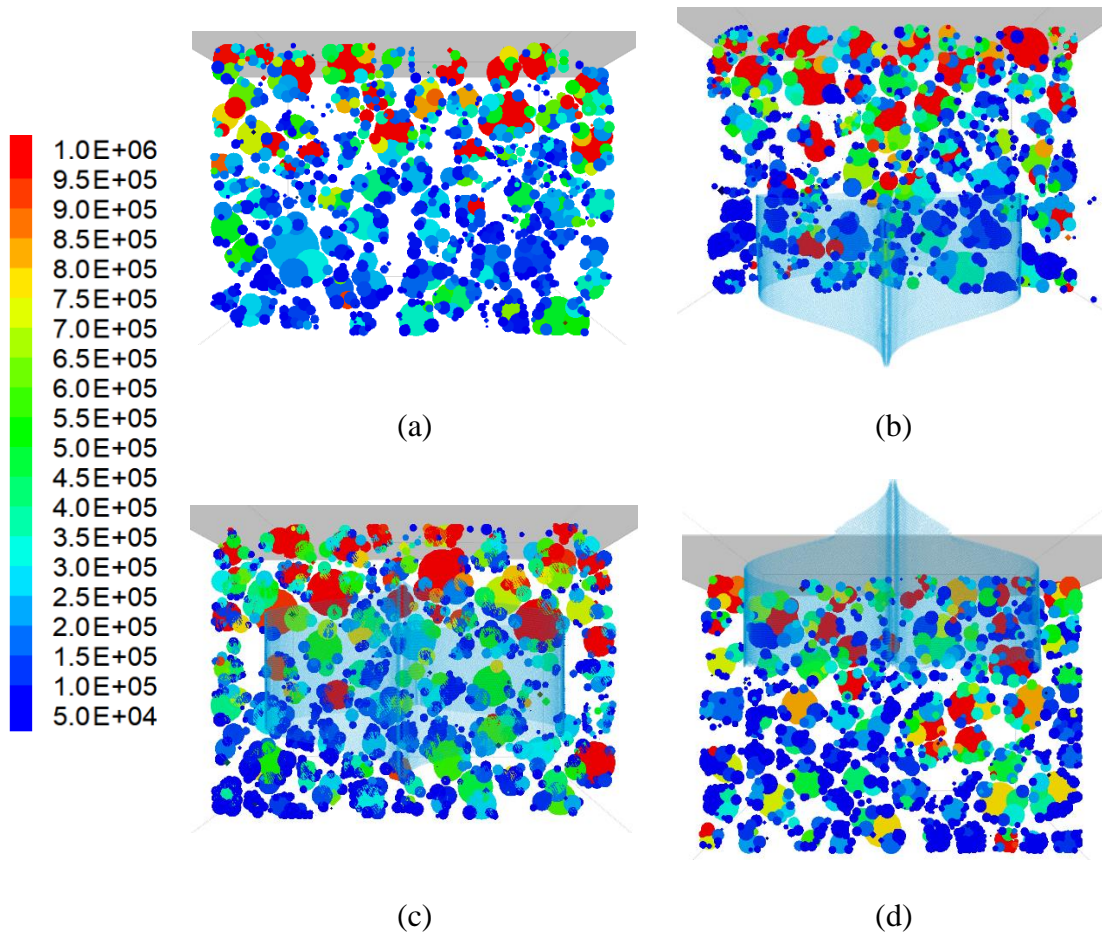


Figure 5.16 Contact force distribution on a cross-section beneath the sleeper centre: (a) Test 1: geocell unreinforced, (b) Test 2: geocell on the base, (c) Test 3: geocell placed 100 mm above the base, and (d) Test 4: geocell placed 200 mm above the base.

Figure 5.17 illustrates the location distribution of ballast breakage, which is represented by failure planes (disks), and categorized by the ballast shapes defined in Table 5.1. The sizes of the failure planes are scaled based on the radius of the broken-off particle and, hence, a large failure plane corresponds to a large sphere that has broken off from a ballast cluster. For all of the model tests, most of breakage occurs near the sleeper where the ballast is subjected to the major monotonic load. It should be noted that the clustered failure planes indicate the occurrence of multiple breaks in one ballast

particle. Conversely, scattered failure planes indicate minor ballast breakage, which suggests corner breakage due to the angular nature of the ballast.

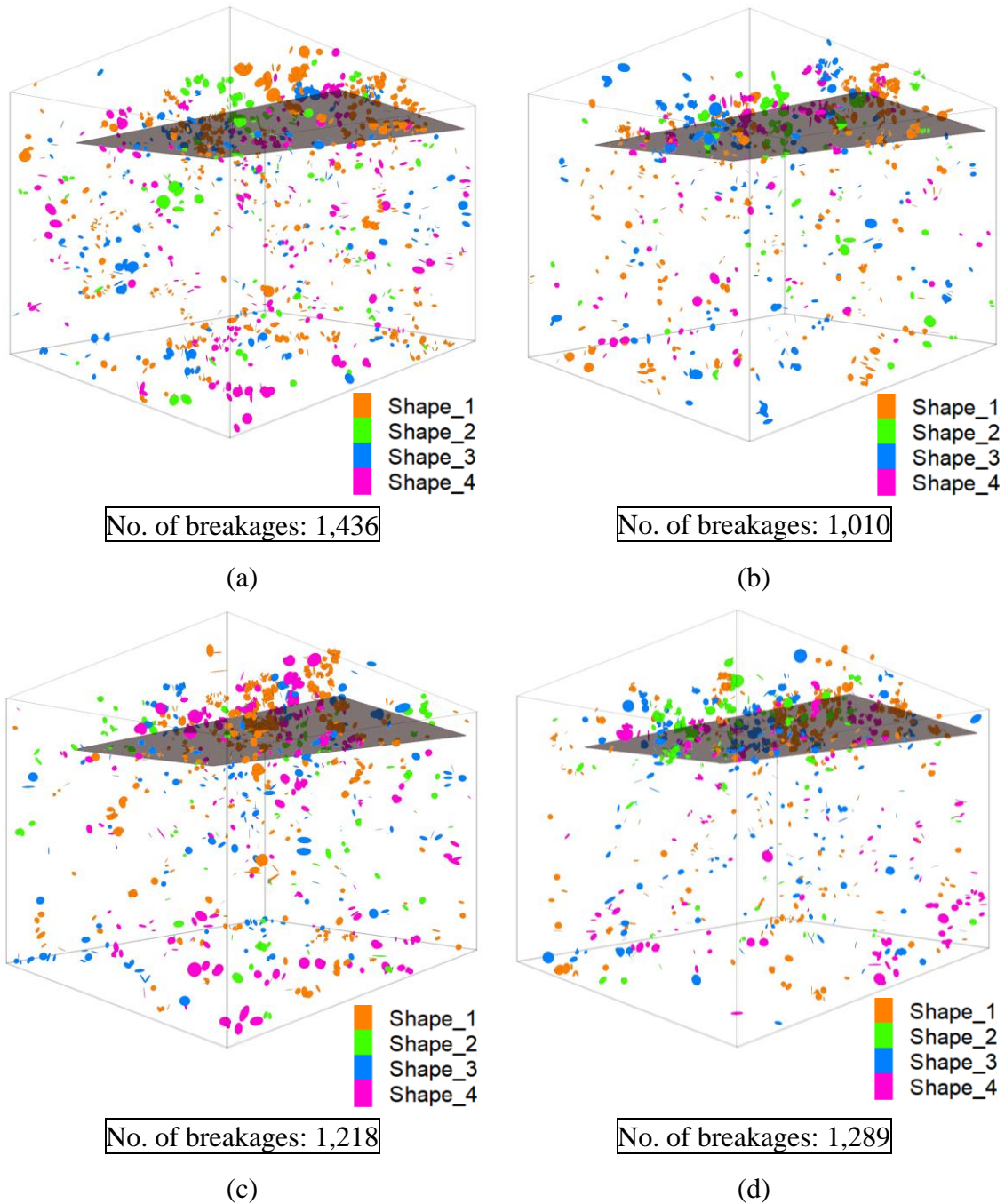


Figure 5.17 Distribution of ballast breakage under monotonic loading: (a) Test 1: unreinforced, (b) Test 2: geocell on the base, (d) Test 3: geocell placed 100 mm above the base, and (d) Test 4: geocell placed 200 mm above the base.

The ballast breakage results are further categorized by the ballast shapes and test models, as summarized in Table 5.7. Shape 1 experiences the greatest number of breakages on average, which as expected is due to its high angularity. The finer spheres at the sharp corners are more vulnerable to breakage as a result of their lower bond strength. A significant breakage reduction is shown in the other three ballast shapes. Shape 2, being the roundest and least angular, shows the least number of breakages. Similar breakage characteristics are observed with Shapes 3 and 4, albeit Shape 4 is more angular than Shape 3. A likely reason for this is that Shape 4 is flat and hence there are more inter-ballast contacts with the surrounding ballast. In addition, all ballast shapes show similar failure strength, independent of their geometrical characters and angularity. This outcome agrees with the point load test carried out in the calibration stage described earlier.

Table 5.7 Ballast breakage results categorized by ballast shape and test model under monotonic loading.

Shape	Behavior	Test model				Average
		1	2	3	4	
1	No. of Breakages	694	482	607	556	585
	Avg. failure strength (kPa)	1,169	1,272	1,319	1,254	1,254
	Avg. breakage dia. (mm)	4.88	5.21	6.53	7.61	6.06
2	No. of Breakages	173	147	164	218	176
	Avg. failure strength (kPa)	1,161	1,248	1,305	1,273	1,247
	Avg. breakage dia. (mm)	5.05	5.34	7.21	9.28	6.72
3	No. of Breakages	259	212	193	265	232
	Avg. failure strength (kPa)	1,263	1,302	1,309	1,272	1,287
	Avg. breakage dia. (mm)	4.34	5.12	6.91	8.28	6.16
4	No. of Breakages	310	169	254	250	246
	Avg. failure strength (kPa)	1,201	1,332	1,205	1,246	1,246
	Avg. breakage dia. (mm)	4.28	5.11	5.23	7.58	5.55

#### 5.4.1.3 Geocell response

Figure 5.18 shows the deformation magnitudes, drawn at the same scale, for the geocell pockets in the three reinforced model tests. The geocell in Test 2 experiences deformation with an average tensile strain of 9.7%, especially at its base due to the restricted ballast movement at this location. In addition, as shown on Figure 5.18(a), the cell-wall to the right deforms laterally, which leads to tensile ruptures in the cell-wall, as shown in Figure 5.19(a). The red disks in Figure 5.19(a) indicate the orientations and diameters of the failure planes. The ballast movement highlighted previously in Figure 5.14(c), pushes the cell-wall to expand and stretch under tensile force. The surrounding ballast (i.e. outside of the geocell pocket) cannot withstand the expansion of the cell-wall and hence it eventually exceeds its tensile strength. Furthermore, the geocell junction also experiences minor failure as a result of ballast penetration. In Test 3, no evident deformation was observed in the geocell pocket, other than vertical displacement along with the ballast settlement, reflected by the least average tensile strain of 8.8%. In Test 4, the geocell pocket experienced the greatest deformation with an average tensile strain of 12.6%. As shown in Figure 5.19(b), the top and bottom edges of the geocell pocket experience shear ruptures under monotonic loading. Figure 5.14(e) illustrates the contributing factor of the bottom ruptures, which is the reduced ballast movement in the layers beneath the reinforced section. As the sleeper displaces into the top ballast layer, the geocell pocket is forced to settle. However, the small contact interface between the base of the geocell and the ballast reduces the deformation of the underlying ballast. As the sleeper compresses further, the high contact pressure induces noticeable deformation in the bottom edge of the geocell resulting in the occurrence of the shear ruptures. Similar ruptures occur at the geocell top edge.

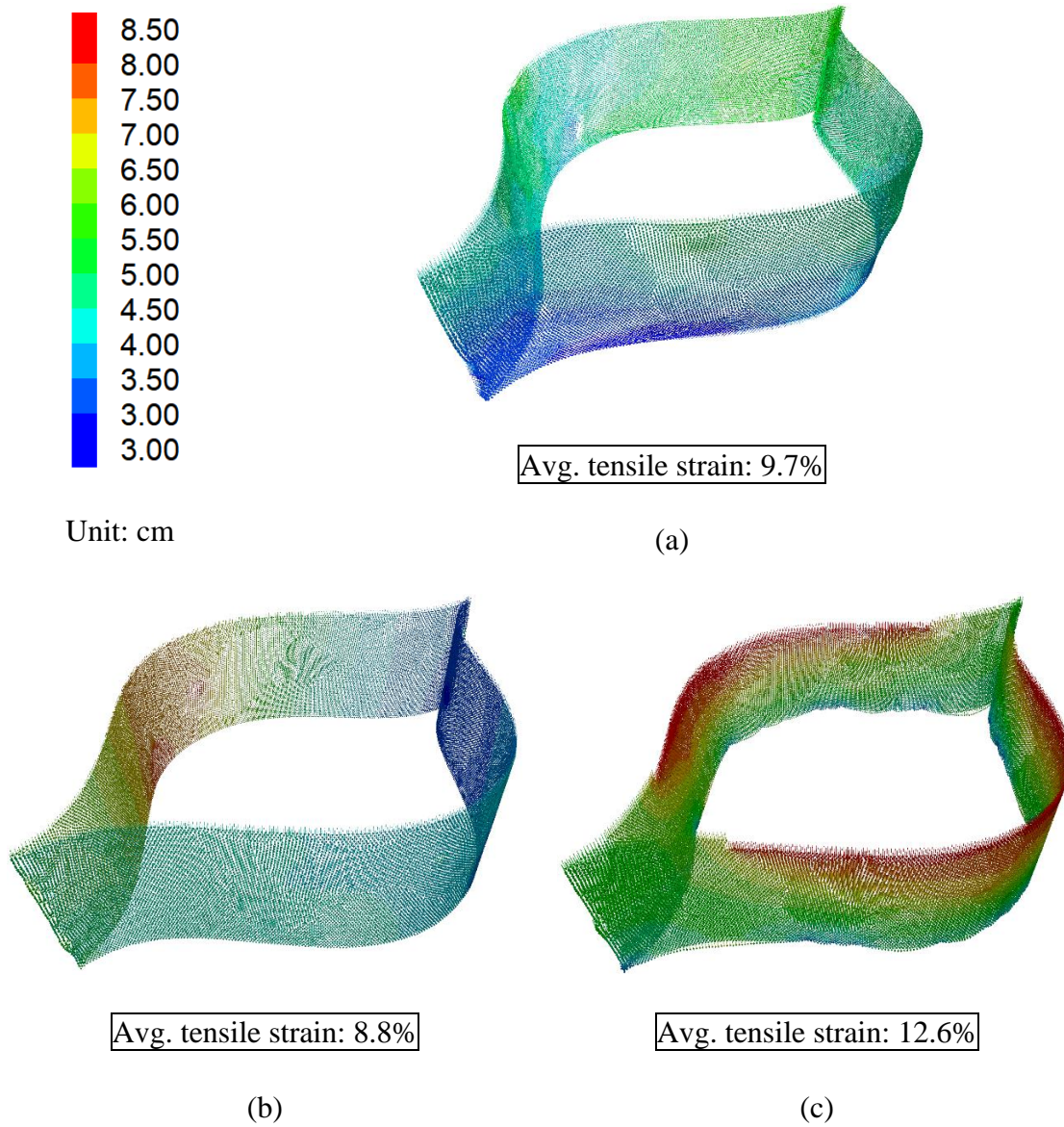


Figure 5.18 Deformation and displacement of geocell pocket under monotonic loading:  
(a) Test 2: geocell on the base, (b) Test 3: geocell placed 100 mm above the base, and (c)  
Test 4: geocell placed 200 mm above the base.



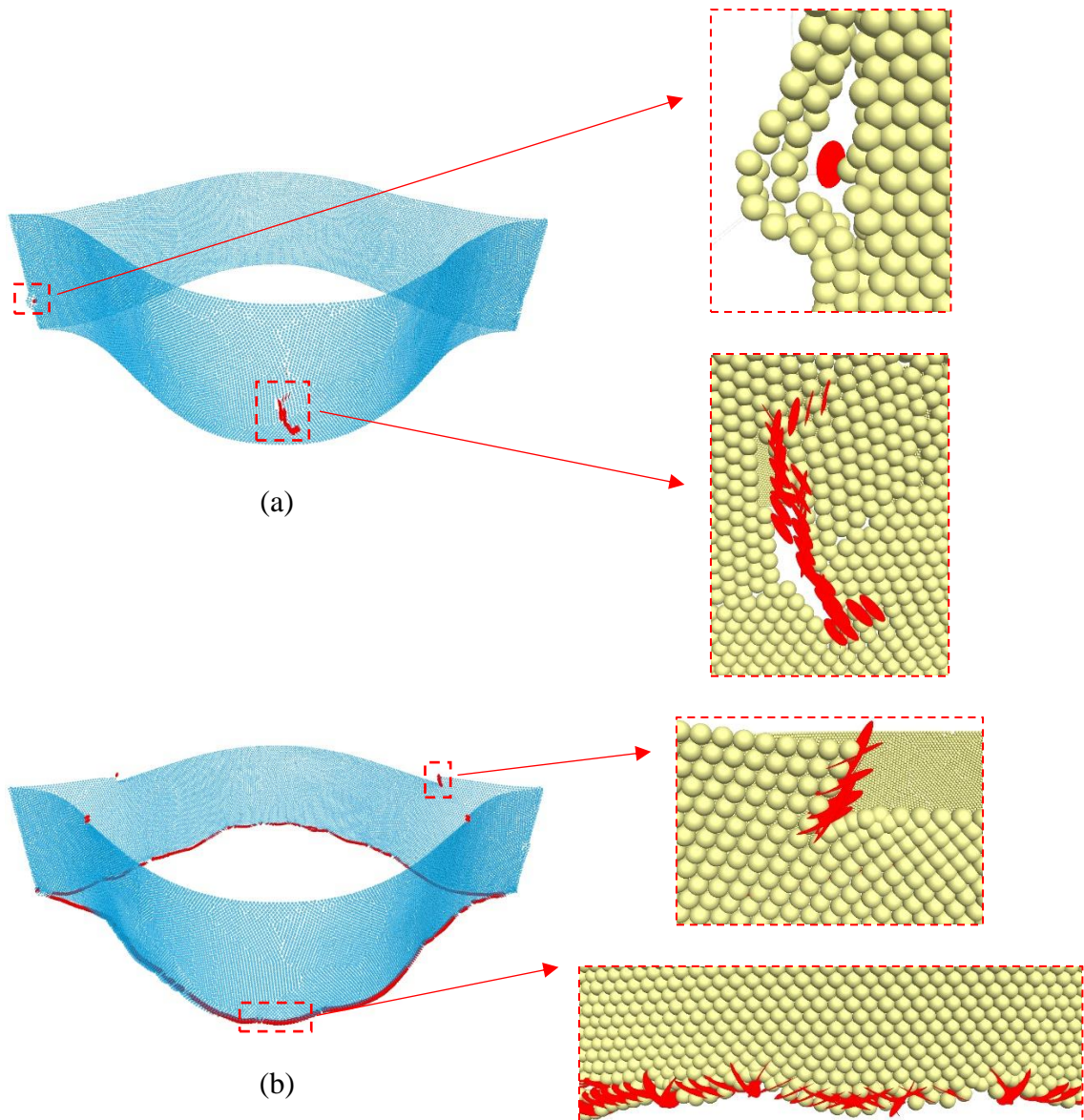


Figure 5.19 Locations of geocell rupture: (a) Test 2: geocell on the base, and (b) Test 4: geocell placed 200 mm above the base.

## 5.4.2 Cyclic loading

### 5.4.2.1 Settlement

The cyclic loading scenario is important in assessing the long-term performance of the geocell and the reinforced ballast. Figure 5.20 shows the relationships between settlement and the number of cycles of the four model tests. The relationships are displayed using a logarithmic scale to account for the large number of cycles. Overall,

the reinforced model tests consistently outperform the unreinforced model over the entire range of cycles examined. For all model tests, the majority of the settlement occurred within the first 1,000 cycles, which is in agreement with previous studies (Leshchinsky & Ling, 2013a; Ngo et al., 2017). As was undertaken with the monotonic load tests, the settlement versus load cycle relationships are again subdivided into three zones: A, from cycles 1 to 10; B, from cycles 10 to 1,000; and C, from cycles 1,000 to 20,000. In Zone A, the reinforced models experience significantly reduced settlement than that exhibited in the unreinforced model (Test 1), demonstrating the benefit of the geocell reinforcement. Greater than 50% settlement reduction (the average reduction within each region) is obtained across all reinforced model tests. This performance agrees with the results obtained in the monotonic loading scenario described earlier. Within Zone A, all model tests exhibit small settlement rates, while Tests 1 and 4 settle faster at the end of Zone A. The settlement increases when all curves enter Zone B. The settlement of Test 2 is more pronounced when compared with that of the other three models, with Tests 3 and 4 yielding an average settlement reduction of 35% and 44%, respectively. The values demonstrate the value of the geocell in reducing settlement as a consequence of cyclic loading. Overall, placing the geocell 200 mm above the base provides the best performance with respect to cyclic loading, attaining a settlement reduction of 27% by the end of the test. In comparison, the reduction rate for model Test 3 is 12% and 3% for model Test 2.



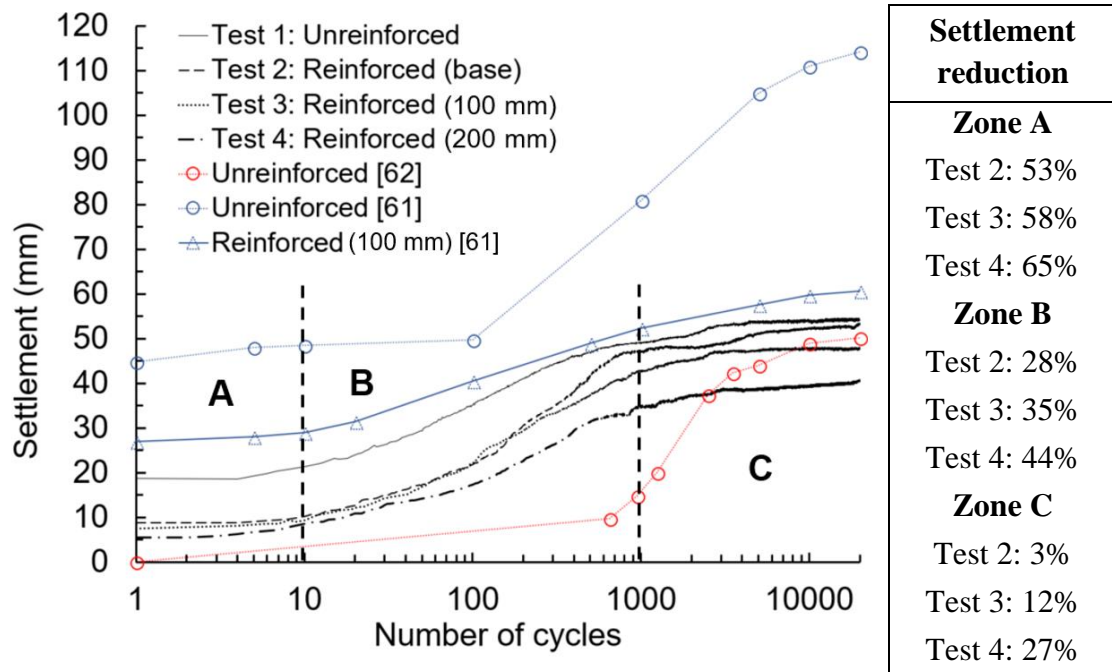


Figure 5.20 Settlement versus number of cycles relationships: (a) Test 1: unreinforced, (b) Test 2: geocell on the base, (d) Test 3: geocell placed 100 mm above the base, and (d) Test 4: geocell placed 200 mm above the base.

The settlement response obtained by Leshchinsky and Ling (2013a) and Satyal et al. (2018) are included in Figure 5.20 for comparison. Leshchinsky and Ling (2013a) applied cyclic loading to a pilot-scale, geocell-reinforced ballast embankment and examined the response of the embankment and Satyal et al. (2018) conducted finite element analysis (FEA) on a full-scale railway structure. As shown in Figure 5.20, there is a discrepancy in the unreinforced cases between the current study and the results of Leshchinsky and Ling (2013a). This is contributed to by the unconfined nature of their ballast embankment, in which the ballast can move freely in both the longitudinal and transverse directions. Additionally, differences in ballast gradation also added to the discrepancy. The current study uses the gradation with a  $D_{50}$  of 42.5 mm, while that adopted by (Leshchinsky & Ling, 2013a) was 15.5 mm. In comparison with the FEA

results, the disagreement in settlement mainly exists in the first 10,000 cycles, where the FEA yielded significantly lower settlement when compared with the current study. Also, the settlement responses are different between these two studies where, as discussed previously, most of the settlement occurred within the first 1,000 cycles in the current study. Whereas, minimal settlement ( $< 8\text{mm}$ ) was recorded in the first 700 cycles in the FEA simulation, and this was followed by a dramatic increase, resulting in a similar final settlement ( $< 3\text{mm}$  difference), when compared with the current study. For the reinforced case (placing the geocell 100 mm above the base), the main discrepancy exists in the early stage of the tests, reflected by an approximate 20 mm difference in settlement after the first load cycle. However, the difference becomes less evident towards the end of both tests, while the experimental, reinforced-prototype exhibited much greater improvement. Apart from the differences in boundary conditions and particle gradation, the geocell material contributes to the settlement discrepancy. Leshchinsky and Ling (2013a) adopted a Novel Polymetric Alloy (NPA) geocell with higher stiffness and tensile strength (27 MPa), compared with the typical HDPE geocell (Yang et al., 2012) used in the present study. The considerably higher material strengths adopted by [61] reduce the embankment vertical displacement.

#### 5.4.2.2 Ballast breakage characteristics

The number of ballast breakages versus the number of cycles for all model tests are provided in Figure 5.21, in which all curves are subdivided into 4 zones: A, from cycles 1 to 10; B, from cycles 10 to 3,000; and C, from cycles 3,000 to 18,000; and D, from cycle 18,000 to 20,000. For each of the model tests, the number of breakages in Zone A remains largely constant. In Zone B, the number of breakages in each of the models increases, which mainly arises from the internal stress build-up. As expected, the

unreinforced model exhibits the most breakages throughout the period of cycles examined. The three reinforced models exhibit a similar number of ballast breakages at the end of Zone B. Subsequently, into Zone C, the reinforced models exhibit noticeable deviation in the number of breakages until the end of each test, with Tests 2 and 4 experiencing greater breakage rates than Test 3. Within the same zone, in the unreinforced model, the number of breakages increases at a reduced rate. For all reinforced models, after approximately the 18,000<sup>th</sup> load cycle (i.e. Zone D), the number of breakages rapidly increases until the end of each test. This is attributed to the internal contact stresses (as a result of the denser assemblies) reaching the strength limits of some of the parallel-bonded spheres, while these particular bonds had already ruptured in the unreinforced model.

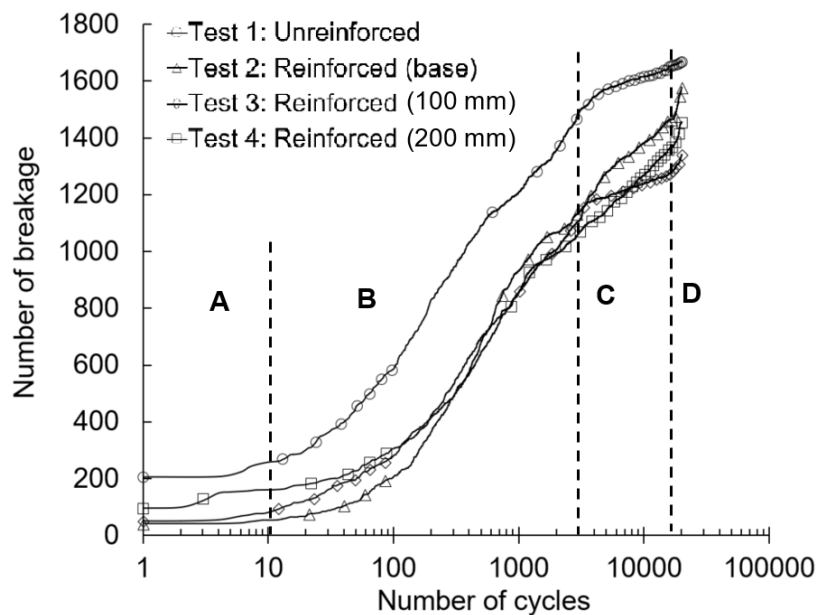


Figure 5.21 Number of breakages versus number of cycles.

As for the monotonic loading scenario, the breakage results are categorized by ballast layers and model tests, as summarized in Table 5.7. Compared to the monotonic loading

situation, the ballast breakages are more evenly distributed across the three layers of interest. Similar distributions of uniform ballast breakage are illustrated in Figure 5.22. The uniform distribution is caused by the lower cyclic load acting on the ballast, whereas under monotonic loading, the applied load is much greater. In Tests 2 and 3, the ballast in the respective geocell-reinforced layers fracture less often than the ballast in the unreinforced layers of the same test. In Test 2, however, the geocell-reinforced layer does not perform as well as its counterpart in the monotonic loading case; resulting in only a 15.5% reduction in ballast breakage, with no increase in failure strength.

Table 5.8 Ballast breakage and failure strength results categorized by layers under cyclic loading.

Test	By layer					Ballast chamber model			
	Layer (mm)	Number of breakages	Breakage reduction	Avg. failure strength (kPa)	Strength increase	Number of breakages	Breakage reduction	Avg. failure strength (kPa)	Strength increase
1	200–300	598		933		1,668	NA	982	NA
	100–200	388	NA	1,012	NA				
	0–100	682		1,001					
2	200–300	780	–30.4%	928	–0.6%	1,577	–5.5%	994	1.2%
	100–200	264	32.0%	1,056	4.4%				
	0–100 (reinforced)	576	15.5%	997	–0.4%				
3	200–300	614	–2.7%	971	4.1%	1,338	–19.8%	1,007	2.6%
	100–200 (reinforced)	257	33.8%	1,028	1.5%				
	0–100	467	31.5%	1,023	2.2%				
4	200–300 (reinforced)	790	–32.1%	991	6.2%	1,452	–12.9%	1,011	3.0%
	100–200	238	38.7%	993	–1.9%				
	0–100	424	37.8%	1,049	4.8%				

For each of the reinforced cases, the ballast in the uppermost layer (200–300 mm) rupture more often than those in the lower layers, independent of the geocell embedment depth. In Tests 2 and 3, the geocell pockets enhance the stiffness of the layer of interest and reduce the corresponding number of breakages. Simultaneously, the geocell pockets restrict ballast movement and rearrangement in the top layers which result in stress concentrations and hence a greater number of breakages. In Test 4, as with monotonic loading, the stiffened top layer restricts stress propagation into the underlying layers, as a result, the stress concentrates in the top layer, resulting in 32.1% more ballast breakages and 6.2% higher average failure strength.

Overall, a slight failure strength increase is exhibited by the reinforced model tests. Placing the geocell 100 mm above the subgrade is the most optimal solution for mitigating ballast breakage, where the highest breakage reduction of 19.8% and strength increase of 2.6% are attained. Placing the geocell directly above the subgrade is less effective when the performance of the model under cyclic loading condition is assessed. In this situation, the improvement percentage is a breakage reduction of 5.5% and a 1.2% failure strength increase.

At end of each test, the final PSDs were examined for all model tests, as shown in Table 5.9. The final PSDs agree with the number of breakages recorded for each test, which is reflected by the evident shifts in each curve. Besides having the least number of breakages, Test 3 performed best in preventing the ballast breaking down into finer particles which, as

mentioned previously, is the most common source of ballast fouling (Selig & Waters, 1994).

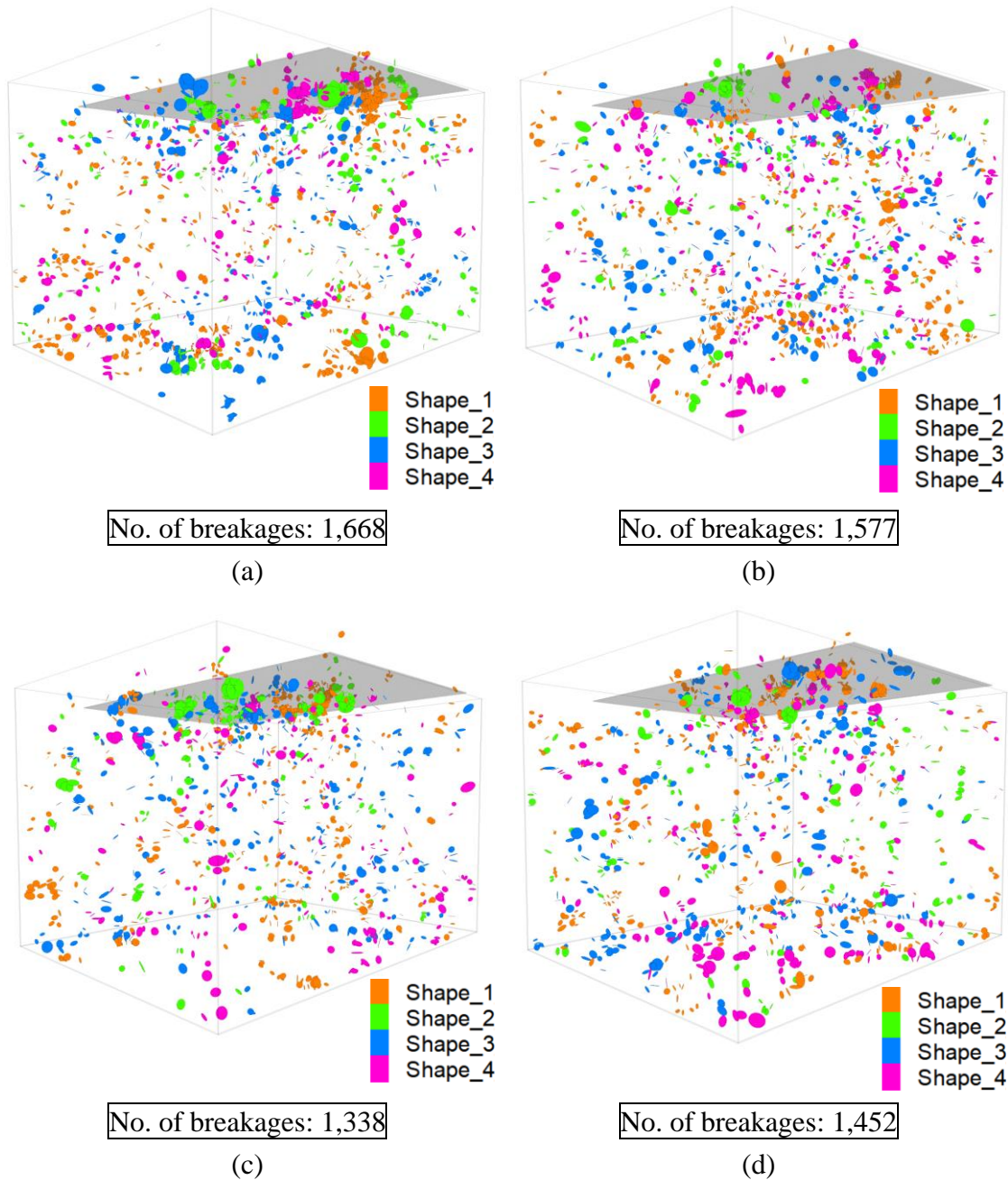
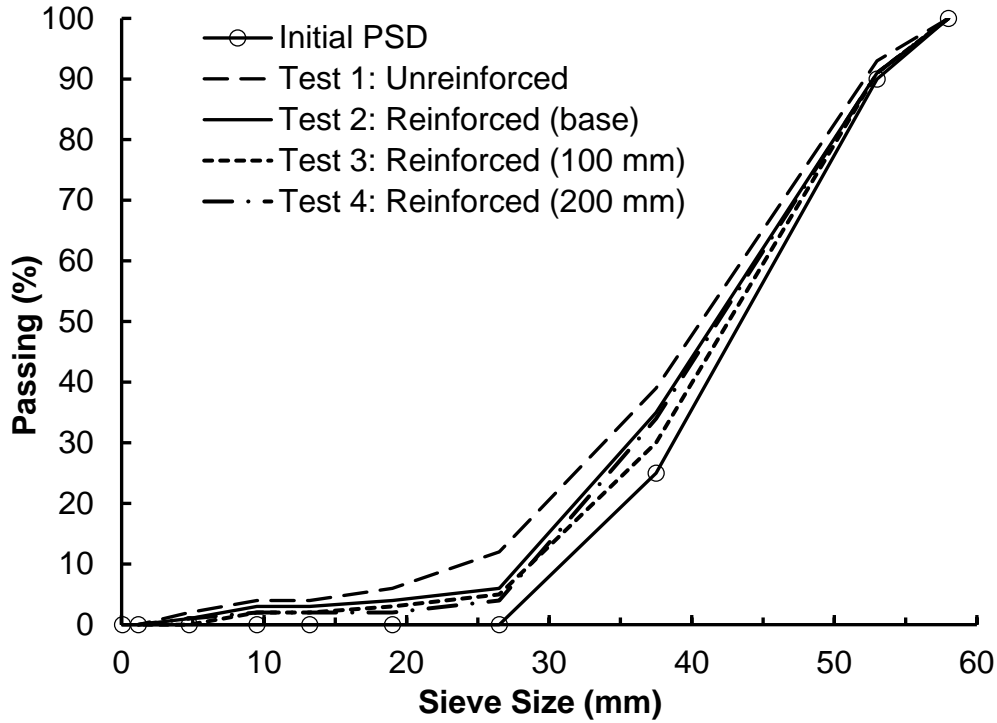


Figure 5.22 Distribution of ballast breakage under cyclic loading: (a) Test 1: unreinforced, (b) Test 2: geocell on the base, (d) Test 3: geocell placed 100 mm above the base, and (d) Test 4: geocell placed 200 mm above the base.

Table 5.9 Final particle size distributions.



Sieve Size (mm)	Initial	Test 1	Test 2	Test 3	Test 4
58	100	100	100	100	100
53	90	93	91	91	91
37.5	25	39	35	30	34
26.5	0	12	6	5	4
19	0	6	4	3	2
13.2	0	4	3	2	2
9.5	0	4	3	2	2
4.75	0	2	1	0	1
1.18	0	0	0	0	0

As with monotonic loading, the ballast breakage results are categorized based on the ballast and model tests, as summarized in Table 5.10. The results agree well with those obtained with the monotonic loading. The number of breakages decreases along with decrease in angularity. The Shape 1 ballast exhibited the greatest number of breakages, with 36–52%



more ruptures than the other ballast shapes. In addition, the Shape 1 ballast resulted in the smallest breakage diameter (i.e. failure plane) on average, which indicates a major proportion of corner breakage. This phenomenon is further validated by the lowest average failure strength (964 kPa) for Shape 1. The other ballast shapes, however, result in, on average, larger breakage diameters. The Shape 2 ballast experiences the least number of breakages, owing to its more rounded surface. It should be noted that the average ballast strengths of all of the four shapes are noticeably lower than their counterparts when subjected to monotonic loading. This is because the broken-off spheres are of smaller diameters, which as expected is due to the significantly lower loading magnitude applied in the cyclic loading condition.

Table 5.10 Ballast breakage results categorized by ballast shape and test model under cyclic loading.

Shape	Behavior	Test				Average
		1	2	3	4	
1	No. of Breakages	575	636	520	548	570
	Avg. failure strength (kPa)	985	954	1,003	996	964
	Avg. breakage dia. (mm)	2.88	3.05	3.07	3.08	3.02
2	No. of Breakages	328	298	203	261	273
	Avg. failure strength (kPa)	946	1,001	956	952	985
	Avg. breakage dia. (mm)	3.53	3.68	3.84	3.97	3.76
3	No. of Breakages	408	305	285	242	310
	Avg. failure strength (kPa)	1,016	1,022	1,086	1,029	1,038
	Avg. breakage dia. (mm)	3.72	3.78	3.83	3.8	3.78
4	No. of Breakages	357	381	330	401	367
	Avg. failure strength (kPa)	982	998	984	969	983
	Avg. breakage dia. (mm)	3.74	3.78	3.96	3.65	3.77

#### 5.4.2.3 Geocell response

The responses of the geocell, in terms of displacement and deformation, are examined at the end of the cyclic loading tests, for all reinforced models, and these are presented in Figure 5.23. In Test 2, the geocell pocket experiences more localized deformation on the lower left-hand side. The local deformation results in a minor rupture at the place of concern. The remaining areas of the geocell experience minimal deformation, i.e. the lowest average tensile strain of 4.3%, and remain in a serviceable condition. No rupture is observed in either the cell-wall nor the junction components of the geocell in Tests 3 and 4. The two test models, however, exhibit relatively large deformation, particularly on the

right-hand side of the respective pockets. The ballast tends to move to one side, resulting in higher average tensile strains of 5.1% and 6.2%, respectively.

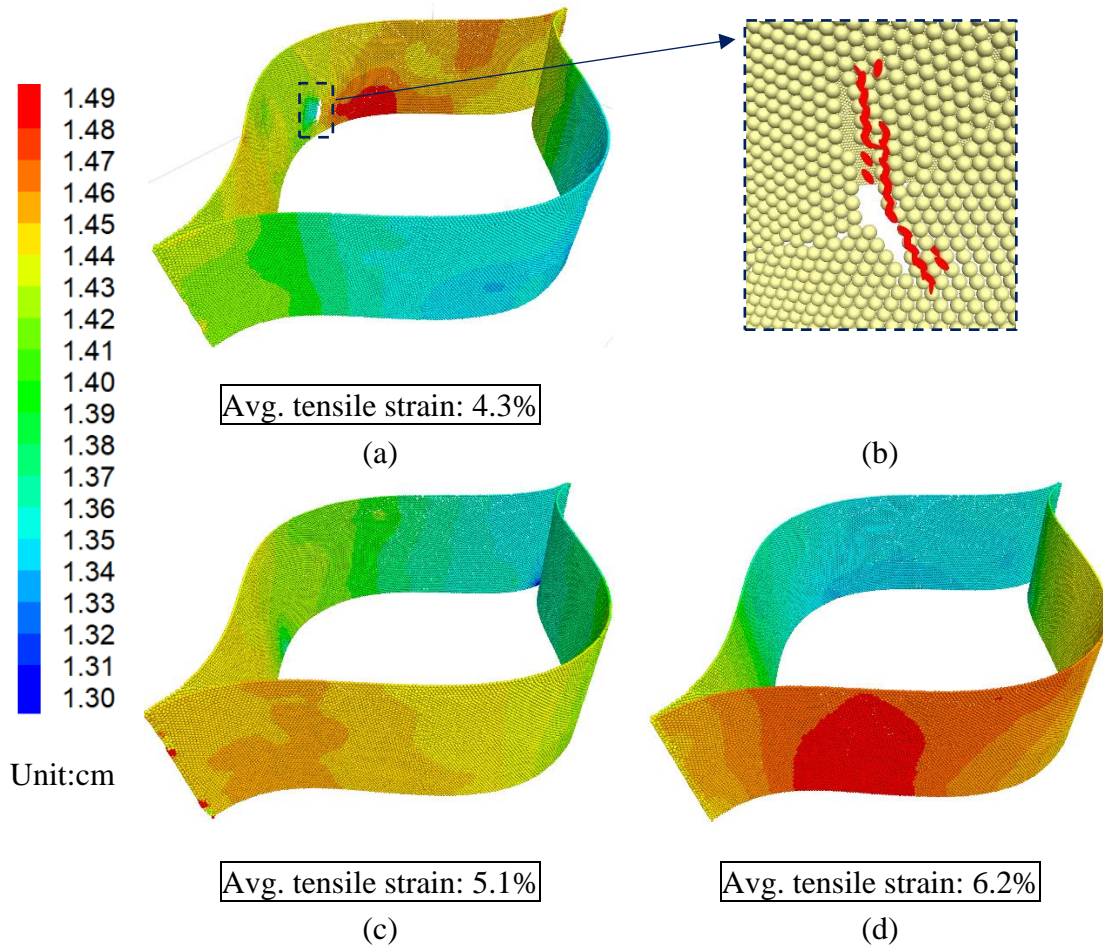


Figure 5.23 Geocell displacement and deformation contours under cyclic loading drawn at the same scale: (a) Test 1: unreinforced, (b) Test 2: geocell on the base, (c) Test 3: geocell placed 100 mm above the base, and (d) Test 4: geocell placed 200 mm above the base.

## **5.5 Conclusions**

This study examines the mechanical behavior of geocell-reinforced railway ballast using the discrete element method (DEM). The ballast is modeled as being breakable and in typical angular shapes. The DEM micro-properties are calibrated based on a series of laboratory tests performed on the ballast and geocell sample materials. The tests include unconfined compressive and point load tests on the ballast, uniaxial tensile strength tests on the cell-wall and seam strength tests on the junction. The ballast chamber models are subjected to the monotonic and cyclic loading. The cyclic loading is continued to 20,000 cycles. From the two load tests, the performance of the geocell in term of reinforcing the ballast is examined. The performance includes assessing ballast settlement, geocell responses, and ballast breakage characteristics. The breakage characteristics include the number of breakages, location distributions, failure strength, breakage diameters and shape effects. Results are compared to those obtained in previous studies. The following conclusions are drawn:

1. From the application of monotonic loading, placing the geocell 200 mm above the base outperforms other model tests with respect to settlement reduction. Placing the geocell directly on the base, however, reduces ballast breakage to the greatest extent.
2. Under monotonic loading, the geocell can effectively reduce the number of ballast breakages and help increase the strength of the reinforced layer if the geocell is placed at the base or 100 mm above. Placing the geocell directly beneath the sleeper reduces the number of breakages in the underlying layers, but increases them in the reinforced layer.

3. Under monotonic loading, placing the geocell 200 mm above the base consistently performs best, reducing settlement by 24% and 15% relative to placing the geocell on the base and 100 mm above the base, respectively. Meanwhile, placing the geocell 100 mm above the base achieves the better performance in breakage reduction by 6.9% compared with placing the geocell 200 mm above the base. Overall, placing the geocell 200 mm above the base is the optimal location where settlement and ballast breakage are concerned. The use of a deeper geocell or a double-layer system may improve settlement and breakage characteristics simultaneously, but these are beyond the scope of the present study and hence require further examination.
4. Ballast shape plays an important role in governing breakage. Ballast with major angularities rupture more, and vice versa. The sharper corners of the ballast are vulnerable to breakage, leading to the small fractures. Rounded ballast exhibits better performance with respect to minimizing breakage.
5. The geocell experiences local failures under both monotonic and cyclic loading. The material is subjected to more damage when the geocell is placed on the base. The center of the cell-wall component is more vulnerable to the failure and where ruptures are more likely to occur. The cell-wall junction was shown to be strong and does not debond. However, minor, local debonding occurs when the geocell is placed on the base and subjected to monotonic loading.

## **Chapter 6. Conclusions**

---

**INTENTIONALLY BLANK**

## **6.1 Research Contributions**

In accordance to the research aims discussed in Section 1.3, this research aim to gain a better understanding on behaviour of geocell-reinforced ballast and the failure mechanism to promote its application in railway engineering. Specifically, the following research contributions are made:

1. Chapter 3 (Paper 1) assesses the use of geocells in reinforcing railway ballast embankments and a DEM simulation framework is developed. Clumped particles are used to simulate angular ballast, to evaluate bearing capacity, vertical displacement and lateral spreading of the embankment, as well as providing insights into the micro-behaviour of the ballast infill and the geocell, including contact forces and displacements. Straight and curved embankments have been subjected to monotonic and cyclic loading conditions and the modelling results have been compared with previous, published test results. This research paper establishes the foundation for the subsequent numerical study conducted in Paper 3; a more realistic geocell-reinforced model in which ballast breakage can be captured.
2. Chapter 4 (Paper 2) assesses the failure mechanisms of geocells when subjected to various load types. An extensive experimental program, which involved six test schemes, are conducted on the cell-walls and welded junctions of the geocell. For cell-walls, short-term uniaxial tensile load and long-term gravitational load are applied to assess its tensile capacity and creep behaviour, while the junctions are subjected to four loading types: uniaxial tension; shear; peeling; and splitting. The stresses and



elongation of the samples are recorded to evaluate the peak strength, and the behaviours of both the cell-wall and junctions in the elastic and plastic regions. The implications for the field application of geocells are derived from observing various failure patterns. Finally, a ductility ratio is developed to measure the failure rapidness of geocell cell-walls and junctions under different loading conditions.

3. Chapter 5 (Paper 3) examines the mechanical behaviour of geocell-reinforced railway ballast using the discrete element method (DEM). This paper adopts the framework developed in Paper 1 while introducing realistic geocell configuration and ballast breakage. The ballast is modelled as being breakable and in typical angular shapes. The DEM micro-properties are calibrated based on a series of laboratory tests performed on the ballast and geocell sample materials, including unconfined compressive and point load tests on the ballast, uniaxial tensile strength tests on the cell-wall and seam strength tests on the junction. The ballast chamber models are subjected to the monotonic and cyclic loading. The cyclic loading adopts a large number of load cycles of 20,000 cycles to reflect the in-field loading condition. For both monotonic and cyclic load cases, the performance of geocell-reinforced ballast chamber is assessed which includes assessing ballast settlement, geocell responses, and ballast breakage characteristics. The breakage characteristics include the number of breakages, location distributions, failure strength, breakage diameters and shape effects.

## **6.2 Limitations and Recommendations**

Whilst this research proposes a valid approach to demonstrate and examine the mechanical responses of geocell-reinforced railway ballast on both macro and micro levels, a number of limitations were adopted to undertake successfully the DEM simulation:

1. The geocell cell-wall model was calibrated solely against a series of tensile strength tests and the geocell junction model was calibrated solely against seem strength test. Other properties such as puncture resistivity, flexural stiffness and torsion stiffness were not considered in the current study. Future research may consider incorporating these material properties in the geocell model to improve the simulation accuracy.
2. Whilst the use of clumps (Paper 1) and clusters (Paper 3) provides a more accurate representation of ballast angularity, when compared with the adoption of entirely spherical particles, their shape does not fully reflect actual ballast angularities and, hence, have limited capability to simulate accurately ballast interlock and inter-particle friction. Along with the advancement in computational technology, it is recommended that more refined and complex clump or cluster models can be used in future research to achieve a more realistic simulation of the inter-ballast and ballast-geocell interactions.
3. Compromises are made in the DEM simulations to optimise the computational effort. In Paper 1, non-breakable clumps are used to simulate scaled-down ballast embankments while a small ballast chamber is used in Paper 3 in order to incorporate

ballast breakage. Additionally, in both studies, the subgrade is simplified by using rigid walls with lower stiffnesses. These compromises may potentially impact the accuracy of the simulation hence prevents the field application of geocell in railway superstructure. Within a few years, modelling the entire engineering structure may become possible along with the advancement in computation (Cundall, 2001). Therefore, future research may attempt a full-scale simulation of a geocell-reinforced railway structure to improve the simulation accuracy so that the field application can be encouraged.

4. Although this research study has demonstrated the superiority of suspending geocell at 100mm and 200mm in mitigating ballasted-track deformation and ballast breakage compared to placing geocell directly above the subgrade, the current practices for track maintenance and new track installation can hinder the its field application. For example, the traditional tamping process is not possible if the geocell layer is placed directly under the sleeper. This limitation may be eliminated in the future along with advancement in the construction and maintenance methods.
5. The geocell-reinforced ballast models are only assessed against monotonic and cyclic loading conditions due to the limitation in the currently available DEM modelling techniques. Whereas, vibrations and other dynamic loads can be a contributing factor towards the deterioration of rail trackbed. Future study should take dynamic loading conditions into consideration once the becomes available in user-developed or commercially available DEM package. In addition, the studies presented in Chapter 3 and 5 both use fixed loading rates/frequencies for monotonic and cyclic loads, hence

rate-dependent behaviours are not parametrically assessed. Therefore, it is recommended that various loading rates/frequencies are to be considered in future study.

6. The failure mechanisms of geocell junctions are not assessed against long-term/creep and cyclic loading conditions, which are common in the field applications of geocell. The creep test carried out on cell-wall is not extensive (i.e. insufficient loading period and loading magnitudes, no cyclic loading condition). It is recommended that future research can carry out comprehensive creep analysis by applying static and cyclic loads to examine the long-term performance of geocell junctions.

**INTENTIONALLY BLANK**

## References

---

**ARTC. (2007).** ETA-04-01 Ballast Specification *Engineering (Track & Civil) Standard* (pp. 6). Australia: Australian Rail Track Corporation Ltd.

**ARTC. (2012).** Engineering (Track & Civil) Code of Practice - Section 4 Ballast (pp. 12). Australia: Australian Rail Track Corporation Ltd.

**ARTC. (2014).** Route Access Standard *General Information*. Australia: Australian Rail Track Corporation Ltd.

**ARTC. (2016a).** *Australian Rail Track Corporation 2016 Annual Report*. Retrieved from Australia:

**ARTC. (2016b).** Engineering (Track & Civil) Code of Practice - Section 5 Track Geometry. Australia: Australian Rail Track Corporation Ltd.

**ARTC. (2017).** Engineering (Track & Civil) Code of Practice - Section 2 Sleepers and Fastenings. Australia: Australian Rail Track Corporation Ltd.

**ARTC. (2018).** Common Interface Requirements WOS 01.200 *WOS 01.211 - Wheels, Design and Manufacture* (pp. 94): Australian Rail Track Corporation Limited (ARTC).

**ASTM. (1993).** *Geosynthetic Soil Reinforcement Testing Procedures* (Vol. STP1190). Philadelphia, United State: ASTM.

**ASTM. (1996).** Standard Test Method for Trapezoidal Tearing Strength of Geotextiles. *ASTM D4533 - 91*.

**ASTM. (2004).** Standard Test Method for Tensile Properties of Plastics *ASTM D638-03*. PA, US: ASTM International.

- 
- ASTM. (2010).** Standard Test Method for Density of Plastics by the Density-Gradient Technique *ASTM D1505 - 10*. PA, USA: ASTM.
- ASTM. (2016).** D5262-07 Standard Test Method for Evaluating the Unconfined Tension Creep and Creep Rupture Behavior of Geosynthetics: American Society for Testing and Materials, Pennsylvania, USA.
- Australia, S. (2015).** AS 2758.7 Aggregates and rock for engineering purposes - Part 7: Railway ballast (pp. 13). Sydney: SAI Global Limited.
- Becker, L. D. B., & Nunes, A. L. L. d. S. (2015).** Influence of soil confinement on the creep behavior of geotextiles. *Geotextiles and Geomembranes*, 43(4), 351-358.
- Bortz, B. S., Hossain, M., Halami, I., & Gisi, A. (2011). *Geocell-Reinforced Crushed Stone Base for Low-Volume Roads*. Paper presented at the Mid-Continent Transportation Research Symposium, Ames, Iowa.
- Chen, C., McDowell, G. R., & Thom, N. H. (2012a).** Discrete element modelling of cyclic loads of geogrid-reinforced ballast under confined and unconfined conditions. *Geotextiles and Geomembranes*, 35, 76–86.
- Chen, C., McDowell, G. R., & Thom, N. H. (2012b).** Discrete element modelling of cyclic loads of geogrid-reinforced ballast under confined and unconfined conditions. *Geotextiles and Geomembranes*, 35, 76-86.
- Chen, C., McDowell, G. R., & Thom, N. H. (2013).** A study of geogrid-reinforced ballast using laboratory pull-out tests and discrete element modelling. *Geomechanics and Geoengineering*, 8(4), 244-253.
- Chen, R.-H., Huang, Y.-W., & Huang, F.-C. (2013).** Confinement effect of geocells on sand samples under triaxial compression. *Geotextiles and Geomembranes*, 37, 35-44.

- Chen, R.-H., Wu, C.-P., Huang, F.-C., & Shen, C.-W. (2013a).** Numerical analysis of geocell-reinforced retaining structures. *Geotextiles and Geomembranes*, 39, 51-62.
- Chen, R. H., Wu, C. P., Huang, F. C., & Shen, C. W. (2013b).** Numerical analysis of geocell-reinforced retaining structures. *Geotextiles and Geomembranes*, 39, 51-62.
- Cheng, S. C. (1993).** *STP 1190 Geosynthetics Soil Reinforcement Testing Procedures*. Philadelphia, PA: American Society for Testing and Materials.
- Choi, B.-H., Weinhold, J., Reuschle, D., & Kapur, M. (2009).** Modeling of the fracture mechanism of HDPE subjected to environmental stress crack resistance test. *Polymer Engineering & Science*, 49(11), 2085-2091.
- Cowland, J. W., & Wong, S. C. K. (1993).** Performance of a road embankment on soft clay supported on a Geocell mattress foundation. *12*, 687-705.
- Cundall, P. A. (2001).** *A discontinuous future for numerical modelling in geomechanics*. Paper presented at the Proceeding of Institution of Civil Engineers: Geotechnical Engineering.
- Cundall, P. A., & Strack, O. D. L. (1979a).** A discrete numerical model for granular assemblies. *Géotechnique*, 29(1), 47-65.
- Cundall, P. A., & Strack, O. D. L. (1979b).** Discrete numerical model for granular assemblies. *Geotechnique*, 29(1), 41-65.
- Dapeng, L., Xiaohua, Y., & Zhengjun, M. (2013).** Research on the Effect of Geocell in Slope Reinforcement Using Anti-Slide Pile with Geocell. 1130-1132.
- Dash, S. K. (2012).** Effect of Geocell Type on Load-Carrying Mechanisms of Geocell-Reinforced Sand Foundations. *International Journal of Geomechanics*, 12(5), 537-548.



- 
- Dash, S. K., & Bora, M. C. (2013).** Improved performance of soft clay foundations using stone columns and geocell-sand mattress. *Geotextiles and Geomembranes*, 41, 26–35.
- Dash, S. K., Krishnaswamy, N. R., & Rajagopal, K. (2001).** Bearing capacity of strip footings supported on geocell-reinforced sand. *Geotextiles and Geomembranes*, 19, 235-256.
- Dash, S. K., Saride, S., & Thallak, S. G. (2007).** Performance of surface footing on geocell-reinforced soft clay beds. *Geotech Geol Engineering*, 25, 509-524.
- Dash, S. K., Sireesh, S., & Sitharam, T. G. (2003).** Model studies on circular footing supported on geocell reinforced sand underlain by soft clay. *Geotextiles and Geomembranes*, 21(4), 197-219.
- Group, I. C. (2008).** *PFC3D: Particle Flow Code in 3 Dimensions*. Minneapolis.
- Han, J., & Yang, X. (2012).** Geocell-reinforced granular fill under static and cyclic loading: A synthesis of analysis. *Geotechnical Engineering Journal of the SEAGS & AGSSEA*, 43(5), 18-24.
- Han, J., Yang, X. M., Leshchinsky, B. A., Parsons, R. L., & Rosen, A. (2008). *Numerical Analysis for Mechanisms of a Geocell-Reinforced Base Under a Vertical Load*. Paper presented at the 4th Asian Regional Conference on Geosynthetics, Shanghai, China.
- Hegde, A., & Sitharam, T. G. (2015a).** 3-Dimensional numerical modelling of geocell reinforced sand beds. *Geotextiles and Geomembranes*, 43(2), 171-181.
- Hegde, A., & Sitharam, T. G. (2015b).** 3-Dimensional numerical modelling of geocell reinforced sand beds. *Geotextiles and Geomembranes*, 43(2), 171–181.

- Hegde, A. M., & Sitharam, T. G. (2015c).** Three-dimensional numerical analysis of geocell-reinforced soft clay beds by considering the actual geometry of geocell pockets. *Canadian Geotechnical Journal*, 52(9), 1396-1407.
- Hossain, Z., Indraratna, B., Darve, F., & Thakur, P. K. (2007).** DEM analysis of angular ballast breakage under cyclic loading. *Geomechanics and Geoengineering*, 2(3), 175-181.
- Huang, H., Tutumluer, E., & Dombrow, W. (2009).** Laboratory Characterization of Fouled Railroad Ballast Behavior. *Transportation Research Record: Journal of the Transportation Research Board*, 2117, 93-101.
- Indraratna, B., Biabani, M. M., & Nimbalkar, S. (2015).** Behavior of Geocell-Reinforced Subballast Subjected to Cyclic Loading in Plane-Strain Condition. *Journal of Geotechnical and Geoenvironmental Engineering*, 141(1), 04014081.
- Indraratna, B., Ionescu, D., & Christie, D. (1998).** Shear Behavior of Railway Ballast Based on Large-Scale Triaxial Testt. *Journal of Geotechnical and Geoenvironmental Engineering*, 124(5), 439-449.
- Indraratna, B., Ionescu, D., & Christie, H. D. (1998).** Shear behavior of railway ballast based on large-scale triaxial tests. *Journal of Geotechnical and Geoenvironmental Engineering*, 124(5), 439-449.
- Indraratna, B., Lackenby, J., & Christie, D. (2005).** Effect of confining pressure on the degradation of ballast under cyclic loading. *Géotechnique*, 55(4), 325-328.
- Indraratna, B., Ngo, N. T., Rujikiatkamjorn, C., & Vinod, J. S. (2014).** Behavior of Fresh and Fouled Railway Ballast Subjected to Direct Shear Testing: Discrete Element Simulation. *International Journal of Geomechanics*, 14(1), 34-44.

- 
- Indraratna, B., & Nimbalkar, S. (2013).** Stress-Strain Degradation Response of Railway Ballast Stabilized with Geosynthetics. *Journal of Geotechnical and Geoenvironmental Engineering*, 139(5), 684-700.
- Indraratna, B., Nimbalkar, S., Christie, D., Rujikiatkamjorn, C., & Vinod, J. S. (2010).** Field Assessment of the Performance of a Ballasted Rail Track with and without Geosynthetics. *Journal of Geotechnical and Geoenvironmental Engineering*, 136(7), 907-917.
- Indraratna, B., & Salim, W. (2002).** Modelling of particle breakage of coarse aggregates incorporating strength and dilatancy. *Geotechnical Engineering*, 155(4), 243-252.
- Indraratna, B., Su, L.-j., & Rujikiatkamjorn, C. (2011).** A new parameter for classification and evaluation of railway ballast fouling. *Canadian Geotechnical Journal*, 48(2), 322-326.
- Indraratna, B., Thakur, P. K., & Vinod, J. S. (2010).** Experimental and Numerical Study of Railway Ballast Behavior under Cyclic loading. *International Journal of Geomechanics*, 10(4), 134-144.
- Indraratna, B., Vinod, J. S., & Lackenby, J. (2009).** Influence of particle breakage on the resilient modulus of railway ballast. *Géotechnique*, 59(7), 643-646.
- Irazábal, J., Salazar, F., & Oñate, E. (2017).** Numerical modelling of granular materials with spherical discrete particles and the bounded rolling friction model. Application to railway ballast. *Computers and Geotechnics*, 85(Supplement C), 220-229.
- Itasca. (2009a).** Particle Flow Code in Three Dimensions *Version 4*. Monnesota, USA: Itasca Consulting Group, Inc.

- Itasca. (2009b).** *PFC3D 4.0 User's Manual*. Minnesota, USA: Itasca Consulting Group, Inc.
- Knight, M. A., & Bathurst, R. J. (1998).** Analysis of geocell reinforced-soil covers over large span conduits. *Computer and Geotechnics*, 22(3/4), 205-219.
- Kwon, H. J., & Jar, P. Y. B. (2008).** On the application of FEM to deformation of high-density polyethylene. *International Journal of Solids and Structures*, 45(11-12), 3521-3543.
- Lackenby, J., Christie, D., Indraratna, B., & McDowell, G. (2007).** Effect of confining pressure on ballast degradation and deformation under cyclic triaxial loading. *Géotechnique*, 57(6), 527-536.
- Latha, G. M., Dash, S. K., & Rajagopal, K. (2009).** Numerical Simulation of the Behavior of Geocell Reinforced Sand in Foundations. *International Journal of Geomechanics*, 9(4), 143-152.
- Le Pen, L. M., Powrie, W., Zervos, A., Ahmed, S., & Aingaran, S. (2013).** Dependence of shape on particle size for a crushed rock railway ballast. *Granular Matter*, 15(6), 849-861.
- Leshchinsky, B., & Ling, H. (2013a).** Effects of Geocell Confinement on Strength and Deformation Behavior of Gravel. *Journal of Geotechnical and Geoenvironmental Engineering*, 139(2), 340-352.
- Leshchinsky, B., & Ling, H. (2013b).** Numerical modeling of behavior of railway ballasted structure with geocell confinement. *Geotextiles and Geomembranes*, 36, 33-43.
- Leshchinsky, B., & Ling, H. I. (2013c).** Numerical modeling of behavior of railway ballasted structure with geocell confinement. *Geotextiles and Geomembranes*, 36, 33-43.

- 
- Leshchinsky, B. A. (2012).** *Enhancing Ballast Performance using Geocell Confinement.* (Doctoral of Philosophy), Columbia University, New York, US.
- Li, H., & McDowell, G. R. (2018).** Discrete element modelling of under sleeper pads using a box test. *Granular Matter*, 20(2).
- Lim, W. L., & McDowell, G. R. (2005).** Discrete element modelling of railway ballast. *Granular Matter*, 7(1), 19-29.
- Liu, Y., Deng, A., & Jaksa, M. (2015).** *Discrete element modelling of geocell-reinforced track ballast under static and cyclic loading.* Paper presented at the Proc. The 12th Australia–New Zealand Conference on Geomechanics, Wellington, New Zealand.
- Liu, Y., Deng, A., & Jaksa, M. (2018).** Three-dimensional modeling of geocell-reinforced straight and curved ballast embankments. *Computers and Geotechnics*, 102, 53-65.
- Lu, M., & McDowell, G. R. (2006).** The importance of modelling ballast particle shape in the discrete element method. *Granular Matter*, 9(1-2), 69-80.
- Lu, M., & McDowell, G. R. (2008).** Discrete element modelling of railway ballast under triaxial conditions. *Geomechanics and Geoengineering*, 3(4), 257-270.
- Lu, M., & McDowell, G. R. (2010).** Discrete element modelling of railway ballast under monotonic and cyclic triaxial loading. *Géotechnique*, 60(6), 459-467.
- Madhavi Latha, G., & Rajagopal, K. (2007).** Parametric finite element analyses of geocell-supported embankments. *Canadian Geotechnical Journal*, 44(8), 917-927.
- Madhavi, L. G., K., D. S., & K., R. (2009).** Numerical simulation of the behavior of geocell reinforced sand in foundations. *International Journal of Geomechanics*, 9(4), 143-152.

- Madhavi, L. G., & Rajagopal, K. (2007).** Parametric finite element analyses of geocell-supported embankments. *Canadian Geotechnical Journal*, 44(8), 917-927.
- Madhavi, L. G., & Somwanshi, A. (2009).** Effect of reinforcement form on the bearing capacity of square footings on sand. *Geotextiles and Geomembranes*, 27(6), 409-422.
- Mandal, J. N., & Gupta, P. (1993).** Stability of geocell-reinforced soil. *construction and Building Materials*, 8(1), 55-62.
- Mandal, J. N., & Gupta, P. (1994).** Stability of geocell-reinforced soil. *Construction and Building Materials*, 8(1), 55-62.
- Manju, G. S., & Latha, G. M. (2013). *Interfacial friction properties of geocell reinforced sand*. Paper presented at the International Conference on Energy and Environment, Kerala, India.
- Marto, A., Oghabi, M., & Eisazadeh, A. (2013).** Effect of geocell reinforcement in sand and its effect on the bearing capacity with experimental test - A review. *Electronic journal of geotechnical engineering*, 18, 3501-3516.
- McDowell, G., & Bolton, M. D. (1998).** On the micromechanics of crushable aggregates. *Géotechnique*, 48(5), 667-679.
- McDowell, G. R., & Li, H. (2016).** Discrete element modelling of scaled railway ballast under triaxial conditions. *Granular Matter*, 18(3).
- Mehdipour, I., Ghazavi, M., & Moayed, R. Z. (2013a).** Numerical study on stability analysis of geocell reinforced slopes by considering the bending effect. *Geotextiles and Geomembranes*, 37, 23-34.

**Mehdipour, I., Ghazavi, M., & Moayed, R. Z. (2013b).** Numerical study on stability analysis of geocell reinforced slopes by considering the bending effect. *Geotextiles and Geomembranes*, 37, 23–34.

**Meuller, W. W. (2007).** *HDPE Geomembranes in Geotechnics*. Berlin: Springer Berlin Heidelberg.

**Mhaiskar, S. Y., & Mandalt, J. N. (1995).** Investigations on soft clay subgrade strengthening using geocells. *construction and Building Materials*, 10(4), 281-286.

**Moghaddas Tafreshi, S. N., Khalaj, O., & Dawson, A. R. (2013).** Pilot-scale load tests of a combined multilayered geocell and rubber-reinforced foundation. *Geosynthetics International*, 20(3), 143-161.

**Moghaddas Tafreshi, S. N., Shaghaghi, T., Tavakoli Mehrjardi, G., Dawson, A. R., & Ghadrdan, M. (2015).** A simplified method for predicting the settlement of circular footings on multi-layered geocell-reinforced non-cohesive soils. *Geotextiles and Geomembranes*, 43(4), 332-344.

**Moghaddas Tafreshi, S. N., Shaghaghi, T., Tavakoli Mehrjardi, G., Dawson, A.R., & Ghadrdan, M. (2015).** A simplified method for predicting the settlement of circular footings on multi-layered geocell-reinforced non-cohesive soils. *Geotextiles and Geomembranes*, 43, 332–344.

**Ngo, N. T., Indraratna, B., & Rujikiatkamjorn, C. (2014).** DEM simulation of the behaviour of geogrid stabilised ballast fouled with coal. *Computers and Geotechnics*, 55, 224-231.

- Ngo, N. T., Indraratna, B., & Rujikiatkamjorn, C. (2017).** Simulation Ballasted Track Behavior: Numerical Treatment and Field Application. *International Journal of Geomechanics*, 17(6), 04016130.
- Ngo, N. T., Indraratna, B., Rujikiatkamjorn, C., & Mahdi Biabani, M. (2015).** Experimental and Discrete Element Modeling of Geocell-Stabilized Subballast Subjected to Cyclic Loading. *Journal of Geotechnical and Geoenvironmental Engineering*, 04015100.
- Nishiura, D., Sakai, H., Aikawa, A., Tsuzuki, S., & Sakaguchi, H. (2017).** Novel discrete element modeling coupled with finite element method for investigating ballasted railway track dynamics. *Computers and Geotechnics*, In press.
- Oliaei, M., Kouzegaran, S. (2017).** Efficiency of cellular geosynthetics for foundation reinforcement. *Geotextiles and Geomembranes*, 45, 11-22.
- Pan, H., Devasahayam, S., & Bandyopadhyay, S. (2017).** Study of microstructure and fracture properties of blunt notched and sharp cracked high density polyethylene specimens. *Sci Rep*, 7(1), 6096.
- Pokharel, S. K. (2010).** *Experimental Study on Geocell-Reinforced Bases under Static and Dynamic Loading.* (Doctor of Philosophy), The University of Kansas.
- Pokharel, S. K., Han, J., Leshchinsky, D., Parsons, R. L., & Halahmi, I. (2010).** Investigation of factors influencing behavior of single geocell-reinforced bases under static loading. *Geotextiles and Geomembranes*, 28(6), 570-578.
- Potyondy, D. O., & Cundall, P. A. (2004).** A bonded-particle model for rock. *International Journal of Rock Mechanics and Mining Sciences*, 41(8), 1329-1364.
- PrestoGeosystems. (2009).** Geoweb Channel Protection System Installation Guideline. Wisconsin, USA.



- Qian, Y., Mishra, D., Tutumluer, E., & Kazmee, H. A. (2015).** Characterization of geogrid reinforced ballast behavior at different levels of degradation through triaxial shear strength test and discrete element modeling. *Geotextiles and Geomembranes*, 43(5), 393-402.
- Rajagopal, K., Krishnaswamy, N. R., & Latha, G. M. (1999).** Behaviour of sand confined with single and multiple geocells. *Geotextiles and Geomembranes*, 17, 171-184.
- Raymond, G. P., & Diyaljee, V. A. (1979).** Railroad Ballast Prescription: State-of-the-Art. *Journal of the Geotechnical Engineering Division*, 105(2), 305-322.
- Sadeghi, J. M. (2008).** Experimental evaluation of accuracy of current practices in analysis and design of railway track sleepers. *Canadian Journal of Civil Engineering*, 35(9), 881-893.
- SAI. (2001).** AS 1145.3 Determination of Tensile Properties of Plastic Materials. Australia: Standards Australia International Pty Ltd.
- Salim, W., & Indraratna, B. (2004).** A new elastoplastic constitutive model for coarse granular aggregates incorporating particle breakage. *Canadian Geotechnical Journal*, 41(4), 657-671.
- Satyal, S. R., Leshchinsky, B., Han, J., & Neupane, M. (2018).** Use of cellular confinement for improved railway performance on soft subgrades. *Geotextiles and Geomembranes*, 46(2), 190-205.
- Sawicki, A. K.-F., K. (1998).** Creep behaviour of geosynthetics. *Geotextiles and Geomembranes*, 16, 365-382.
- Selig, E. T., & Waters, J. M. (1994).** *Track Geotechnology and Substructure Management*. London: Thomas Telford Publications.

- Shenton, M. J. (1978). Deformation of Railway Ballast Under Repeated Loading Conditions *Railroad Track Mechanics and Technology* (pp. 405-425). Derby: British Railway Research and Development Division.
- Sireesh, S. (2010).** *Settlement Prediction of Geocell-Reinforced Clay Foundations*. Paper presented at the Indian Geotechnical Conference.
- Sitharam, T. G., & Hegde, A. (2013).** Design and construction of geocell foundation to support the embankment on settled red mud. *Geotextiles and Geomembranes*, 41, 55-63.
- Sitharam, T. G., & Sireesh, S. (2006).** Effects of base geogrid on geocell-reinforced foundation beds. *Geomechanics and Geoengineering*, 1(3), 207-216.
- Song, F., Liu, H., Chai, H., & Chen, J. (2017).** Stability analysis of geocell-reinforced retaining walls. *Geosynthetics International*, 24(5), 442-450.
- Sun, Y., & Zheng, C. (2017).** Breakage and shape analysis of ballast aggregates with different size distributions. *Particuology*, 35, 84-92.
- Tafreshi, S. N. M., & Dawson, A. R. (2010).** Comparison of bearing capacity of a strip footing on sand with geocell and with planar forms of geotextile reinforcement. *Geotextiles and Geomembranes*, 28(1), 72-84.
- Tafreshi, S. N. M., & Khalaj, O. (2012). *Repeated Load Response of Square Footings on Geocell Reinforced Soil - Comparing Use of Single and Multiple Layered Geocells*. Paper presented at the World Conference on Earthquake Engineering, Lisbon.
- Tafreshi, S. N. M., Khalaj, O., & Dawson, A. R. (2014).** Repeated loading of soil containing granulated rubber and multiple geocell layers. *Geotextiles and Geomembranes*, 42(1), 25-38.

- Taghavi, R. (2011).** *Automatic Clump Generation Based on Mid-Surface*. Paper presented at the Continuum and Distinct Element Numerical Modeling in Geomechanics, Melbourne, Australia.
- Tanyu, B. F., Aydilek, A. H., Lau, A. W., Edil, T. B., & Benson, C. H. (2013).** Laboratory evaluation of geocell-reinforced gravel subbase over poor subgrades. *Geosynthetics International*, 20(2), 47–61.
- Tanyu, B. F., Lau, A. W., Edil, T. B., Benson, C. H., & Aydilek, A. H. (2013).** Laboratory evaluation of geocell-reinforced gravel subbase over poor subgrades. *Geosynthetics International*, 20(2), 47-61.
- Tariq, F., Naz, N., Khan, M. A., & Baloch, R. A. (2011).** Failure Analysis of High Density Polyethylene Butt Weld Joint. *Journal of Failure Analysis and Prevention*, 12(2), 168-180.
- Thakur, J. K., Han, J., & Parsons, R. L. (2013a).** Creep Behavior of Geocell-Reinforced Recycled Asphalt Pavement Bases. *Journal of Material in Engineering*, 25(10), 1533-1542.
- Thakur, J. T. (2007).** *Experimental Study on Geocell-Reinforced Recycled Asphalt (RAP) bases under static and cyclic loading*. (Master of Science), Tribhuvan Univesity, Nepal.
- Thakur, J. T., Han, J., & Parsons, R. L. (2013b).** Creep Behavior of Geocell-Reinforced Recycled Asphalt Pavement Bases. *Journal of Materials in Civil Engineering*, 25(10), 1533-1542.
- Wang, B., Martin, U., & Rapp, S. (2017).** Discrete element modeling of the single-particle crushing test for ballast stones. *Computers and Geotechnics*, 88, 61-73.
- Wang, C., Deng, A., & Taheri, A. (2018).** Three-dimensional discrete element modeling of direct shear test for granular rubber–sand. *Computers and Geotechnics*, 97, 204-216.

**Wang, G. Y., Zhang, J. P., & Y., X. T. (2013).** Numerical Analysis of Geocell Protective Slope Stability. *The Open Civil Engineering Journal*(7), 223-231.

**Wang, Y. H., & Leung, S. C. (2008).** A particulate-scale investigation of cemented sand behavior. *Canadian Geotechnical Journal*, 45(1), 29-44.

**Wang, Y. M., Chen, Y. K., Wang, G. S., & Hou, Z. X. (2008).** Large-scale direct shear testing of geocell reinforced soil. *Advances in Transportation Geotechnics*, 759-764.

**Wang, Z., Jacobs, F., & Ziegler, M. (2016).** Experimental and DEM investigation of geogrid–soil interaction under pullout loads. *Geotextiles and Geomembranes*, 44(3), 230-246.

**Webster, S. L., & Alford, S. J. (1978).** *Investigation of Construction Concepts for Pavement across Soft Ground*. Retrieved from Vicksburg, MS, USA:

**Webster, S. L., & Watkins, J. E. (1977).** *Investigation of Construction Techniques for Tactical Bridge Approach Roads across Soft Ground*. Retrieved from Vicksburg, MS, USA:

**Xiao, J., Zhang, D., Wei, K., & Luo, Z. (2017).** Shakedown behaviors of railway ballast under cyclic loading. *Construction and Building Materials*, 155, 1206-1214.

**Xu, M., Hong, J., & Song, E. (2017).** DEM study on the effect of particle breakage on the macro- and micro-behavior of rockfill sheared along different stress paths. *Computers and Geotechnics*, 89(Supplement C), 113-127.

Xu, Y., & Wang, J. P. (2013). *Stability and performance of ground improvement using geocell mattresses under extreme weather*. Paper presented at the 18th International Conference on Soil Mechanics and Geotechnical Engineering, Paris.

**Yan, Y., Zhao, J., & Ji, S. (2014).** Discrete element analysis of breakage of irregularly shaped railway ballast. *Geomechanics and Geoengineering*, 10(1), 1-9.

- 
- Yang, X. (2010a).** *Numerical analyses of geocell-reinforced granular soils under static and repeated loads.* (Ph.D), The University of Kansas, Lawrence, KS.
- Yang, X., Han, J., Parsons, R. L., & Leshchinsky, D. (2010).** Three-dimensional numerical modeling of single geocell-reinforced sand. *Frontiers of Architecture and Civil Engineering in China*, 4(2), 233-240.
- Yang, X., Han, J., Pokharel, S. K., Manandhar, C., Parsons, R. L., Leshchinsky, D., & Halahmi, I. (2012).** Accelerated pavement testing of unpaved roads with geocell-reinforced sand bases. *Geotextiles and Geomembranes*, 32, 95-103.
- Yang, X. M. (2010b).** *Numerical Analyses of Geocell Reinforced Granular Soils under Static and Repeated Loads.* (Doctor of Philosophy), The University of Kansas.
- Yuu, J., Han, J., Rose, A. R., Parsons, R. L., & Leshchinsky, D. (2008).** *Technical Review of Geocell-reinforced Base Courses Over Weak Subgrade.* Paper presented at the The First Pan-American Geosynthetics Conference and Exhibition.
- Zhang, L., Zhao, M., Shi, C., & Zhao, H. (2010).** Bearing capacity of geocell reinforcement in embankment engineering. *Geotextiles and Geomembranes*, 28(5), 475-482.
- Zhang, L., Zhao, M., Shi, C., & Zhao, H. (2012).** Nonlinear analysis of a geocell mattress on an elastic–plastic foundation. *Computers and Geotechnics*, 42(Supplement C), 204-211.
- Zhang, Q., Zhu, H., Zhang, L., & Ding, X. (2011).** Study of scale effect on intact rock strength using particle flow modeling. *International Journal of Rock Mechanics and Mining Sciences*, 48(8), 1320-1328.

## **Appendix A: Copy of Paper 1 (as published)**

---

**INTENTIONALLY BLANK**



Contents lists available at ScienceDirect

## Computers and Geotechnics

journal homepage: [www.elsevier.com/locate/compgeo](http://www.elsevier.com/locate/compgeo)

Research Paper

## Three-dimensional modeling of geocell-reinforced straight and curved ballast embankments



Yang Liu, An Deng\*, Mark Jaksa

School of Civil, Environmental and Mining Engineering, The University of Adelaide, SA 5005, Australia

## ARTICLE INFO

## Keywords:

Discrete element  
Railway embankment  
Ballast  
Geocell  
Cyclic

## ABSTRACT

This paper outlines a three-dimensional modeling study conducted on straight and curved geocell-reinforced embankments. The study uses the discrete element method to represent varying angularities of ballast infill and models their mechanical response under monotonic and cyclic loading conditions. The simulation results show good agreement with test results and the case studies indicate that the geocell enhances embankment stiffness under monotonic loading and improves its resilience when subjected to cyclic loading. The geocell more evenly distributes stresses within the ballast embankments. The reinforced ballast embankments also exhibit less vertical displacement and lateral spreading than the unreinforced ballast embankments do.

## 1. Introduction

As time progresses, trains travel faster, railways become longer and convey heavier goods, and more stringent safety standards mandate a higher level of below-rail alignment for longer design periods. However, the main below-rail ballast layer, which is referred to in the present study as the ballast embankment, eventually becomes misaligned due to ballast breakage and rearrangement [1–4]. As a result, the embankment is prone to subsidence and lateral spreading, which undermines the safety of the tracks. The damage to the embankment is more pronounced on sharp track curves where the train creates large centrifugal forces, which can result in significant settlement in the track embankment, which exacerbates rail misalignment. Poor track geometry results in significant expenditure due to ballast inspection, maintenance and sometimes reconstruction. For example, in the year ending 30 June 2016, the Australian Rail Track Corporation (ARTC) – one of Australia's largest rail network owners – expended more than \$AUD188 million on railway infrastructures maintenance work, accounting for 22.3% of their total revenue in the same year [5]. To minimize this expenditure, studies [6–9] have successfully applied geosynthetics to reinforce embankments. Of the suite of available geosynthetics, geocells provide a promising means to reinforce railway embankments [7,8].

The geocell, as shown in Fig. 1, is a cellular confinement system developed to reinforce granular infills. The system is supplied in a folded form and, when in use, outstretched into a honeycomb-like, three-dimensional (3D) panel. The stretched panel provides a space to accommodate and confine the infill materials and facilitates the joining

of individual cell panels into an integrated mattress. When fully outstretched, the panel usually measures a couple of meters in width and up to 20 m in length, with an individual cell space of around 250 mm square, in width, and between 75 and 200 mm deep. The panel size and the cell space can be varied as part of the manufacturing process to suit individual requirements. The cell wall, which is around 5 mm thick, commonly consists of high-density polyethylene (HDPE) or other polymer material, and is perforated to allow water drainage, facilitate root growth between cells and provide interlocking with the infill.

Geocell panels have been widely used in a variety of infrastructures, such as foundations and subbases [10–16], slopes [17], retaining structures [18] and embankments [19,20]. All of these studies have shown that using geocells improves performance of the infrastructures by reinforcing the granular infill materials. More recently, Leshchinsky and Ling [7,8] conducted a prototype test and a finite element (FE) analysis on a geocell-reinforced railway embankment. Their studies confirmed the superiority of the geocell in reinforcing the embankment. Similar approaches were attempted in other studies [21–23]. In parallel with the FE method, Liu et al. [24] employed the discrete element method (DEM) to examine the performance of straight, geocell-reinforced embankments. As a further step, this study extends the DEM approach to curved embankments. Additional work includes the advanced contact model used to simulate the geocell and the examination on geocell embedment depth.

The DEM possesses the capability to represent, with appropriate engineering accuracy, distinct ballast particles and to simulate particle motion [25]. The method does not rely on a constitutive model for continuum media; rather, it incorporates a contact model developed

\* Corresponding author.

E-mail address: [an.deng@adelaide.edu.au](mailto:an.deng@adelaide.edu.au) (A. Deng).<https://doi.org/10.1016/j.compgeo.2018.05.011>Received 18 November 2017; Received in revised form 16 May 2018; Accepted 25 May 2018  
0266-352X/ © 2018 Elsevier Ltd. All rights reserved.



Notation			
$D_0$	center-to-center distance of neighboring spheres, before displacement	$P_V$	vertical load
$D_1$	center-to-center distance of neighboring spheres, after displacement	$R$	track horizontal curve radius
$D_{50}$	diameter of particles 50% finer by weight	$\bar{R}$	bond radius
$k_n$	normal stiffness	$v$	train velocity
$k_s$	shear stiffness	$\mu$	friction coefficient
$\bar{k}_n$	parallel-bond normal stiffness	$\theta$	angle of inclination
$\bar{k}_s$	parallel-bond shear stiffness	$\rho$	density
$\hat{k}_s$	softening stiffness	$\sigma_c$	parallel-bond normal strength
$\hat{k}_n$	normal stiffness in tension	$\bar{\sigma}_t$	tensile strength
$P_L$	lateral load	$\bar{\tau}_c$	parallel-bond shear strength
$P_R$	resultant load	$\zeta$	local damping coefficient
		$\epsilon$	geocell strain
		$\epsilon_y$	geocell yielding strain
		$\epsilon_f$	geocell failure strain

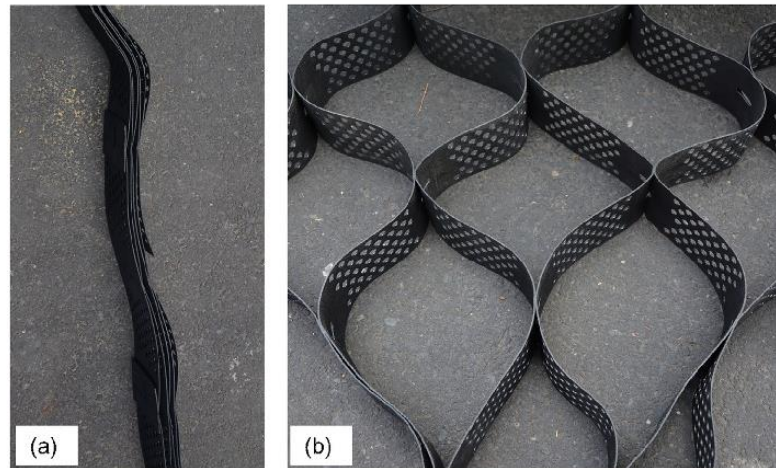


Fig. 1. Information on cell size and wall depth: (a) folded and (b) outstretched (250 W × 250 L × 100 D mm for a cell).

between the individual particles. The method is also able to replicate variable angularities of the ballast, and similarly reflects variable material micro-properties, such as stiffness and friction [6,26,27]. More importantly, it enables 3D modeling. This is particularly important for the accurate simulation of the 3D geocell panel, as 2D modeling neglects, or at least simplifies, the interaction between cells and so underestimates the performance of the geocell panel. However, an additional calibration stage is required in order to yield simulated behavior substantially similar to that observed in reality. Further, it is not possible to simulate a full-scale structure as replacing a continuum with particle assemblies is computationally intensive. Thus, the simulation of a full-scale railway structure in DEM is beyond current computational capacity and the scope of this study.

This study adopts the commercially-available DEM program, Particle Flow Code in 3 Dimensions (PFC3D) version 4.0 [28], to simulate a geocell-reinforced embankment. The railway embankment examples included in the paper are established in accordance with the relevant codes of practice, which are discussed later. The paper aims to establish a DEM-based framework for modeling railway ballast and to evaluate the performance of incorporating geocells in ballasted embankments. Chen et al. [6] adopted DEM to simulate geogrid-reinforced railway ballast and they successfully demonstrated the capability of using DEM in modeling geosynthetics-reinforced ballast. The methodologies used in [6], such as material generation, have inspired the framework proposed in the current study. Improvements have also been

made in the geometric complexity of ballast model as well as in the behaviors and contact models of geocell and ballast in DEM.

## 2. Model development

This section outlines the development of the ballast-geocell model in PFC3D and provides details of the particle contact and the calibration of the geocell and ballast assemblage.

### 2.1. Particle contact

DEM simulation is governed by the physical contact between particles. The contacts are present as a combination, in series and/or parallel, of the following basic physical elements: a bond, slider, spring and dashpot. When applying an external force to an assemblage of particles, the contacts between them determine how individual particles will respond and where they will travel at each time step in the simulation. PFC3D incorporates the contact mechanism and allows the user to encode a material-oriented, contact, constitutive model. Once validated, the model is implemented to reproduce the mechanical response of the material used in any desirable field application. The model usually defines a set of material micro-properties, such as particle stiffness, bond strength and friction coefficient, which are determined through material calibration tests.

## 2.2. Material calibration

In this section the procedures for calibrating the input parameters for the geocell and railway ballast in PFC3D are discussed.

### 2.2.1. Geocell

The geocell material was calibrated by conducting a tensile strength test. The test setup is shown in Fig. 2. A geocell strip was cut from a full panel and cropped into a standard specimen shape for tensile strength testing, in accordance with AS 1145.3 [29]. The specimen was tested using an Instron mechanical device [Fig. 2(a)] and three replicates, as the one illustrated in Fig. 2(a), were tested to obtain representative results. The stress-displacement relationship of the averaged results was then compared with the DEM simulation. The DEM simulation involved discretizing the specimen strip into 32 equal-sized spheres – an object in PFC3D for modeling materials [26]. The 32 spheres are arranged in two columns, forming a strip [Fig. 2(b) and (c)]. Each sphere is assigned an equivalent diameter of 5 mm, and so the sphere-based strip (5 mm thick  $\times$  10 mm wide  $\times$  80 mm long) is equal in size to the specimen section, which is elongated during the test.

Table 1 shows the material micro-properties used to simulate the behavior of the geocell. The properties were determined using the formulation proposed by Potyondy and Cundall [30] and the stress-displacement results presented in Fig. 3. As can be seen, close agreement is obtained between the simulation and test results. Both sets of results show a very close peak strength, a clear elongation process and similar residual strength. The agreement was achieved by encoding a ductile model [26] to provide a softening slope. A previous study [24] used conventional linear parallel-bond which can only provide a linear-elastic stress-strain response before reaching peak tensile strength. The ductile model is a modification, rather than a replacement to the contact-bond, and it is invoked when brittle failure occurs in bonded particles, so that the geocell model does not experience sudden failure when it reaches its peak tensile strength. Instead, the bond reduces its strength to behave like HDPE, the material from which the geocells used in this study are manufactured from. As can also be observed, there is a disparity between the simulation and experimental results in the elastic regions. This phenomenon can be attributed to the nature of the parallel-bond, which is essentially designed to model linear-elastic behavior. The model incorporates three contacts: stiffness (i.e. springs), a parallel bond and a slip. As a further note, the micro-properties shown in Table 1 were attained using an iterative approach – harmonizing the simulations with the test results [26]. Whilst this approach is somewhat indirect, satisfactory outcomes are obtained. The geocell model obtained a yielding strain  $\epsilon_y = 11.02\%$  and a failure strain  $\epsilon_f = 46.7\%$ , identified as points A and B respectively in Fig. 3.

### 2.2.2. Ballast

Railway ballast is usually produced by blasting and/or fragmenting a rock mass, and hence exhibits variable angularities. Past studies [3,31,32] have demonstrated the importance of accurately modeling the particle angularities, and suggested that reflecting angularities in simulations better reproduces the actual behavior of the ballast. To achieve this, four ‘clump templates’ were developed: trapezoidal, triangular, rectangular and hexagonal (Table 2), which account for the major geometric shapes of ballast infills. Clumps are groups of ‘slaved’ spheres that are firmly bonded together. In the modeling undertaken in the present study, debonding within the clump is prohibited, so as to focus on the motion of the ballast and eliminate the possibility of problems associated with breakage.

The calibration of the ballast is similar in concept to that of the geocell. Lim and McDowell [32] suggested the use of a triaxial test simulation to calibrate the ballast in PFC3D, and test results by Indraratna et al. [4] were used for this purpose. As suggested by Lim and McDowell [32] and Lu and McDowell [33], the interlocking of the clumps was represented by applying a weak and breakable parallel

bond between two contacting clumps. The bond can reconstitute at a new contact if particles rearrange. In addition, the membrane used to confine a sample is represented as a wall and assumed to be frictionless [6]. As PFC adopts the lower friction coefficient of two contacting entities, the friction between the clumps and the membrane is ignored. This approach is also adopted in subsequent ballast embankment models, which helps focus on the mechanical response of the geocell-reinforced ballast. Similarly, the sleepers situated on the top of the embankment act merely as loading platens and the friction between the sleepers and the ballast is ignored.

The test setup, as shown in Fig. 4, comprises a cylindrical cell of 300 mm in diameter  $\times$  600 mm high. The cell is initially filled with a number of spheres of varying diameters, 20–50 mm [Fig. 4(a)], in accordance with the ballast grading characteristics specified by Indraratna et al. [4]. The spheres are then replaced [Fig. 4(b)], in equal volume, with the clump templates shown in Table 2. The replacement is conducted in equal allocations among the four templates, and at random orientations within the cell. It is important to note that particle overlap occurs when assigning the clump templates to the spheres due to the created clump angularities. To negate this effect, as well as a prestressing problem, the top cap of the cell is allowed to move upward at an extremely slow rate of 0.1 mm/s until an equilibrium of inter-clump contact forces is achieved [32]. The equilibrium is determined by the ratio of the average mechanical solve ratio, defined as unbalanced force over the average value of the sum of contact forces, body forces and applied forces over all particles. The ratio is set as  $1 \times 10^{-3}$ , which is small enough to signal the equilibrium. The specimen porosity at equilibrium is 0.39, which is the average measured by two spheres. The spheres, 300 mm diameter each, are inscribed in the triaxial chamber. The spheres sit edge-to-edge, enabling the most occupation of the chamber space. The inscribing avoids possible boundary effect of the chamber. A total of 632 clumps (i.e. 7584 spheres) are incorporated in the specimen.

The specimens are then subjected to triaxial compression tests at 6 different confining pressures: 15, 30, 60, 90, 120 and 240 kPa. The loading is achieved by moving top wall downward at a rate of 0.045 mm/s and the tests continue until an axial strain of 20% is attained. It should be noted that all loading rates used in this study have been selected by trial and error to achieve desirable numerical stability while reasonable computational effort is spent. A numerical, servo-control algorithm [26] is incorporated in the simulation to maintain a constant confining pressure throughout the respective loading phases. The top loading wall is assigned with following micro-properties: a normal stiffness of  $1 \times 10^{10}$  N/m; shear stiffness of  $1 \times 10^{10}$  N/m and a

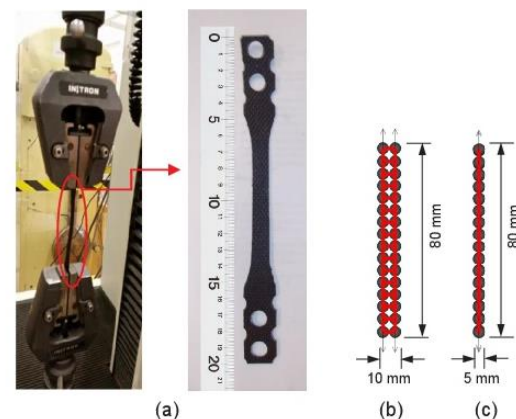
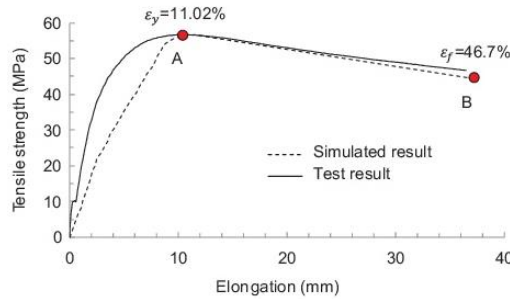


Fig. 2. Geocell tensile strength test: (a) setup and detail of representative tested specimen; (b) front view in DE simulation; (c) side view in DE simulation.



**Table 1**  
Micro-properties for geocell.

Micro-property	Value
Density $\rho$ (kg/m <sup>3</sup> )	$1.0 \times 10^3$
Normal stiffness $k_n$ (N/m)	$3.2 \times 10^3$
Shear stiffness $k_s$ (N/m)	$3.2 \times 10^3$
Parallel-bond normal stiffness $\bar{k}_n$ (N/m <sup>2</sup> )	$2.8 \times 10^4$
Parallel-bond shear stiffness $\bar{k}_s$ (N/m <sup>2</sup> )	$4.5 \times 10^4$
Parallel-bond normal strength $\bar{\sigma}_c$ (N/m <sup>2</sup> )	$6.8 \times 10^4$
Parallel-bond shear strength $\bar{\tau}_c$ (N/m <sup>2</sup> )	$6.5 \times 10^4$
Parallel-bond radius $\bar{R}$ (mm)	2.5
Tensile strength $\bar{\sigma}_t$ (N/m <sup>2</sup> )	$5.598 \times 10^4$
Softening stiffness $\hat{k}_s$ (N/m <sup>3</sup> )	$2.75 \times 10^4$
Normal stiffness in tension $\hat{k}_n$ (N/m)	$3.2 \times 10^4$
Friction coefficient $\mu$	0.3

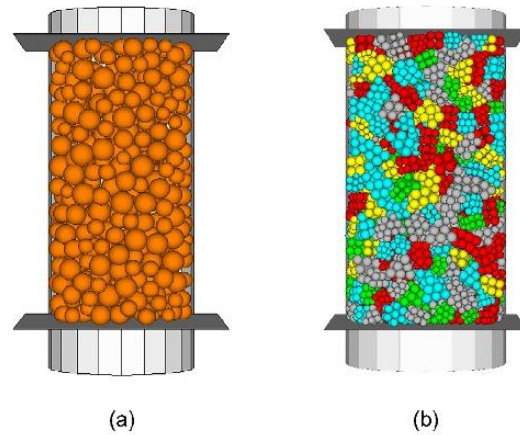


**Fig. 3.** Tensile strength of geocell specimen.

**Table 2**  
Clump templates developed for ballast.

Clump template	Geometry	Number of spheres
Trapezoidal		10
Triangular		10
Rectangular		12
Hexagonal		14

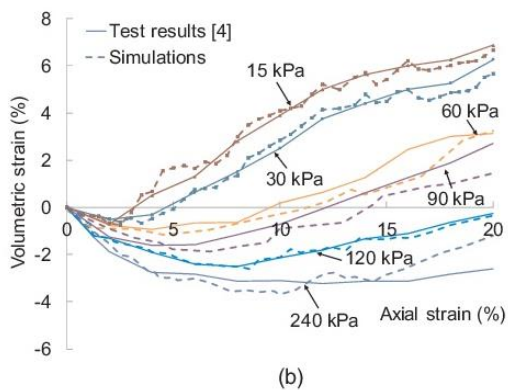
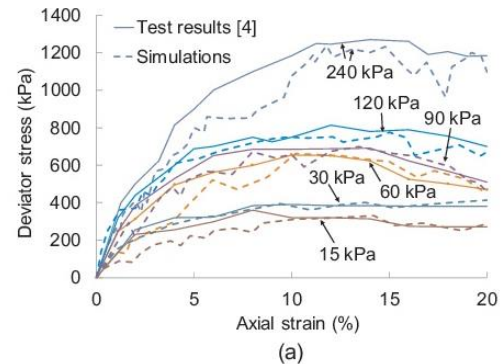
friction coefficient of 0.5 (i.e.  $\tan 27^\circ$ ). The wall stiffnesses are higher than the ballast stiffness in order to prevent ballast penetration. Fig. 5 shows the simulation and test results of the triaxial tests. The simulation was achieved by encoding a linear contact model [26] and using the micro-properties provided in Table 3, which were obtained through trial and error. The micro-properties show that the model, similar to that for the geocell, also incorporates the three contacts: stiffness, a parallel bond and a slip. Similarly close agreement is found across the entire series of confining pressures. The accuracy of the simulations is further validated by the dilation observed under lower confining pressures and contraction under higher ones. These results demonstrate that the material properties and encoded models are capable of appropriately modeling the mechanical behavior of the ballast.



**Fig. 4.** Triaxial test specimen simulated by: (a) spheres; (b) clumps.

**3. Modeling procedure**

A full-scale embankment simulation is computationally, extremely time-consuming, owing to the large number of spheres needed to simulate the geocell and ballast infills, and is beyond current and available computer capability. This concern has been confirmed in a similar simulation study [6]. Therefore, the embankment is scaled down by a



**Fig. 5.** Triaxial compression test results: (a) deviator stress vs. axial strain; (b) volumetric strain vs. axial strain.

**Table 3**  
Micro-properties for ballast clumps.

Micro-property	Value
Density $\rho$ (kg/m <sup>3</sup> )	$2.5 \times 10^3$
Normal stiffness $k_n$ (N/m)	$5 \times 10^9$
Shear stiffness $k_s$ (N/m)	$5 \times 10^9$
Parallel-bond normal stiffness $\bar{k}_n$ (N/m <sup>2</sup> )	$1.8 \times 10^5$
Parallel-bond shear stiffness $\bar{k}_s$ (N/m <sup>2</sup> )	$1.8 \times 10^5$
Parallel-bond normal strength $\bar{\tau}_n$ (N/m <sup>2</sup> )	$6 \times 10^{10}$
Parallel-bond shear strength $\bar{\tau}_c$ (N/m <sup>2</sup> )	$6 \times 10^{10}$
Parallel-bond radius $\bar{R}$ (mm)	1.0
Frictional coefficient $\mu$	1.0

factor of five in terms of its crest and base width with regards to the actual dimensions specified by ARTC [34,35]. In this context, there are still approximately 78,000 spheres incorporated in the reinforced embankment. The scaling does not significantly influence performance comparison made between the reinforced and unreinforced embankments, as both embankments are subject to the same level of scaling. Moreover, the scaled embankment is comparable in size with the one adopted in a prototype test [7] and so provides an opportunity to validate the simulation results against those from the test. In order to focus on the contribution of the geocell to embankment stability, a simplified track assemblage is adopted, where only sleepers are included in the DEM model and rails, fastenings and anchors are excluded.

3.1. Straight embankment

The straight rail embankment is summarized in Fig. 6. A crest width of 500 mm, base width of 1080 mm, height of 300 mm and a length of 1000 mm are adopted. The gradient of its shoulder slope is approximately 1:1. Six sleepers, each 50 mm wide and 500 mm long, are founded on the crest at an edge-to-edge spacing of 120 mm. The sleepers were simulated using stiff walls – an object in PFC3D for materials with line segments [26], which exhibit dimensions of actual, heavy-duty, prestressed concrete sleepers. As the contact forces between two contacting objects are governed by their stiffnesses, the sleepers are assigned with the micro-properties used for the loading wall in the triaxial simulation, enabling a consistent stress – strain behavior of the ballast assembly. Considering the 2D nature of the embankment (i.e. no longitudinal movement of the infill), the front and rear cross-sections were simulated using non-movable walls, with normal and shear stiffnesses of  $1 \times 10^{10}$  N/m, and a higher friction coefficient of 1.0 (i.e.  $\tan 45^\circ$ ) to reflect the ballast-to-ballast friction along the section boundaries. In order to reflect embankment subsidence caused by the underlying subgrade, the subgrade was also represented by a wall, with lower normal and shear stiffnesses of  $1 \times 10^8$  N/m, and a friction coefficient of 0.5.

The role of the geocell in the stability of rail embankments is examined by placing the geocell at two different levels within the ballast layer: at the base of the embankment [Fig. 7(a)] and 50 mm above the base [Fig. 7(b)]. At each level, as shown in Fig. 7(c), the geocell panel is centered within the ballast-filled embankment. The panel [Fig. 7(d)] includes 8 cells and measures 748 mm  $\times$  480 mm edge-to-edge. Each cell is 75 mm deep and 175 mm  $\times$  175 mm wide. The long and short sides of the panel are aligned with the embankment’s longitudinal and transverse directions, respectively. The short side is less than the width of embankment crest, so that a 10 mm margin is present along the embankment crest edges. In the longitudinal direction, the panel length is 252 mm shorter than the extension of the embankment, which negates boundary effects associated with the panel. The geocell panel is longitudinally divided into two halves: A and B. Representative cell junctions are marked as a to g for subsequent displacement analysis. As is required by PFC3D, the geocell material is also simulated by a layer

of spheres. The spheres are aligned and bonded together contiguously using the micro-properties shown previously in Table 1. A total of 12,762 spheres are used to generate the entire geocell panel.

The ballast infill is generated using the procedures similar to those used in the ballast triaxial calibration. Temporary walls are generated first on the embankment slopes and crest as boundaries. The geocell and associated bonds are then generated within the pre-defined boundaries, followed by generation of ballast and corresponding parallel-bond. The geocell can deform freely and it is breakable during this process. It should be noted that the ballast is generated in three layers (i.e. 100 mm thick each). As contact forces between clumps are created due to overlapping during clumps generation, additional time steps are permitted between the generations of each layer, so that previous layers can reach equilibrium (i.e. release contact forces). The temporary walls prevent the escape of clumps due to the contact forces and they are permitted to move slowly outward until the inter-clump contact forces dissipate, upon which they are removed. During the ballast generation process, no constraint is applied to the interaction between the geocell and ballast. This is to reflect the actual placement of ballast in the field. A total of 4002 clumps (i.e. 56,083 spheres) are used for the infill in the situations where a geocell panel is used. For the unreinforced embankment, similar numbers of clumps (4106) and spheres (57,479) are generated for the infill.

3.2. Curved embankment

A horizontally-curved embankment has its outer rail elevated to provide a banked curvature. This super-elevation, also known as a cant,

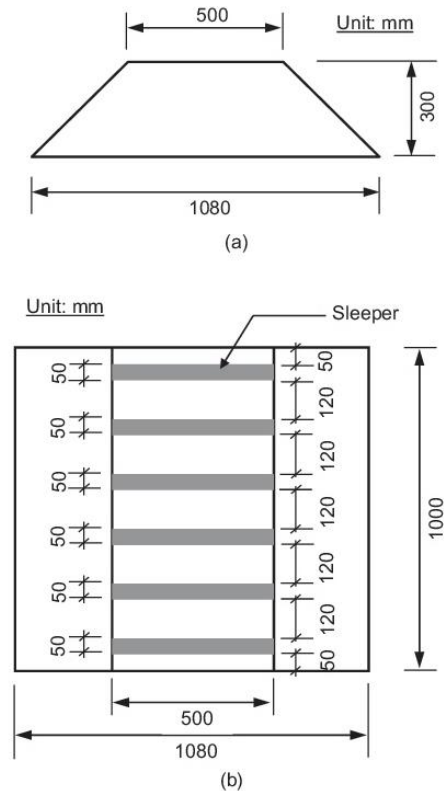


Fig. 6. Straight embankment: (a) cross section; (b) plan view.



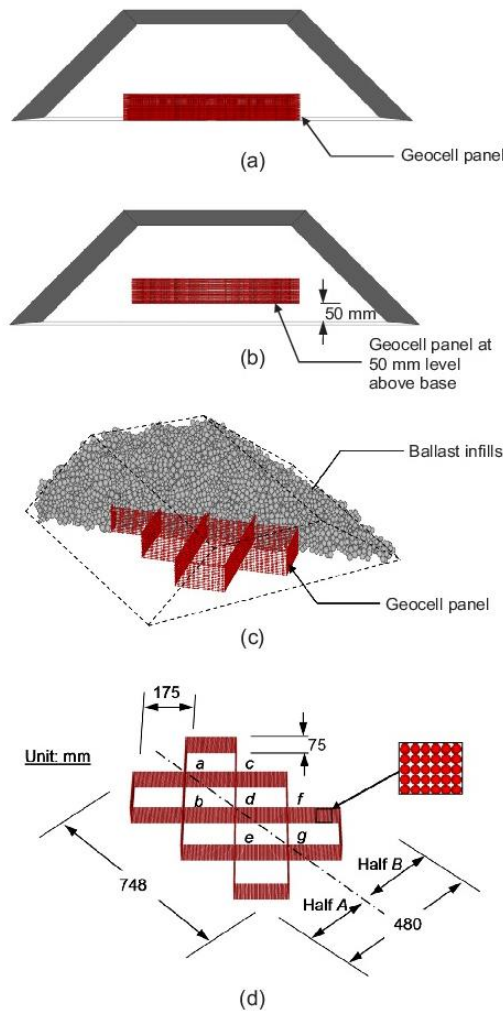


Fig. 7. Geocell panel: (a) at embankment base; (b) 50 mm above the base; (c) 3D perspective: infilled with ballast; and (d) 3D perspective: simulated using spheres.

serves the purpose of providing a centripetal force to balance the centrifugal force exerted by the train's motion, which in turn allows the train to negotiate bends at higher speed. Fig. 8 shows a diagram of the curved embankment used in this study. The diagram is similar to that for the straight embankment except for the 5% gradient adopted at the crest. This gradient is set in accordance with ARTC [35] and the value corresponds to the typical limit of super-elevation for an intrastate line in Australia. Compared with the straight embankment, the curved embankment uses the same geocell arrangements and material micro-properties, and a similar number of spheres for the geocell and ballast.

3.3. Monotonic and cyclic loading

This sub-section describes the monotonic and cyclic loading adopted in the study. The aim of the monotonic loading is to determine the embankment subsidence in response to a slowly increasing vertical load and is similar in nature to a plate load test. For the straight

embankment, the numerical model constrains the sleepers to move in a downward direction along a trajectory normal to the crest. The sleepers advance at a rate of 0.1 mm/s to cause the embankment to settle at the desired strain of 20% (60 mm). The modest value of the loading rate improves the simulation accuracy by allowing sufficient time to calculate the inter-particle contact forces. The strain-limiting value is consistent with that used in the triaxial calibration and helps predict the load extremes that the embankments can sustain. The monotonic loading applied to the curved embankment acted at an angle of inclination  $\theta$  (i.e.,  $54.5^\circ = \arctan(P_L/P_V)$ ) [Fig. 9], where  $P_V$  is the vertical applied load and is calculated to equal 125 kPa for a 30-tonne axle load of a heavy haul train wagon [34];  $P_L$  is the lateral load acting on the sleepers and equal to the centrifugal force as:

$$P_L = \frac{mv^2}{R} \tag{1}$$

where  $m$  is the axle load,  $v$  is the speed of the train, and  $R$  is the horizontal curve radius. ARTC [34] specifies  $R = 200$  m as the minimum allowable horizontal curve radius for a heavy haul line. Thus,  $P_L$  is approximately 175 kPa when the haul train wagon passes through the curve at the ARTC's design speed of 60 km/h [36]. The values for the vertical load, radius and design speed are adopted to reflect adverse situations in practice and so amplify the loading conditions and expedite the simulation process. To achieve a displacement direction at the angle  $\theta$ , the sleepers advance at a lateral rate of 0.14 mm/s and vertical rate of 0.1 mm/s; that is, at a velocity ratio of 1.4, which is equivalent to the  $P_L/P_V$  ratio.

Cyclic loading, on the other hand, is of higher significance in regard to the assessment of the long-term serviceability of railway embankments. For the straight embankment, a vertical load of  $P_V = 125$  kPa, which reflects a full-scale 25-tonne heavy freight train passing through, was applied normal to the sleepers in the form of loading-complete unloading-reloading cycles. Although the geometry of the railway structure and geocell is downscaled, the strength and mechanical behavior are calibrated against laboratory and full-scale experimentation, therefore no scale factor is applied to the loading values. The load applied has been shown to be frequency-independent, as reported by Shenton [37]. Due to the long computational time when performing the simulation, a total of 20 loading cycles were performed for each simulation. Even with this somewhat modest number, the simulations utilized the full capability of the PC hardware (Intel core i7-4500U, 8 GB DDR3L 1333 RAM with integrated Intel HD Graphics 4400) and the entire modeling process took approximately two months to complete. Albeit with the constraint of computational time, the simulations provide indicative observations of embankment subsidence and the performance of geocells in the early stages of the cyclic loading. Similar simulations were applied to the curved embankment, except for the load applied. The resultant force ( $P_R$ ) of the vertical ( $P_V$ ) and lateral ( $P_L$ ) loads was calculated as 215 kPa and acted at an angle of  $\theta$  with respect to the vertical direction (Fig. 9). It is worth mentioning that for both straight and curved embankment subject to cyclic loading cases, all sleepers advance simultaneously at the same rates. No lag is applied to the sleepers to reflect train passage as the freight can pass the sleepers gap in an extremely short period of time over a 1-meter embankment.

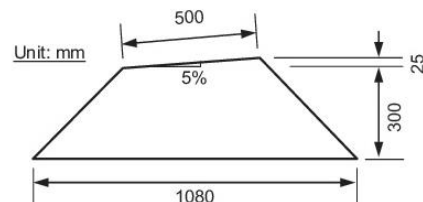


Fig. 8. Curved embankment cross section.

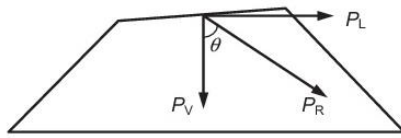


Fig. 9. Forces acted on curved embankment.

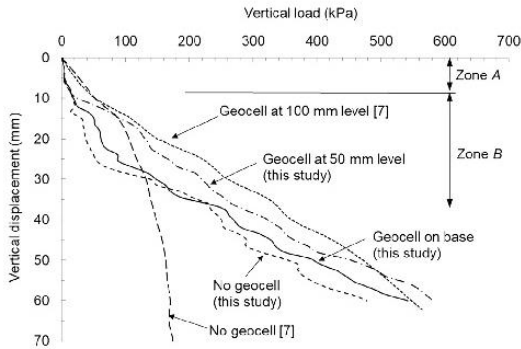


Fig. 10. Vertical displacement for straight embankment under monotonic loading.

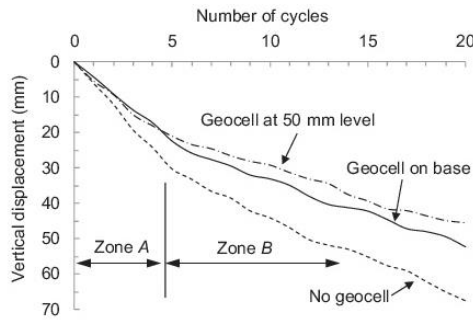


Fig. 11. Vertical displacement for straight embankment under cyclic loading.

Local damping was activated for ballast clumps only to absorb the vibration energy generated in the cyclic loading process. The clumps tend to rebound and occasionally escape from the embankment boundaries during the unloading phases, as a result of accumulated internal forces. The introduction of a damping coefficient,  $\zeta$ , facilitates the dissipation of these forces in the agitated clumps and allows the ballast assembly to cease oscillating more rapidly [26]. In this study, the local damping ratio was set to 1.0.

#### 4. Results and discussion

##### 4.1. Straight embankment

Fig. 10 shows the vertical displacement of the sleepers plotted against the applied vertical load for the straight embankments under monotonic loading, where the results of the numerical simulations from this study are compared with the test results presented by Leshchinsky and Ling [7]. The simulated vertical displacement is the average of the 6 sleepers and the load is the average resistance measured at the base of the sleepers [Fig. 6(b)]. The boundary effects caused by the walls in longitudinal direction are neglected in this study as the individual data set for each sleeper shows insignificant differences in axial stress value.

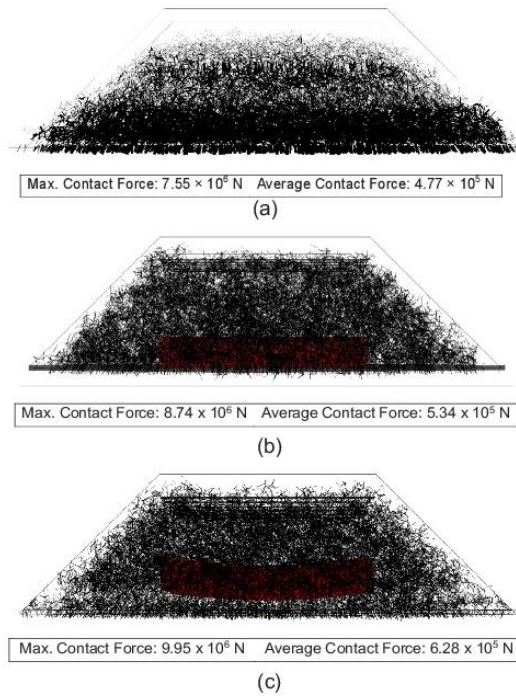


Fig. 12. Contact forces drawn at the same scale for straight embankment after the 20th cycle: (a) unreinforced; (b) geocell at base; and (c) geocell 50 mm above the base.

Unlike traditional FE analysis, the results of the DEM modeling show a somewhat irregular curve with slight fluctuations. These are associated with the rearrangement of clumps as the applied load increases. Overall, the vertical displacement rises with increased load for the three design cases, without defined yielding for the range of loads applied. It is clear that using a geocell panel has a noticeable influence on the vertical displacement of the embankment. With the same applied load, the geocell-reinforced embankment exhibits less vertical displacement than that of the unreinforced embankment. Specifically, given a load of 125 kPa, the vertical embankment displacements are 18.9 mm, when the geocell is located 50 mm above the base, 27.9 mm when the geocell is founded at the base, and 29.5 mm when the embankment is unreinforced. As shown in Fig. 10, the performance of the geocell reinforcement is in agreement with the test results presented by Leshchinsky and Ling [7], who conducted a similar monotonic loading test on a geocell-reinforced ballast embankment. This implies that incorporating a geocell panel in a railway embankment will reduce vertical displacement, and placing it 50 mm above the base, yields superior performance to that when the geocell is placed at the base. The superiority can be attributed to the position of geocell. The suspended geocell limits the loading propagating into the bottom 50 mm layer, which minimizes the settlement and lateral spreading of the bottom layer.

The monotonic loading curves, given in Fig. 10, can be subdivided into two zones: A and B, which correspond, respectively, to vertical displacements of less than 10 mm and those beyond 10 mm. In Zone A, the early stages of vertical embankment displacement, the sleepers displace in a similar fashion across the three cases examined and exhibit largely equal stiffness. This implies that the ballast skeleton supports the majority of the load when the load remains at a relatively low level, and the geocell is ‘at rest’ and contributes little to the embankment



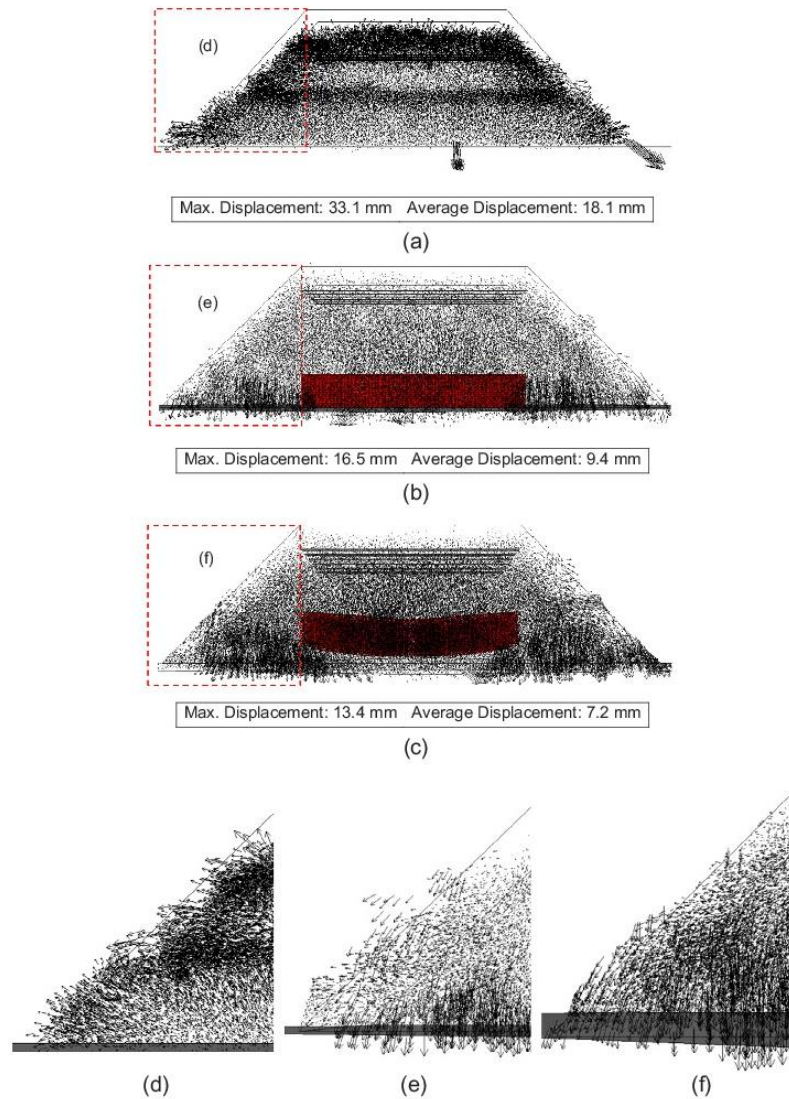


Fig. 13. Total displacement vectors drawn at the same scale for straight embankment after the 20th cycle: (a) unreinforced; (b) geocell at base; (c) geocell 50 mm above the base; (d–f) zoomed-in views of the left-hand-side unreinforced sections of three embankments.

stiffness. In Zone B, where the vertical displacement exceeds 10 mm, the geocell demonstrates a strain-hardening effect. It aids in reinforcing the ballast skeleton and increases the stiffness of the embankment. As a result, for an equal vertical displacement, the geocell-reinforced embankment is able to support a higher load than the unreinforced embankment. Due to the curves fluctuation, however, there is a section disagreeing the comparison. Where the vertical load falls into 165–220 kPa, the reinforced embankment with geocell at base experiences slightly higher vertical displacement than the unreinforced does, with a maximum difference of 2.3 mm. The curves fluctuation is caused by the DE simulation attaining convergence at some time steps. In addition, placing a geocell 50 mm above the base provides an improved stiffness response than placing it at the base.

Fig. 10 also presents a comparison of the stiffness development

between the simulation results and the prototype test results presented by Leshchinsky and Ling [7] who placed geocell at 100 mm above base. The inclusion of this set of experimental data is not for making quantitative comparison against the results obtained from this study (place geocell at 50 mm above base). The intention is to claim that by suspending geocell within ballast embankment, further improvements can be made, and it has been validated by previous experimentation. As can be seen, both sets of results show a short segment of low stiffness, in the early stages of monotonic loading, followed by a more prolonged development of improved stiffness. Once the results enter Zone B, placing geocell at 100 mm above the base becomes more advantageous in reducing sleeper's displacement than placing geocell at 50 mm does. The displacement difference is up to 5.2 mm when the vertical load reaches 285 kPa. From this point onward, the reinforcing effect decreases and

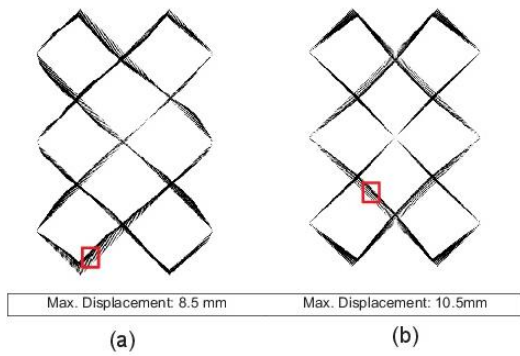


Fig. 14. Total displacement vectors drawn at the same scale for geocell panel after the 20th cycle: (a) geocell on base; (b) geocell at 50 mm above the base.

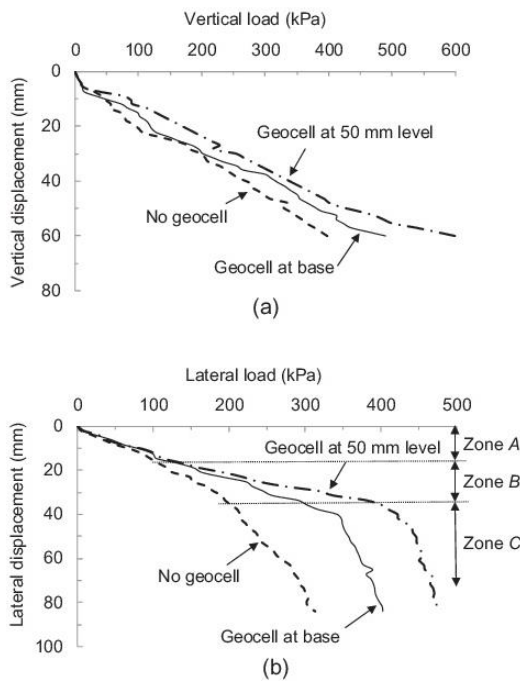


Fig. 15. Monotonic loading-induced sleepers movement in curved embankment: (a) Vertical displacement, (b) lateral displacement.

the two curves cross over where the vertical load increases to 498 kPa. Afterward, placing geocell at 50 mm offers better performance until the end of simulation. Overall, both studies indicate that suspending geocell within the ballast embankment can yield better load-bearing performance. This agreement, however, is not observed with the unreinforced embankments. Strain-softening was observed in the test embankment, whereas the simulated embankment exhibits strain-hardening throughout. Therefore, the unreinforced test embankment yields a lower secant stiffness than in the simulation: 2916 kPa/m for the test and 7975 kPa/m for the simulation, at a vertical displacement of 60 mm.

This disagreement arises mainly from the unconfined nature (in both longitudinal and transverse directions of the embankment) of the

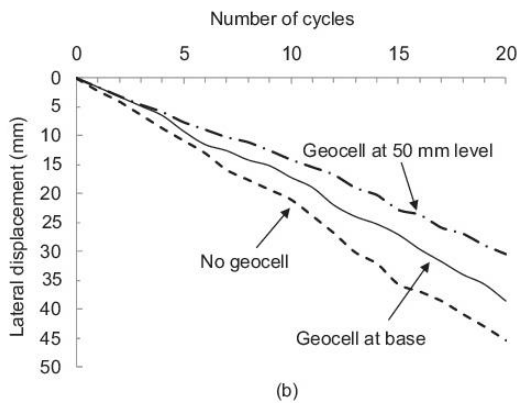
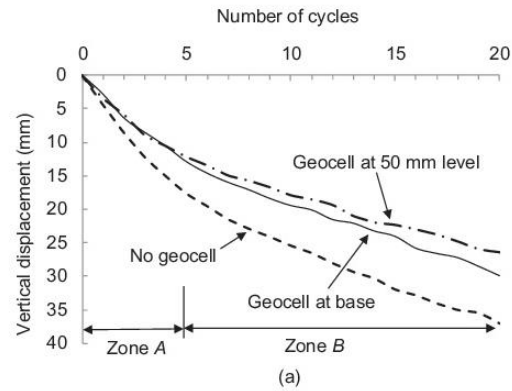


Fig. 16. Cyclic loading-induced sleepers movement in curved embankment: (a) vertical displacement; (b) lateral displacement.

prototypical test conducted by Leshchinsky and Ling [7]. The ballast can move freely in both directions, whereas the longitudinal movement is prohibited in the current models by installing two boundary walls. In addition, the difference between the test and simulated ballast infill, as well as other factors such as embankment geometry, loading plate size, geocell strength and boundary conditions, may also contribute to the significant difference in vertical displacement. The gravel that was used in the test is smaller on average than the ballast used in the simulation ( $D_{50} = 15.5$  mm and 35 mm, respectively) and so yields a lower shear strength. This is confirmed by the respective triaxial test results; for example, a shear strength of approximately 400 kPa for the gravel in the test [7] and 700 kPa for the coarser aggregate in the simulation, when subjected to the same confining pressure of 90 kPa. The lower shear strength for the gravel leads to its strain-softening behavior and lower stiffness. It is interesting to note that the discrepancy occurred with the unreinforced embankment, whose behavior is dissimilar to that of the reinforced embankment. This implies that the use of a geocell panel is able to mitigate potentially ‘weak’ properties of the ballast infill and increase stiffness through its reinforcement effects.

Fig. 11 shows sleeper’s vertical displacement plotted against the number of load cycles for the straight embankment under cyclic loading. It is evident that the geocell is effective in reducing vertical displacement associated with cyclic loading. During the initial 5 loading cycles (Zone A), all three cases exhibit a high displacement rate. Similar behavior is observed in a previous study [6] where geogrid is used. The early-stage quick displacement also agrees with the results



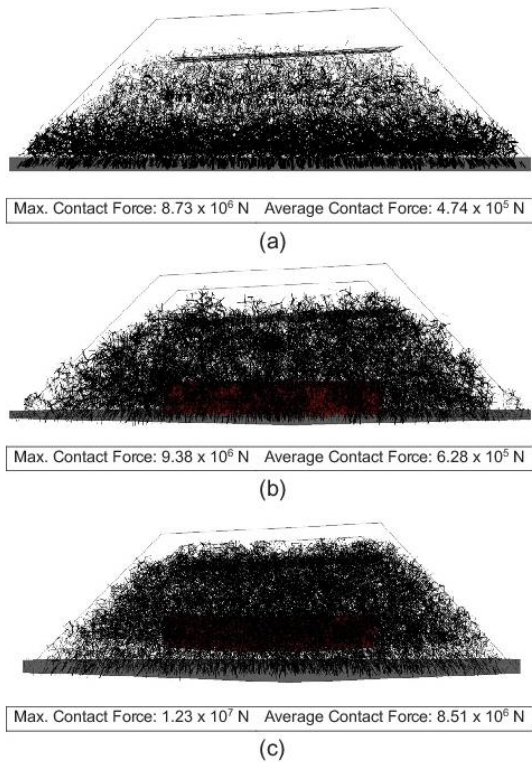


Fig. 17. Contact forces drawn at the same scale for the curved embankment after the 20th cycle: (a) unreinforced; (b) geocell at base; and (c) geocell 50 mm above the base.

obtained by Selig and Waters [38] who found that the relatively rapid displacement in the early stage is associated with the poorly consolidated nature of infills. In Zone A, the vertical displacement is reduced due to the use of geocell. However, no noticeable difference is observed between placing geocell at base and 50 mm above the base. The role of geocell becomes more pronounced as the cycle number increases which is suggested by the noticeably slower displacement rates in Zone B (5th to 20th loading cycle). This phenomenon can be attributed to the passive-confinement mechanism of geocell. Where cyclic loading continues, the infills is further compacted, stiffening the geocell mattress, which in turn provides better reinforcement to the ballast embankment. In Zone B, placing geocell at 50 mm above base outperforms placing geocell at base. The reinforcing effect improves slightly along with the increase of load cycle number, resulting in a final vertical displacement of 45.5 mm versus 52.3 mm if placing geocell at base. Interestingly, Chen et al. [6] who installed geogrid in ballast embankment as reinforcement at 50, 100 and 150 mm concluded otherwise. Their study reported that placing geogrid at lower levels (i.e. 50 mm above subgrade) better prevents the displacement. There is no clear reason to this disagreement, but the two geosynthetic materials work in different modes: cell confinement by the geocell and grid-particle friction by the geogrid. It is suggested that the confinement matter works better if placed next to the load on ground; the geogrid is placed at a lower level where the load becomes spread and reduced.

Comparison to the past study [7] has been made in the final vertical displacement only as the original displacement versus loading cycle relationship is unavailable. After the 20th cycle, the simulations show higher vertical displacement than that indicated by tests. The vertical

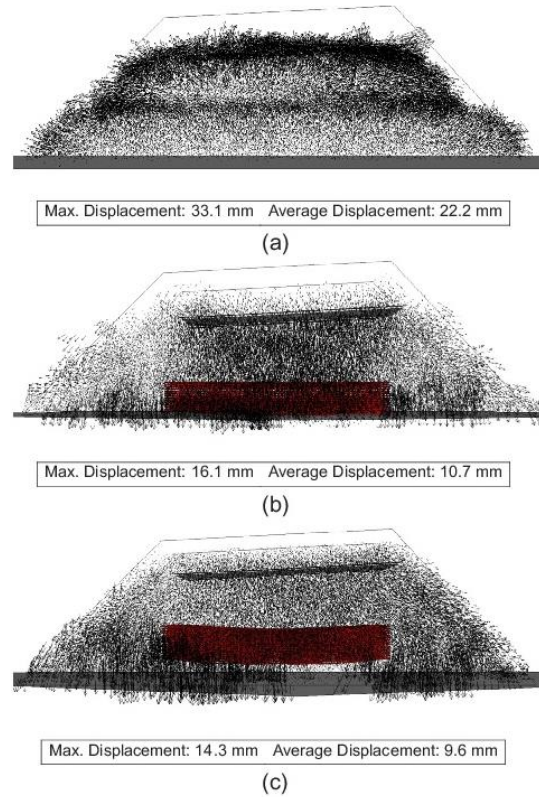


Fig. 18. Total displacement vectors drawn at the same scale for the curved embankment after the 20th cycle: (a) unreinforced; (b) geocell at base; and (c) geocell 50 mm above the base.

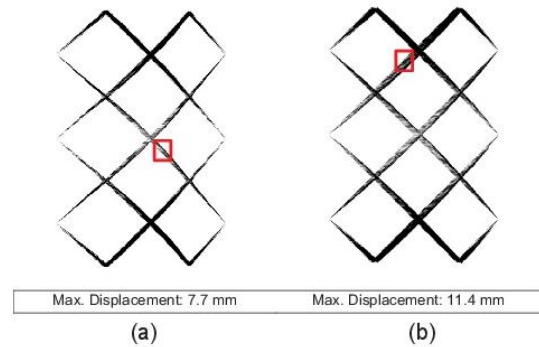


Fig. 19. Total displacement vectors drawn at the same scale for geocell panel after the 20th cycle: (a) geocell on base; (b) geocell at 50 mm above the base.

displacement is 67.5 mm for the simulation and approximately 48 mm for the unreinforced embankment test; and 52.3 mm when placing geocell at 50 mm above base for the simulation and approximately 31 mm for the test of the embankment incorporating the geocell at the 100 mm above base. In addition to the compaction effort, other factors that may contribute to the final settlement difference are the size effect at the plate-infill interface and the geocell types used. The simulations use a sleeper of 50 mm × 500 mm and infill of  $D_{50} = 35$  mm, and the test used a square plate, 356 mm × 356 mm in size, and infill of

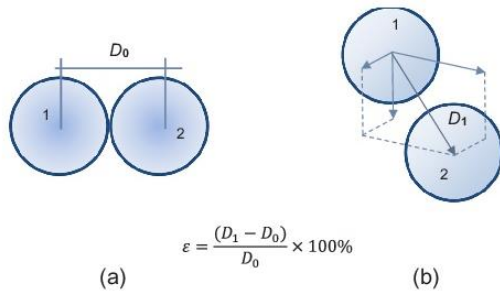


Fig. 20. Illustration on the calculation methodology of strain in geocell: (a) before displacement; (b) after displacement.

Table 4  
Geocell panel strains.

Position	Strain (%)			
	Monotonic loading		Cyclic loading	
	Geocell at base	Geocell 50 mm above base	Geocell at base	Geocell 50 mm above base
Junction a	29.1	34.1	10.9	11.3
Junction b	39.2	39.8	15.6	14.8
Junction c	39.2	21.1	18.7	18.3
Junction d	24.1	29.7	13.3	13.4
Junction e	30.2	38.9	12.0	10.2
Junction f	41.6	41.2	18.0	15.3
Junction g	26.9	33.0	16.2	10.0
Panel half A	18.9	35.3	19.8	16.1
Panel half B	24.4	39.1	27.0	22.7
Maximum strain	39.7	45.5	28.4	23.4

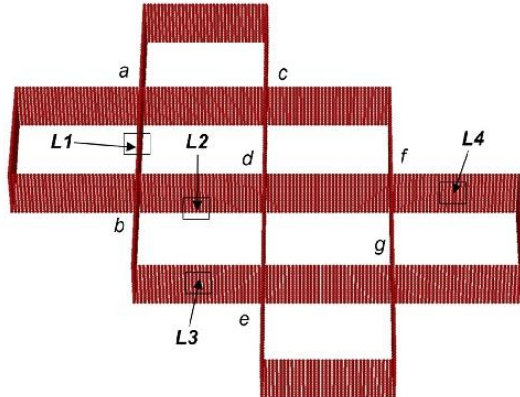


Fig. 21. Locations of maximum strain.

$D_{50} = 15.5$  mm. The smaller sleeper-infill size ratio for the simulations results in the sleepers ‘punching’ to a greater extent into the infill than the test does. This punching effect likely reduces with depth as the lateral resistance (arching) of the infill between neighboring sleepers increases, and the displacement stabilizes. On the other hand, Leshchinsky and Ling [7] adopted Novel Polymeric Alloy (NPA) geocell which exhibits higher stiffness and tensile strength (27 MPa) than typical HDPE geocell [14,31]. The material strength difference can also prevent embankment settlement.

In order to gain a greater insight into the force distribution and

transmission mechanism of unreinforced and reinforced ballast embankments, as shown in Fig. 12, contact forces are drawn at the same scale for the straight embankments after the 20th cycle. The contact forces are observed through the front cross section of the respective embankments. It can be seen that the contact forces develop in different patterns between the unreinforced and reinforced embankments. The unreinforced embankment shows an uneven distribution of contact forces. The forces adjacent to the base of the embankment are more concentrated than elsewhere in the embankment. In contrast, the contact forces for the geocell-reinforced embankments are distributed more evenly. This even distribution of contact forces helps eliminate over-stressing of the infill and reduces the likelihood of localized displacement and/or failure, thus improving the resilience of the embankment. In addition, an increase in the maximum and average contact forces within the ballast are recorded among the three cases simulated. The unreinforced case exhibits the lowest contact force value comparing to the two reinforced cases. This difference can be attributed to the higher internal contact forces induced by a reduced settlement. The internal stress caused by loading cannot dissipate through particle movement as it is restricted by the geocell panel. The highest contact force is observed where the geocell panel is placed 50 mm above the base, which implies less ballast movement should be expected. This observation agrees with results shown in Fig. 10 (monotonic loading case). That is, at the same settlement, the reinforced cases sustain loads greater than the unreinforced case does.

Fig. 13 shows the total particle displacement vectors (i.e. the combination of vertical and lateral displacement) of the ballast after the 20th cycle, again drawn at the same scale as that shown previously to allow visualization of the microstructure strain evolution of the embankments. Fig. 13(c) is tilted by 5° for better visualization of the displacement vectors, which causes the vectors appear slightly denser and longer. Apart from the reduced particle displacement, the major difference between the unreinforced and the reinforced embankments lies in the direction of the ballast displacement. The infill in the reinforced embankments [Fig. 13(b and c)] displace mainly toward the base, whereas the infill in the unreinforced embankment [Fig. 13(a)] tends to move laterally. This can be better visualized in Fig. 13(d–f) which provide zoomed-in views of the left-hand-side unreinforced sections of three embankments. These observations confirm the ability of the geocell panel to prevent the ballast infill from spreading. That is, the geocell panel helps confine the infills, creating a rigid pad. In this way, the pad effectively absorbs overlying loads and transfers them downward, avoiding or reducing lateral spreading. This is consistent with the distribution of contact forces shown previously in Fig. 12(b and c), where the contact force concentration is less significant at the base of the embankments and thus reduces embankment displacement. The central part of the elevated geocell panel [Fig. 13(c)] undergoes modest subsidence (approximately 10 mm), which suggests slight lateral movement of the infill underlying the panel.

Fig. 14 shows the total displacement vectors for the geocell panels after the 20th loading cycle, as well as the maximum displacements and their approximate locations. These displacement vectors are scaled up by a factor of 50 in order to achieve better visualization. As can be seen, the panels undergo a limited amount of displacement and they hence remain effectively in their original configuration after repetitive loading, demonstrating their strength. In the case where the geocell is placed at the base [Fig. 14(a)], the maximum displacement occurs at the bottom-left of the panel. This location shifts upward when the panel is located 50 mm above the base. The relocation implies that the geocell panel settles noticeably (10 mm approximately) together with the ballast assembly. In addition, the displacement is not position-dependent. All cell walls, at the center and along the edges, undergo a similar level of deformation. This behavior aids in evening out the stresses acting on the panel, eliminating local failures, maintaining its long-term reinforcement capability and, more importantly, accommodating the displacement of the infill and harmonizing the particle contact forces.



#### 4.2. Curved embankment

The vertical and horizontal displacements plotted against the corresponding loads of the curved embankment that was subjected to the resultant load,  $P_R$ , (Fig. 9) are shown in Fig. 15. The load-vertical displacement curves [Fig. 15(a)] develop in a form similar to those observed with the straight embankment [Fig. 10]. Non-yielding is clearly evident upon the load of 600 kPa. The three curves exhibit largely equal stiffness when the displacement is low (i.e. less than 10 mm), where the vertical displacement mainly arises from rearrangement of the uncrushable infill (in the DEM model, in any case) and the geocell provides a marginal contribution to stiffness. The geocell's reinforcement effect becomes clear when the displacement exceeds 10 mm. It can be seen that the geocell-reinforced embankments obtain stiffness higher than that of the unreinforced embankment, and so support a greater load, given the same vertical displacement. Placing the geocell 50 mm above the base yields a higher stiffness. Similar improvement occurs in the lateral direction [Fig. 15(b)], where the sleepers of the reinforced embankments displace less than the sleepers of the unreinforced embankment, with an equal resultant load. This is attributed to the geocell enhancing the interlocking of the infill and so restraining the rearrangement and rotation of the ballast particles. In the later stages of loading (i.e. > 40 mm lateral displacement), lateral yielding occurs in all simulations, showing a marked displacement in response to the cyclic loading. This is a result of the sleepers having partially moved out of the region influenced by the geocell, and thus having to rely on the shoulder ballast to provide lateral resistance. This observation is valid for all simulations performed for curved embankments. Although this phenomenon is unlikely to occur in actual railways, as catastrophic accidents can be caused due to de-railing, the results are presented for the purpose of demonstrating the improvements derived from placing geocell in railway ballast embankments.

Fig. 16 shows the vertical and lateral displacement of the sleepers due to cyclic loading. As was evident with monotonic loading, the geocell-reinforced embankments outperform the unreinforced embankment. The reinforced embankments exhibit less vertical and lateral displacements than those observed in the unreinforced embankment. Placing a geocell 50 mm above the base, again, better controls displacement in both the vertical and horizontal directions. The vertical displacement [Fig. 16(a)] is more pronounced over the first 5 cycles, and then shows a decreased rate over the remaining cycles. The lateral displacement of the sleepers is relatively high, given the low number of cycles [Fig. 16(b)]. This is likely caused by the unrestrained nature of the sleepers, where the restraining influence of the track structure, such as the rails, rail anchors and fastenings, were not taken into account in the simulations, as mentioned earlier. As a result, the sleepers are able to displace more freely than would occur in the field.

Fig. 17 shows the inter-particle contact forces drawn at the same scale after the 20th load cycle. As for the straight embankments, the geocell panels also appear to promote an even stress distribution for the curved embankments. This is in agreement with the particle displacement vectors shown in Fig. 18, where reduced spreading is observed for the reinforced embankments, when compared with the unreinforced embankment. Moreover, comparing the displacement vectors with those for the straight embankments (Fig. 12) implies that the geocell panels in the curved embankments are similarly effective in forming a relatively rigid platform and to mitigate ballast spreading.

Fig. 19 shows the total displacement vectors for the geocell panels after the 20th cycle. The panels maintain their respective initial shape and demonstrate the geocell's capability to sustain the lateral load for the curved embankments. The geocell walls, in particular the walls adjacent to the longitudinal centerlines, deflect to the right – in line with the direction of the resultant forces. The concurrent deflection of the walls helps counteract the lateral load, confine the lateral load within the area of the panel, and reduce spreading of the infill along the edges. The panel situated 50 mm above the base appears to deflect

slightly more than does the panel at the base. This is consistent with the geometric deformation which occurs in a 'suspended' panel [Fig. 18(c)], and suggests it is likely to degrade sooner than the panel located at the base. This can be examined through additional case studies, such as increasing load cycles and placing panels at higher levels in the embankment. This is, however, beyond the scope of the present paper.

To gain a further insight into the deflection of the geocell panel, geocell strains are captured. As illustrated in Fig. 20, for a pair of neighboring spheres of interest, the strain,  $\epsilon$ , is defined as the edge-to-edge distance after displacement,  $D_1 - D_0$ , to the initial center-to-center distance,  $D_0$ . The strain values at locations of interest are summarized in Table 4. These include junctions *a* to *g*, panel halves *A* and *B*, as shown in Fig. 7(d), and locations of maximum strain for the geocell panels at the base and 50 mm above the base, subjected to the monotonic and cyclic loading scenarios. Panel halves *A* and *B* rest on the lower and the higher side of the embankment, respectively.

The initial center-to-center distance is 5 mm, as shown in Fig. 2(b). The strain at a junction is calculated as the average strain of all spheres within 20 mm (i.e. 11.4% of the cell side) to the junction. The selected percentage is intended to reflect the strain in the proximity of the junction. The strain for either half panel is the average strain of all the spheres belonging to that half panel. The strain values in Table 4 show that the geocell deforms at every junction with varying magnitude, for instance, ranging from 24.1% to 41.6% for the geocell at the base when subjected to monotonic loading. Where the sleepers advance less under the cyclic loading, noticeably lower strains of 14.1% on average occur to the junctions. There is a clear difference in strain between the panel halves *A* and *B*, where all other design details remain the same. For instance, the average strain is 18.5% for panel half *A* and 24.9% for panel half *B* under monotonic loading. This implies that greater deflection occurs at the part of the geocell that provides direct reaction to the inclined train load  $P_R$ . Lower strains occur to both halves where the geocell is placed 50 mm above the base than the geocell placed at the base, which agrees with the embankment displacement results shown in Figs. 11 and 16. Under the monotonic loading, the entire panel is subject to a maximum strain of 39.7%, if placed at the base, and 45.6%, when placed 50 mm above. If subjected to the cyclic loading, the panel shows a maximum strain of 28.4%, when at the base, and 23.4%, when 50 mm above. The magnitude of these strains indicates that the geocell panel remains at the pre-failure state for the load levels simulated. The approximate locations, L1 to L4, where maximum strains were recorded, are highlighted in Fig. 21; i.e. L1 for 39.7% and L2 for 45.6% under the monotonic loading scenario, and L3 for 28.4% and L4 for 23.4% under the cyclic loading scenario. There is no clear pattern to the locations of maximum strain, however, as can be seen, they are all consistent with the center of a cell-wall. This indicates that cell-walls undergo greater deflection than the junctions do, as one might expect.

#### 5. Conclusions

This study assesses the use of geocells in reinforcing railway ballast embankments. Discrete element modeling has been conducted, using clumped particles to simulate angular ballast, to evaluate bearing capacity, vertical displacement and lateral spreading of the embankment, as well as providing insights into the micro-behavior of the ballast infill and the geocell, including contact forces and displacements. Straight and curved embankments have been subjected to monotonic and cyclic loading conditions and the modeling results have been compared with previous, published test results. The conclusions of this study are as follows:

1. The simulation results for the straight, reinforced embankment are in reasonably good agreement with the test results. This suggests that the discrete element modeling is valid and is an appropriate method to assess the mechanical response of railway embankments.
2. For the unreinforced, straight embankment, however, simulation



results show modest agreement with the past test results. The sub-optimal agreement may be attributed to the differences in the particle size distribution, embankment geometry and loading magnitude. These factors influence the embankment performance where reinforcement is not used.

- The presence of a geocell within the ballast stiffens both straight and curved embankments. Geocell-reinforced embankments exhibit less vertical displacement and lateral spreading compared with unreinforced embankments and so aid in maintaining a safer track alignment in the longer term. The embankments with a geocell suspended 50 mm above the base are stiffer than the embankments with a geocell located at the interface between the ballast and the subgrade. The former, however, deflects more than the latter and so risks having a reduced operational life. The geocell embedment depth results disagree with results in Chen et al. [6] which used geogrid to reinforce straight embankment. Their study suggests that placing geogrid at a higher level causes less vertical displacement than placing it close to the subgrade.
- The geocell constrains the displacement of the encased ballast infill to form a relatively solid mattress. The mattress helps absorb overlying loads, increase the stiffness of the embankment, reduce spreading of the infill and balance forces in the embankment.

Whilst the study proposes a valid approach to demonstrate and examine the effects of reinforcing railway ballast with geocell, a number of limitations and assumptions were adopted to undertake successfully the DEM simulation:

- The geocell model was calibrated solely against a series of tensile strength tests. Other properties such as puncture resistivity, flexural stiffness and torsion stiffness were not considered in the current study. Attempts will be made to incorporate these material properties in future studies to improve the reliability of the modeling framework.
- Whilst the use of clumps provides a more accurate representation of ballast angularity, when compared with the adoption of entirely spherical particles, their shape does not fully reflect actual ballast angularities and, hence, have limited capability to simulate accurately ballast interlock and inter-particle friction. Defining the clumps as non-breakable in the simulation, may also result in overestimating the long-term performance of the embankment. It is plausible to conduct a 3D simulation of the embankment, but the scaled-down embankment may compromise the simulation accuracy.
- In simulation, the ballast is calibrated against the monotonic test results. The calibration can possibly improve where cyclic loading test results are available and used. However, as stated in previous study [33], the calibration against cyclic test results can be extremely time consuming. Due to this reason, this calibration step was neglected, enabling a focus on the simulation of ballast embankments.
- Due to the limited number of load cycles applied to the embankment, the results presented may not accurately reflect the long-term performance of the ballast embankment. Along with advancement in PFC3D and computational capacity, this issue can be resolved in future studies. In addition, the number and location of inter-clump parallel-bond breakage, which can provide in-sight on the ballast rearrangement, was not recorded. It will be taken into consideration in our future studies when ballast breakage is incorporated into the modeling framework.

#### Acknowledgement

The authors wish to thank Mr. Rod Fyfe from Geofabrics Australasia for his assistance in this research.

#### References

- Hossain Z, Indraratna B, Darve F, Thakur PK. DEM analysis of angular ballast breakage under cyclic loading. *Geomech Geoeng* 2007;2(3):175–81.
- Salim W, Indraratna B. A new elastoplastic constitutive model for coarse granular aggregates incorporating particle breakage. *Can Geotech J* 2004;41(4):657–71.
- Yan Y, Zhao J, Ji S. Discrete element analysis of breakage of irregularly shaped railway ballast. *Geomech Geoeng* 2014;1–9.
- Indraratna B, Ionewscu D, Christie HD. Shear behavior of railway ballast based on large-scale triaxial tests. *J Geotech Geoenviron Eng* 1998;124(5):439–49.
- ARTC. Australian Rail Track Corporation 2016 Annual Report. Australia: Australian Rail Track Corporation Ltd.; 2016.
- Chen C, McDowell GR, Thom NH. Discrete element modelling of cyclic loads of geogrid-reinforced ballast under confined and unconfined conditions. *Geotext Geomembr* 2012;35:76–86.
- Leshchinsky B, Ling H. Effects of geocell confinement on strength and deformation behavior of gravel. *J Geotech Geoenviron Eng* 2013;139(2):340–52.
- Leshchinsky B, Ling H. Numerical modeling of behavior of railway ballasted structure with geocell confinement. *Geotext Geomembr* 2013;36:33–43.
- Miao C-X, Zheng J-J, Zhang R-J, Cui L. DEM modeling of pullout behavior of geogrid reinforced ballast: the effect of particle shape. *Comput Geotech* 2017;81:249–61.
- Hegde A, Sitharam TG. 3-Dimensional numerical modelling of geocell reinforced sand beds. *Geotext Geomembr* 2015;43(2):171–81.
- Moghaddas Tafreshi SN, Shaghghi T, Tavakoli Mehrjardi G, Dawson AR, Ghadrani M. A simplified method for predicting the settlement of circular footings on multi-layered geocell-reinforced non-cohesive soils. *Geotext Geomembr* 2015;43:332–44.
- Tanyu BF, Aydiilek AH, Lau AW, Edil TB, Benson CH. Laboratory evaluation of geocell-reinforced gravel subbase over poor subgrades. *Geosynth Int* 2013;20(2):47–61.
- Dash SK. Effect of geocell type on load-carrying mechanisms of geocell-reinforced sand foundations. *Int J Geomech* 2012;12(5):537–48.
- Yang X, Han J, Polkarek SK, Manandhar C, Parsons RL, Leshchinsky D, et al. Accelerated pavement testing of unpaved roads with geocell-reinforced sand bases. *Geotext Geomembr* 2012;32:95–103.
- Oliaei M, Kouzegaran S. Efficiency of cellular geosynthetics for foundation reinforcement. *Geotext Geomembr* 2017;45:11–22.
- Dash SK, Bora MC. Improved performance of soft clay foundations using stone columns and geocell-sand mattress. *Geotext Geomembr* 2013;41:26–35.
- Mehdipour I, Ghazavi M, Moayed RZ. Numerical study on stability analysis of geocell reinforced slopes by considering the bending effect. *Geotext Geomembr* 2013;37:23–34.
- Chen R-H, Wu C-P, Huang F-C, Shen C-W. Numerical analysis of geocell-reinforced retaining structures. *Geotext Geomembr* 2013;39:51–62.
- Zhang L, Zhao M, Shi C, Zhao H. Bearing capacity of geocell reinforcement in embankment engineering. *Geotext Geomembr* 2010;28(5):475–82.
- Madhavi Latha G, Rajagopal K. Parametric finite element analyses of geocell-supported embankments. *Can Geotech J* 2007;44(8):917–27.
- Nishiura D, Sakai H, Aikawa A, Tsuzuki S, Sakaguchi H. Novel discrete element modeling coupled with finite element method for investigating ballasted railway track dynamics. *Comput Geotech* 2018;96:40–54.
- Xu M, Hong J, Song E. DEM study on the effect of particle breakage on the macro- and micro-behavior of rockfill sheared along different stress paths. *Comput Geotech* 2017;89:113–27.
- Zhang L, Zhao M, Shi C, Zhao H. Nonlinear analysis of a geocell mattress on an elastic-plastic foundation. *Comput Geotech* 2012;42:204–11.
- Liu Y, Deng A, Jaska M. Discrete element modelling of geocell-reinforced track ballast under static and cyclic loading. In: *Proc The 12th Australia-New Zealand Conference on Geomechanics*, Wellington, New Zealand; 2015. p. 279–86.
- Cundall PA, Strack ODL. Discrete numerical model for granular assemblies. *Geotechnique* 1979;29(1):41–65.
- Itasca. PFC3D 4.0 User's Manual. Minnesota, USA: Itasca Consulting Group Inc, 2009.
- Imzábaj J, Salazar F, Oñate E. Numerical modelling of granular materials with spherical discrete particles and the bounded rolling friction model. Application to railway ballast. *Comput Geotech*. 2017;85:220–9.
- Itasca. Particle Flow Code in Three Dimensions Version 4. Minnesota, USA: Itasca Consulting Group Inc; 2009.
- SAI. Determination of Tensile Properties of Plastics Materials. AS 1145.3: Standards Australia International Ltd.; 2001.
- Poyondy DO, Cundall PA. A bonded-particle model for rock. *Int J Rock Mech Min* 2004;41(8):1329–64.
- Le Pen IM, Powrie W, Zervos A, Ahmed S, Aingaran S. Dependence of shape on particle size for a crushed rock railway ballast. *Granul Matter* 2013;15(6):849–61.
- Lim WL, McDowell GR. Discrete element modelling of railway ballast. *Granul Matter* 2005;7(1):19–29.
- Lu M, McDowell GR. DEM of railway ballast under monotonic and cyclic triaxial loading. *Geotechnique* 2010;60(6):459–67.
- ARTC. Engineering (Track & Civil) Code of Practice. Section 2 Sleepers and Fastenings. Australia: Australian Rail Track Corporation Ltd.; 2017.
- ARTC. Engineering (Track & Civil) Code of Practice. Section 5 Track Geometry. Australia: Australian Rail Track Corporation Ltd.; 2016.
- ARTC. Route Access Standard. General Information. Australia: Australian Rail Track Corporation Ltd.; 2014.
- Shenton MJ. Deformation of Railway Ballast Under Repeated Loading Conditions. *Railroad Track Mechanics and Technology*. Derby: British Railway Research and Development Division; 1978. p. 405–25.
- Selig ET, Waters JW. *Track geotechnology and substructure management*. London, UK: Thomas Telford; 1994.

**INTENTIONALLY BLANK**